

# COASTAL WATER CLARITY MODELING FEASIBILITY STUDY

## FINAL REPORT

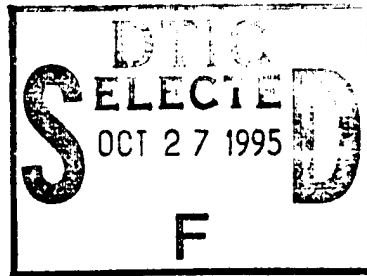
28 February 1995

•Original  
plates  
ion:  
wh'



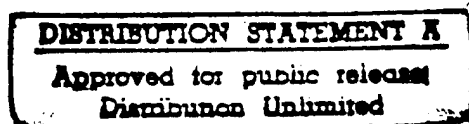
*Science Applications International Corporation*

*An Employee-Owned Company*

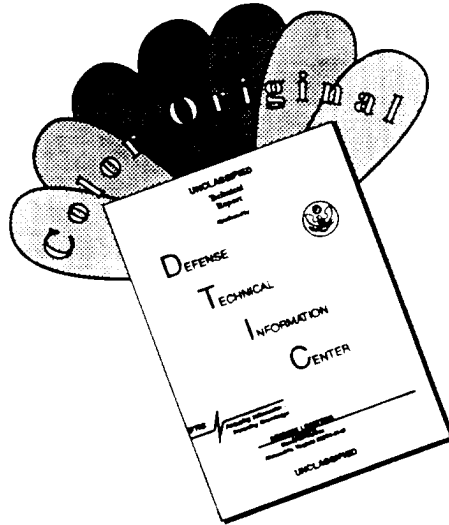


19951026 083

•Original contains color  
plates: All DTIC reproduct-  
ions will be in black and  
white



# DISCLAIMER NOTICE



THIS DOCUMENT IS BEST QUALITY AVAILABLE. THE COPY FURNISHED TO DTIC CONTAINED A SIGNIFICANT NUMBER OF COLOR PAGES WHICH DO NOT REPRODUCE LEGIBLY ON BLACK AND WHITE MICROFICHE.

# COASTAL WATER CLARITY MODELING FEASIBILITY STUDY

## FINAL REPORT

28 February 1995

\*Original contains color  
plates: All DTIC reproduct-  
ions will be in black and  
white\*

Prepared by:

Robert R. Hammond  
Scott A. Jenkins (Consultant)  
Joan S. Cleveland (Consultant)  
John C. Talcott  
Alan L. Heath  
Joe Wasyl (Consultant)  
Stanley G. Goosby  
Kurt F. Schmitt  
Lisa A. Levin (Consultant)  
Bonnie MacRitchie

Science Applications International Corporation  
Technology Research Group  
10260 Campus Point Drive  
San Diego, CA 92121

### DISTRIBUTION STATEMENT A

Approved for public release  
Distribution Unlimited

Submitted to:

Office of Naval Research  
800 North Quincy Street  
Arlington, VA 22217-5000

Accession For	
NTIS CRA&I	<input checked="" type="checkbox"/>
DTIC TAB	<input type="checkbox"/>
Unannounced	<input type="checkbox"/>
Justification	
By <i>per lts</i>	
Distribution /	
Availability Codes	
Dist	Avail and/or Special
A-1	

In fulfillment of:  
Basic Contract No. N00014-93-C-0140



OFFICE OF THE UNDER SECRETARY OF DEFENSE (ACQUISITION)  
DEFENSE TECHNICAL INFORMATION CENTER  
CAMERON STATION  
ALEXANDRIA, VIRGINIA 22304-6145

IN REPLY  
REFER TO

DTIC-OCC

SUBJECT: Distribution Statements on Technical Documents

TO: OFFICE OF NAVAL RESEARCH  
CORPORATE PROGRAMS DIVISION  
ONR 353  
800 NORTH QUINCY STREET  
ARLINGTON, VA 22217-5660

1. Reference: DoD Directive 5230.24, Distribution Statements on Technical Documents, 18 Mar 87.

2. The Defense Technical Information Center received the enclosed report (referenced below) which is not marked in accordance with the above reference.

FINAL REPORT  
N00014-93-C-0140  
TITLE: COASTAL WATER CLARITY  
MODELING FEASIBILITY STUDY

3. We request the appropriate distribution statement be assigned and the report returned to DTIC within 5 working days.

4. Approved distribution statements are listed on the reverse of this letter. If you have any questions regarding these statements, call DTIC's Cataloging Branch, (703) 274-6837.

FOR THE ADMINISTRATOR:

1 Encl

GOPALAKRISHNAN NAIR  
Chief, Cataloging Branch

FL-171  
Jul 93

1995 1026 083



DISTRIBUTION STATEMENT A:

APPROVED FOR PUBLIC RELEASE: DISTRIBUTION IS UNLIMITED

DISTRIBUTION STATEMENT B:

DISTRIBUTION AUTHORIZED TO U.S. GOVERNMENT AGENCIES ONLY;  
(Indicate Reason and Date Below). OTHER REQUESTS FOR THIS DOCUMENT SHALL BE REFERRED  
TO (Indicate Controlling DoD Office Below).

DISTRIBUTION STATEMENT C:

DISTRIBUTION AUTHORIZED TO U.S. GOVERNMENT AGENCIES AND THEIR CONTRACTORS;  
(Indicate Reason and Date Below). OTHER REQUESTS FOR THIS DOCUMENT SHALL BE REFERRED  
TO (Indicate Controlling DoD Office Below).

DISTRIBUTION STATEMENT D:

DISTRIBUTION AUTHORIZED TO DOD AND U.S. DOD CONTRACTORS ONLY; (Indicate Reason  
and Date Below). OTHER REQUESTS SHALL BE REFERRED TO (Indicate Controlling DoD Office Below).

DISTRIBUTION STATEMENT E:

DISTRIBUTION AUTHORIZED TO DOD COMPONENTS ONLY; (Indicate Reason and Date Below).  
OTHER REQUESTS SHALL BE REFERRED TO (Indicate Controlling DoD Office Below).

DISTRIBUTION STATEMENT F:

FURTHER DISSEMINATION ONLY AS DIRECTED BY (Indicate Controlling DoD Office and Date  
Below) or HIGHER DOD AUTHORITY.

DISTRIBUTION STATEMENT X:

DISTRIBUTION AUTHORIZED TO U.S. GOVERNMENT AGENCIES AND PRIVATE INDIVIDUALS  
OR ENTERPRISES ELIGIBLE TO OBTAIN EXPORT-CONTROLLED TECHNICAL DATA IN ACCORDANCE  
WITH DOD DIRECTIVE 5230.25, WITHHOLDING OF UNCLASSIFIED TECHNICAL DATA FROM PUBLIC  
DISCLOSURE, 6 Nov 1984 (Indicate date of determination). CONTROLLING DOD OFFICE IS (Indicate  
Controlling DoD Office).

The cited documents has been reviewed by competent authority and the following distribution statement is  
hereby authorized.

<u>A</u> (Statement)	OFFICE OF NAVAL RESEARCH CORPORATE PROGRAMS DIVISION ONR 353 800 NORTH QUINCY STREET ARLINGTON, VA 22217-5660	_____ (Controlling DoD Office Name)
_____ (Reason)	DEBRA T. HUGHES DEPUTY DIRECTOR CORPORATE PROGRAMS OFFICE	_____ (Controlling DoD Office Address, City, State, Zip)
<u>Debra T. Hughes</u> (Signature & Typed Name)	_____ (Assigning Office)	<u>19 SEP 1995</u> (Date Statement Assigned)

## TABLE OF CONTENTS

SECTION	PAGE
ABSTRACT .....	iv
1.0 BACKGROUND .....	1-1
2.0 PVM SUMMARY & DESCRIPTION .....	2-1
2.1 Fixed Parameters .....	2-3
a. General Site Attributes .....	2-6
b. Boundary values .....	2-8
c. Archived and Tabled Data Inputs .....	2-10
2.2 Time Variable Inputs .....	2-10
a. Time Variable Surface Forecasts .....	2-10
b. TIROS Twice Daily Local Time Variable Input .....	2-11
2.3 Simulation Procedures .....	2-12
a. Basic Environmental Descriptions .....	2-13
b. Particulate Source Models .....	2-13
c. Spatial Distribution Models .....	2-15
d. Optical Models .....	2-16
e. Image/Plot Comparisons .....	2-18
2.4 Suggested PVM Input/Model Improvements .....	2-19
3.0 SUSPENDED PARTICLE DISPERSION MODEL FOR COASTAL WATERS .....	3-1
3.1 Architecture .....	3-2
3.2 Module Detail and Theory .....	3-9
a. OCEANBAT· f .....	3-9
b. OCEANRDS· f .....	3-10
c. SEDXPORT· f .....	3-11
1. BOTTMBND· f and BOTXPORT· f .....	3-12
2. SURXPORT· f .....	3-27
3. RIVXPORT· f .....	3-29
d. TIDES1DAY· f and TIDECUR· f .....	3-31
e. NULLPT· f .....	3-33
f. BIOXPORT· f .....	3-34
3.3 24-Hour Simulation .....	3-37
a. Initialization .....	3-37
b. Time Step Execution .....	3-38
c. Calibration .....	3-42
d. Results .....	3-43
3.4 Sensitivity Analysis .....	3-62
a. Bathymetry Resolution Limitations .....	3-62

	b. Bottom Composition .....	3-66
	c. Sensitivity to Wind.....	3-66
	d. Sensitivity to Wave Height .....	3-76
	e. Sensitivity to River Discharge .....	3-82
3.5	Discussion of Data Requirements .....	3-82
	a. Updated Files .....	3-84
	b. Inventory Files .....	3-84
4.0	BIOLOGICAL COMPONENTS OF THE COASTAL WATER CLARITY MODELING FEASIBILITY STUDY .....	4-1
4.1	Phytoplankton Biomass Model .....	4-4
4.1.1	Model Structure.....	4-4
4.1.2	Phytoplankton Size Classes .....	4-5
4.1.3	Irradiance at Surface and Depth.....	4-6
4.1.4	Growth Terms .....	4-8
	a. Photosynthesis as a Function of Irradiance .....	4-8
	b. Influence of Nitrate on Photosynthetic Rate .....	4-9
	c. Excretion of Photosynthate .....	4-10
	d. Growth Rate .....	4-11
4.1.5	Nitrate Fluxes .....	4-11
4.1.6	Losses .....	4-12
	a. Respiration .....	4-13
	b. Mortality .....	4-13
	c. Grazing .....	4-13
4.1.7	Local Changes in Biomass .....	4-15
4.1.8	Sinking Rates .....	4-17
4.1.9	Initial Conditions.....	4-17
	a. Biomass .....	4-17
	b. Nitrate.....	4-20
4.1.10	Results of Phytoplankton Biomass Prediction Model.....	4-21
4.1.10.1	Local Growth and Loss Model.....	4-21
4.1.10.2	Standard 24-hour Run of Integrated Model .....	4-22
	a. Temporal Patterns .....	4-22
	b. Spatial Patterns.....	4-23
4.1.10.3	10-day Growth and Mixing Run .....	4-23
4.1.11	Sensitivity Analysis for Growth Model; Effects on Biomass .....	4-24
4.1.12	Discussion of Phytoplankton Biomass Prediction Model.....	4-25
4.2	Colored Dissolved Organic Matter Model .....	4-27
4.2.1	Model Structure.....	4-27
4.2.2	Sources of CDOM.....	4-28

	a. River Sources .....	4-28
	b. Phytoplankton Sources .....	4-30
	c. Macrophyte Sources .....	4-30
4.2.3	Losses of CDOM .....	4-31
	a. Photodegradation .....	4-31
	b. Bacterial Consumption .....	4-32
4.2.4	Results of CDOM Prediction Module .....	4-32
4.3	Benthic Sources and Effects .....	4-32
4.3.1	Release of Material from the Seafloor .....	4-33
	a. Active Release .....	4-33
	1. Sediments .....	4-33
	2. Reproductive Products .....	4-35
	3. Adults, Waste Products, and Dissolved Substances .....	4-36
	b. Passive Resuspension of Benthic Organisms .....	4-37
4.3.2	Benthos as a Sink .....	4-38
	a. Active Removal of Material from the Water by Benthos .....	4-38
	b. Passive Removal of Material from the Water by Benthos .....	4-39
4.3.3	Light Attenuation by Shading .....	4-40
4.3.4	Indirect Effects of Benthos .....	4-40
	a. Sediment Stability .....	4-40
	b. Solutes and Gases .....	4-42
4.3.5	Summary Remarks .....	4-43
4.5	Summary and Recommendations .....	4-44
5.0	OPTICS MODULE FOR THE PREDICTIVE VISIBILITY MODEL .....	5-1
5.1	Optics Module Development .....	5-2
5.2	Particle Size Distribution .....	5-4
5.3	Optical Property Estimation Procedures .....	5-8
	5.3.1 Particulate scattering .....	5-11
	5.3.2 Particulate absorption .....	5-21
5.4	Oceanside Nearshore Example .....	5-24
5.5	Sensitivity to Sediment & Biological Parameters .....	5-30
5.6	Model Status & Recommendations .....	5-34
6.0	CONCLUSIONS AND RECOMMENDATIONS .....	6-1
7.0	REFERENCES .....	7-1
	APPENDIX A .....	A-1
	APPENDIX B .....	B-1

## ABSTRACT

The goal of the ONR Coastal Water Clarity Program was to assess the feasibility of developing an integrated computer model for predicting diurnal and episodic changes in near-coastal water optical properties. The approach was to build a detailed coastal environmental computer simulation, based on local meteorological, hydrological, and oceanographic observables, to predict spatial and temporal variations of optically significant constituents in the coastal water column. Because comprehensive space/time data for the nearshore regime is not available, the level of feasibility was limited to demonstration of a working predictive visibility model (PVM), producing reasonable optical and interim environmental parameter variations over extended periods of time (multiple days).

This PVM resides on a Sun SPARC workstation and provides spatial and temporal estimates of suspended sediment, biological populations, and hydrodynamic transport, and their impact on subsurface optical properties. Inorganic source estimates include river, surf, and bottom resuspension and biological estimates include time variable plankton growth, as well as dissolved organic materials of river and plankton origin.

Off-line coastal topography, bathymetry, hydrology, and processed remote sensor input are required in GIS data layers to begin the simulation. The model concept would employ sets of calibration parameters selected to cover generic geological, biological, benthic, and optical environmental situations. From these categories, composite sites would be established to provide the spatial and temporal estimates required. This report evaluates sensitivity to required input parameters and the parametric resolutions required for this type of simulation. The assumptions employed, and critical experiments required, for model improvement are also discussed.

The PVM is demonstrated for one California coastal location. Spatial and temporal parameters are estimated at nominal 90 meter grid spacings on a 200 x 200 array (= 10 x 10 mi), on 2-hour intervals requiring roughly 15 minutes of computation time per interval. The space and time scales are

selected to adequately sample the two principle environmental drivers, swell waves, and tidal currents, which are fortunately the most predictable environmental parameters. This demonstration case optimistically suggests that the PVM can be used to estimate not only subsurface optical properties, but the dynamic trajectories of other point and distributed contaminant sources in the nearshore coastal region.

## 1.0 BACKGROUND

The capability to predict normal diurnal and episodic variations in coastal water clarity is critical to Navy operations and planning, as well as for civil environmental monitoring. Under contract to the Office of Naval Research, SAIC has conducted a broad evaluation of the feasibility of modeling dynamically driven changes in the subsurface coastal optical environment. The overall goal of this effort is to establish cause and effect relationships with standard meteorological and oceanographic observables to understand the causes of extreme variations in the background, rather than relying on sporadic archival data averages to make predictions and interpret observations.

Unlike optical properties in the open ocean where biological activity is the dominant factor (Morel Case I water), coastal optical properties are dependent on elevated concentrations of dissolved organic materials and inorganic particulates associated with terrestrial runoff, as well as sedimentary materials constantly resuspended from the bottom. These coastal ocean regions are termed Morel Case II waters.

The U.S. Navy has a wide range of requirements for predicting underwater visibility in coastal areas of the world, where future conflicts could arise or humanitarian missions become necessary. This represents a significant change in Navy priorities from the open ocean to the extremely complicated coastal areas. Examples of Navy coastal missions and depth regimes are shown in Table 1-1. Success in each of these Naval mission applications critically depends on our ability to predict spatial and temporal variations in the inherent optical properties of coastal waters. Table 1-2 is an attempt to summarize some of the corresponding applications for environmental sensing missions. Although it is clear that the inherent water properties of the medium can be the controlling factor in all these applications, what is not clear is the extent to which a carefully crafted combination of environmental modeling, climatic forecasting, and remote sensing feedback can be used to optimize prediction, planning, and performance.

The fact is that spatial and temporal variations in coastal optical properties are driven by independently observable and/or sensible physical phenomena, both terrestrial and aquatic. Factors like river runoff resulting from local and/or distant inland precipitation, swell arriving from far off

storm centers, and local wind-driven surf conditions, produce strong signals which complicate local remote sensing problems and must be separately identified and quantified, if valid conclusions are to be drawn from the data.

Table 1-1. Navy Near Coastal Optical Sensing Applications

Coastal Visibility Systems	Antisubmarine ASW	Mine Countermeasures MCM	Amphibious Operations AMPHIB	Special Forces NSW
Depths	< 300 m	< 100 m	< 10 m	< 10 m
Above Surface Sensors	Subsurface Target Detection	Shallow Mine Identification & Detection	Bathymetry & Obstacle Location	Subsurface Visibility Estimation
Underwater Sensors	Target Surveillance	Bottom Mine Identification & Neutralization	Bathymetry & Obstacle Location	Turbid Water Swimmer Recon.

Table 1-2. Environmental Shallow Water Optical Sensing Applications

Coastal Visibility Systems	Bathymetric Chart Updating	Littoral Ecology Assessment	Sub-littoral Biological Monitoring	Pollutant Source Detection, & Plume Tracking
Depths	0-300 m	0-10 m	10-200 m	10-200 m
Passive Multi/Hyper-Spectral Scanners	Obstruction Detection & Delineation	Biological Species Signatures	Spectral Change, Detection Indicators	Surface Horizontal Extent
Active Volume Scanners	Airborne Laser Bathymetric Soundings	Subsurface Weed, Grass, & Nekton Monitoring	Kelp, Fish, & Mammal Population Statistical Variations	Laser Induced Fluorescence Chemical Evaluation
Laser Line Scanning Systems	Obstruction Investigation	Benthic Populations & Bioturbation	Sediment & Plant Dynamics	Pipeline & Outfall Monitoring
Camera Systems	Benthic Materials Evaluation	Hand-Held High Resolution Photography	Still Camera & Dynamic Video Species Identification	Plume and Ocean Current Tracking



The input data and methods required for dynamic coastal water clarity estimation for any of the environmental or Navy applications is common to both. This involves a multi-layered water column, interacting with both off and onshore drivers, to model the organic and particulate sources which determine the spatial and temporal variations in optical properties. Due to the extreme difficulty in anticipating specific locations, an estimation capability covering the full gamut of generic coastal conditions is needed. Review of the archived optical information clearly indicates that these data may have good spectral resolution, but grossly inadequate spatial and temporal resolution for coastal applications. These data are capable of supporting monthly or seasonal statistical predictions, but the observations needed to support cause and effect modeling of the mechanisms responsible for diurnal and episodic changes simply were not recorded.

There are only a few locations where comprehensive observation of the inherent optical properties of the entire water column have been attempted. Optical transmission data exists for the bottom layer, but are usually limited to the red end of the spectrum. Red transmission data are used in measuring sediment burden, but, again, without extensive supportive data, they cannot be related to optical properties in other parts of the spectrum, where longer range visibility could be achieved. Additionally, full water column spatial and temporal characterizations are not directly derivable from satellite spectral observations of the surface layer. The thousands of historic "Secchi depths," which constitute much of the archived diffuse attenuation data, are only applicable to the surface layer. The short term, externally-driven, prediction capability, essential for observation planning and remote sensing data interpretation and reconciliation, is completely unavailable for the near shore water column and largely restricted to the "persistence forecast" for offshore surface layers. What satellite observations do conclusively demonstrate is that coastal oceans, seas, bays, estuaries, and shelves, are subject to extreme spatial and temporal variations due to river and aeolian particulate plumes, biological cycles, and surf zone and bottom resuspension sources.

In situ measurements have shown bottom turbid layers on the order of 10's of meters thick, displaying temporal variations on the order of cycles per day, and independent spatial variations over kilometer separations. This makes interpretation of the existing randomly spaced, incompletely documented, optical observations nearly impossible, and estimates of water properties for specific locations heavily contingent upon the development of

a "predictive model," based on time-dependent biological, geological, oceanographic, meteorological, and tidal observables.

Section 2.0 presents a brief overview of the workings of the ONR/SAIC coastal water clarity predictive visibility model (PVM). Sections 3.0, 4.0, and 5.0 present detailed descriptions of major sub-modules and Section 6.0 summarizes our conclusions and recommendations. While the goal of this end-to-end simulation model is the estimation of subsurface inherent optical properties, the required modeling of the aquatic and terrestrial physical parameters (drivers) suggest the incorporation of this extensive environmental description into other applications.

## 2.0 PVM SUMMARY & DESCRIPTION

The primary objective of this coastal water clarity effort has been to analytically determine the controlling mechanisms and demonstrate the feasibility of developing an interactive, workstation-level, computerized PVM. This was to be a three-dimensional time-step model containing the environmental drivers essential to: 1) forecast diurnal and episodic changes of operational and environmental significance, and 2) to predict subsurface scattering, absorption, and diffuse attenuation coefficients within a factor of two. These forecasts are required for shelf waters; nominally from 100 meters to the coastline and within major bays and estuaries. The following describes the ordered calculational sequence: inputs required, interim parameters (displays), output available, and pivotal assumptions.

The PVM currently envisions the use of five coastal geological type categories and leaves space for expanding categorizations of bottom sediment types and biological parameters to provide optical estimates within the relatively crude goals set forth above. The geological classifications provide a ballpark estimate of shelf geometry and bottom types, and the biological categories will also accommodate generic species and seasonal variations. Adapting to a new area would be accomplished by selecting from similar locations/situations for which environmental simulation parameters are already resident in the PVM data base. This approach is meant to generate the smallest tractable basic environmental data bank within the PVM, but model calibration experiments will be essential for each new category added.

Table 2-1. Generic Coastal Categories

1. **Collision coastline**, narrow steep abrupt quartz derived shelf bottom where tectonic plates converge, nutrient poor
2. **Trailing edge coastline**, wide sloping bottoms associated with receding plate movement, nutrient rich
3. **Marginal sea coastlines**, depressed plate areas away from plate edges

4. **Coral beaches and island fringe reefs**, calcium carbonate rich, nutrient poor warm waters
5. **Arctic coastlines**, cold island arcs with granite power suspensoids

The PVM presently contains parameters supporting only one coastal situation, with categories based on collision coastal quartz sand beaches, generic chlorophyte plankton, and dissolved organic materials (DOM) used in initial PVM parametric sensitivity analysis. It is suggested, however, that these parameters will be transportable to other locations, and the downstream question of the number of categories needed will require a trade-off between optical precision required, the diversity of prediction locations included, and the comprehensive field experimental calibration efforts undertaken. Note that model calibration and validation should be viewed as separate, but associated, endeavors involving reconciliation and comparison of hindcast predictions with field measured data. Forecasting, on the other hand, involves the application of climate forecasts and PVM optical predictions are held hostage to the accuracy of these climatological forecasts. Clearly optical forecasts can be no better than the climatic forecasts upon which they are based, and ideally would show proportional improvements as new Navy initiatives improve coastal climatic forecasting capabilities.

Simulation ----> Calibration ----> Validation ----> Forecasting

Each computer model is initially calibrated by adjusting input parameters so that output variables remain within the range of seasonal observations reported in the literature or, in the many cases where data do not exist, within reasonable limits. This is accomplished first on the sub-model level over the range of driving parameters expected. Next, the submodels are calibrated running in consort with associated submodels within the complex PVM feedback environment. Parametric feedback can result in unstable conditions when incompatible input parameters are gleaned from incomplete measurements reported in the literature. Parameters undergo large excursions until they converge to a compatible set reasonably responding to impulsive changes in driving mechanisms and displaying cyclic diurnal variations.

Although optical property sensitivity is the bottom line measure-of-effectiveness (MOE), causal effects can be tracked back through the

computational sequence, and models are deleted when their effects are negligible and added, as necessary, for adequate description of a wider range of potential circumstances. An extensive multivariate sensitivity analysis effort is required for each new sub-model added, providing strong motivation to constrain input variables to an absolute minimum.

Figure 2-1 presents a detailed dependency diagram of the overall data flow intended for the fully developed PVM. Of the twenty-four individual submodels shown (3.xx models in Figure 2-1), sixteen are running as current versions (shown in blue), and eight remain as suggested additions (red). The term "current" version is appropriate since all models have been subject to constant revision. The red models for surface wind and coastal current are meant to define spatial variation, which is presently input as only a temporal variable, based on local observations or forecasts. This currently provides end-to-end throughput of water constituent concentrations, modeled optical properties, and visibility estimates.

A 200 x 200 computational grid with three arc-second spacing (95 x 75 meter pixel separations at 33 degrees north latitude) is being used. The computational grid need not be square, but the pixel separation must be small enough to ensure Nyquist sampling across the wavelength of the dominant surface waves. If the area covered omits point sources of important constituents, rectangular or nested grids will have to be adapted to provide boundary concentrations to the Nyquist-limited computational region.

Figure 2-2 demonstrates the spatial variability of optical parameters over the region selected for calibration. In this demonstration, diffuse attenuation coefficient variability, it is evident that variations occur at sub-kilometer scales. The optical constituent models currently active in the PVM describe sediment and plankton particle number concentrations and colored dissolved organic material (CDOM) contributions, using models of bottom and surf resuspension, river runoff, and biological growth/death.

## **2.1 Fixed Parameters**

Initiating a simulation model sequence begins with the selection of an existing location, or the creation of a new one, by combining environmental files from similar environments with new or updated information.

**Geometric Fidelity Evaluation**

**Spatial/Temporal Variation Evaluation**

**Parametric Sensitivity Evaluation**

**Source Contribution Evaluation**

**BASEMAP**

**IMAGE/PROFILE/PLT COMPARISONS**

**INITIALIZATION & FEEDBACK**

**Temporal Variable Input**

**INPUT Image Data**

- LANDSAT
- CZCS/SeaWiifs
- AVHRR
- AVIRIS/HYDICE
- SPOT

**8.2/EOC**

**8.1**

**8.3**

**8.4**

**8.5**

**8.6**

**8.7**

**8.8**

**8.9**

**9.0**

**9.1**

**9.2**

**9.3**

**9.4**

**9.5**

**9.6**

**9.7**

**9.8**

**9.9**

**10.0**

**10.1**

**10.2**

**10.3**

**10.4**

**10.5**

**10.6**

**10.7**

**10.8**

**10.9**

**11.0**

**11.1**

**11.2**

**11.3**

**11.4**

**11.5**

**11.6**

**11.7**

**11.8**

**11.9**

**12.0**

**12.1**

**12.2**

**12.3**

**12.4**

**12.5**

**12.6**

**12.7**

**12.8**

**12.9**

**13.0**

**13.1**

**13.2**

**13.3**

**13.4**

**13.5**

**13.6**

**13.7**

**13.8**

**13.9**

**14.0**

**14.1**

**14.2**

**14.3**

**14.4**

**14.5**

**14.6**

**14.7**

**14.8**

**14.9**

**15.0**

**15.1**

**15.2**

**15.3**

**15.4**

**15.5**

**15.6**

**15.7**

**15.8**

**15.9**

**16.0**

**16.1**

**16.2**

**16.3**

**16.4**

**16.5**

**16.6**

**16.7**

**16.8**

**16.9**

**17.0**

**17.1**

**17.2**

**17.3**

**17.4**

**17.5**

**17.6**

**17.7**

**17.8**

**17.9**

**18.0**

**18.1**

**18.2**

**18.3**

**18.4**

**18.5**

**18.6**

**18.7**

**18.8**

**18.9**

**19.0**

**19.1**

**19.2**

**19.3**

**19.4**

**19.5**

**19.6**

**19.7**

**19.8**

**19.9**

**20.0**

**20.1**

**20.2**

**20.3**

**20.4**

**20.5**

**20.6**

**20.7**

**20.8**

**20.9**

**21.0**

**21.1**

**21.2**

**21.3**

**21.4**

**21.5**

**21.6**

**21.7**

**21.8**

**21.9**

**22.0**

**22.1**

**22.2**

**22.3**

**22.4**

**22.5**

**22.6**

**22.7**

**22.8**

**22.9**

**23.0**

**23.1**

**23.2**

**23.3**

**23.4**

**23.5**

**23.6**

**23.7**

**23.8**

**23.9**

**24.0**

**24.1**

**24.2**

**24.3**

**24.4**

**24.5**

**24.6**

**24.7**

**24.8**

**24.9**

**25.0**

**25.1**

**25.2**

**25.3**

**25.4**

**25.5**

**25.6**

**25.7**

**25.8**

**25.9**

**26.0**

**26.1**

**26.2**

**26.3**

**26.4**

**26.5**

**26.6**

**26.7**

**26.8**

**26.9**

**27.0**

**27.1**

**27.2**

**27.3**

**27.4**

**27.5**

**27.6**

**27.7**

**27.8**

**27.9**

**28.0**

**28.1**

**28.2**

**28.3**

**28.4**

**28.5**

**28.6**

**28.7**

**28.8**

**28.9**

**29.0**

**29.1**

**29.2**

**29.3**

**29.4**

**29.5**

**29.6**

**29.7**

**29.8**

**29.9**

**30.0**

**30.1**

**30.2**

**30.3**

**30.4**

**30.5**

**30.6**

**30.7**

**30.8**

**30.9**

**31.0**

**31.1**

**31.2**

**31.3**

**31.4**

**31.5**

**31.6**

**31.7**

**31.8**

**31.9**

**32.0**

**32.1**

**32.2**

**32.3**

**32.4**

**32.5**

**32.6**

**32.7**

**32.8**

**32.9**

**33.0**

**33.1**

**33.2**

**33.3**

**33.4**

**33.5**

**33.6**

**33.7**

**33.8**

**33.9**

**34.0**

**34.1**

**34.2**

**34.3**

**34.4**

**34.5**

**34.6**

**34.7**

**34.8**

**34.9**

**35.0**

**35.1**

2-4

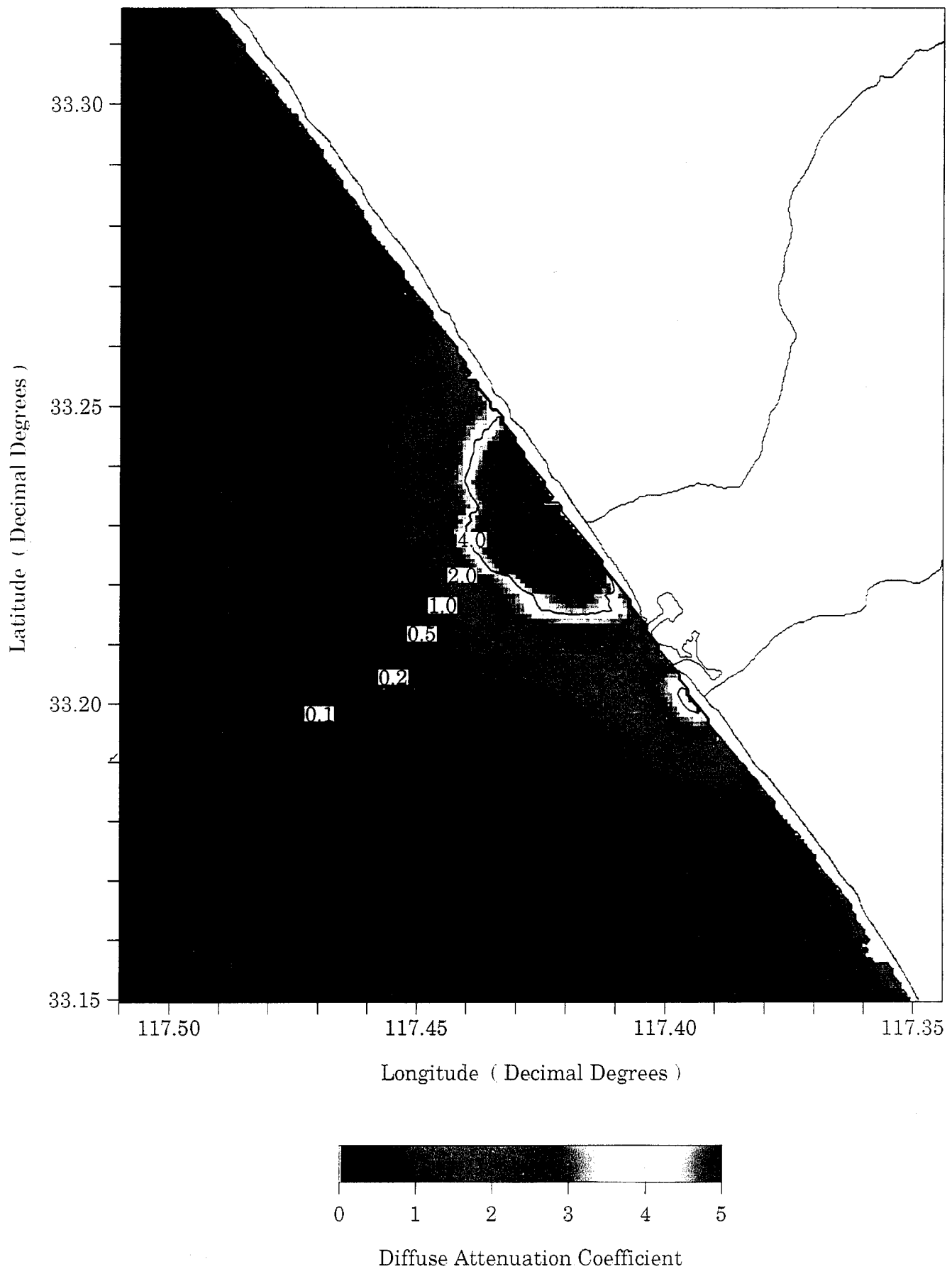


Figure 2-2. Surface diffuse attenuation coefficient for 10 a.m., 23 Jan 93

**a. General Site Attributes.** These initialization parameters are constant throughout the entire simulation and they are not modified during the run. Site attributes refer to the general descriptors which link the BASELINE MAP and the generic input files to be used in the simulation. These are shown in Table 2-2.

Table 2-2. Location Selection/Description Inputs

1. Computational region corner coordinates  
[lat/long], local date & time, time zone and  
primary optical wavelength of interest
2. Map files: Bathymetry, Bottom type, Land Cover and  
topographic contours
3. Applicable local tide constituents
4. Local geologic coastal category
5. Local biologic category
6. Optical calibration lookup table
7. Reference sediment size distribution
8. Switches, situation specific model alternatives

Once the location of the computational region is defined, off-line compilation of geographic data must be completed to provide the basic files for the selected area of interest. Available local maps and charts must be obtained in digital form from the DMA, or their hard copy renditions scanned and combined into a BASELINE CHART, providing a GIS-layered data base for registering horizontal plan views for both input and calculated values. DMA bathymetry is generally available on 3-arc second grids for the U.S., but overseas bathymetry must, in many cases, be obtained by scanning DMA charts originally prepared by corresponding foreign sources. While the area of interest is coastal waters, predictions can rely heavily on local land use, local topography, and on reference points for precise registration of all these data sources on the base chart.



DMA digital terrain elevation data (DTED-1) is produced on comparable 100-meter grid spacings for many Northern Hemisphere areas and on 30-meter spacings (DTED-2) in a few areas. These data are input into a hydrological model which is used off-line to estimate local runoff response to the time and rate of local precipitation. GIS layers defining the boundaries between bottom quality types (chart notation) and land use regions (map symbols) are input to estimate bottom particle size variations, bottom reflectivity, and coastal hydrology model inputs. A land classification (foliage/soils) estimation program should also be run off-line to estimate runoff constituents from multispectral satellite images, if available. Data from mine pilots can also be layered on the baseline chart. A common problem is the variable age and scope of the data on various maps and charts which can significantly impact sub-model outputs and the derived optical predictions.

The geological category refers to the generic coastal classification scheme discussed above and is used to link parameters common to a specific site type so that they can be applied to similar locations. Selection of a geological Category 1 to 5 will load all the files associated with the site chosen as representative of the coastal category shown in Table 2-1. Files covering items 1 through 3 in Table 2-2 must be replaced with files for the new location, and the remaining items would then be selected from the data base, as appropriate. Note that only Category "1" has been populated as of this writing, but as the location selections are expanded, a wider variety of similar sites will become available.

The local biologic species category selection simply loads a complete file containing a few site specific and a few general parameters. Note that only one biological category corresponding to the geological Category "1" test area is presently available.

A parameterized optical scattering coefficient matrix is calculated off-line because it requires excessive computer time. These optical scattering coefficients, parameterized by optical wavelength and the slope of the particle size distribution, are generated using a Bohren-Huffman type Mie scattering code adapted by SAIC. Entered with wavelength and slope, this code produces scattering and absorption values which are required input for the optics models within the PVM. These data are input in a file which currently describes all reported coastal water types using a single index of refraction. This generality should be expected to break down, at which time a limited number of additional files (variations on the index of refraction)

would be required to describe the range of coastal volume scattering functions for which no data is currently available.

A reference sediment size distribution was selected for each coastal category. This sets up the deep water percent of particles in each of nine particle size bins present in the offshore sediments for each coastal category. This parameter file was intended to go along with the geological category, but was called out in case different size distributions were encountered.

Finally, the option of turning off or on, what are referred to as "switches," to activate specific model alternatives. River runoff may be present (currently 0, 1, or 2 rivers) and the coastal water may require a one- or two-layer model, or wish to calculate mixed layer depth directly from input wind velocity. Other "switch" options allow the user to turn off individual sources for calibration purposes.

The hydrological model is another extremely run-time intensive computer module. In the initial PVM design, provision was made for rivers to feed in through the inner land boundaries, since it would not be possible to handle the head waters of major river systems. The precipitation within the local region was to be simply added to this larger river throughput to give a hydrograph of the runoff for each local river mouth. The local region hydrological treatment was parameterized in terms of the data commonly available, 24-hour total (inches), and estimated time of maximum precipitation.

For now, a single storm event is assumed and the local hydrography model is run off-line with the total runoff entered directly into each river's total throughput used in the river plume calculations. This has a distinct advantage in model validation since USGS gage stations provide direct observations of runoff rates for input to the river plume models. For now, we have only attempted independent validation of the hydrology model with these station readings. We have then used the observations, not the modeled hydrographs, for the coastal simulation examples included here.

**b. Boundary values.** As alluded to above, the small size of the computational region required for refraction of local swell may make it necessary to nest larger grids containing river mouths or other significant contributors of sediment particulate that lie outside the immediate computational region. This would be used to assign variable boundary values for the computational region. For now, boundary values are assigned

to describe the first three parameters listed in Table 2-3 for the entire offshore region.

Table 2-3. Outer Boundary Parameter Estimates

1. Sediment concentration S [mg per liter]
2. Chlorophyll concentration Chla [ $\mu\text{g}$  per liter]
3. Dissolved organic material DOM [ $\alpha 440$ ]
4. Mixed layer depth[m]
5. Peak precipitation time[hour]
6. Surface nitrate[umolar]
7. Deep water nitrate level[umolar/]
8. Phosphate[umolar]
9. Default particle distribution size slope

These background values are extracted from satellite multispectral image data as close to the simulation time as available coverage and cloud cover permit. Aircraft multispectral imagery permits more accurate estimates to supplement the larger format satellite imagery.

For this feasibility study, only two, three visible band, LANDSAT 5 images could be purchased and the sediment and chlorophyll estimates were of questionable quality. Alternatively, less noisy SPOT images could be used, but the added expense and the absence of published algorithms for parameter extraction precluded this approach. In the future, the soon to be operational SeaWiifs satellite is expected to provide these estimates, but internal optical reflections, when the image swath is close to land, will likely provide these estimates multiple kilometers offshore of the computational region, depending on coastline orientation.

Items four and five in Table 2-3 are single values provided for the entire region by the current forecast. Items 6 through 8 are seasonably dependent values which must be gleaned from the literature or from archived data. The final item (9) in Table 2-3 is a variable used to represent the maximum particle size distribution slope for nearshore waters. This controls the background number of particles less than one micron in diameter which do not settle out in the turbulent nearshore region. This constant, which must be determined by indirect experiments, has been estimated from the old optical scattering data, as will be discussed in a subsequent section, and is now receiving new attention because of increased interest in coastal water clarity.

**c. Archived and Tabled Data Inputs.** Although every effort is being made to minimize the use of historic data in favor of recent observations, certain parameters are otherwise unavailable. These vary from the precisely known parameters to rough estimates, as shown in Table 2-4. These parameters are self-explanatory and the models requiring each of these values are indicated in Figure 2-1.

Time variations of the last parameter (mixed layer depth) is available for some, but not all, parts of the world from FNOC. In cases where it is unavailable or uncertain, it must also be extracted from archived data. An alternative mode calculates an MLD from the temporarily varying wind speed to establish mixing rates in the surface layer.

Table 2-4. Archival and tabular data input

1. Sun ephemeris [declination, time]
2. Local offshore tidal constituents
3. Standard atmosphere [temp, press, density]
4. Background optical properties for clear open ocean seawater: absorption, scattering and diffuse attenuation coefficients; Smith and Baker [a, b,  $K_d$ ]
5. Historic values of regional Colored Dissolved Organic Material [CDOM] observations
6. Historic coastal runoff locations [lat,long] and external river throughput statistics [monthly volume flow rate, washload, constituents]
7. Predominant coastal surface current [set and drift]
8. Mixed layer depth

## 2.2 Time Variable Inputs

**a. Time Variable Surface Forecasts.** A forecast prediction simulation begins with nowcast/forecast inputs from the Fleet Numerical Oceanography Center (FNOC) describing conditions at an offshore coordinate location selected as close as possible to the area of interest. These inputs include the time variables shown in Table 2-5, which are interpolated to support the calculations. A 2-hour time step is used as a time scale comparable with the major fractions of the tidal cycle, a principle driving mechanism. These inputs are point values used over the entire computational region for the simulation. Their variation in time is entered

into a run time matrix displayed in the standard parameter output listings. Alternatively, for a hindcast prediction, field measured values can be directly input into the run matrix to obtain optical predictions when direct observations are available.

Table 2-5. Time Step Parameter Variation

1. Cloud cover [%]
2. Local air & sea surface temperature
3. Local barometric pressure variation
4. Precipitation [24-hour total]
5. Surface wind [speed and direction]
6. Wind wave [period, height, & propagation direction]
7. Swell [period, height, & propagation direction]

**b. TIROS Twice Daily Local Time Variable Input**

Additional local time variable input is available for Sea Surface Temperature (SST) and cloud cover (CLD) on crude kilometer image scales during the overhead passage of Tiros-N satellites. Both these image inputs could be crudely registered and displayed on the above mentioned Base Chart to aid in the interpretation of other output images, and to provide timely local parameter estimates for model calculations. Also, potentially available within the satellite data stream, are local Ozone and Aerosol concentrations which are very important for correction of optical transmission and path radiance for satellite and high altitude airborne multi-spectral scanners. This is particularly true for humid coastal ocean atmospheres in tropical island and U.S. Gulf coastal areas. Algorithms to accomplish these corrections should be added within Model 4.5 in Figure 2-1, along with other pertinent parameters.

1. Sea surface temperature
2. Cloud over
3. Ozone
4. Aerosols

Hopefully, it will be possible in the near future to apply these atmospheric data in the algorithms used to estimate initial offshore boundary values for chlorophyll and sediment concentration, and algorithms are available to handle each of these variables separately, and revisions are underway in hopes of separating these constituents. However, the latter revisions are not currently available, much less tested, and since the model is currently constrained by satellite data availability to the use of LANDSAT TM and/or SPOT spectral images, only simple spectral band ratios are currently included in the sensor applications models (Model 8.2 in Figure 2-1).

Another important application of aerospace image data, which is dependent on the sensitivity of the sensors used, is the detection, plotting, and potential tracking of surface features such as eddies, surfactant patches, river plumes, and wakes downstream of prominent coastal headlands, which could help to estimate surface current direction, speed, and patterns. Surface current eddy structures prevalent along irregular coastlines represent an unresolved modeling deficiency where direct observations would prove invaluable. All available surface patterns should be registered and displayed for feature enhancement and use in appropriate models. Feedback from this enterprise (Model 8.3) would be applied in the various models indicated in Figure 2-1. Synthetic Aperture Radar (SAR) data might also be employed to identify translating surfactant patches and identify fixed wind shadows, but this data is currently only available from foreign sources at high cost and is not exploited at this time. All of the input and processed image combinations are generated off-line, but could be made displayable (Model 8.1) and stored internally for future reference.

### **2.3 Simulation Procedures**

The following paragraphs move through each step in the PVM simulation process with a brief discussion covering the scope of the model and its output. This process includes each of the models and operations shown in Figure 2-1. The models discussed include those with a version presently running in the end-to-end PVM (blue), as well as those thought to be important for future inclusion (red).

### **a. Basic Environmental Descriptions**

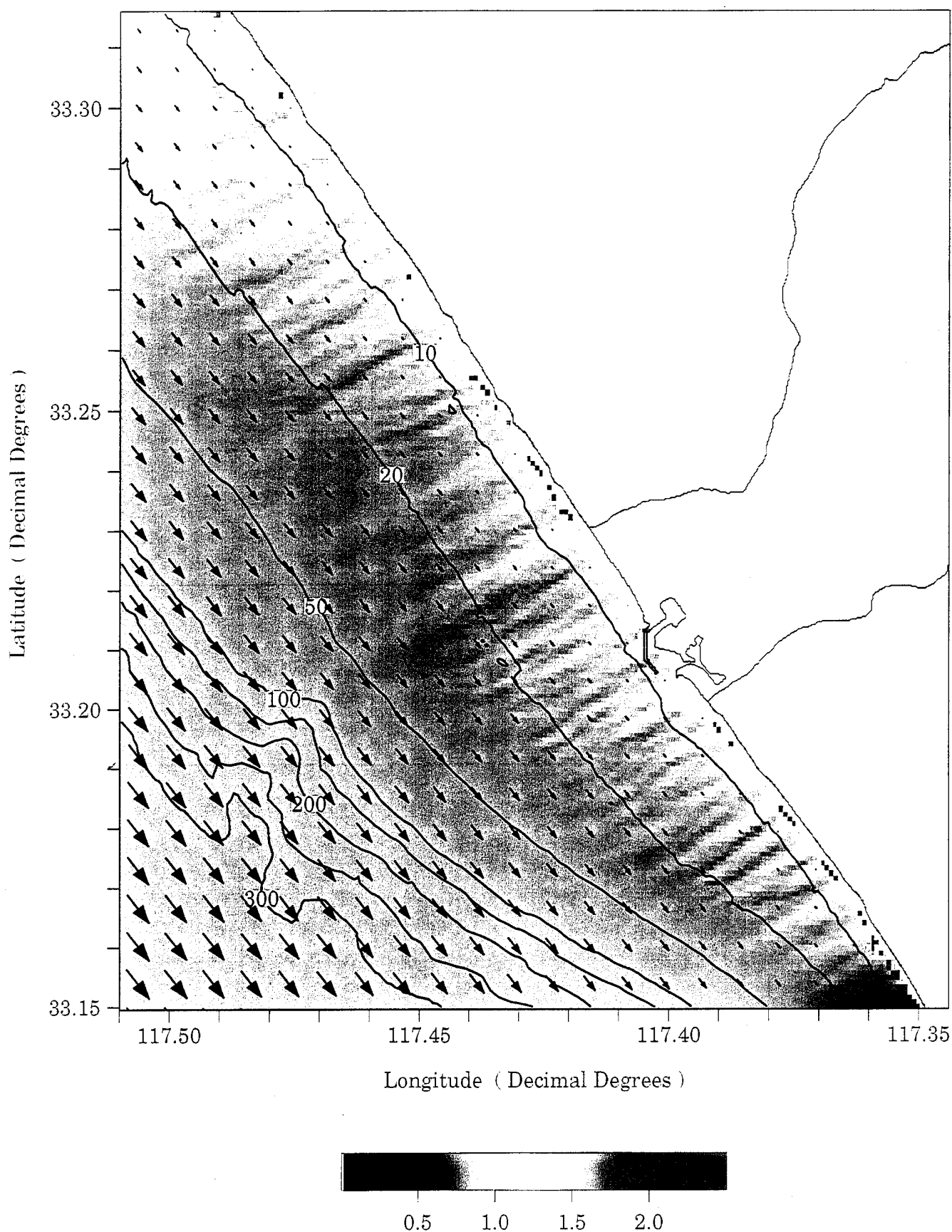
There are ten models in this category describing environmental drivers of importance to coastal water clarity. These occupy the bottom two rows in Figure 2-1. The seven fundamental models shown in blue are major PVM drivers; these are populated with currently running versions. Tidal heights are calculated directly from the locally applicable celestial constituents with inshore and/or irregular coastline amplitude and phase corrections applied where appropriate. Finer scale bathymetry would help describe the bottom current components of importance for bottom sediment resuspension.

The local hydrology model is similar to the Corps of Engineers' HEC-1 model, adopted as its standard for runoff prediction by the EPA. This model converts precipitation into coastal runoff for the local modeled area, and cases involving large river throughput require an additional volume rate estimate to be input separately. An improved river/basin model using aerospace remotely sensed land cover/land use, and soil types to vary washload characteristics should be added as soon as possible, and a coastal upwelling model is suggested for the future. While a formal treatment of upwelling is not presently included, vertical mixing is presently modeled in 3.15.

The remaining two environmental drivers, which are needed to describe the local coastal wind field and local current eddies down to 100-meter scales, represent the most critical weaknesses in ALL coastal modeling efforts. No viable capability is presently available, but suggested approaches combining real-time sensor data with time step modeling will be discussed in Section 2.4. The sea surface descriptors of the refracted wave amplitude components, directional wave numbers, and current vectors, are (x,y) displayed (Function 8.1) and stored for use in future calculations. An example of wave amplitude and horizontal current output is displayed in Figure 2-3.

### **b. Particulate Source Models**

Nine models are identified in the third row from the bottom of Figure 2-1 as potential sources of particulate and dissolved materials dominating coastal water optical properties. Of the six sources represented by up and running models, bottom resuspension is the most significant in the absence of heavy river outflow. The DOM look-up-table model used to



Wave Height (m): Swell - 12 sec, 238 deg; Windwave - 8 sec, 255 deg; Max Current Vector, 1 kn

Figure 2-3. Wave amplitude and current vectors for 10 a.m., 23 Jan 93  
2-14



estimate local spectral absorption ( $\alpha_{440}$ ) is a rather crude description of a property which varies from  $0.4 \text{ m}^{-1}$  in the upper Baltic, down to perhaps 0.04 in shallow water along more realistic coastlines. The plankton/detritus is very sensitive to the initial chlorophyll and nitrate concentrations input as "outer boundary parameters." Compatible parameter sets significantly improving initial estimation accuracy. The three source models shown in red are lower level sources which, nonetheless, can be locally very important and should be added when time and funding permit.

The outputs of each of these models, except CDOM, describe the spatial distribution (x,y,z) of particulate material which is vertically mixed and horizontally advected in the next steps. These source distributions are each carried along in nine sediment particulate size bins and two plankton cell sizes that can be independently displayed or combined for display in the Image/Plot/Profile program (Function 8.1).

### c. Spatial Distribution Models

The most crucial spatial models include vertical mixing and horizontal advection, which support the display of any of the particulate sources as individual or combined particle size bins. These spatial constituent distributions form the basis for calculation of the desired optical properties. Initial versions of the advection and mixing models are presently producing realistic distributions which will require validation experiments in real coastal environments for calibration and definitive accuracy determination.

Although not explicitly included in this effort, the aeolian particulate transport model suggested above to handle the special cases of arid windy coastlines, will require the addition of a surface film model. Particulate of aeolian origin is thought to accumulate by a size-sorted surface deposition process in a thin film layer, where it remains until wind-driven hydrodynamic processes release and mix it downward into the water column.

The downwelling sun/sky irradiance used for plankton growth is provided by a simplified version of LOWTRAN, using standard marine atmospheric parameters, and input cloud cover (%). A wind-generated spatial distribution of surface roughness should also be added to support the comparisons of calculated optical properties when remotely sensed spectral

image data become available. Output of the spatial models are (x,y) displayable in layers with fixed z and t, as well as vertical profiles (z) at const (x,y,t).

#### d. Optical Models

The objective of the PVM is estimation of subsurface inherent optical properties only (Model 4.1). This means that the introduction of an illumination source is not directly required. However, in order to obtain the quantitative surface images needed to determine reference values for offshore parameters like plankton and sediment concentrations, and to identify runoff source locations and surface current direction from river plumes and headland wakes, it is necessary to have the capability to extract the best remote image data possible. This, in turn, requires a more sophisticated spectral atmospheric correction capability than the present model (Model 4.5), and the calculation of both upwelling (Model 4.2) and downwelling light fields (Model 4.3). The calculation of the surface glint distribution (Model 4.4) is also recommended for the interpretation of upwelling radiance, and as a basic input requirement for future surface films and surfactant patch identification.

The optical model begins with the clear seawater properties of Smith and Baker (1981), adds the absorption of coastal DOM, and then calculates the contribution of particulates using a Bohren-Huffman Mie scattering code. This code is similar to that of Morel (1975) in many ways, except that it uses a complex index or refraction to compensate for the spherical particle assumption. Complex indices have also been used by Zaneveld (1972). These indices were adjusted to the data of Petzold (1972), as shown in Figure 2-4 for San Diego Bay water, to obtain a reasonable fit between the extremes of the Sargasso Sea and San Diego Bay.

With a non-zero complex index coefficient, which corresponds to internal particulate absorption, the model also yields absorption values. Category-specific *in situ* calibration coefficients must be determined to convert these values into meaningful sediment absorption coefficients. The particle size distribution presently being used is the hyperbolic distribution used by Bader (1970), Morel (1975), and summarized by Apel (1987).

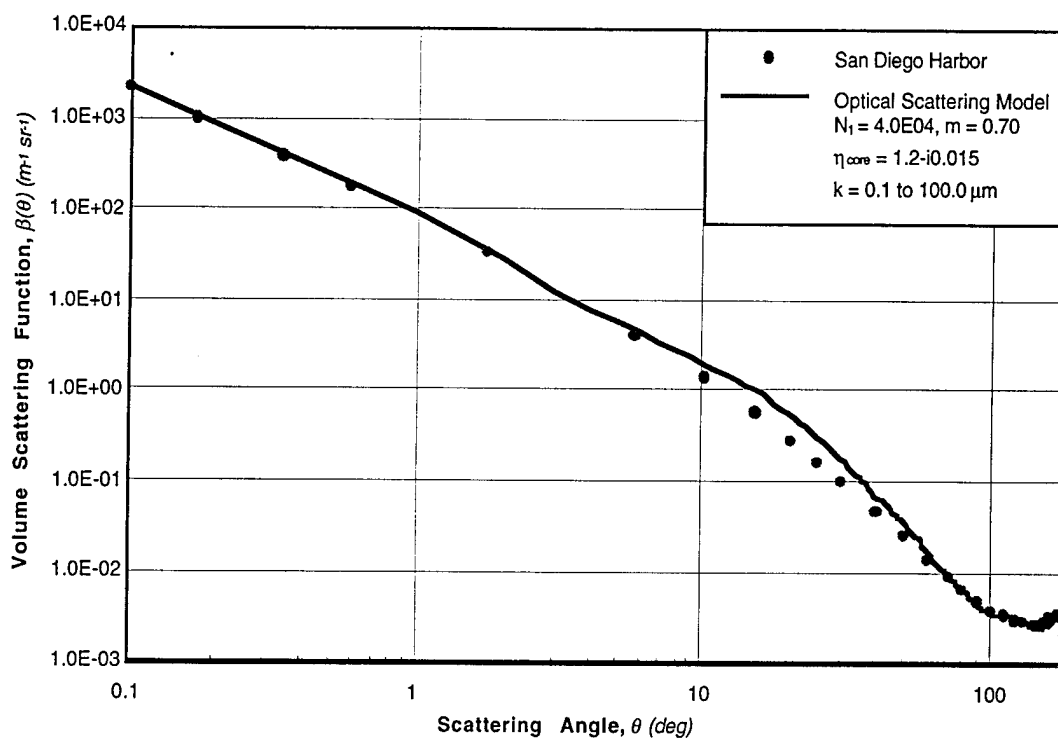


Figure 2-4. Calculated volume scattering function as compared with data measured by Petzold (1972)

The input parameters are the following:

1. Clear seawater absorption ( $a_\lambda$ ) and scattering ( $b_\lambda$ )
2. Estimated local DOM absorption ( $\alpha_{440}$ )
3. Estimated index of refraction ( $\eta = \eta_1 - j \eta_2$ )
4. Modeled particulate source distribution [ $N = N_1 \exp(-\gamma)$ ]
5. Modeled biological particulate fraction. [F%]

The output spectral optical properties routinely calculated are:

1. Particulate absorption coefficient,  $a_\lambda$
2. Particulate scattering coefficient,  $b_\lambda$
3. Particulate hemispheric backscatter coefficient,  $b_{b\lambda}$
4. Cumulative volume scattering function,  $\beta_\lambda(\theta)$

5. Diffuse attenuation coefficient ( $K_{d\lambda}=[a_{\lambda}+0.245a_{\lambda}b_{\lambda}]^{1/2}$ )
6. Total attenuation coefficient ( $c_{\lambda}=a_{\lambda}+b_{\lambda}$ )

Output of all of the calculated optical parameters is displayable in layers (x,y) with fixed z and t, in profiles (z) at const (x,y,t). Output of the diffuse attenuation coefficient distributions calculated separately with river, bottom, and surf resuspension sources at Oceanside, California, was shown in Figure 2-2.

#### e. Image/Plot Comparisons

In addition to displaying the spatial distribution of any of the above optical parameters for direct comparison with input image data sources shown in Figure 2-1, the spatial variations of the following parameters and their driving mechanisms could be displayed to show the effects of the individual models.

1. The amplitude and wave number distributions ( $k_x, k_y$ ) over the coastal wave refraction pattern. These values could also be used to produce an animated sea surface,  $z(x,y,t)$
2. The nearshore current vector field based on progressive tidal and mean offshore current estimate or any other model or vector field input,  $V(x,y,z)$
3. The modeled river plume particulate dispersal,  $N_i(x,y)$
- 3a. The modeled bottom resuspended particulate dispersal,  $N_i(x,y)$
- 3b. The modeled surf resuspended particulate dispersal,  $N_i(x,y)$
4. The combined number distribution by particle size bin (i),  $N_i(x,y,z)$
- 5.\* Aeolian particulate number/size distribution settling rate sorted and integrated within the surface film by time variable deposition,  $NA_i(x,y)$ (part of proposed effort)
6. Chlorophyll-a concentration ,  $Chla(x,y,z)$

---

\* Suggested future additions

7. Biological cell number concentrations,  $N_B(x,y,z)$
- 8.\* Surface film distribution,  $Film(x,y)$ (part of proposed effort)
- 9.\* Surface roughness,  $h_{rms}(x,y)$

In addition, the off-line image enhancement operations indicated in Figure 2-1 for manipulating input images and the evaluation operations indicated on the top row of Figure 2-1 can routinely be applied using one of several commercially available image comparison software systems. Spatial fidelity, spatial and temporal frequency analysis, and sensor sediment and chlorophyll constituent separation capabilities can be quantitatively evaluated.

Taken together, all of these outputs can then be directly compared with other remote sensor inputs and with any surface truth collected during the model validation process. Appendix A contains a User's Manual providing more description of the computer interface.

## 2.4 Suggested PVM Input/Model Improvements

If higher resolution currents and wind data were available for the coastline, it should greatly improve prediction capabilities, but the present FNOC models are restricted to offshore areas. Higher resolution coastal current models operating on kilometer scales like the Blumberg-Mellor, Princeton Three-Dimensional Coastal Ocean Circulation Model, may have significant potential in the future, but are currently starved for boundary values when attempting descriptions at the scales of interest here.

This type of model is adaptable for sub-kilometer scales, if such things as the tidal inputs are specified on a finer grid, rather than the present 5 arc-minute grid, which includes less than 6 points in our simulated area, but will still rely on unknown boundary conditions. Furthermore, these models will have to be reconfigured to include the larger orbital velocities which dominate the resuspension of the materials, and are the key driver for optical properties estimation.

Since these models are extremely time consuming, even when run on large main frame computers, and FNOC is currently pursuing these coastal predictions, it makes more sense for these models to be added at the bottom of FNOC's hierarchy of ocean to coastal forecasting chain, where outputs would be available to multiple users. The appropriate question to ask is

what surface sensor data, acquired to support local prediction requirements, might help to improve FNOC's forecasts.

### **3.0 TIME STEPPED SUSPENDED PARTICLE DISPERSION MODEL FOR COASTAL WATERS**

#### **INTRODUCTION**

A numerical model has been developed for time stepped simulations of the suspended sediment and biological particle dispersion due to waves, currents, and wind mixing acting upon sources derived from river discharges, surf zone suspensions, and bottom resuspension. The code inputs nowcast and forecast values of wind and wave statistics as well as river discharge flow rates and computes suspended particle distributions in successive two-hour time steps between the nowcast and forecast conditions. For any given time step, solutions are available for suspended particle concentrations at 100 vertical points through the water column for each grid cell in a 200 x 200 point, horizontal, spacial array (or grid network). Furthermore, the suspended sediment solutions are decomposed into nine separate particle size bins, which are segregated according to sediment source, e.g., river, bottom, or surf zone. The suspended biological particles are treated for two cell sizes. The 200 x 200 point computational grid network is distributed over a solution domain that extends from the surf zone offshore to the deep water limit of the shoaling regime for surface gravity waves, (typically the 300 meter depth contour although any arbitrary depth regime may be selected). In the present application, solution output over the entire grid network has been limited to only four user defined depths. At each depth, the nine particle size bins are summed and the lowest order slopes of the particle size distributions are computed. These limitations have been imposed to keep disk storage requirements at a manageable level for a computer the size of which would be expected on a Naval vessel. Even with these restrictions (that have nothing to do with the capability of the model), active disk storage requirements for the solutions from a single-time step are O (39 megabytes). If the user requires more depth resolution in the vertical distribution of suspended sediment, the option of selecting a 100 point vertical profile at any arbitrary grid cell in the grid network has been incorporated in the input file.

Time stepping begins from an initial steady state solution based upon an internally predicted tidal current field at the nowcast time, as well as externally provided nowcast values for the river flow rates, wind speed, deep water wave heights, periods, and directions. The tidal currents are computed for the nowcast condition and all the following time steps based upon as

many as 37 tidal constituents which prescribe the relative proportion of progressive and standing components in the deep water tides. These deep water tides drive a coastal boundary layer module which computes the orthogonal tidal velocity components at each grid cell for each time step. The deep water wave statistics, on the other hand, are derived for each time step by interpolation between the externally provided nowcast and forecast conditions. These nowcast and forecast wave statistics will be generally provided by the Fleet Numerical Oceanographic Center (FNOC), but in the particular hindcast example in Section IV, by actual offshore measurements using the Coastal Wave Data Network, as provided by the Coastal Data Information Program (see CDIP, 1993). From either database source, the deep water wave statistics are used to drive a refraction diffraction module which calculates the local wave height, direction, and wave number at each grid cell in the 200 x 200 computational domain. These refraction diffraction calculations are tidally compensated for each time step based upon the tidal elevation changes computed from the 37 tidal constituents. Consequently, the refracted and diffracted waves are varying with each time step due to changes in local water depth arising from tidal variations and changes in the wave heights, periods, and directions as the time step sequence advances from the nowcast to the forecast conditions. In addition, the river discharge rates vary continuously through the time step sequence based upon the flood hydrographs of the rivers. The flood hydrograph is provided as an input either from gauge station measurements or from the output of a hydrographic model which is driven by rainfall forecasts.

### **3.1 Architecture**

The architecture of the particle dispersion model has been designed to be modular as much as possible. This was done to allow for segregation of sources and processes which may vary from site to site, and to allow for future upgrades of certain algorithms without the need to rebuild the entire model. The modules are divided into two major clusters: 1) Those which prescribe hydrodynamic forcing functions; and 2) those which prescribe the particle sources acted upon by the hydrodynamic forcing to produce suspension and transport (see Figure 3-1). At the heart of this architecture is the primary computational module, "SEDXPORT-f," which inputs the hydrodynamic forcing and sediment source loading for each time step and then performs the advection and mixing calculations for the sediment dispersion. "SEDXPORT-f" does not rely on time splitting approximations for certain discrete sources, and, therefore, the processes of advection and



# PVM COMPUTATIONAL ENGINE (LOWER END)

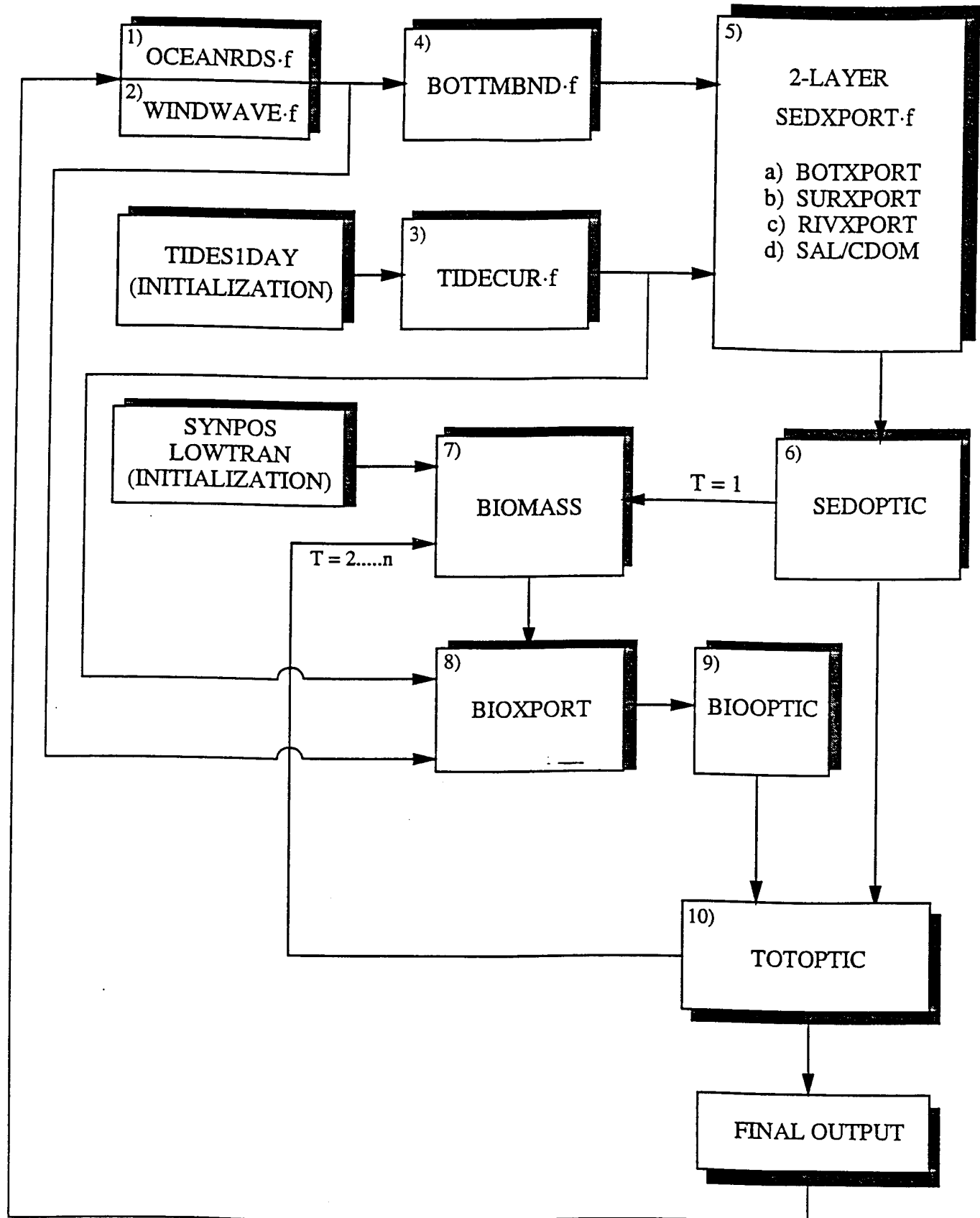


Figure 3-1. Flow chart of the PVM Computational Engine

mixing cannot be segregated within "SEDXPORT.f". However, "SEDXPORT.f" does maintain a segregation among the individual sediment sources, on which the advection-mixing processes work. This is accommodated through a subroutine library within "SEDXPORT.f", which allows for modular substitutions or upgrades in the advection-mixing algorithms for bottom resuspension (in "BOTXPORT.f"), surf zone suspension (in "SURXPORT.f"), and river dispersion (in "RIVXPORT.f" and "SAL/CDOM"). In the running of "SEDXPORT.f", any user defined combination of these three, primary, sediment sources may be simulated, allowing dominant sediment sources to be diagnosed and specific features associated with a particular source to be isolated and studied apart from the overall background.

The cluster of modules for hydrodynamic forcing ultimately prescribes the velocities and diffusivities induced by wind, waves, and tides for each depth increment at each grid cell in the grid network (see Figure 3-2). Both the shallow water tidal currents and the shoaling wave field depend critically on the bathymetry variations over the grid network. The module "OCEANBAT.f" generates the computational grid network and its associated depth files from packed bathymetry data files derived from any one of several possible database sources, including: National Ocean Survey (NOS) depth soundings, GIS or GRASS, and NOAA or DMA nautical charts. The structured depth files written by "OCEANBAT.f" are then throughput to the module "OCEANRDS.f", which performs a refraction-diffraction analysis from nowcast and forecast values of deep water wave statistics. "OCEANRDS.f" computes local wave heights, wave numbers, and directions for the swell component of a two-component, rectangular spectrum. These values are then throughput to "WINDWAVE.f", which completes the refraction-diffraction analysis of the two-component spectrum including wind wave effects up to Nyquist frequencies. "WINDWAVE.f" also computes points of wave breaking throughout the grid network and solves for the associated breaker heights and breaker angles. The resulting arrays of wave parameters are then throughput to the sediment source clusters (see Figure 3-2).

The hydrodynamic forcing arising from the tidal currents are based upon inputs of the tidal constituents derived from Fourier decomposition of tide gauge records. Approximately 40,000 tide gauge stations exist world-wide and the premise is made herein that one or more of these stations is

# SEDXPORT COMPUTATIONAL SEQUENCE

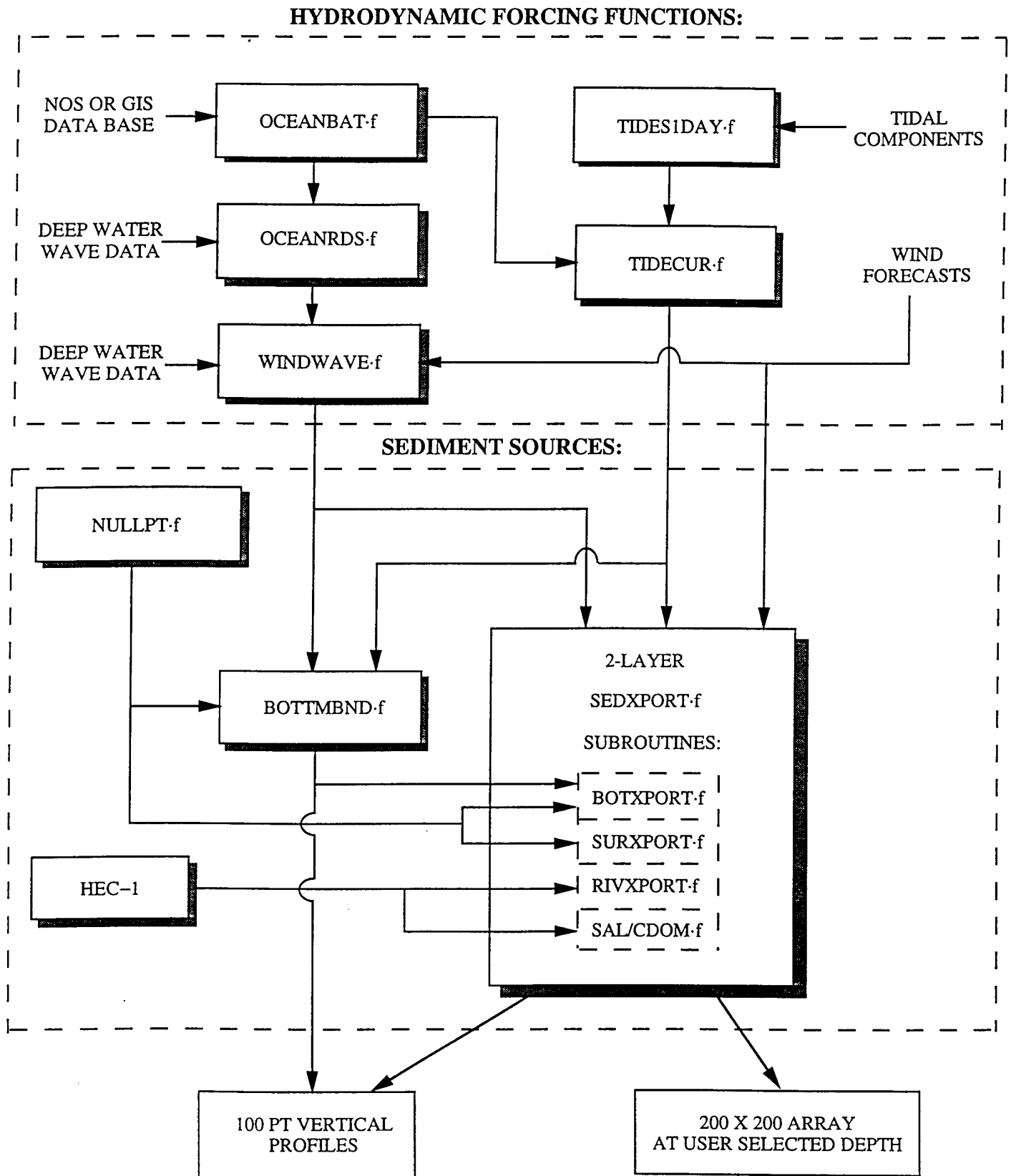


Figure 3-2. Flow chart of the hydrodynamic and sediment source clusters

within reasonable proximity to any given stretch of coastline of concern. Otherwise, tidal current computations from first principles would require rather large computers with long end-to-end run times in shallow water that would exceed the available nowcast/forecast time interval, e.g., the Bedford Tidal Model or the Blumberg-Mellor, 3-D, Circulation Model (see Blumberg and Mellor (1987)). Even then, these models would only provide current resolution on a 5 arc minute scale, when O (100 m) scales are necessary for resolving sediment dispersion in coastal waters. To circumvent these difficulties, the PVM model uses synoptic tidal constituents to drive coastal tidal boundary layer algorithms, which allow for fine scale resolution of tidal currents on small to moderate sized computers.

Tidal constituents are input into the module "TIDES1DAY.f", which resides in the hydrodynamic forcing function cluster (see Figure 3-2). "TIDES1DAY.f" computes the distribution of sea surface elevation variations over the computational grid network after compensating for phase shifts associated with travel time between the nearest open ocean tide gauge station and the PVM simulation site. The files of tidal elevation are then throughput to the module "TIDECUR.f", which computes the deep water tidal current and assigns a cross shelf coastal boundary layer profile for each time step. The coastal boundary layer profiles are computed based upon the relative proportions of progressive and standing components as determined from the mix of tidal constituents input to "TIDES1DAY.f". The coastal boundary layer solutions from "TIDECUR.f" enable a current vector to be assigned for each grid cell during each time step. The arrays of current vector components are then throughput to the sediment source clusters for use in the advection diffusion calculations.

The cluster of sediment source modules (as shown in Figure 3-2) is partitioned into two categories: 1) Source fluxes and grain size, and 2) advection and mixing. The source fluxes arising from resuspension of sea floor sediments by the shear stresses of the bottom boundary layer are calculated by the module "BOTTMBND.f". Wave and tidal currents are inputs to "BOTTMBND.f" from the hydrodynamic forcing cluster, and used to calculate bottom shear stresses. A threshold of motion criteria inside "BOTTMBND.f" calculates whether these bottom shear stresses are sufficient to suspend the sediment grain sizes which make up the bottom material at a particular grid cell. The variation in grain sizes from grid cell to grid cell is resolved by the module "NULLPT.f", which inputs grain size

distributions to "BOTTMBND.f", based upon local water depth, wave climate, geological setting, and bottom composition data from nautical charts. The grain size distribution is subdivided among 9 particle size bins by "NULLPT.f". The numbers of particles from each size bin that are subsequently resuspended in the bottom boundary layer, are calculated by "BOTTMBND.f", according to excess shear stress,  $\tau - \tau_c$ , where  $\tau_c$  is the critical shear stress required to initiate motion of a particular particle size. "BOTTMBND.f" outputs a 100 point vertical profile of particle numbers across the boundary layer for each size bin, as well as the total particle number. "BOTTMBND.f" also sends particle numbers and gradients at the top of the boundary layer as throughput to the advection diffusion module "SEDXPORT.f" (see Figure 3-1). The subroutine "BOTXPORT.f" in "SEDXPORT.f" then mixes these particles of bottom origin up into the water column, after advecting them over the computational grid according to an rms vorticity-based time splitting scheme. Vertical mixing includes two mixing mechanisms at depths above the pycnocline: 1) fossil turbulence from the bottom boundary layer, and 2) wind mixing. The pycnocline depth is treated as a zone of hindered settling and varies in response to the wind speed and duration. Below the pycnocline, only turbulence from the bottom wave/current boundary layer contributes to the local diffusivity.

Generally, "NULLPT.f" prescribes particle size distribution whose median grain size becomes progressively coarser as the computation sweeps shoreward. The width of the grain size distribution at a particular location in a sweep varies according to bottom composition maps of the PVM site. At some point during these sweeps, the breakpoint is reached and the bottom resuspension transitions from a boundary layer process to a surf zone process involving the coarsest fractions of the particle size distribution. Surf zone particle suspension is treated as a line source of particles by a subroutine in "SEDXPORT.f". The coarse particles suspended from the bar berm section of the beach profile are exported to the offshore waters by the subroutine "SURXPORT.f", which calculates seaward mixing from fossil surf zone turbulence, and seaward advection from rip currents embedded in the line source. Both the eddy diffusivity of the line source and the strength and position of the embedded rip currents are computed from the shoaling wave parameters evaluated at the breakpoint, as throughput of "OCEANRDS.f" and "WINDWAVE.f".

River discharges are treated as an embedded point source in the surf zone line source. The strength of these embedded point sources and their

associated particle loading is determined from the flood hydrograph of the river. The flood hydrograph is a throughput from a GRASS system software package based upon "HEC-1", which was developed by the U.S. Army Corps of Engineers to estimate river runoff from precipitation records or forecasts. River flow rates, cross sections, suspended load bulk density, and particle size distributions are throughput to the advection-mixing module, "SEDXPORT.f" (see Figure 3-1). The subroutine, "RIVXPORT.f" exports the river discharge over the computational grid for each time step under the influence of wave-induced mixing and nearshore tidal currents. Time variations of both river discharges, wave heights, directions, and tidal currents are accounted through successive time steps without time splitting. Similar dispersion computations are also performed for salinity and colored, dissolved, organic material (CDOM) by the subroutine "SAL/CDOM."

Outputs from "SEDXPORT.f" for each time step include both 100 point vertical profiles at any user defined grid cell for particle number concentrations in each of 9 particle size bins, as well as 200 x 200 point plan view arrays of total particle number concentrations, and slopes of particle numbers versus particle size at as many as 4 user-defined depths. Two of these four depths are presently assigned to 1 meter below the sea surface and 1 meter above the sea bed. The total particle number and particle versus size slope files are throughput to the cluster of optics modules in the PVM, as shown in Figure 3-1.

The module "SEDOPTIC" in Figure 3-1 inputs sediment particle number and slope files from "SEDXPORT.f", and calculates the diffuse attenuation coefficients over the 200 x 200 pt. plan view array. For the first time step,  $T = 1$ , these diffuse attenuation coefficient files (due only to the presence of the sediment) are throughput directly to a Plankton growth module, "BIOMASS." The "BIOMASS" module computes the growth of Nano Plankton 0 (5 microns) and Net Plankton O (20 microns) over a two-hour growth period, and throughputs 200 x 200 pt. arrays of Plankton populations for the surface, and for the depth of the 1% light level to the advection-mixing module, "BIOXPORT.f." Under the assumption that biological growth is slow in relation to hydrodynamic mixing and transport; time splitting is imposed here to separate growth from advection and mixing. The biological advection-mixing module, "BIOXPORT.f", has a number of features in common with the subroutine "BOTXPORT.f" in "SEDXPORT.f," except that the source layer is now at the surface where light levels are greatest and not at the bottom. Consequently, both mixing

and settling act together in "BIOXPORT.f" to spread and diminish the gradients in cell numbers downward through the water column. Outputs of "BIOXPORT.f" are then throughput to both the optics cluster, as well as back to "BIOMASS", to serve as the new, initial conditions for all remaining two-hour growth periods,  $T = 2.....n\Delta t$ . Optical computations on the "BIOXPORT.f" files for both cell size bins are done by the module, "BIO\_OPTIC". Output of "BIO\_OPTIC" is then throughput to "TOTOPTIC", where the optical properties arising from the sediments and from the biology are combined to yield final outputs of absorption, volume scattering function, backscatter coefficient, diffuse attenuation coefficient, and visibility distance. These properties are available over the entire 200 x 200 pt. area grid for as many as four user defined depths. One hundred point profiles of these properties are also available for any user defined grid cell.

### 3.2 Module Detail and Theory

#### A. OCEANBAT.f

This code generates a 200 x 200 point bathymetry grid from the National Ocean Survey (NOS) digital data base. This data base presently contains no bathymetry deeper than 305 meters. The gridding is by latitude and longitude with a resolution of 3 x 3 seconds of arc length. All dimensions within the grid are in meters. A specific study site is selected by the latitude and longitude of the upper left-hand corner of the bathymetry grid. In the initial application described in Section 3.3 for Camp Pendleton, CA, at 33.2°N latitude, the grid resolution produces 77.2m by 92.6m rectangular cells. This small amount of grid distortion is converted internally to Cartesian coordinates, using a Mercator projection of the latitude-longitude grid centered on 33.2°N. The convention for Cartesian coordinates uses x-grid spacings for longitude and y-grid spacings for latitude, with the origin (0,0) in the upper left-hand corner per RASTER and GRASS format. The output file for "oceanbat.f" is called "ifile.grd." Any depths below 305 meters are assigned default values of 305m while any land masses or shoals above 0-MSL are assigned default values of -1.14m.

The primary sources of bathymetry errors in the resulting depth grid from "OCEANBAT.f" are due to imperfections in the data base. In the case of the NOS database, there are two potential types of errors. The first arises from slight navigational inaccuracies in some of the older bathymetric surveys. In areas where two or more surveys overlapped, the most recent

survey was used. The second type of bathymetry error results from changes in shallow water bathymetry over time, due to recent sediment movement. These type of errors tend to be systematic and are difficult to both find and correct. To lessen their likelihood, the completed grid was contoured and screened for bad points through comparison to NOS and USGS nautical charts.

## B. OCEANRDS·f

This code calculates the simultaneous refraction and diffraction patterns of the swell wave component of a two-component, rectangular spectra propagating over the depth grid generated from "OCEANBAT·f." "OCEANRDS·f" uses the parabolic equation method (PEM), Radder (1979), applied to the mild-slope equation, Berkhoff (1972). To account for very wide-angle refraction and diffraction relative to the principle wave direction, "OCEANRDS·f" also incorporates the high order PEM Pade' approximant corrections like those developed by Kirby (1986). Unlike the recently developed REF/DIF1 model, due to Kirby and Dalrymple (1993), the Pade approximants in "OCEANRDS·f" are written in tesseral harmonics, a la Jenkins and Inman (1985); in some instances improving resolution of diffraction patterns associated with steep, highly variable bathymetry along the shelf break. These refinements allow calculation of the evolution and propagation of directional modes from a single incident wave direction; which is a distinct advantage over the more conventional directionally integrated ray methods that are prone to caustics (crossing rays) and other singularities in the solution domain where bathymetry varies rapidly over several wave lengths. Similar logic and algorithms are utilized by the code to "WINDWAVE·f," which calculates the refraction/diffraction patterns of a two-component, rectangular spectrum that considers the windwave component and sums the components together.

Input parameters to both "OCEANRDS·f" and "WINDWAVE·f" are assembled from the "CWC Global Input Parameter File." This input file begins with designating the orientation of the coastline by specifying "icoast." The convention used for "icoast" is as follows: 1) west facing shoreline, 2) north facing shoreline, 3) east facing shoreline, and 4) south facing shoreline. The tide elevation relative to mean sea level is calculated by a separate module and offsets the bathymetry for wave refraction-diffraction. The parameter "rot" may be set between  $\pm 90^\circ$  to rotate the entire grid relative to the orientation of the available image. The grid spacing, in



meters of longitude, is set by the parameter "sx," while the grid spacing, in meters of latitude, is set by the parameter "sy." These values are calculated by "oceanbat". The overall computational grid need not be square and can consist of fewer points than 200 x 200, as input from "OCEANBAT.f". The number of grid cells across any longitudinal sweep is set by "nx," while the number of grid cells across any latitudinal sweep is set by "ny." The deep water swell wave period, in seconds, is set by the parameter "persw;" the direction from which the deep water swell waves approach the shoreline in degrees from true north is set by the parameter "asw." The deep water swell wave height (the trough-to-crest wave height) is set by the parameter "hsw" in meters. The corresponding wave heights, periods, and directions for the wind waves, are set by the parameters: "hwin," "perwin," and "awin," respectively. Additional inputs to "OCEANRDS.f" are from a formatted 200 x 200 real number array called "ifile.grd," which is the gridded bathymetry generated by the "OCEANBAT.f" module.

"OCEANRDS.f" and "WINDWAVE.f" output ASCII files for wave amplitude in meters, wave angle in degrees true, and wave number in reciprocal meters. Output files are designated by an eight-character site name followed by .WHT, .WVN, and .ANG for wave height, wave number, and direction, respectively.

### C. "SEDXPORT.f"

This module calculates advection mixing processes associated with sediment transport, due to time varying hydrodynamic forcing in a two-layer coastal ocean. For resuspension from a distributed source like the bottom, advection is treated by time splitting in the resuspension module "BOTTMEND.f" and the subroutine, "BOTXPORT.f." These modules allow for sediment to be moved from one grid cell to the next in certain transport regimes, e.g., vortex ripples or sheet flow. The sediment is subsequently mixed into the upper water column by the subroutine "BOTXPORT.f" with no subsequent exchange of sediment among grid cells during that particular time step. Discrete sources, on the other hand, such as surf zone suspension and river discharge, do not invoke time splitting. Material moves from grid cell to grid cell in subroutines such as "SURXPORT.f" and "RIVXPORT.f" under the simultaneous action of mixing and advection.

1. "BOTTMBND.f" and "BOTXPORT.f"

This module and subroutine calculates the resuspension of sediments from the sea floor due to the action of bottom shear stresses from oscillating wave motion and slowly varying mean currents. Logical "if" statements are utilized to compute bottom resuspension in three distinct regimes of suspended transport: 1) incipient motion and saltation; 2) vortex ripple regime; and 3) sheet flow regime. The particular regime of transport is selected according to a dynamic similitude parameter known as the Shields parameter,  $S_h$ , defined as:

$$S_h = \frac{f_w u^2}{(\rho_s/\rho_0 - 1) gD}$$

$u_m$  = orbital velocity over the bottom  
 $\rho_s$  = particle density  
 $\rho_0$  = density of sea water  
 $g$  = acceleration of gravity  
 $D$  = particle diameter  
 $u_0$  = mean velocity above bottom boundary layer  
 $u = u_0 + u_m$

(1)

In Equation (1),  $f_w$  is a friction factor derived from Jonsson (1966) and written

$$f_w = \exp \left[ 5.2 (2.5 D/d_o)^{0.2} - (u_0/W_0)^{0.06} \right]$$

(2)

where  $W_0$  is the settling velocity of grain size  $D$ ; and  $d_o$  is the near bottom orbital diameter for the potential motion from linearized wave theory,

$$d_o = H/\sinh kh = 2u_m/\sigma$$

and  $\sigma = 2\pi/T$  where  $T$  is the wave period.

$H$  and  $k$  are the wave height and wave number, respectively, at each grid cell according to the refraction/diffraction results from "OCEANRDS.f" and

"WINDWAVE-f." The Shields' parameter represents a ratio of the two leading order forces involved in sediment transport, i.e., a ratio of the bottom shear stress to immersed gravitational forces per unit area acting on the sediments of each grid cell. The following ranges of Shields' parameter define the suspended transport regimes (see Shibayama and Horikawa, 1982, and Inman & Bagnold, 1965).

$S_h < 0.05$	NO MOTION
$0.05 \leq S_h < 0.09$	INCIPIENT MOTION/SALTATION
$0.09 \leq S_h < 0.48$	VORTEX RIPPLES
$S_h \geq 0.48$	SHEET FLOW

(3)

From Equation (3),  $S_h \approx 0.05$  defines the critical shear stress,  $\tau_c$ , required to initiate motion of a particular particle size. The incipient motion/saltation regime occurs for bottom stresses slightly in excess of the critical shear stress, where sediment is largely moving in contact with the bed (bed load) while individual grains are episodically ejected into the flow along parabolic trajectories. The near bottom flow is characterized by a transitional periodic boundary layer that remains attached to the surface of the bed.

For higher shear stresses, bed forms appear and the boundary layer separates at the crest of each ripple, introducing vortices into the near bottom flow. The induced velocity of these vortices both dislodge sediment from the bed as well as raise it into suspension.

At still higher shear stresses, bed forms are eroded away, leaving a flat bottom with an attached turbulent boundary layer. The boundary layer from top to bottom is laden with a dense suspension of sediment, hence, the term "sheet flow." Because of grain to grain shearing in sheet flow, the boundary layer also develops strong shear instabilities leading to turbulent bursting

and the transferal of plumes of suspended sediment into the upper water column (see Conley and Inman, 1993).

For any grid cell in which the local Shields parameter exceeds the threshold of motion condition set forth in Equation (3), the density of the fluid-sediment suspension,  $\rho_m$ , may be written

$$\rho_m = \rho_s N_2 + (1 - N_2) \rho_0 \quad (4)$$

where  $N_2$  is the volume concentration equal to the volume of sediment per volume of the fluid sediment mixture. The density of the sediment component of this mixture,  $\rho$ , is sometimes referred to as the excess or bulk density and is defined

$$\rho = \rho_s N_2. \quad (5)$$

Equation (5) can be used to express the particle number concentration  $P_n$  from knowledge of the grain size,  $D$ , under the assumption of spherical grains, or

$$P_n = \frac{6\rho}{\rho_s \pi D^3}. \quad (6)$$

For ordering the various terms of the transport equation appropriate to the particular regimes of transport in Equation (3), it is useful to non-dimensionalize according to the following scalings:

$$\begin{aligned} x &= \hat{x}S_x, & s &= 1/2(S_x + S_y) \\ y &= \hat{y}S_y \\ z &= \hat{z}/\delta = \hat{z}S/A_f \\ t &= \hat{t}/\Delta t \\ (u, v, w) &= (\hat{u}, \hat{v}, \hat{w}) u_m \\ \rho &= \rho_c \hat{\rho} \end{aligned} \quad (7)$$

where carets denote dimensionless variables;  $A_f = S/\delta$  is the boundary layer aspect ratio;  $S$  is the mean horizontal dimension of a grid cell;  $\delta$  is the

boundary layer thickness;  $\Delta t$  is the time step length; and  $\rho_c$  is the bulk density of the seabed sediments. The sediment transport equation written in terms of the non-dimensional variables of Equation (7) is:

$$\begin{aligned} \left( \frac{\delta^2}{\Delta t \epsilon} \right) \frac{\partial \hat{\rho}}{\partial \hat{t}} = & \frac{\partial^2 \hat{\rho}}{\partial \hat{z}^2} - R_f \left[ \left( \hat{w} + \frac{W_0}{u_m} \right) \frac{\partial \hat{\rho}}{\partial \hat{z}} + \hat{\rho} \frac{\partial \hat{w}}{\partial \hat{z}} \right] \\ & - \frac{R_f}{A_f} \left( \hat{\rho} \frac{\partial \hat{u}}{\partial \hat{x}} + \hat{u} \frac{\partial \hat{\rho}}{\partial \hat{x}} + \hat{\rho} \frac{\partial \hat{v}}{\partial \hat{y}} + \hat{v} \frac{\partial \hat{\rho}}{\partial \hat{y}} \right) \\ & - \frac{1}{A_f^2} \left( \frac{\partial^2 \hat{\rho}}{\partial \hat{x}^2} + \frac{\partial^2 \hat{\rho}}{\partial \hat{y}^2} \right) \end{aligned} \quad (8)$$

where  $W_0$  is the particle settling velocity;  $R_f = u_m \delta / \epsilon$  is the mass flux Reynolds number equal to a ratio of advective to diffusive mass fluxes and  $\epsilon$  is the mass diffusivity. Since ocean survey data is relatively sparse, the mean grid cell spacing,  $S$ , is large relative to the boundary layer thickness,  $\delta$ , and hence,  $A_f \gg 1$ . Consequently, the leading order terms in Equation (8) are the unsteady term, the vertical mixing term, and the vertical advection terms. It will be found that horizontal advection is embedded in the formulation of the vertical advection terms.

At the initial time step,  $m = 0$ , the bottom resuspension is calculated from a steady state initial condition for any grid cell whose Shields' parameter exceeds the threshold of motion condition set by Equation (3). This requires that wave and current conditions remain invariant long enough for a steady state to develop. That amount of time would be  $\Delta t > \delta^2 / \epsilon \sim 0$  ( $10^3$  sec). For this initial condition,  $m = 0$ , the steady state suspension of particles will be governed to lowest order by:

$$\frac{\partial^2 \hat{\rho}}{\partial \hat{z}^2} - R_f \left[ \left( \hat{w} + \frac{W_0}{u_m} \right) \frac{\partial \hat{\rho}}{\partial \hat{z}} + \hat{\rho} \frac{\partial \hat{w}}{\partial \hat{z}} \right] = 0 \quad (9)$$

subject to the boundary conditions:

$$\begin{aligned} \hat{\rho} &= 1 \quad \text{at} \quad \hat{z} = 0 \\ \hat{\rho} &\rightarrow 0 \quad \text{as} \quad \hat{z} \rightarrow \infty \end{aligned} \quad (10)$$

The first order solution to (9), subject to (10), may be written in dimensional form for the  $n^{\text{th}}$  grid cell (see Jenkins and Wasyl, 1990):

$$\rho_{n,0}^{(1)} = \rho_c \exp \left\{ \frac{2}{\epsilon A_w} \left[ I_1(x, y, z) - I_1(0) + \frac{z}{(h - z_m)} I_1(0) - \frac{z}{(h - z_m)} I_1(h - z_m) \right] + \frac{z}{\delta} \log \frac{\rho_t}{\rho_c} \right\} \quad (11)$$

where  $A_w$  is the horizontal aspect ratio of the grid cell,  $A_w = S_y/S_x$ ;  $\rho_c$  is the sediment bulk density of the bottom;  $z_m$  is the elevation of the pycnocline above the bed and  $\epsilon$  is the eddy diffusivity. Following the work of Thorade (1914), Schmidt (1917), Durst (1924), and Neumann (1952), both the mixed layer depth,  $h - z_m$ , and the eddy diffusivity from wind mixing,  $\epsilon'$ , have two distinct regimes, depending upon the wind speed,  $V$ . A series of logical if statements select the appropriate regime. For weak winds,  $V < 6$  m/sec, the following formulations are selected:

$$h - z_m (\text{meters}) = \frac{3.67 \sqrt{[V(\text{m/sec})]^3}}{\sqrt{\sin \phi}} \quad \text{for } V > 6 \text{ m/sec}$$

$$\epsilon' (\text{cm}^2/\text{sec}) = 1.02 V_{(\text{m/sec})}^3$$

where  $\phi$  is the latitude angle. For strong winds,  $V > 6$  m/sec,

$$h - z_m (\text{meters}) = \frac{7.6 V_{(\text{m/sec})}}{\sin \theta} \quad \text{for } V < 6 \text{ m/sec}$$

$$\epsilon' (\text{cm/sec}) = 4.3 V_{(\text{m/sec})}^2$$

If the mixed layer depth exceeds the local water depth,  $h - z_m > h$ , then  $z_m$  assumes negative values. A second series of logical if statements compares the mixed layer depth to the local depth of water for a particular grid cell,  $n$ . If the mixed layer depth exceeds the local depth, then the

diffusivity, due to wind mixing, is augmented by wave mixing from the bottom boundary layer. Eddy diffusivity from wave mixing,  $\epsilon_w$ , is derived from the work of Nielsen (1979), and written:

$$\epsilon_w = 0.00035 \left[ \frac{u(h-z)}{W_0 h} \right]^{0.68} S_h^{0.4} \delta g T$$

and the total eddy diffusivity in Equation (11) is written:

$$\epsilon = \epsilon' + \epsilon_w \quad \text{for } h - z_m \geq h$$

else: (12)

$$\text{and } \left. \begin{array}{l} \epsilon(z > z_m) = \epsilon' \\ \epsilon(z \leq z_m) = \epsilon_w \end{array} \right\} \quad \text{for } h - z_m < h.$$

The terms  $I_1(x, y, z)$ ,  $I_1(0)$ , and  $I_1(h)$  are integrals which account for the total rms-vorticity of the near bottom flow of a particular grid cell. The functional form of these integrals differs among each of the transport regimes given by Equation (3). For the saltation regime, particle trajectories are only a few boundary thicknesses in length, and consequently, particles remain in suspension over the grid cell from which they originated. There is no net advection of particles from one grid cell to the next in this regime, and the integrals in Equation (11) are relatively simple:

$$I_1(0) = I_1(x, y, z = 0); I_1(\delta) = I_1(x, y, z = \delta) \text{ and for } 0.05 \leq S_h \leq 0.09$$

$$\begin{aligned} I_1(x, y, z) = & -\frac{\Gamma_0}{4\pi} \left\{ \tan^{-1} \left[ \frac{(z-b)(z+z_m)}{x\sqrt{x^2 + (y+S)^2 + (z-b)^2}} \right] - \tan^{-1} \left[ \frac{(z+b)(z+z_m)}{x\sqrt{x^2 + (y+S)^2 + (z+b)^2}} \right] \right\} \\ & -\frac{\Gamma_0}{4\pi} \left\{ \tan^{-1} \left[ \frac{(z+b)(z-z_m)}{x\sqrt{x^2 + (y-S)^2 + (z+b)^2}} \right] - \tan^{-1} \left[ \frac{(z-b)(z-z_m)}{x\sqrt{x^2 + (y-S)^2 + (z-b)^2}} \right] \right\} \end{aligned}$$

(13)

where  $\Gamma_0$  is the integrated root mean squared (rms) vorticity generated over the  $n^{\text{th}}$  grid cell:

$$\Gamma_0 = \int_0^\delta \int_{x_n}^{x_{n+1}} \left\{ \Re \left( \frac{\partial u}{\partial z} \right)^2 \right\}^{1/2} dx dz.$$

$\Re$  is the real part operator and the shear of the near bottom flow,  $\partial u / \partial z$ , is prescribed from the wave/current boundary layer profile

$$u = u_m e^{i\sigma t} (1 - e^{-\alpha}) + u_0 \left[ -\alpha e^{-\alpha^*} + \left(1 - \frac{3}{2}i\right) e^{-\alpha^*} - \frac{i}{2} e^{-\alpha} + \left(\frac{i}{2} - \frac{1}{4}\right) e^{-2Z/\delta} - \frac{3}{4} + \frac{3}{2}i \right] \quad (14)$$

where  $\alpha = (1 + i) Z/\delta$ ;  $u_0$  is the mean current at the top of the boundary layer, and \* denotes complex conjugates. The first term on the right hand side of (14) is the oscillatory part of the boundary layer profile, while the second term is the current boundary layer. The boundary layer thickness used to evaluate (11) and (13) is derived from the work of Jenssen and Carlsen (1976), wherein:

$$\delta = 0.072 d_0 \left[ (2.5 D/d_0)^{0.2} + (u_0 D/\epsilon)^{0.13} \right]. \quad (15)$$

The factor  $d_0/D$  in (15) accounts for wave effects through the inverse Strouhal number while the second term in (15) gives the rectification from mean currents by way of the granular Reynolds number. The factor "b" used to evaluate the integrals in (13) is the displacement thickness associated with the rms vorticity of the grid cell and is calculated by

$$b = \int_0^\infty \left( 1 - \frac{\Gamma_0}{u\delta} \right) dz \cong 1.344\delta. \quad (16)$$

The remaining term in the general solution to be defined is  $\rho_t$ , the bed load bulk density. When the applied fluid stress exceeds the critical threshold stress, the bed dilatates as the grains slide over one another in bed load motion. This reduces the bulk density of the fluid bed interface from the at-



rest value,  $\rho_c$ , to the in-motion value  $\rho_t$ ; which is proportional to the excess applied stress, written  $(S_h - 0.05)$  in non-dimensional form. From the empirical work of Nielsen (1978), we write

$$\rho_t = ak(S_h - 0.05) \frac{2}{\pi} \cos^{-1} \left( \frac{0.05}{S_h} \right)^{1/2} \quad (17)$$

where  $ak$  is an empirically derived coefficient.

As the Shield's parameter exceeds 0.09, the resuspended transport moves above the top of the boundary layer and comes under the influence of advection by the mean bottom currents,  $u_0$ . Once this happens, in either the vortex ripple or sheet flow regimes, the suspended sediment can be carried from one grid cell to the next. In this case, the integrals in the first order solution for any grid cell,  $n$ , become considerably more complex:

$$I_1(0) = I_1(x, y, z = 0); \quad I_1(\delta) = I_1(x, y, z = \delta) \quad \text{and for } S_h > 0.09$$

$$\begin{aligned} I_1(x, y, z) = & -\frac{\Gamma_o}{4\pi} \left\{ \tan^{-1} \left[ \frac{(z-b)(z+z_m)}{x\sqrt{x^2 + (y+S)^2 + (z-b)^2}} \right] - \tan^{-1} \left[ \frac{(z+b)(z+z_m)}{x\sqrt{x^2 + (y+S)^2 + (z+b)^2}} \right] \right\} \\ & -\frac{\Gamma_o}{4\pi} \left\{ \tan^{-1} \left[ \frac{(z+b)(z-z_m)}{x\sqrt{x^2 + (y-S)^2 + (z+b)^2}} \right] - \tan^{-1} \left[ \frac{(z-b)(z-z_m)}{x\sqrt{x^2 + (y-S)^2 + (z-b)^2}} \right] \right\} \\ & -\frac{\Gamma_n}{4\pi} \left\{ \tan^{-1} \left[ \frac{(z+b)}{y-S} \right] - \tan^{-1} \left[ \frac{(z-b)}{y-S} \right] \right\} \\ & -\frac{\Gamma_n}{4\pi} \left\{ \tan^{-1} \left[ \frac{x(z+b)}{(y-S)\sqrt{x^2 + (y-S)^2 + (z+b)^2}} \right] - \tan^{-1} \left[ \frac{x(z-b)}{(y-S)\sqrt{x^2 + (y-S)^2 + (z-b)^2}} \right] \right\} \\ & -\frac{\Gamma_n}{4\pi} \left\{ \tan^{-1} \left[ \frac{(z-b)}{y+S} \right] - \tan^{-1} \left[ \frac{(z+b)}{y+S} \right] \right\} \\ & -\frac{\Gamma_n}{4\pi} \left\{ \tan^{-1} \left[ \frac{x(z-b)}{(y+S)\sqrt{x^2 + (y+S)^2 + (z-b)^2}} \right] \right\} + \frac{\Gamma}{4\pi} \left\{ \tan^{-1} \left[ \frac{x(z+b)}{(y+S)\sqrt{x^2 + (y+S)^2 + (z+b)^2}} \right] \right\} \end{aligned} \quad (18)$$

The integrated rms vorticity from any particular grid cell,  $\Gamma_0$ , is advected to neighboring grid cells, augmenting the local vorticity distribution there. This is accounted for by the new terms containing  $\Gamma_n$  in Equation (18), where from Peace and Riley (1983), we write in finite difference form:

$$\Gamma_n = \Gamma_0 f(x) \quad (19)$$

and

$$f(x) = 1 - \frac{1}{u_0} \sum_{x_n}^{x_{nx}-n} \left\{ u_n + \left[ \frac{(x_n - x_{n-1}) C_1}{A_w S} \right]^{1/2} u_{n-1} \right. \\ \left. \left[ \frac{(x_{n-1} - x_{n-2}) C_1}{A_w S} \right] \left[ u_{n-2} + \left( \frac{u_n - u_{n-1}}{x_n - x_{n-1}} \right) S \right] \right\}$$

n-subscripts are grid cell index numbers and

$$C_1 = \Gamma_0 / u_0 \delta.$$

In the vortex ripple regime,  $0.09 < S_h \leq 0.48$ , the ripple height becomes the dominant vertical length scale at which the vorticity is released into the flow. The vorticity displacement thickness in Equation (18) is thus determined by the ripple height, which from ripple measurements by Steve and Battjes (1984), is written

$$b = 21.0(d_0)/S_h^{1.85} \quad \text{for } 0.09 < S_h \leq 0.48 \quad (20)$$

In the sheet flow regime,  $S_h > 0.48$ , the ripples vanish and the dominant vertical length scale is once again the boundary layer thickness. However, turbulent bursting intervenes in this regime to disrupt the boundary layer and eject vertical plumes well above boundary layer elevations expressed by Equation (16); see Conley & Inman (1992). Elevations of the burst/sweep cycle have been observed under both laboratory and field conditions by Conley (1993), from which we write:

$$b = 420\gamma/u_* \quad \text{for } S_h > 0.48$$

where

$$u_* = \left\{ \frac{\rho u_m^2}{2\pi} \left[ (1 + 0.18\zeta^2) \sin^{-1}(0.3\zeta) + 0.9\zeta \sqrt{1 - 0.9\zeta^2} \right] \right\}^{1/2} \quad (21)$$

$$\zeta = \frac{Hk}{2 \sinh(kh)}$$

The first order solution (11) and its governing integrals are grain size dependent in each of the transport regimes. To account for this, the code incorporates an "ipart" loop which sequentially performs the computations for discrete particle size bins. Nine such particle size bins, ipart = 1, 2...9, are accommodated in both "BOTOMBND.f" and all of the subroutines of "SEDXPORT.f." The size bins range from 1.0 to 200 microns according to Table 3-1. The settling velocities corresponding to this nine size bins are called up from a look-up table stored inside "BOTOMBND.f" and "SEDXPORT.f." The partitioning of  $\rho_c$  and  $\rho_t$  into the corresponding mass fractions for each size bin is accommodated in either of two ways: 1) By a user configured input file called "MASSTOTAL.DAT," or 2) by an automated driver module called "NULLPT.f" that derives a cross shore grain size distribution from wave height data and from bottom composition data derived from the GRASS system base map. The theoretical details of "NULLPT.f" are discussed further in Section 3.2E.

After calculating the initial sediment resuspension based upon nowcast conditions applied to a steady state, we proceed through  $m = 12$  equally spaced time steps, each of duration  $\Delta t = 2$  hours. For each time step, wave and current conditions progressively change until reaching forecast values 24 hours later, as discussed in Sections 3.0 and 3.1. Because of these variations in the hydrodynamic forcing, we relax the steady state assumption for each successive time step,  $m$ , and transport is governed to lowest order by:

$$\frac{\partial \hat{\rho}_m}{\partial \hat{t}} = \frac{\epsilon \Delta t}{\delta^2} \frac{\partial^2 \hat{\rho}_m}{\partial \hat{z}^2} - \frac{u_0 \Delta t}{\delta} \left[ \left( \hat{w}_m + \frac{W_0}{u_0} \right) \frac{\partial \hat{\rho}_m}{\partial \hat{z}} + \hat{\rho}_m \frac{\partial \hat{w}_m}{\partial \hat{z}} \right] \quad (22)$$

where subscripts containing "m" are time step index numbers. The solutions to (22) are subject to the boundary conditions of Equation (10), and written in dimensional form for the  $n^{\text{th}}$  grid cell and  $m^{\text{th}}$  time step as:

Table 3-1. Grain size distribution for "MASSTOTAL.DAT" files

## SEDIMENT SIZE CATEGORIES

Bin	Diameter( $\mu$ )	Interval( $\mu$ )	Number	Concentration	Percent	Effective Dia.( $\mu$ )
1.	1.0	1.0 - 2.0.	1.000	$\times 10^5$	82.23 $\times 10^0$	1.150
2.	2.0	2.0 - 4.0	1.768	$\times 10^4$	14.56 $\times 10^0$	2.300
3.	4.0	4.0 - 7.0	3.125	$\times 10^3$	2.354 $\times 10^0$	4.594
4.	7.0	7.0 - 10.	7.714	$\times 10^2$	4.552 $\times 10^{-1}$	7.874
5.	10.	10. - 20.	3.162	$\times 10^2$	2.603 $\times 10^{-1}$	11.502
6.	20.	20. - 40.	5.590	$\times 10^1$	4.602 $\times 10^{-2}$	23.005
7.	40.	40. - 60.	9.882	$\times 10^0$	6.296 $\times 10^{-3}$	45.325
8.	60.	60. - 100	3.586	$\times 10^0$	2.586 $\times 10^{-3}$	68.722
9.	100	100 - 200	1.000	$\times 10^0$	8.232 $\times 10^{-4}$	115.024
	200		1.768	$\times 10^{-1}$		

$$\dot{\rho}_{n,m}^{(2)} = \rho_{n,m-1}^{(2)}(z) \left\{ 1 - \exp \left[ -z / (2m\Delta t W_0) \right] \right\} + \rho_{n,m}^{(1)}(z) \quad , \quad (23)$$

where  $\rho_{n,m-1}^{(2)}$  is the solution from the previous time step and  $\rho_{n,m}^{(1)}(z)$  is the first order solution (11) evaluated for the  $m^{\text{th}}$  time step conditions and corresponding transport regime of the  $n^{\text{th}}$  grid cell. The first term in Equation (23) may be thought of as the "history term," accounting for the residual resuspension from the previous time step; while the second term in (23) represents the "now term," accounting for new resuspension due to present conditions in the  $m^{\text{th}}$  time step. Both the history and now terms in Equation (23) depend upon the settling velocity,  $W_0$ , which is a function of particle diameter. Logical if statements select either of two settling regimes, depending upon the particular size bin for which Equation (23) is solved. For size bins less than 30 microns, particle settling is controlled by the viscous settling regime for which the settling velocity depends upon  $D^2$ , or:

$$W_0 = \frac{1}{18} \frac{\rho_s - \rho}{\mu} g D^2 \quad \text{for } D < 30 \text{ microns},$$

where  $\mu$  is the molecular viscosity of water. Particles larger than 30 microns are governed by the inertial settling regime for which

$$W_0 = \sqrt{c_0 \frac{\rho_s - \rho}{\rho} g D} \quad \text{for } D > 30 \text{ microns},$$

where  $c_0$  is a constant. At the pycnocline,  $z = z_m$ , settling is hindered by the density interface and by particle to particle stress transfer. This phenomena has been treated as a magneto-hydrodynamic effect by Aijaz and Jenkins (1994), whose theory provides the basis for a hindered settling velocity,  $W'_0$ , at the bottom of the mixed layer according to:

$$W'_0 = W_0 - \left\{ \frac{a(1+Ka)\alpha\alpha_1\mu^2 u_e^2 n}{\epsilon\pi D^2} + \frac{\beta\beta_1}{\pi D^2} + C_1 \frac{h-z_m}{h} \right\}^{1/2}$$

$$\alpha = \frac{4\pi(h-z_m)^2}{\left[h^2 - (h-z_m)^2\right]^2 \epsilon_0}$$

$$\beta = \frac{4\pi(h-z_m)^2 w^2 \rho_e^2 \mu}{z_m(z_m+2h)^4} \left[ h^2 - \frac{1}{3} \left[ (h-z_m)^2 + h^2 + h(h-z_m) \right] \right]^2$$

$$\alpha_1 = \frac{h^3}{(h-z_m)z_m} \left[ h \ln \left( \frac{h-z_m}{h} \right) - z_m \right] + \frac{1}{4} \left[ \frac{h^3 - (h-z_m)^3}{3z_m} - \frac{(h-z_m)^3}{h} \right]$$

$$\beta_1 = \frac{1}{3z_m} \left[ \frac{h^2 - (h-z_m)^2}{6} + (h-z_m)^3 \left[ h^{-1} - (h-z_m)^{-1} \right] \right]$$

K is the Debye-Huckel length or thickness of the electric double layer of charged silt particles; and  $u_e$  is the electrophoretic mobility, both of which are dependent upon sediment minerology.

It is interesting to examine the particle size dependence of the steady state and time stepped solutions from Equations (11) and (23). The parameters of these solutions vary with grain size for the fine grained optically active particles away from the pycnocline according to:

$$W_o \sim D^2$$

$$\epsilon \sim 1/W_o^{0.68}$$

$$\text{or } W_o/\epsilon \sim D^{3.36}$$

$$\text{Also, } \rho_t \sim 1/D$$

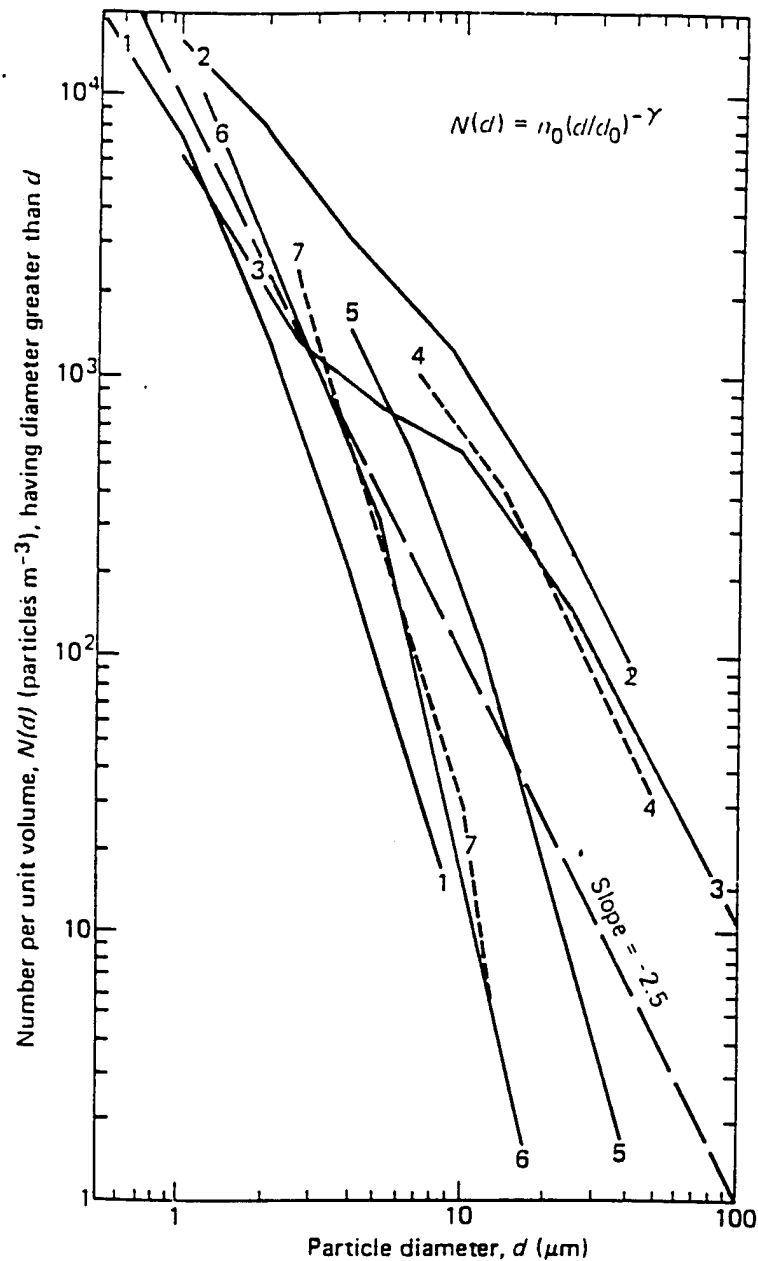
Hence, a log/log plot of particle number versus particle size will have the form

$$\log P_n = \text{CONST}_1 - \gamma \log D - Z \text{CONST}_2 D^{3.36} \quad (24)$$

Close to the bottom where  $z$  is small, the particle size distribution tends to be hyperbolic, so that a log/log plot of particle number versus particle size for small particles will have a straight line decay with a slope of  $\gamma$ . Above the bottom and especially near the surface in deep water, this straight line decay in the logarithmic particle size abundance will tend to roll off as  $-D^{3.36}$ . For an assumption of constant eddy diffusivity, this roll-off would be  $-D^2$ . For the very small particles, the departure from linearity in the log/log will be slight, while rapidly increasing toward the large particle end of the size spectrum. This behavior can be found in the suspended particle size distributions from a number of widely varying ocean bodies (see Figure 3-3). The average log/log slope is  $\gamma = -2.5$ , and deviations from the straight line hyperbolic distribution tend to increase towards the coarser size fractions.

The program for "BOTTM·f" and "BOTXPORT·f" uses the "bottm·inp" input file, an unformatted binary gridded bathymetry file, 'ifile·grd' from OCEANBAT, and an unformatted binary wave height array 'ifile'·bwh, from "OCEANRDS·f." The gridded input files use MKS units. The output file is called "'ifile'·bot" and uses CGS units.

Specific input values required to run "BOTTM·f" and "BOTXPORT·f" are: "nx", the number of grid cells in each longitudinal sweep (0 to 200); "ny", the number of grid cells in each latitudinal sweep (0 to 200); "igrdx", the location of a specific grid cell in a longitudinal sweep (0 to 200); "igrdy", the location of a specific grid cell in a latitudinal sweep (0 to 200); "sx" is the longitudinal grid spacing in meters; "sy" is the latitudinal grid spacing in meters; "per" is the wave period in seconds; "amp" is the deep water wave amplitude;  $u_0$  is the tidal or inertial current time series; "rci" is the total sediment bulk density ( $\text{gm/cm}^3$ ) of the bottom for all size fractions which make up the bottom; "rc1.....rc115" are the relative mass fractions for 9 separate particle-size bins between 1 micron and 200 microns for the bottom sediments from the input file "MASSTOTAL·DAT"; and "ak2" which is the mixing length stretching factor to modify the constant in Equation (12).



Cumulative size distributions of oceanic particles. (1) Pacific deep water; (2) Swedish fjord; (3) Mediterranean (microscopic); (4) mean North Atlantic; (5) western North Atlantic; (6) Mediterranean (particle counter); (7) subtropical western Pacific. Average exponent for power law is  $\gamma = 2.5$ . [Adapted from Jerlov, N. G., *Marine Optics* (1976).]



## 2. "SURXPORT.f"

"SURXPORT.f" solves for the particle resuspension occurring in the surf zone and treats that suspended load as a line source to the offshore particle distribution calculated by "BOTTMBND.f" and "BOTXPORT.f". The code inputs the breaking wave heights, breaker angles, and x-y grid cell number of waves breaking from the file 'ifile'.bra output by "OCEANRDS.f" and "WINDWAVE.f". "SURXPORT.f" internally computes the cross-shore rip currents and solves for the seaward dispersion of surf zone suspended load due to the combination of rip advection and lateral mixing. Horizontal diffusivities are computed internally. The subroutine outputs the vertical distribution of sediment bulk density and particle numbers for 9 separate size bins at any selected location within the study site grid. The output files are called "ifile.sur" and 'ifile'.srl and are in CGS units.

The line source for surf zone suspension is taken as the locus of breakpoints along the shore at whatever grid cell the condition for wave breaking is satisfied, namely

$$H_b = \xi h_b(x, y)$$

where  $H_b$  is the breaking wave height;  $h_b$  is the depth of water at the breakpoint; and  $\xi$  is a constant of proportionality  $\approx 1.3$ . The seaward (x-directed) dispersion of particles from this line source is governed by the lateral advection/diffusion equation, Bowen (1980).

$$\frac{\partial \rho}{\partial t} = \epsilon_x \frac{\partial^2 \rho}{\partial x^2} - u_s \frac{\partial \rho}{\partial x} - \lambda_0 \rho \quad (25)$$

where

$\epsilon_x$  = horizontal diffusivity

$\lambda_0 = W_0/h_b$ ; and

$$u_s = K_b \sqrt{g H_b} \left( \frac{\tan \beta}{c_f} \right) \frac{\Delta H_b}{\Delta y}$$

$\tan \beta$  = beach slope

$$K_b = \frac{2g \tan^2 \beta}{H_b \sigma^2} \text{ reflection coefficient}$$

For the initial condition  $m = 0$ , in the time step sequence, we assume a steady state,  $\partial\rho/\partial t = 0$ , for which the solution to Equation (25) for the  $n^{\text{th}}$  grid cell is:

$$\rho_{n,0} = \frac{G_{n,0}}{\sqrt{u_s^2 + 4\epsilon_x \lambda_0}} \exp[B_{n,0}(x_b - x_n)] \quad (26)$$

where  $x_b$  = the breakpoint

$$B_{n,0} = \frac{u_s - \sqrt{u_s^2 + 4\epsilon_x \lambda_0}}{2\epsilon_x} \quad (27)$$

Here,  $G_{n,0}$  is the strength of the line source and is specified by the total suspended load of the surf zone as derived by the energetics-based model of Inman and Bagnold (1963) or

$$G_{n,0} = \frac{24 K_s \rho H_b^2 \sqrt{gh_b^2} \tan\beta}{(\rho_s - \rho) K_b h_b^2 s_x} \quad (28)$$

where  $K_s = 2.2\sqrt{K_b}$ , suspended load efficiency.

For variable wave conditions in each of the subsequent time steps,  $m > 0$ , solutions to Equation (25) may be written:

$$\begin{aligned} \rho_{n,m} = \rho_{n,m-1} \left\{ 1 - \exp\left[-(x_b - x)^2 / 4\epsilon_x m \Delta t\right] \right\} & \quad \text{History Term} \\ + \frac{G_{n,m}}{\sqrt{u_s^2 + 4\epsilon_x \lambda_0}} \exp[B_{n,m}(x_b - x)] & \quad \text{Now Term} \end{aligned} \quad (29)$$

where  $\rho_{n,m-1}$  is the solution for the  $n^{\text{th}}$  grid cell from the previous time step, and  $B_{n,m}$ ,  $G_{n,m}$  are evaluated from Equations (27) and (28), respectively, according to existing conditions for the  $m^{\text{th}}$  time step in the  $n^{\text{th}}$  grid cell.

The suspended particle load computed in "SURXPORT.f" using Equations (26) through (29) is then used to re-initialize the surface

concentration in the offshore regime; where these particles are subsequently mixed downward by "BOTXPORT.f"-like FORTRAN statements incorporated in "SURXPORT.f" to get the modified particle depth profiles and size distributions.

Input parameters to "SURXPORT.f" are identical to "BOTXPORT.f" with the following additional parameters: "tanbeta" is the beach slope in radians; "aks" is the suspended load efficiency which has a default value of 0.78; "akb" is the beach packing which will vary from 0.54 for cubic packing to 0.68 for ramboid packing; and "ak4" is the lateral mixing length stretching factor which modifies the constant in Equation (12).

### 3. "RIVXPORT.f"

This subroutine treats the suspended wash load of a river discharge as an additional point source superimposed on the surf zone line source of "SURXPORT.f". Seaward of this embedded point source, the spreading from lateral mixing and advection is calculated from a solution to the two-dimensional advection diffusion equations, Armi (1979) or

$$\frac{\partial \rho}{\partial t} = (u_{r0} - \nabla \epsilon_H) \cdot \nabla \rho - \epsilon_H \nabla^2 \rho \quad (30)$$

where  $\epsilon_H$  is the horizontal diffusivity, and  $u_{r0}$  is the vector resultant of the river discharge velocity,  $u_r$ , and the tidal/inertial current,  $u_0$ . In Equation (30), the term  $-\nabla \epsilon_H$  acts much like an additional advective field in the direction of high to low eddy diffusivity. This additional "gradient eddy diffusivity velocity" is the result of local variations in wave intensity associated with the refraction/diffraction pattern, and is strongest in the wave shoaling region nearshore.

For the initial,  $m = 0$ , steady state,  $\partial \rho / \partial t = 0$ , the solution to Equation (30) for the  $n^{\text{th}}$  grid cell is

$$\rho_{n,0} = Q_{n,0} \exp \left[ R_{n,0} \left( \sqrt{(x_r - x_n)^2 + (y_r - y_n)^2} \right) \right] \quad (31)$$

where

$$Q_{n,0} = \frac{u_r \rho_i}{\sqrt{u_{r0}^2 + 4\lambda_{r0}\epsilon_H}} \quad (32)$$

$$R_{n,0} = \frac{u_{r0} - \sqrt{u_{r0}^2 + 4\lambda_{r0}\epsilon_x}}{2\epsilon_H} \quad (33)$$

$$u_{r0} = (q_0/A_0) \cos\theta - \sqrt{u_{n,x}^2 + u_{n,y}^2} \sin\theta$$

Here,  $\lambda_{r0} = W_0/d_r$ ;  $x_r, y_r$  are the coordinates of the axis of the river mouth;  $\rho_i$  is the bulk density of the river's wash load, and  $w_0$  is the settling velocity of the various size fractions which make up the river wash load, and  $d_r$  is the river depth,  $q_0$  is the river flow rate;  $A_0$  is the river cross section,  $\theta$  is the angle of the coastline;  $(u_{n,x}, u_{n,y})$  are the orthogonal tidal velocity components; and  $(x_n, y_n)$  refer to the coordinates of the  $n^{\text{th}}$  grid cell.

For the sequence of time steps following the initial conditions, i.e., for  $m > 0$ , variable wave, currents, and river discharges lead to finite difference solutions to (30), which may be written in general form in the  $m^{\text{th}}$  time step for the  $n^{\text{th}}$  grid cell as:

$$\begin{aligned} \rho_{n,m} = \rho_{n,m-1} \left\{ 1 - \exp \left[ - \left( (x_r - x_n)^2 + (y_r - y_n)^2 \right) / 4\epsilon_m \Delta t \right] \right\} & \text{History Term} \\ + Q_{n,m} \exp \left\{ R_{n,m} \left( \sqrt{(x_r - x_n)^2 + (y_r - y_n)^2} \right) \right\} & \text{Now Term} \end{aligned} \quad (34)$$

where  $\rho_{n,m-1}$  is the solution from the previous time step and  $Q_{n,m}$  and  $R_{n,m}$  are evaluated from Equations (32) and (33), respectively, for the wave, current, and river discharge conditions of the  $m^{\text{th}}$  time step. Solutions calculated from Equation (32) through (34) are then superimposed on "SURXPORT.f" and "BOTXPORT.f" subroutines to calculate final outputs of "SEDXPORT.f".

Input parameters to "RIVXPORT.f" are identical to "SURXPORT.f" with the following additions: "q" is the river discharge rate ( $\text{m}^3/\text{sec}$ ) derived

from the hydrology module HEC-1; "irx1" is the x-coordinate of the right-hand bank of the river mouth; "iry1" is the y-coordinate of the right-hand bank of the river mouth; "irx2" is the x-coordinate of the left-hand bank of the river mouth; "iry2" is the y-coordinate of the left-hand bank of the river mouth; "dr" is the depth of the river mouth on its centerline axis (m); "rrs" is the bulk density of the river washload, (gm/cm<sup>3</sup>); D<sub>1</sub> ... D<sub>q</sub> are the characteristic size fractions of the river washload, and "rwidth" is the width of the river mouth (m).

#### D. "TIDES1DAY.f" and "TIDECUR.f"

Depth integrated tidal currents on a fine scale near shore are calculated from deep water solutions to Laplaces tidal equations (see Lamb, 1932), which are used to drive a coastal boundary layer after Longuet-Higgins (1978). The deep water solutions are calculated from a local tidal elevation map generated by the module "TIDES1DAY.f." "TIDES1DAY.f" uses Long's Code (U.S. Dept. of Commerce, SP #98, 1988) to calculate tidal elevations,  $\zeta$ , from as many as 37 tidal constituents:

M(2)	N(2)	S(2)	O(1)	K(1)	K(2)
L(2)	2N(2)	R(2)	T(2)	LAMBDA (2)	MU(2)
NU(2)	J(1)	M(1)	00(1)	P(1)	Q(1)
2Q(1)	RHO(1)	M(4)	M(6)	M(8)	S(4)
S(6)	M(3)	S(1)	MK(3)	2MK(3)	MN(4)
MS(4)	2SM(2)	MF	MSF	MM	SA
SSA					

Tidal elevations derived by "TIDES1DAY.f" are then throughput to "TIDECUR.f" to compute the orthogonal components of the deep water tidal currents:

$$\begin{aligned}
u_{x,\infty} &= \frac{ig}{a} \left[ \frac{2\Omega s \cot \theta (\zeta - \bar{\zeta}) + \omega \left( \frac{d\zeta}{d\theta} - \frac{d\bar{\zeta}}{d\theta} \right)}{\omega^2 - (2\Omega \cos \theta)^2} \right] \\
u_{y,\infty} &= \frac{g}{a} \left[ \frac{s\omega \csc \theta (\zeta - \bar{\zeta}) + 2\Omega \cos \theta \left( \frac{d\zeta}{d\theta} - \frac{d\bar{\zeta}}{d\theta} \right)}{\omega^2 - (2\Omega \cos \theta)^2} \right] \quad (35)
\end{aligned}$$

where  $\theta$  is the co-latitude;  $\bar{\zeta}$  is the equilibrium tide;  $g$  is the acceleration of gravity;  $\Omega$  is the angular speed of rotation of the earth,  $a$  is the mean radius of the earth;  $s$  is an integer;  $\omega$  is the radian frequency of the potential tide as determined from the tidal constituents.

There are three distinct types of coastal boundary layers, which can be driven by the deep water tidal currents of Equation (35), namely: 1) progressive, 2) standing, and 3) mixed. The progressive type results from deep water tides whose phases are dependent upon position, typically those dominated by the M(2) component. These give rise to coastal boundary layers of the form for the  $n^{\text{th}}$  grid cell:

$$u_n = u_1 \{1 - \exp[-(1+i)\hat{r}_n]\} \quad (36)$$

where

$$\hat{r}_n = \sqrt{(x_b - x_n)^2 + (y_b - y_n)^2} / \delta_x$$

$\delta_x$  = coastal boundary layer thickness

$u_1$  = vector sum of progressive  $(u_{x,\infty}, u_{y,\infty})$  components.

The standing coastal boundary layers are driven by deep water tidal currents whose phases are independent of position, typically those with large

Mu(2) and 2N(2) constituents. These coastal boundary layers have the general form for the  $n^{\text{th}}$  grid cell:

$$u = u_2 \left\{ (1+i)\hat{r} \exp[-(1-i)\hat{r}] + \left( \frac{5}{2}i - 1 \right) \exp[-(1-i)\hat{r}] - \frac{i}{2} \exp[-(1+i)\hat{r}] + \left( \frac{i}{2} - \frac{1}{4} \right) \exp(-2\hat{r}) + \frac{5}{4} - \frac{3}{2}i \right\} \quad (37)$$

where  $u_2$  = vector sum of standing ( $u_{x,\infty}$ ,  $u_{y,\infty}$ ) components.

For mixed tides, the coastal boundary layer is a linear combination of the progressive and standing components from Equations (36) and (37).

#### E. "NULLPT·f"

This module prescribes the mass fractions for the nine separate particle size bins listed in Table 3-1. The model is based upon the null point theory and validation experiments of Ippen and Eagleson (1955) for the cross shore sorting of sediments by waves. The "NULLPT·f" module inputs wave heights, wave numbers, depths, and bottom composition data for each grid cell, and computes the mass fraction in each of nine particle bins for the  $n^{\text{th}}$  grid cell from

$$rc_{n,i} = 6.092 \ r_n \frac{(\mu D_i)^{i_b}}{(i_b)!} \exp(-\mu D_i) \quad (38)$$

$$\mu = \left[ \left( \frac{H_n}{h_n} \right)^2 \left( \frac{C_n}{W_{0,i}} \right) \left( \frac{2\pi}{k_n H_n} \right) - 11.6 \right] \left( \frac{k_n}{D_i} \right)^{1/2}$$

where  $i_b$  is the total number of size bins = 9;  $D_i$  is the grain diameter of the  $i^{\text{th}}$  size bin;  $H_n$  is the wave height of the  $n^{\text{th}}$  grid cell;  $h_n$  is the local water depth of the  $n^{\text{th}}$  grid cell,  $k_n$  is the wave number of the  $n^{\text{th}}$  grid cell;  $C_n = \sigma/k_n$  is the local phase velocity of the  $n^{\text{th}}$  grid cell, and  $W_{0,i}$  is the settling velocity of the  $i^{\text{th}}$  size bin. The factor  $r_n$  is the characteristic bulk density of 14 different possible bottom types. Values of  $r_n$  are read from a look-up table internal to "NULLPT·f." The local value of  $r_n$  for the  $n^{\text{th}}$  grid cell is determined from an input file called "bottom·type·hdf," which is

constructed from a base map that charts discrete patches of bottom sediment types after scanning nautical or DMA maps. Each of the 14 bottom types is given an integer code and stored in "bottom-type-hdf" files according to:

Bottom type	Integer code	$r_n$ gm/cm <sup>3</sup>
kelp	(1)	0.15
brown sand	(2)	0.48
green sand	(3)	0.46
sand	(4)	0.58
muddy sand	(5)	0.43
green mud	(6)	0.21
gray mud	(7)	0.25
green mud, sand, shell	(8)	0.36
mud	(9)	0.18
rocky	(10)	0.94
rock	(11)	1.40
green mud & sand	(12)	0.33
gray mud & sand	(13)	0.31
brown mud & sand	(14)	0.39

The sum of all the mass fractions gives the total bulk density of the immobile bed or

$$\rho_{c,n} = \sum_{i=1}^{i_b} rc_{n,i} \quad (39)$$

#### F. "BIOEXPORT.f"

This module calculates the mixing and sinking of the net and nano plankton at the end of each 2-hour growth period computed by the module "BIOMASS.f" (see Figure 3-1). Time splitting is invoked between the growth and the advection-mixing processes under the assumption that growth is slow relative to the advection-mixing processes. The advection-mixing solutions are distinctly different for the biological particles for two reasons: 1) settling and mixing are both downward from a source layer at the surface, and 2) the dimensions of the source layer are controlled by



optical rather than hydrodynamic effects. The source layer thickness for the biological particles is on the order of the 1% light level depth,  $Z_{PAR}$ . Consequently, distinctly different transport equations govern the dispersion of biological particles. For these particles, the transport equation may be written:

$$\frac{\partial^2 N}{\partial \eta^2} + a \frac{\partial N}{\partial \eta} = 0 \quad (40)$$

where  $N$  is a cell number concentration;  $\eta$  is a similarity variable equal to:

$$\eta = Z / \sqrt{\epsilon m \Delta t}$$

and  $a$  is a parameter defined as:

$$a = \frac{(Z_{PAR} + 2W_0 m \Delta t)}{2\sqrt{\epsilon m \Delta t}}.$$

Initial conditions to Equation (40) are set by the output of the biological growth model, "BIOMASS.f." The "BIOMASS.f" growth model passes three parameters to "BIOEXPORT.f" at the end of each growth period, namely: cell numbers at the surface,  $N_{z=0}$ , cell numbers at the 1% light level,  $N_{ZPAR}$ , and the depth of the 1% light level,  $Z_{PAR}$ . Consequently, the boundary conditions on Equation (40) are:

$$N = N_{z=0} \quad @ \quad \eta = 0 \quad (41)$$

$$\int_0^h N(m) \, dz = \int_0^h N(m+1) \, dz$$

The second boundary condition requires that the cell numbers are conserved during the advection/mixing time step, i.e., that only the growth cycles can change the total number of cells from one time step to the next.

The solution to Equation (40) subject to (41) for the  $m^{\text{th}}$  time step at the  $n^{\text{th}}$  grid cell is

$$N_{n,m} = N_{n,0} - K_{n,l} (1 - e^{-a\eta}) \quad (42)$$

where

$$N_{n,0} = N_{ZPAR} + \frac{(N_{Z=0} - N_{ZPAR})ZPAR}{(ZPAR + 2ZPAR_n \sqrt{\epsilon m \Delta t} / h_n + W_0 m \Delta t)}$$

$$K_{n,l} = (N_{n,0} - N_{n,k}) / (1 - e^{-a/\sqrt{\epsilon m \Delta t}})$$

$$N_{n,k} = N_{n,0} e^{-[(4.61)Z / (ZPAR + 2ZPAR_n \sqrt{\epsilon m \Delta t} / h_n + W_0 m \Delta t)]}$$

$N_{z=0}$  = Cell number at the surface at start of  $m^{th}$  time step

$N_{ZPAR}$  = Cell number at the 1% light level at start of  $m^{th}$  time step

$ZPAR$  = The 1% light level

Computations using Equation (42) are performed for two distinct cell sizes: 1) a nano plankton where diameter is 5 microns with a settling velocity  $W_0 = 0.0001736$  cm/sec; and 2) a net plankton whose diameter is 20 microns with a settling velocity  $W_0 = 0.0009259$  cm/sec. The output files for "BIOEXPORT.f" are:

XCELL_5.1m	5 micron cell numbers 1 meter below surface
XCELL_5.2EE	5 micron cell numbers at 1% light level
XCELL_5.BOT	5 micron cell numbers 1 meter above bottom
XCELL_20.1m	20 micron cell numbers 1 meter below surface
XCELL_20.ZEE	20 micron cell numbers at 1% light level
XCELL_20.BOT	20 micron cell numbers 1 meter above bottom

### 3.3 24-Hour Simulation

A 24-hour simulation was performed to hindcast the conditions for a  $\approx 100$  square mile study site at Camp Pendleton, CA, for January 23, 1993.

The simulation sequentially performed 12, 2-hour, time steps of the hydrodynamic forcing functions and calculated the sediment and prological response to yield the optical properties of the water column at the end of each two-hour time step.

#### A. INITIALIZATION

Prior to performing the time step loop, the following modules were executed to generate the parameters and boundary values necessary to perform the calculations:

- 1) "OCEANBAT.f" generates a 200 x 200, 3-arc, second resolution bathymetry grid ("camppend.grd"), from the NOS data base. The northwest corner of the study grid was specified to be 33°, 19.0' Latitude, 117°, 30.6', Longitude. The output is stored as an ASCII array in a file called "camppend.grd."
- 2) TIDCUR1DAY calculates the water elevation relative to MSL and a single mean offshore tidal current and direction for each of the 12, 2-hour, time steps and stores the information in a file called "tidcur1day.dat."
- 3) SUNPOS & ATMPROP calculate the solar irradiance array for the 24-hour simulation and store the information in "irad.dat."
- 4) NOWFOR performs a linear interpolation for the other time varying parameters. Initial and forecast values for Cloud Cover, Air Temperature, Sea Surface Temp, Sea Surface Pressure, 24-hour Precipitation, Surface Wind Speed, Sea Period, Sea Direction, Sea Height, Swell Period, Swell Direction, Swell Height, and Offshore Current Velocity were obtained from NODDS for the morning of January 23, 1993, and the morning of January 24, 1993, and linear interpolated values were made available to the appropriate program module in the form of a run time matrix.

In a similar fashion, Offshore Current Velocity and Direction, Salinity, Santa Margarita River Output, and San Luis Rey River Output were estimated from climatic data for both Jan. 23, and Jan. 24, 1993, and linear interpolated values were calculated by NOWFOR and incorporated in the run time matrix.

Sediment size distribution and mass fraction for each source of sediment, offshore bottom, surfzone, and suspended load from rivers 1 and 2, Santa Margarita, San Luis Rey, are obtained and incorporated into a data file called "MASSTOTAL.DAT."

## B. TIME STEP EXECUTION

During execution, each module in the time step sequence interrogates its unique input file, "module-inp," which is updated prior to execution by the run time matrix. The order of execution is as follows: TIDECUR, OCEANRDS, WINDWAVE, BOTTMBND, SEDXPORT, BIOMASS, and BIOXPORT. The outputs of each of these modules are in the form of 200 x 200 spatial arrays at four, user-selected depths. The general form of the output files is "layer(n).(xxx)." For example, an output of SEDXPORT evaluated at the surface is "layer1.sed." By convention, Layer 1 is the surface, Layer 2 is the bottom, and Layers 3 and 4 are user-selectable to any arbitrary depth.

The information generated by each of these modules is passed along to the next module in the sequence, as needed. In addition, a binary file is written for the sediment distribution parameters to allow a "memory" of the previous time step. That memory file is continually updated by direct access during execution of SEDXPORT.

Details of the execution of the individual modules in the time steps are as follows:

TIDECUR calculates the local currents from the mean, offshore, tidal current, the bathymetry, "camppend.grd," and any inertial current and direction specified by the run time matrix. For Jan. 23, 1993, the inertial current was set to 0. The local current information for each of the 200 x 200 grid cells is resolved into x and y vectors, true east, true north, and stored as "xcur.xpt," and "ycur.xpt" files.

OCEANRDS performs refraction-diffraction of the swell component of the wave spectra with input conditions for initial and forecast values of wave period, height, and direction, received from linear interpolated NODDS data, bathymetry from "camppend.grd," and water elevation from tidcurlday. Outputs are wave height, wave angle, and wave number for each of the 200 x 200 grid cells; files are called "camppend-wh1," "camppend-an1," and "camppend-wn1."

WINDWAVE tracks the high frequency component of the wave spectra from the NODDS forecast and after interpolation to estimated values for each 2-hour time step; performs a similar refraction-diffraction calculation as OCEANRDS. Outputs of WINDWAVE are "camppend-wh2," "camppend-an2," "camppend-WN2," and the combined wave height, "camppend-wht."

BOTTOMBND use wave, current, and bathymetry files to calculate the bottom resuspension to the top of the bottom boundary layer. It uses, as a fundamental input, the sediment size distribution and mass fraction from the data file mass "total.dat." BOTTOMBND treats each size fraction independently and outputs the bulk density for each fraction at each grid cell in output files called bin 'n'.BND, for the simulation of Jan. 23, 1994. The total sediment distribution was modeled as nine, separate size bins.

SEDXPORT advects the inorganic sediment from each of four sources, offshore bottom boundary layer, surfzone, river1 (Santa Margarita), and river 2 (San Luis Rey). The subroutine "NULLPT.f" gives the mass fraction for each of 9 size bins from each sediment source in the base map bottom composition distribution shown in Figure 3-4. Examples of the resulting cross shore variation in grain size distribution are shown in Figure 3-5. The hydrodynamic forcing parameters, North & East current vectors, wave height, wave angle, and wave number, are read in, and total particle numbers/ml for each grid cell at the four layers are output. For example, the particle numbers/ml at the surface are located in "layer1-sed," by convention.

BIOXPORT advects and mixes plankton numbers using the identical, hydrodynamic forcing parameters as SEDXPORT. Files for plankton number/ml are read from BIOMASS for two plankton sizes (5 & 20  $\mu\text{m}$ ) at two vertical layers; 1 meter below the surface and at the depth of the 1% height level z-par. These four files are called cell\_5.1m, cell\_5.2ee, etc.

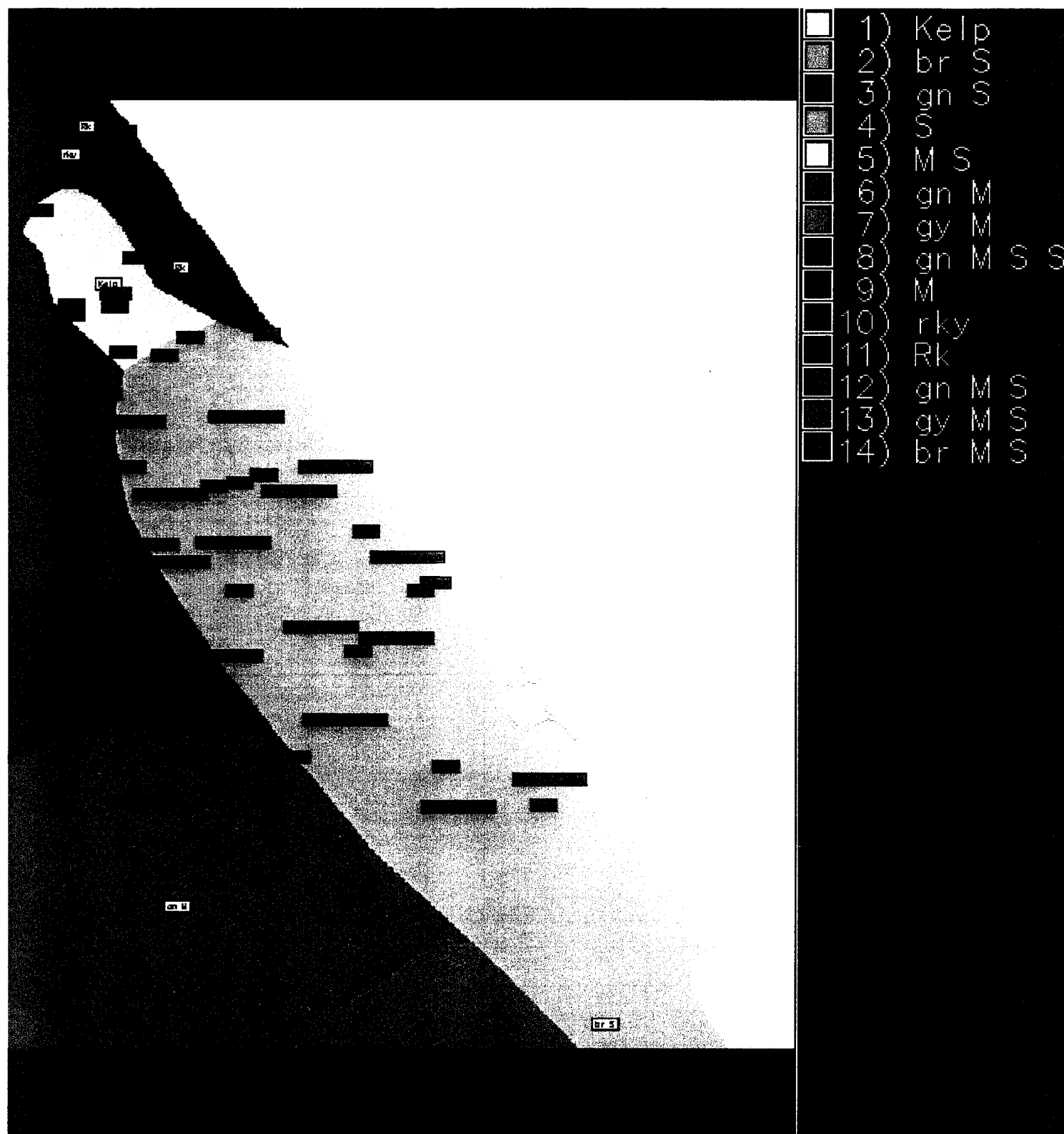


Figure 3-4. Bottom composition map for the 24-hour time stepped simulation

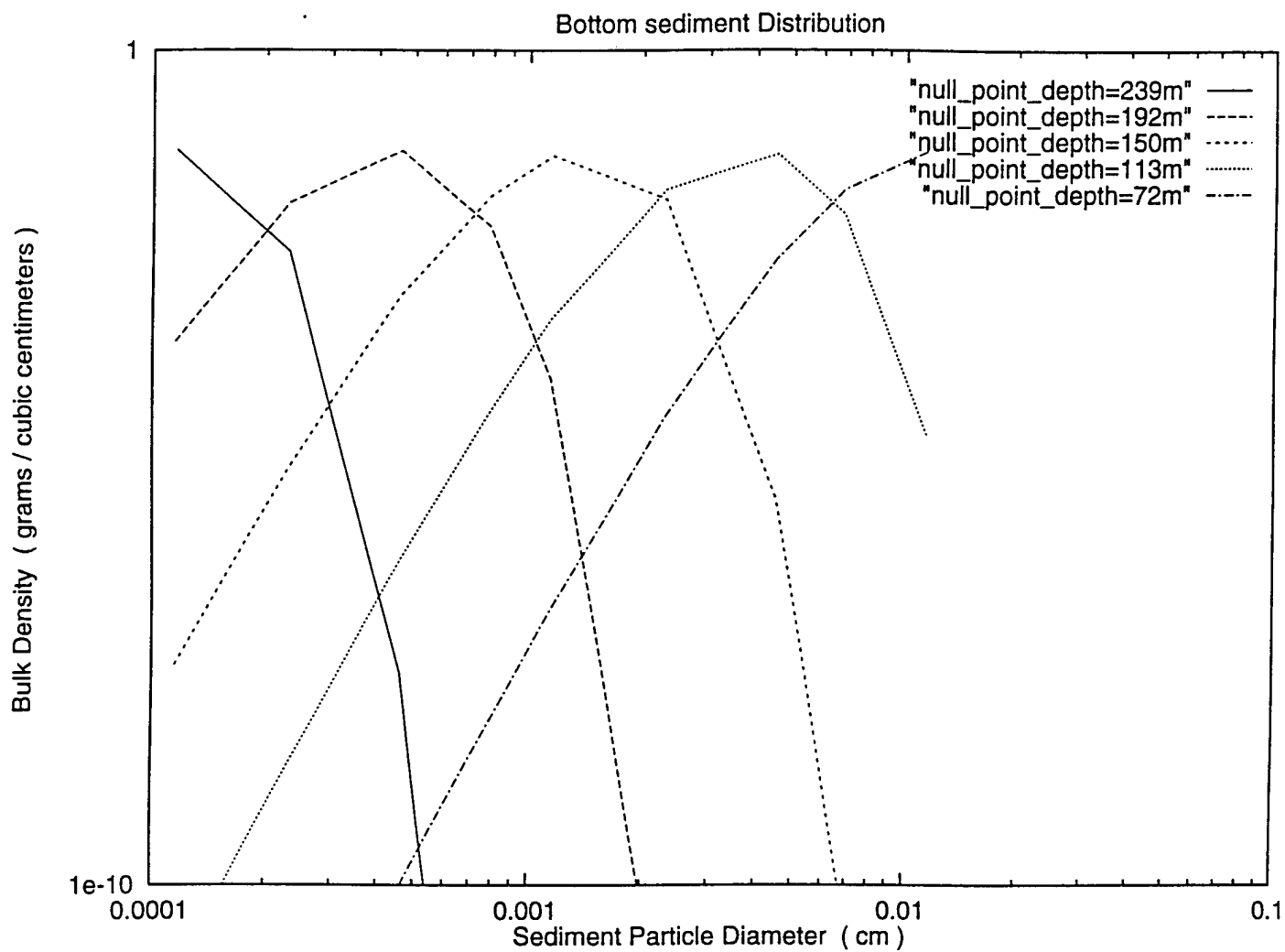


Figure 3-5. Cross shore variability in grain size distributions  
from "NULLPT.f"

The cell numbers are redistributed and returned as xcell\_5.1m, xcell\_5.2ee, etc.

### C. CALIBRATION

The subroutines of "SEDXPORT.f" contain seven free parameters which are selected by a calibration data set specific to the coastal type for which the hindcast/forecast simulation is run. These parameters are as follows according to subroutine:

#### BOTXPORT.f

- \*ak2 - stretching factor for vertical eddy diffusivity,  $\epsilon$
- \*ak - adjusts source strength of the bed load bulk density,  $\rho_t$

#### NULLPOINT.f

- \*ak7 - adjusts the asymmetry of the grain size distribution curve,  $\mu$

#### SURXPORT.f

- \*aks - adjusts the surf zone suspended load efficiency,  $K_s$
- \*ak4 - stretching factor for the horizontal eddy diffusivity,  $\epsilon_x$

#### RIVXPORT.f

- \*ak3\_1 - adjusts the wash load source strength through the bulk density of the river discharge,  $\rho_i$
- \*ak3 - stretching factor for the horizontal eddy diffusivity of the river plume,  $\epsilon_H$

Calibration data for these parameters was gathered at two separate moorings off the mouth of the Santa Margarita River near Oceanside,



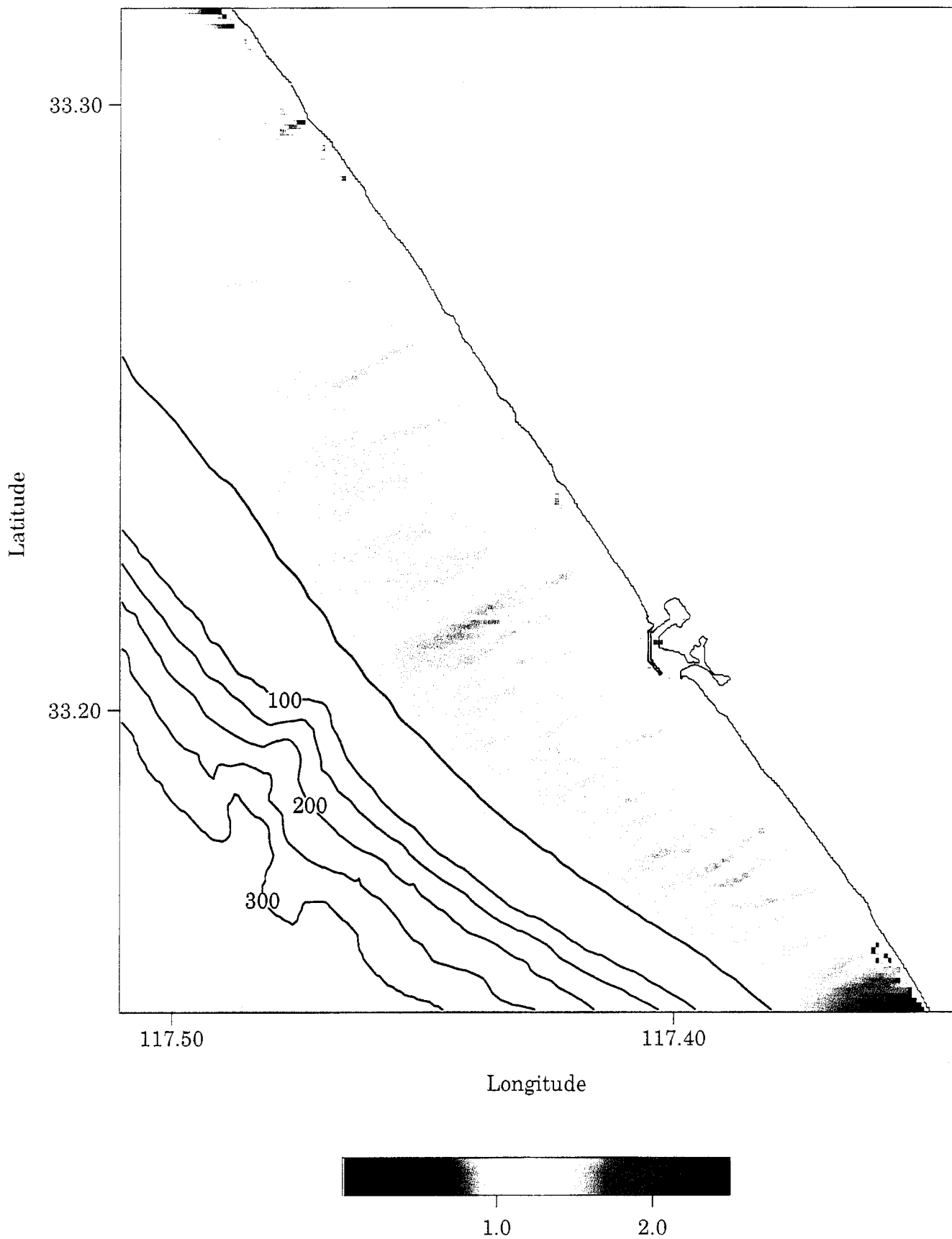
California, on 27 Nov 1993. One of these moorings was located in 20 m depth water, while the other was inshore at 14 m depth along a range line connecting the 20 m mooring with the river mouth. At each mooring site, water samples were collected at 3 depths: a) 1 meter above the bottom; b) 3 meters below the sea surface; and 3) mid depth, i.e., 10 meters below the surface for the 20 m mooring, and 7 meters below the surface for the inshore mooring. These water samples were analyzed for particle number concentrations using a laser particle sizer and counter. Wave measurements were provided by a four-element pressure sensor array off Oceanside Harbor; operated by the Coastal Data Information Program, which recorded 0.94 meter high swell waves from  $258^\circ$  at 14 sec. and 0.28 meter high wind waves from  $297^\circ$  at 7 seconds. A USGS gauge station on the Santa Margarita River recorded low river flow rates at 6.8 meters<sup>3</sup>/seconds. With these data, and hindcasted tidal currents from TIDCUR1DAY, the SEDXPORT.f model was run through a sequence of calibration iterations in which the above parameters were varied until minimizing the mean squared error between the modeled output and the measured particle numbers at depth. Once these calibration parameters were "tuned" to give particle number profiles which conformed with the measured 3-point profiles, the model was then run end-to-end in a full 24-hour hindcast simulation for 23 Jan 93.

#### D. RESULTS

Figure 3-6 shows the wave height distribution resulting from the refraction/diffraction pattern of a two-component, rectangular spectra for the "nowcast" conditions at the start of the time step sequence. The deep water swell component had a 12-second period and a 0.556 meter height approaching from  $239^\circ$ . The windwave component was at 8 seconds period with a deep water height of 0.484 meters and a direction of  $255^\circ$ . The directional spreading of the swell and windwave components over the irregular shelf geometry produces the patterns of "shadows" and "bright spots" along the coastline, and a certain degree of longshore variation of wave height that contributes to rip current generation.

Figure 3-7 shows the resulting distribution of suspended sediment at the sea surface due to bottom and surfzone resuspension by the waves in Figure 3-6. We find that the Shield's criteria for onset of motion causes surface particle concentrations to rise above background levels inshore of a depth contour of about 18 meters. The "fabric" in the nearshore suspended

Wave Height Distribution, 00:00 Jan 23, 1993



Wave Height (m): Swell - 12 sec, 239 deg; Windwave - 8 sec, 255 deg

Figure 3-6. Wave height distribution for the First Time Step  
3-44

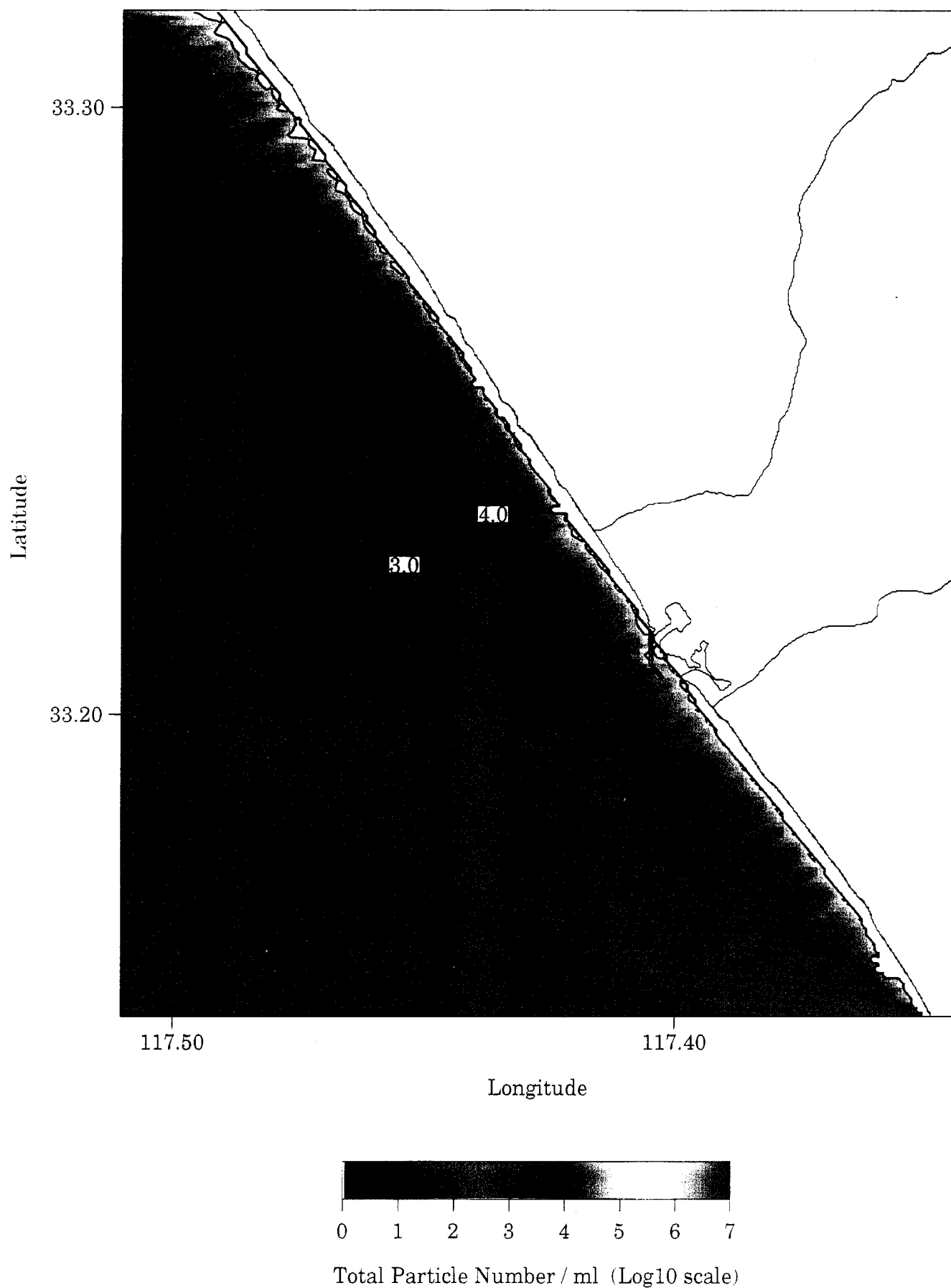


Figure 3-7. Suspended sediments at the surface for the First Time Step 3-45

sediment concentration resembles the pattern of shadows and bright spots found in the refraction/diffraction plot of Figure 3-6. The fingers in the particle concentration contours which project seaward correspond to the location of rip currents.

Figure 3-8 shows the flood hydrographs for the two rivers which appear in Figure 3-7. The northernmost river is the Santa Margarita and the other is the San Luis Rey. Figure 3-8 also plots cumulative rainfall. We see that at 2400 hours on 22 Jan 93, at the start of the time step sequence, there was no rainfall accumulation and, consequently, there is no river runoff shown in Figure 3-7. However, two distinct squalls followed, with one peak rainfall event at 0200 hours and the other at 0600 hours on 23 Jan 93. These two squalls induced flow in both rivers that peaked at 1400 hours and continued throughout the remainder of the 24-hour time step sequence.

At 1000 hours on 23 Jan 93, the LANDSAT made images of the study region. The tidal currents at that time were flood flowing to the south as computed by "TIDECUR-f" in Figure 3-9. The resulting surface dispersion of suspended sediments due to both wave resuspension and river discharge is shown in Figure 3-10. At this time step, the Santa Margarita was discharging 89.76 cubic meters/sec, while the San Luis Rey was flowing at 17.95 cubic meters/sec. Wave heights had dropped slightly to 0.495 meters for the swell waves and 0.390 meters for the wind waves. Figure 3-10 shows that even at these modest flow rates, the river plumes overwhelm the wave resuspension in elevating particle number concentrations. We also find in Figure 3-10 that the river plumes are bending to the south and that they bear remarkable qualitative similarity to the LANDSAT image in Figure 3-11. Figures 3-10 and 3-11 give indications of the horizontal distribution of total numbers of particles. These will be distributed among the 9 particle size bins (some of which are more or less optically active), according to the hyperbolic approximation given by Equation (24), and represented by most of the mid-ocean data of Figure 3-3. The slope of the particle size distribution at the surface is shown in Figure 3-12 for the 1000 hours time step, and at one meter above the bottom in Figure 3-13. The gross features of these two plots represent the large scale influence of the river wash load, where size distribution is distinctly different from those of the shelf sediments. The size distribution slopes of the suspended shelf sediments shows distinct patches, which are due to null point effects acting on variations shown in the bottom composition map of Figure 3-4. The shelf

# TIME STEP ANIMATION EXAMPLE RIVER RUNOFF PLUMES FOR 23 JANUARY 1993

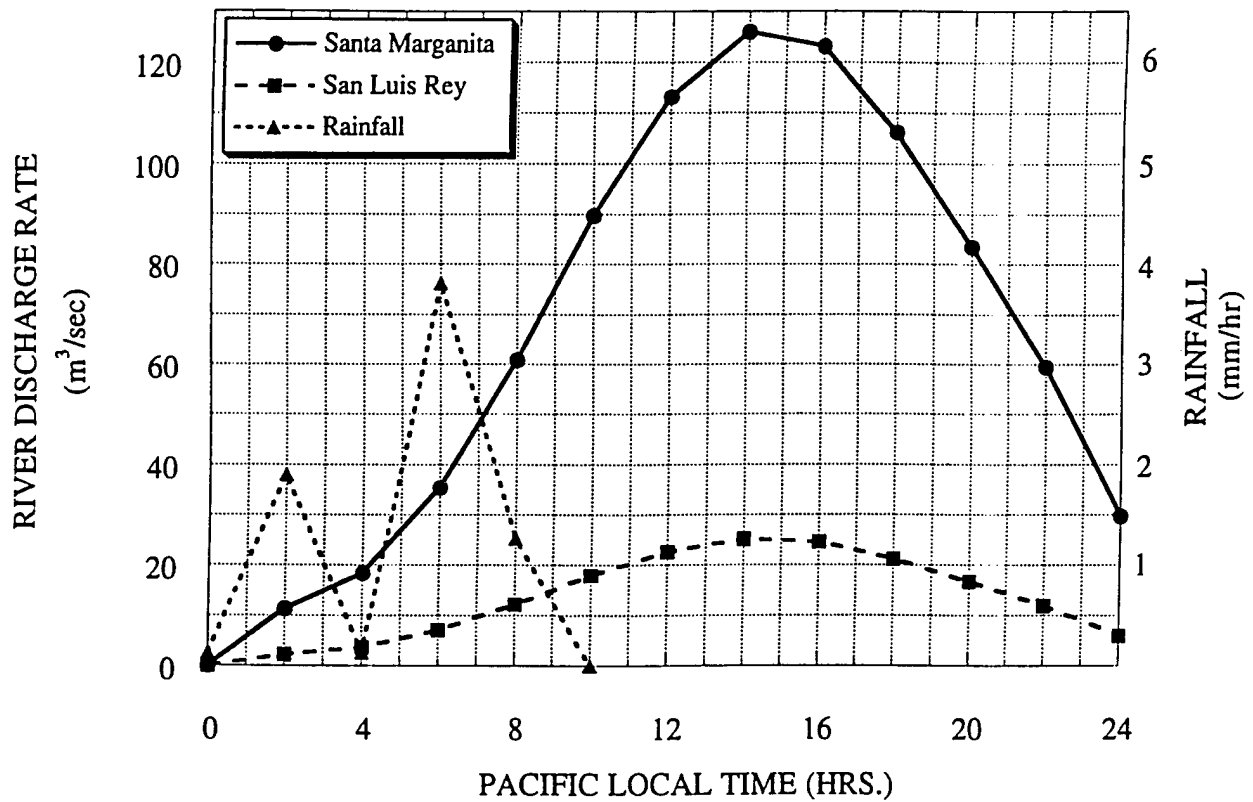


Figure 3-8. Rainfall and flood hydrographs for the  
24-hour time stepped simulation  
3-47

Progressive Vector Plot of Tidal Currents, 10:00 Jan 23, 1993

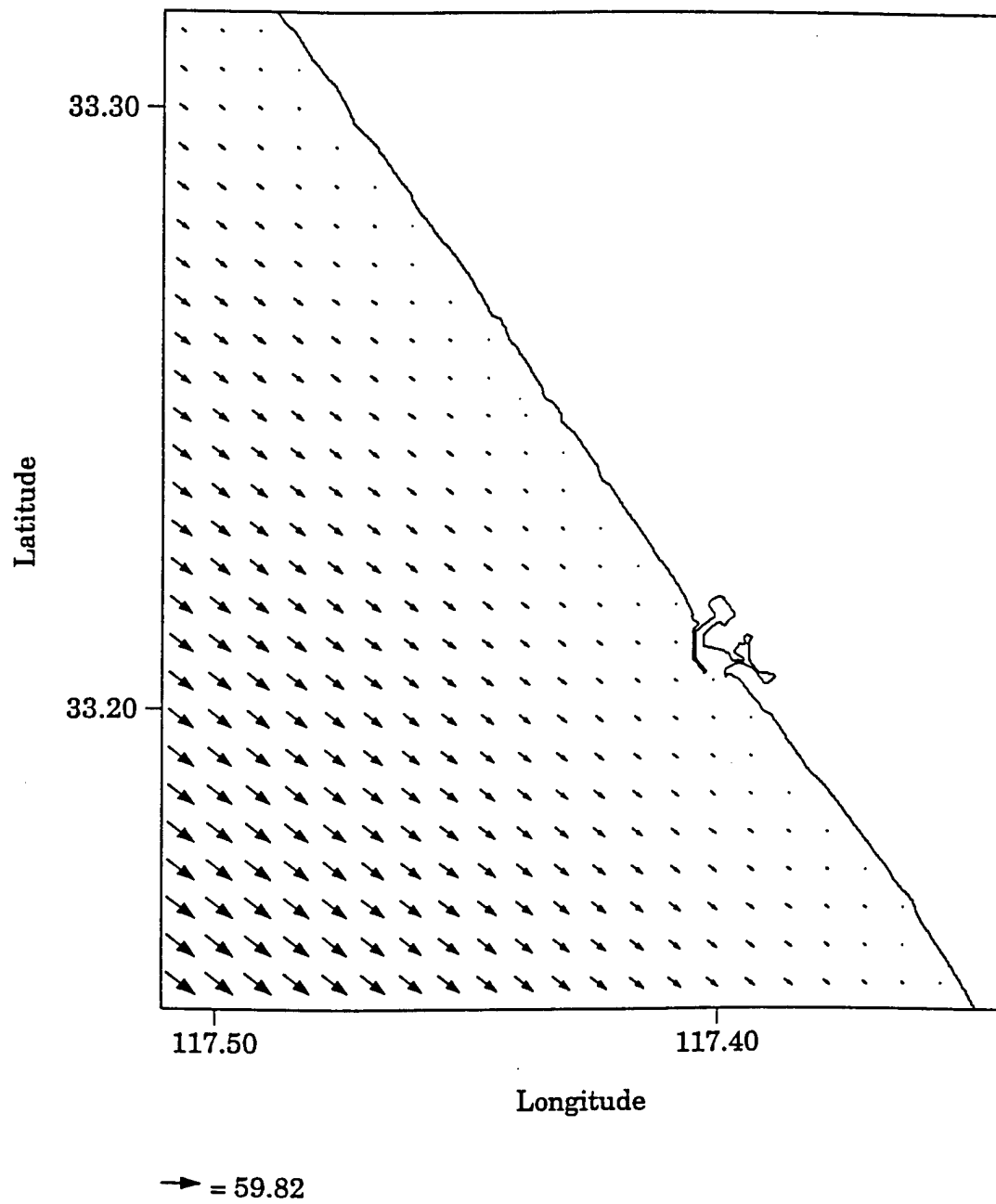


Figure 3-9. Nearshore current field for the Fifth Time Step  
3-48

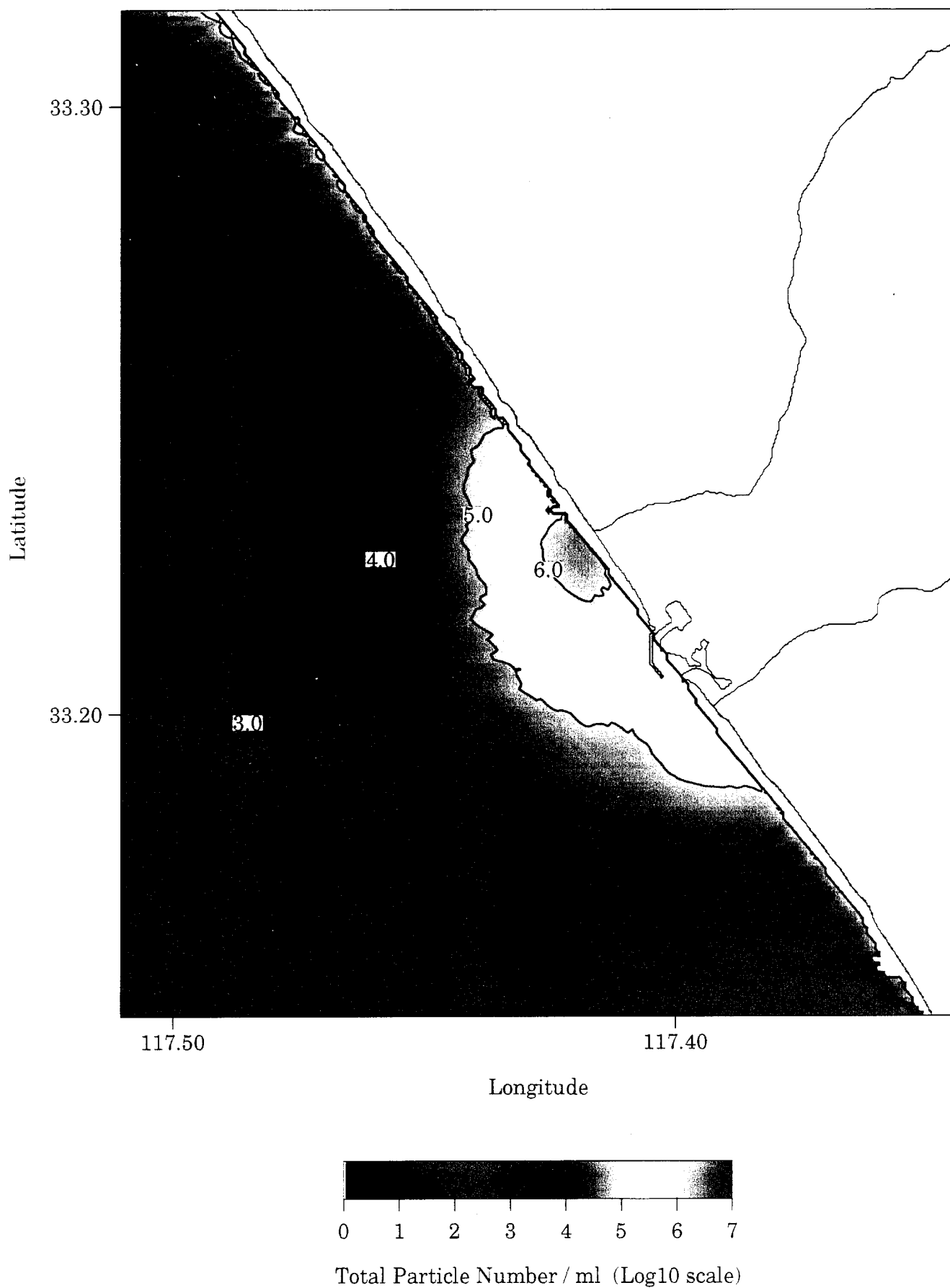


Figure 3-10. Suspended sediments at the surface for the Fifth Time Step  
3-49



Figure 3-11. LANDSAT image for the Fifth Time Step  
3-50



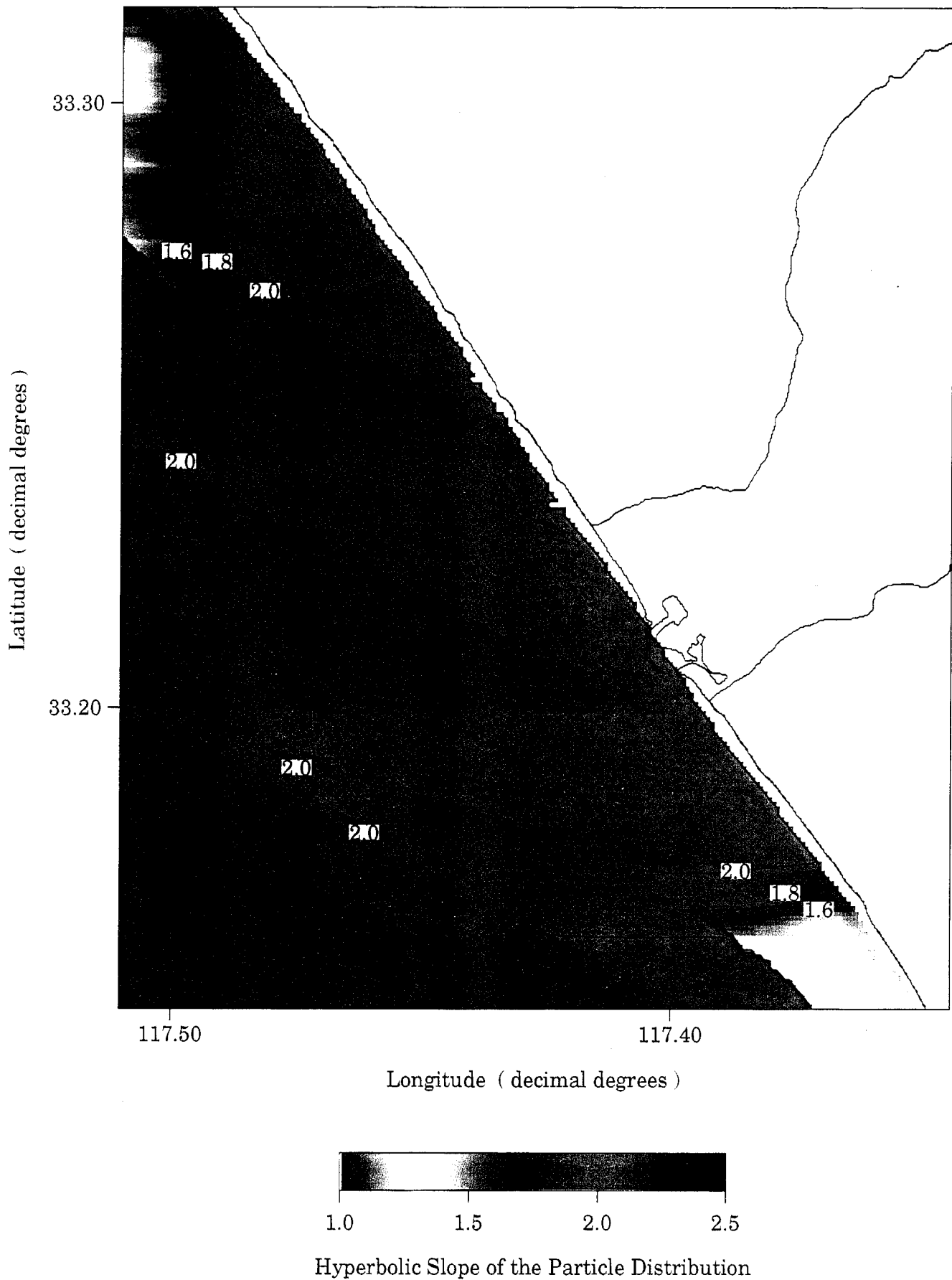


Figure 3-12. Hyperbolic particle size distribution slope map for the surface at the Fifth Time Step

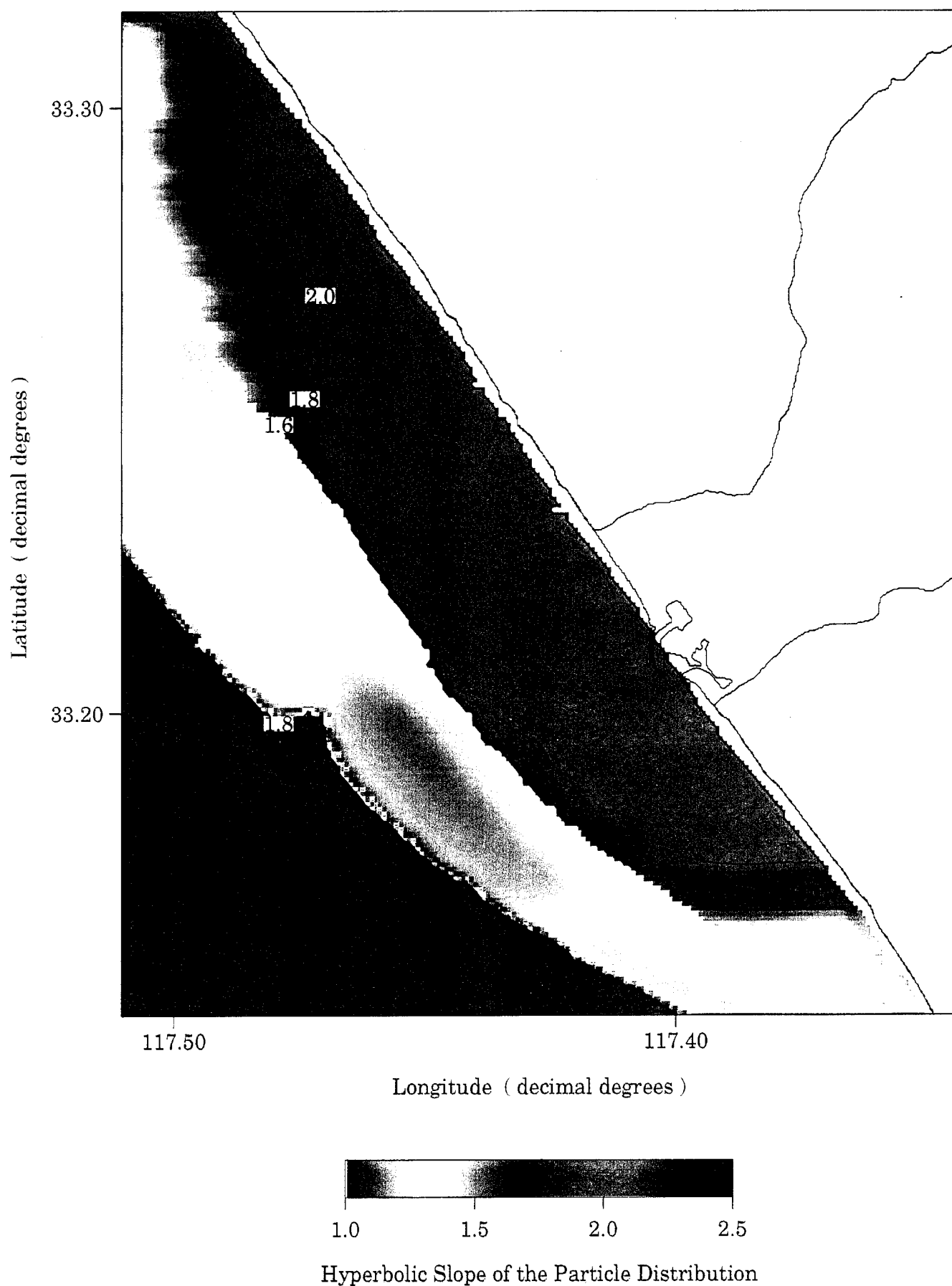


Figure 3-13. Hyperbolic particle size distribution slope map for suspended sediments 1 meter above the bottom at the Fifth Time Step

sediment size distribution slopes also show a sharp demarcation along the depth contour of incipient motion, seaward of which the slopes correspond to the ambient deep water particulates.

At the time the river discharges peaked at 1400 hours, the Santa Margarita was discharging at 126.01 cubic meters/sec and the San Luis Rey at 25.20 cubic meters/sec. The tidal currents were still in flood flow to the south, as seen in Figure 3-14. The resulting river plumes in Figure 3-15 have greatly enlarged and spread further south. The rapid attenuation of light in these river plumes prevents plankton growth, producing a plankton patch with a large hole that extends seaward well beyond the shelf break, as shown in Figure 3-16. The plankton is generally depleted on the shelf due to light limitations from shelf resuspension and enhanced mixing from the wave shoaling, which acts downward along the concentration gradient. Plankton depletion on the middle and inner shelf is consistent with the model results and observations of Gregg and Walsh (1992).

Later in the day, the tide currents reverse while the river discharge rates decline to 85.53 cubic meters/sec for the Santa Margarita and 16.7 cubic meters for the San Luis Rey. At 2000 hours, a weak-to-moderate ebb flow to the north is shown in Figure 3-17. The waves have diminished in height to 0.434 meters for the swells and 0.297 meters for the wind waves with a small directional shift producing the refraction/diffraction pattern shown in Figure 3-18. The reversal in tidal current direction has now spread the river plumes toward the north, as shown in Figure 3-19.

To demonstrate the vertical profiling capability of the model, a grid point in the middle shelf at  $x = 40$ ,  $y = 100$ , was chosen and evaluated for each time step in Figure 3-20. Wind anemometer records at the nearby Camp Pendleton Auxiliary airfield indicated two squalls with brief gusting to 20 knots near 0200 and 0600 hours on 23 Jan 93. Otherwise, the winds remained light and variable at approximately 10-12 knots throughout the 24-hour simulation period. This produced a mixed layer, which slowly grew in depth from 15 to 17 m over the duration of the simulation, as shown in Figure 3-21. The associated pycnocline at these depths caused a discontinuity in the suspended particle profiles shown in Figure 3-20. Above the pycnocline, at 15-17 m, the suspended particle profiles are dominated at later time steps by particles discharged from the rivers, which mix and settle downward until hindered settling impedes further downward

Progressive Vector Plot of Tidal Currents, 14:00 Jan 23, 1993

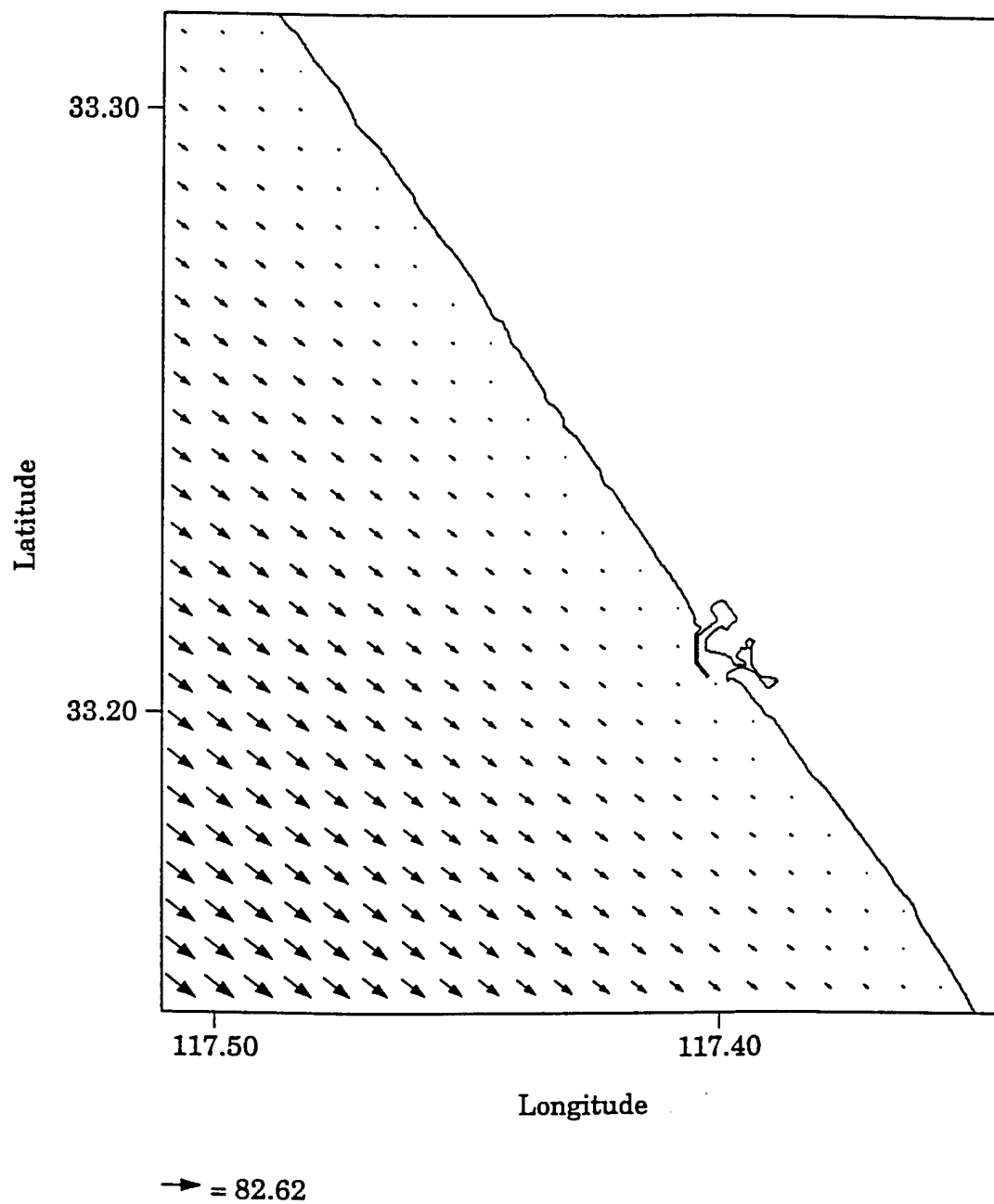


Figure 3-14. Nearshore current field for the Seventh Time Step  
3-54

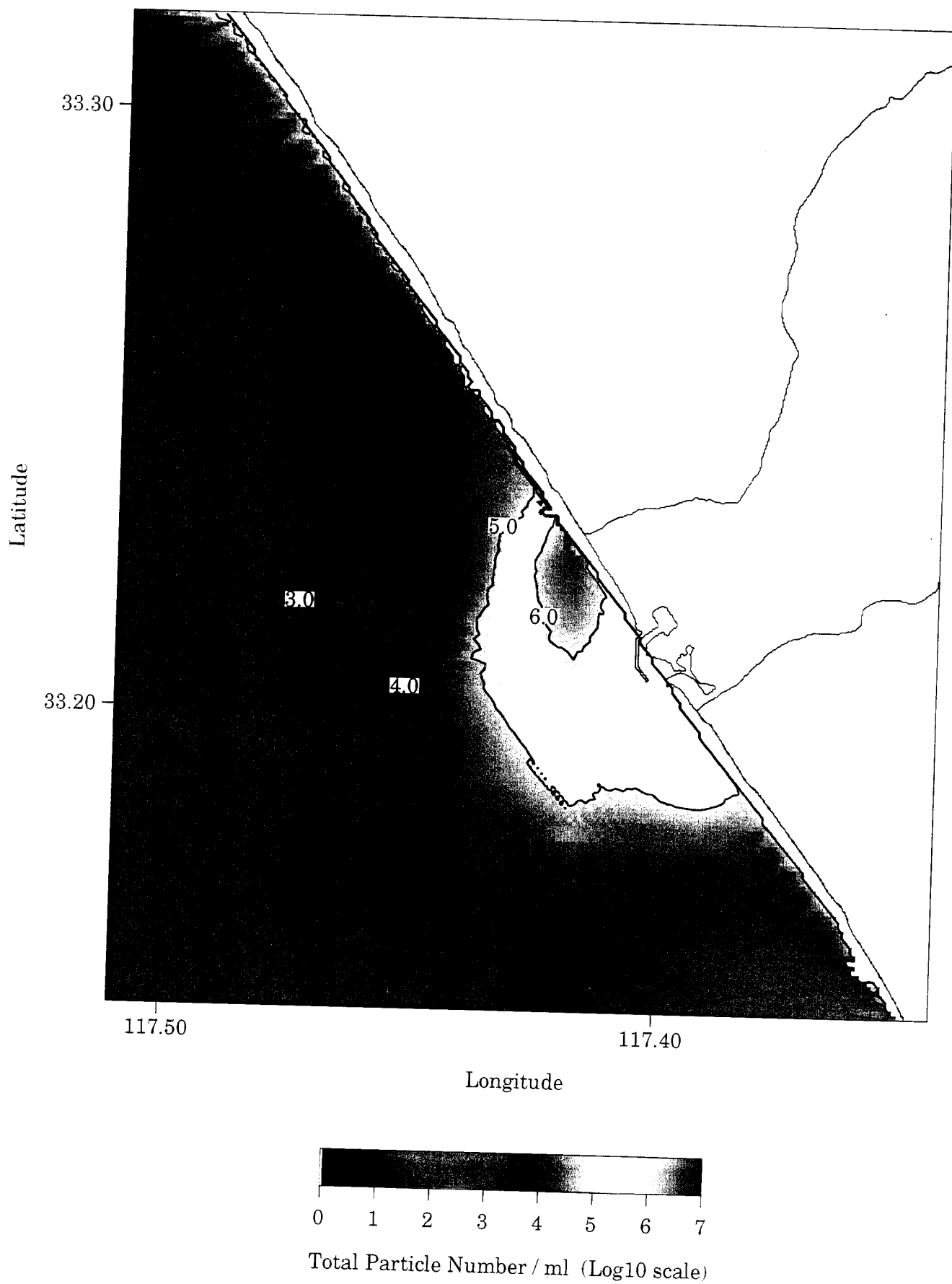


Figure 3-15. Suspended sediments at the surface for the Seventh Time Step  
3-55

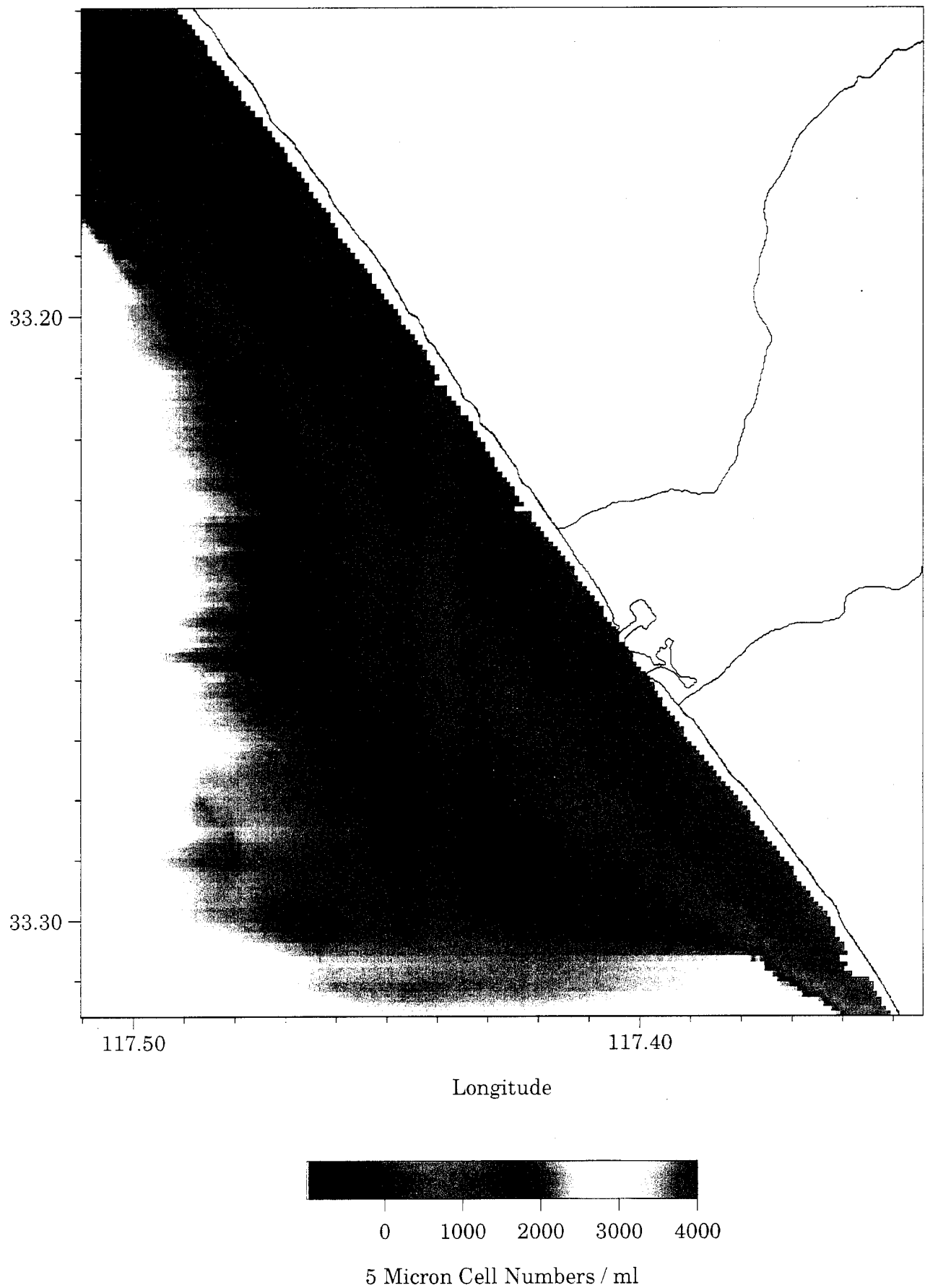


Figure 3-16. Nanoplankton at one meter below the surface  
for the Seventh Time Step  
3-56

Progressive Vector Plot of Tidal Currents, 20:00 Jan 23, 1993

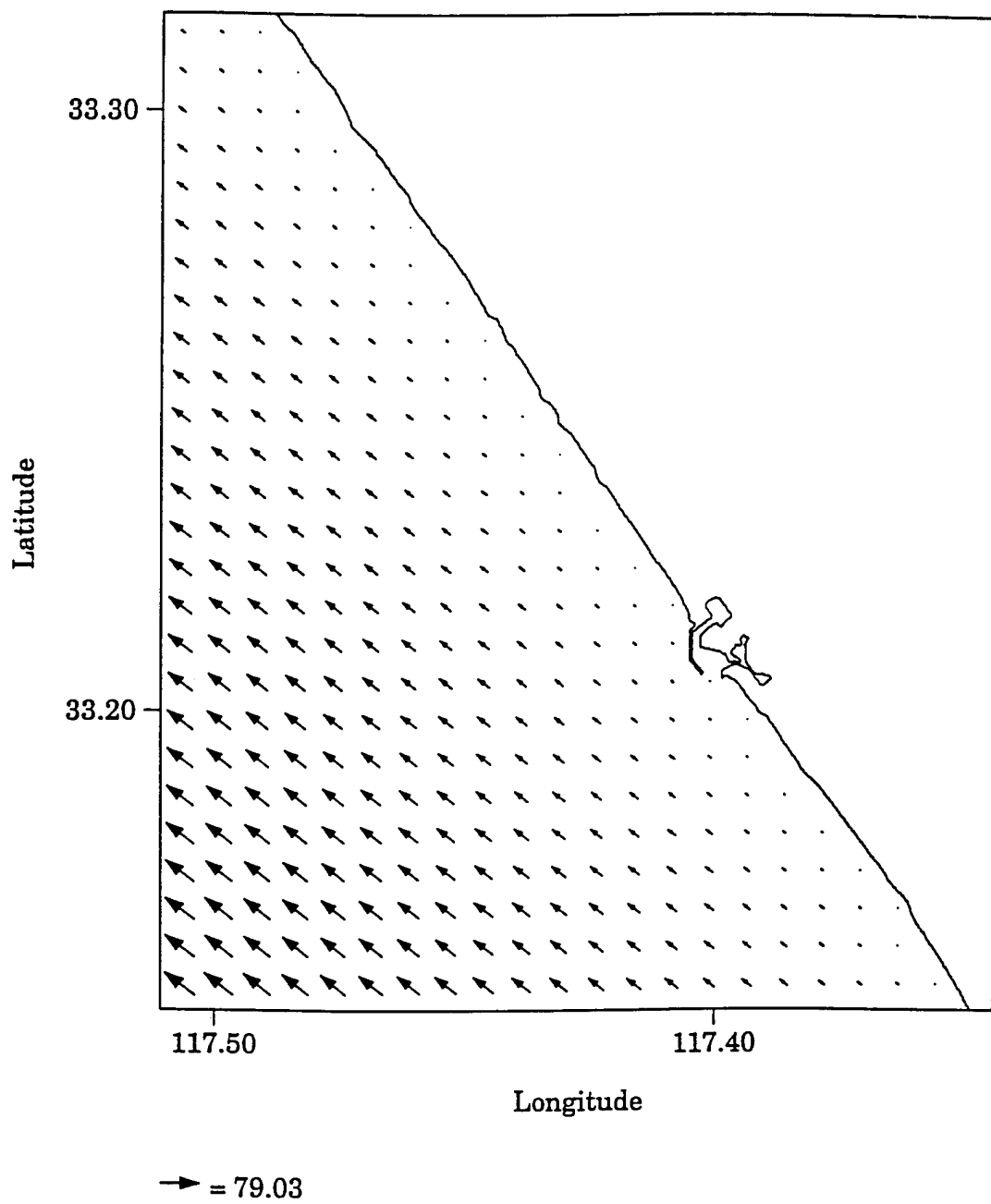
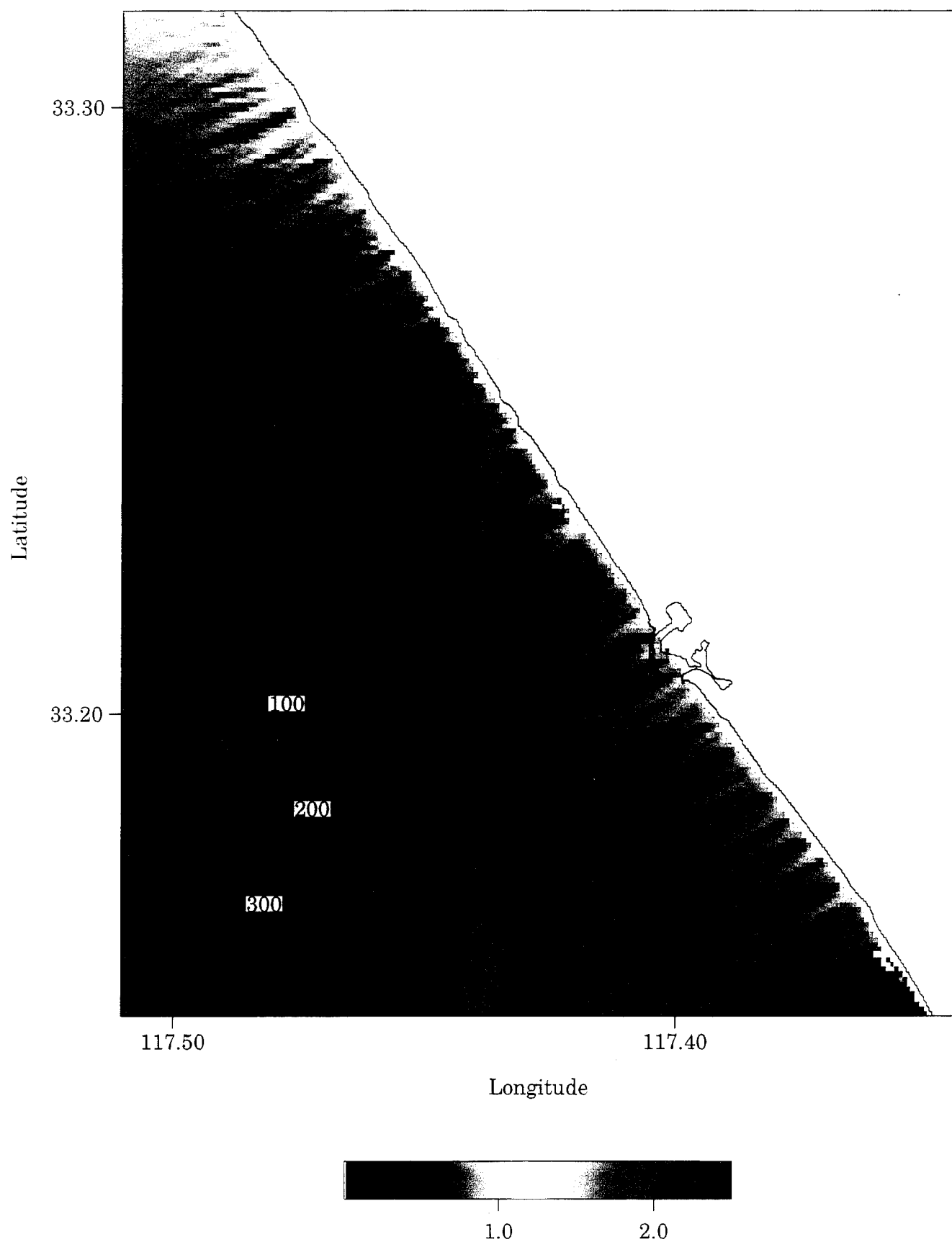


Figure 3-17. Nearshore current field for the Tenth Time Step  
3-57

Wave Height Distribution, 20:00 Jan 23, 1993



Wave Height (m): Swell - 12 sec, 237.33 deg; Windwave - 8 sec, 256.83 deg

Figure 3-18. Wave height distribution for the Tenth Time Step  
3-58



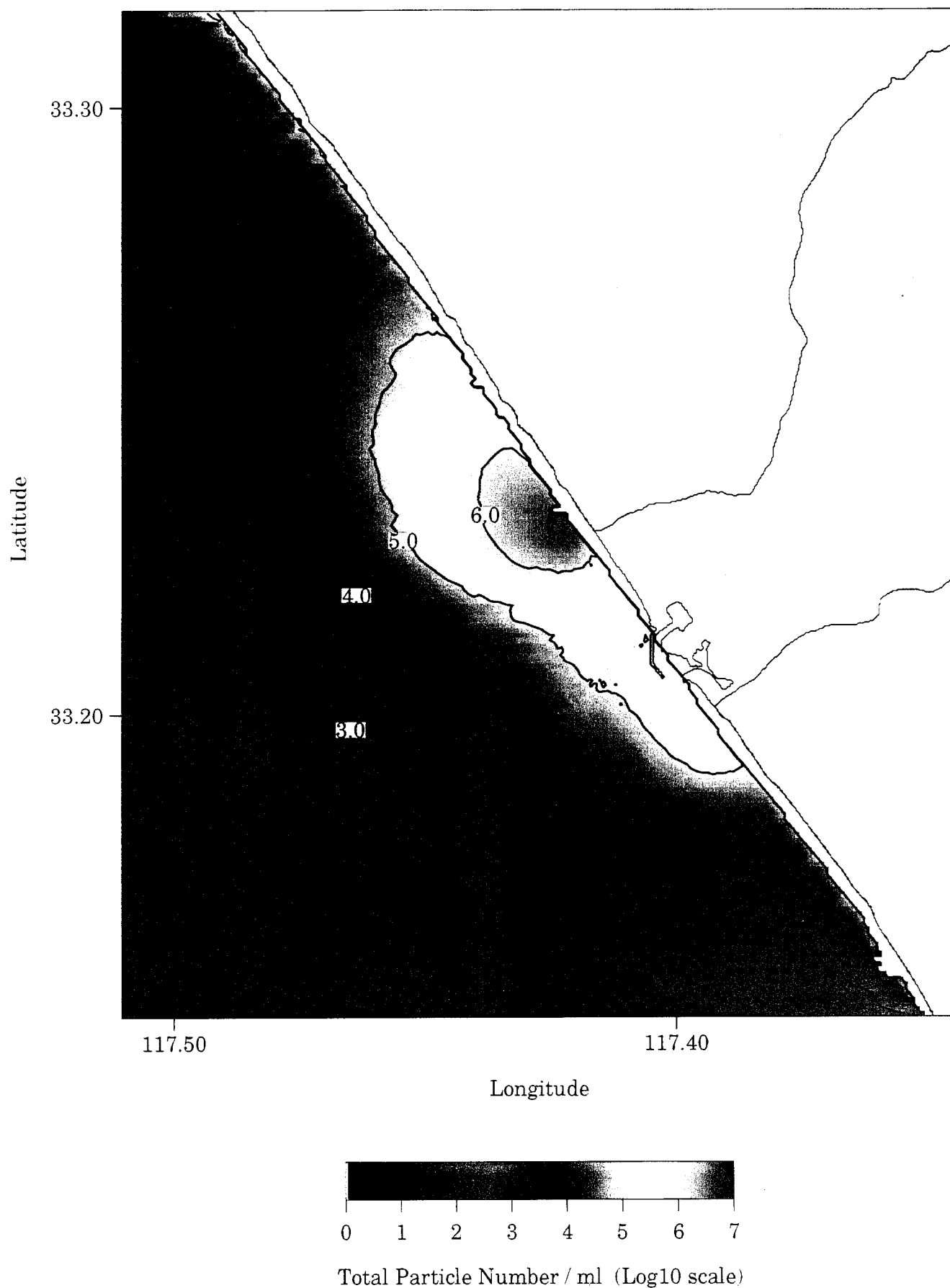


Figure 3-19. Suspended sediments at the surface for the Tenth Time Step  
3-59

**SEDIMENT CONCENTRATION PROFILES  
GRID CELL LOCATION: x=40, y=100  
JANUARY 23, 1993 OCEANSIDE, CA**

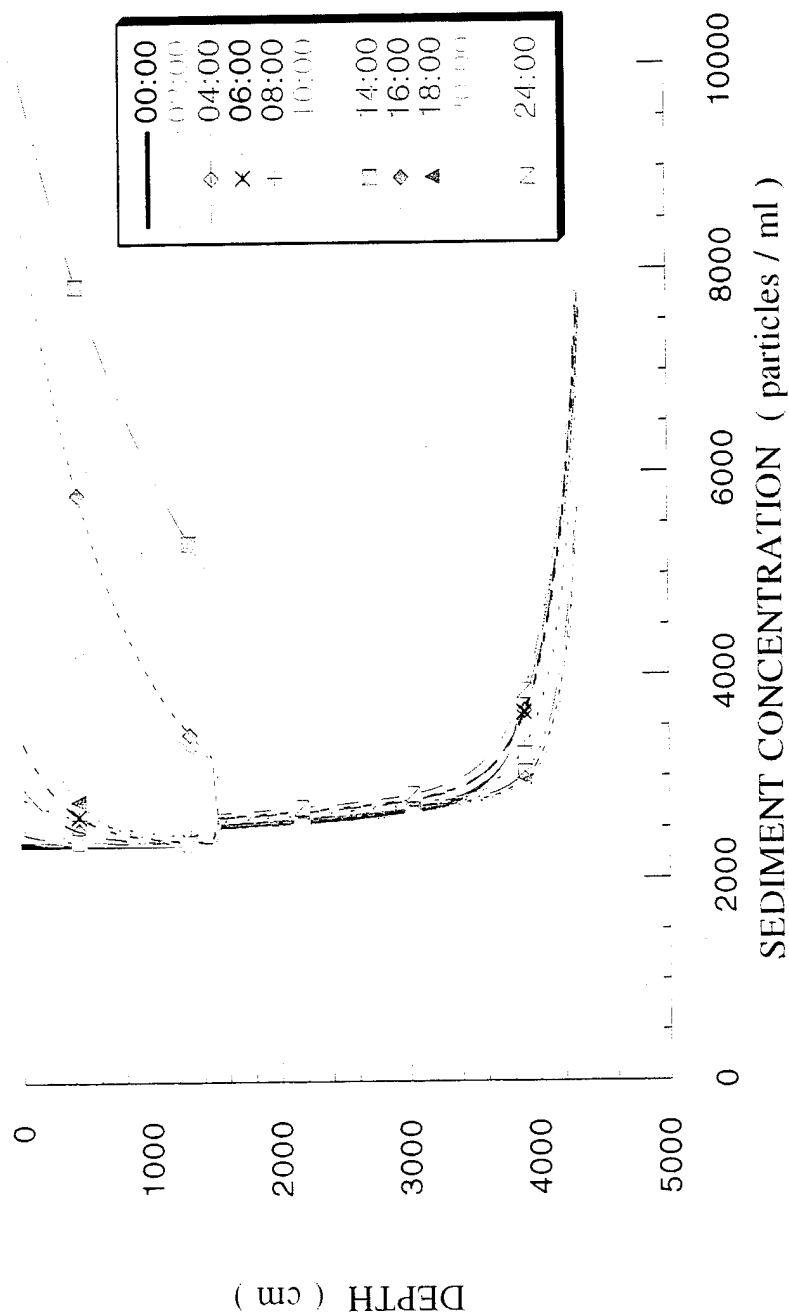


Figure 3-20. Suspended sediment concentration profiles at grid cell  $x = 40$ ,  $y = 100$ , for each time step of the 24-hour simulation

# MODELED MIXED LAYER DEPTH FOR CONSTANT WIND

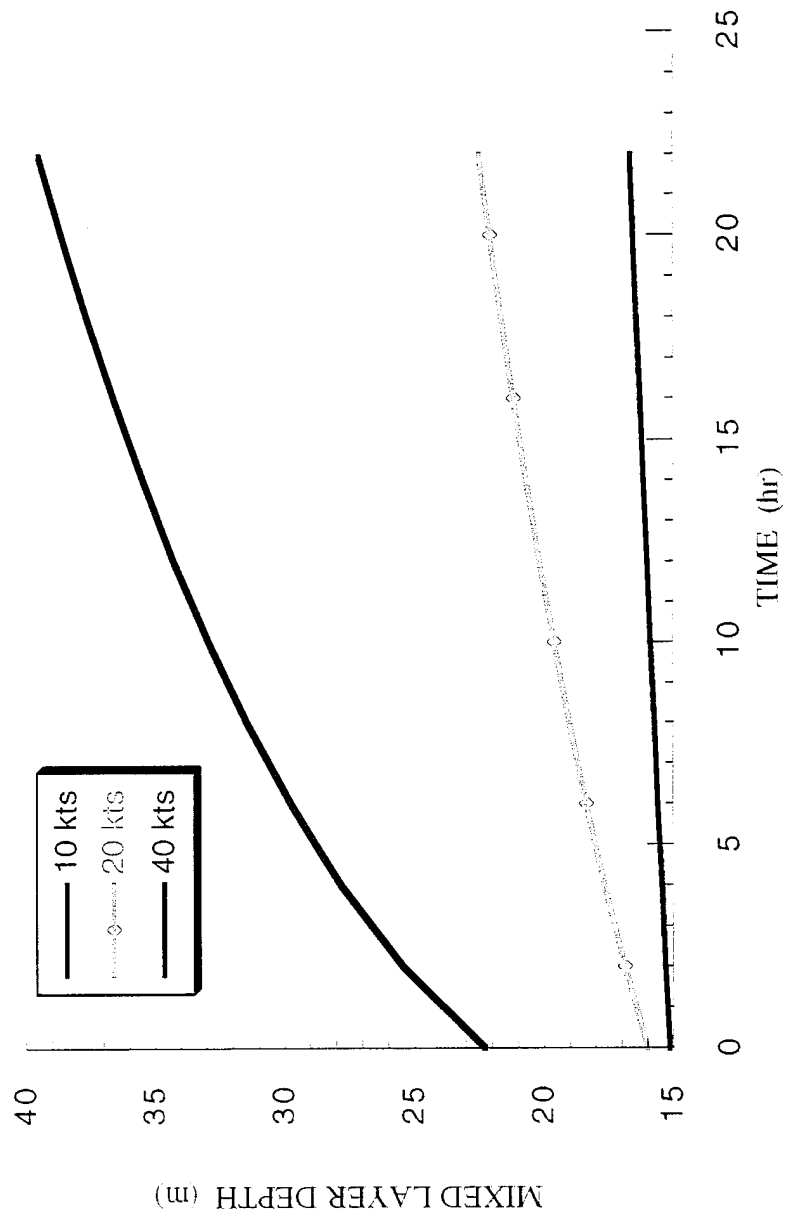


Figure 3-21. Growth of mixed layer depth for selected constant wind speeds over a 24-hour duration

fluxes across the pycnocline interface. Below the pycnocline, the suspended particle distribution is due to wave and current resuspension which mixes upward from the bottom boundary layer. In the early time steps, this upward mixing of bottom resuspension is clearly retarded in Figure 3-20 by the presence of the pycnocline interface. Particle numbers above the pycnocline peaked with the peak river discharge at 1400 hours, while particle numbers below the pycnocline peak with the maximum tidal currents over the middle shelf.

### 3.4 Sensitivity Analysis

Sensitivity analyses were conducted on both limiting factors of initial inputs and on variations in the strength of environmental forcing functions. Analysis of limiting inputs considered: 1) bathymetry resolution limitations, and 2) bottom composition deviations. Analysis of environmental forcing included 1) wind speed and duration variations, 2) wave height variations, and 3) river discharge variations.

#### A. Bathymetry Resolution Limitations

Two basic effects arise with respect to bathymetry resolution: 1) effects due to smoothness of the bathymetry, and 2) effects due to grid cell size. To examine the first, the incident deep water waves of the first time step, 0:00 hours, were run on three varying degrees of bathymetric smoothing. In Figure 3-22, a highly variable digital bathymetry from the NOS data sets was tested with the refraction/diffraction codes of "OCEANRDS.f" and "WINDWAVE.f." In Figure 3-23, a more smoothed version of this bathymetry taken from NOAA nautical charts was tested for the exact same incident wave conditions. Carrying the exercise to the extreme, a thoroughly smoothed plain parallel contoured bathymetry was tested in Figure 3-24, again for the same incident wave conditions as the first time step. Comparing Figure 3-22, 3-23, and 3-24 against Figure 3-6, we conclude that the fine scale structure of the refraction/diffraction pattern is a direct result of bottom irregularities for a given deep water wave condition. As the bottom becomes smoother, there is clearly less longshore variability in wave height, fewer shadows, and bright spots with less contrast, and ultimately less fabric in the suspended sediment distributions.

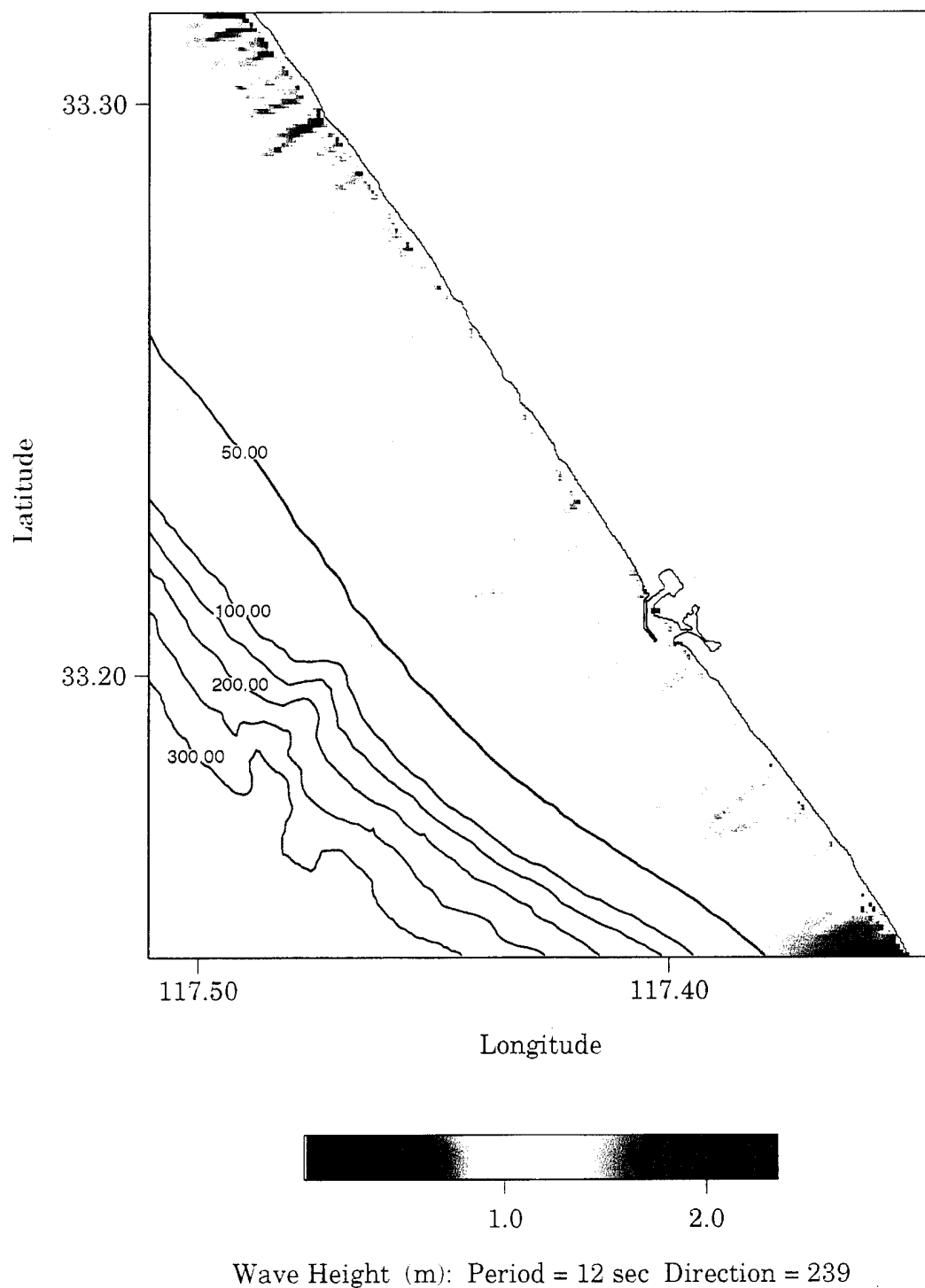


Figure 3-22. Wave height distribution using digital bathymetry  
3-63

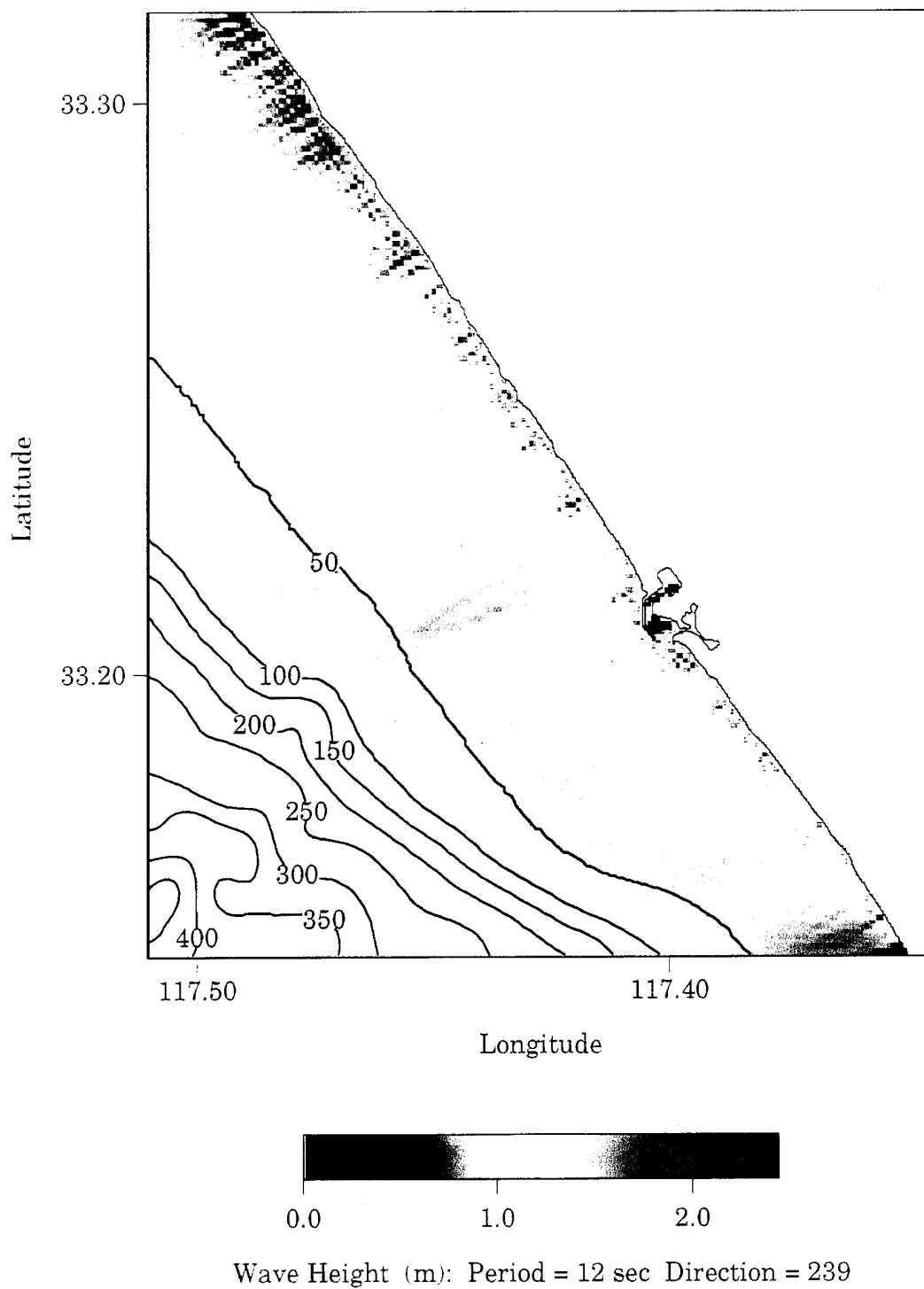
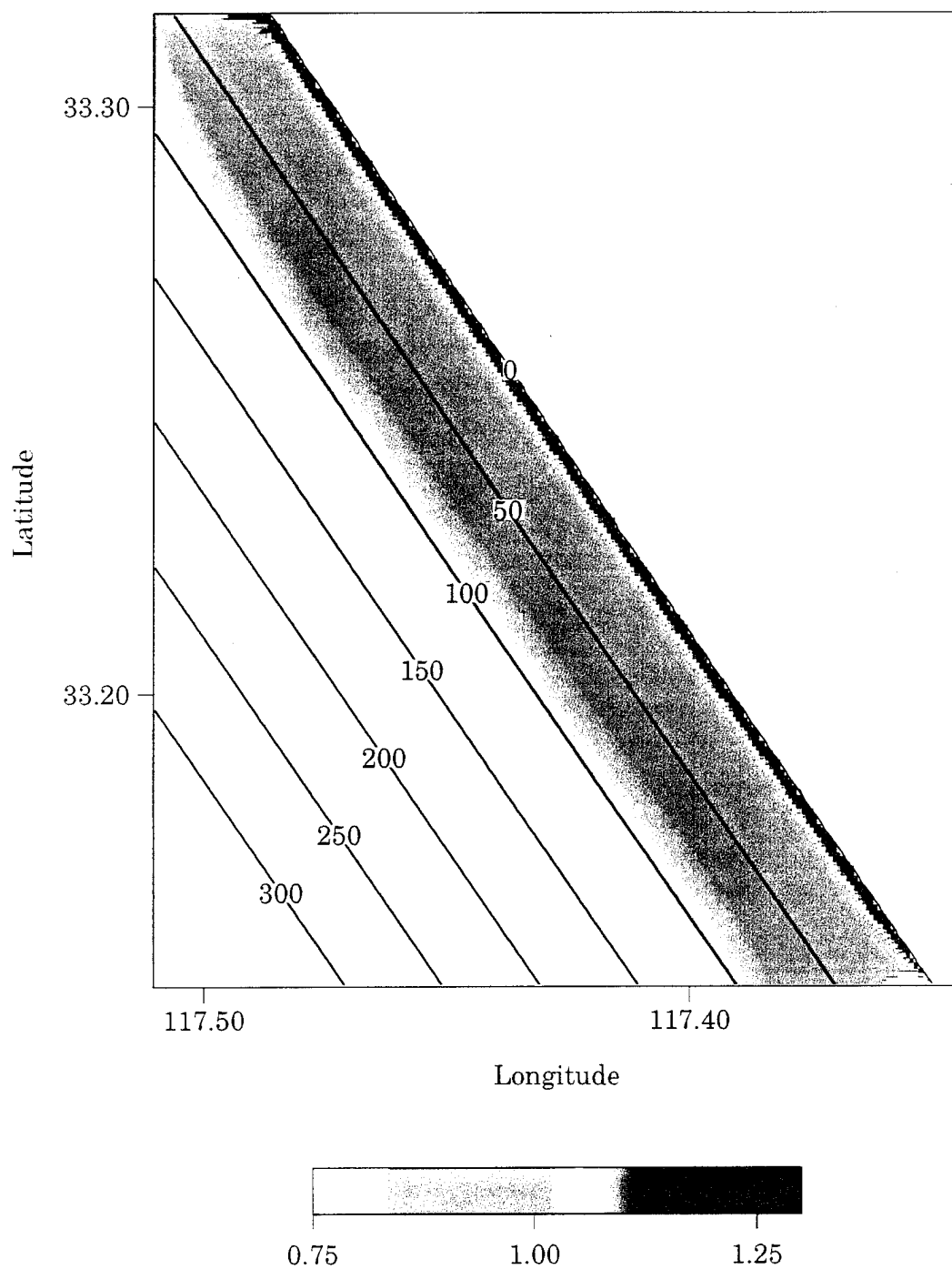


Figure 3-23. Wave height distribution using smoothed contour bathymetry  
3-64



Wave Height (m): Swell - 12 sec, 239 deg; Windwave - 8 sec, 255 deg

Figure 3-24. Wave height distribution for a plane sloping bottom  
3-65

Grid cell dimensions pose a Nyquist problem once grid cells are greater than or equal to half the wave length of the highest frequency wave. To observe these effects, deep water wave heights and directions were fixed while the period is varied in Figures 3-25 through 3-27. As the period becomes smaller, the shadows and bright spots in the refraction/diffraction pattern increase in numbers and contrast until finally at Nyquist, Figure 3-27, a shadow or bright spot appears at every other grid cell. For the 3 arc-second resolution bathymetry, Nyquist effects ensue for wave periods less than 8 seconds. To resolve waves shorter than 8 seconds, a nested gridding system must be introduced. For example, if we wish to resolve 6-second swells and 3-second windwaves, a shallow water nearfield grid must be employed with a cell dimension 0 (7 m). To account for the initial refraction/diffraction, the nearfield grid must be extended seaward to a depth comparable to 1/4 the deep water wavelength of the lowest frequency waves.

#### B. Bottom Composition

To examine how small changes in bottom composition effect suspended particle concentrations, the first time step was re-run in Figure 3-28 for a uniform mud/sand bottom composition, which has a larger proportion of fine grained sediments than the particle size distributions used to calculate Figure 3-7. Approximately 2% more fines by mass fraction are found to increase suspended particle concentrations in the nearshore by an order of magnitude or more. Furthermore, the onset of motion has been extended seaward to about the 65 meter depth contour and the fabric of the suspended sediment distributions has been smeared out by the slower settling velocities and larger eddy diffusivity associated with the finer-grained sediment (see Equation 12). Thus, relatively small errors in the mass fraction of the bottom composition data can lead to large errors in the suspended particle numbers.

#### C. Sensitivity to Wind

Figure 3-21 reveals how the mixed layer depth responds in the model to constant winds of various intensities blowing for a 22-hour duration. For light winds, 0 (10 knots), the mixed layer depth begins at 15 m and only increases slightly to 17 m after 22 hours. However, doubling the wind speed to 20 knots leads to more rapid growth in the mixed layer depth over 22 hours, even though the initial depth is only slightly more than for 10



Wave Height Distribution - Nyquist Test, Camp Pendleton, CA

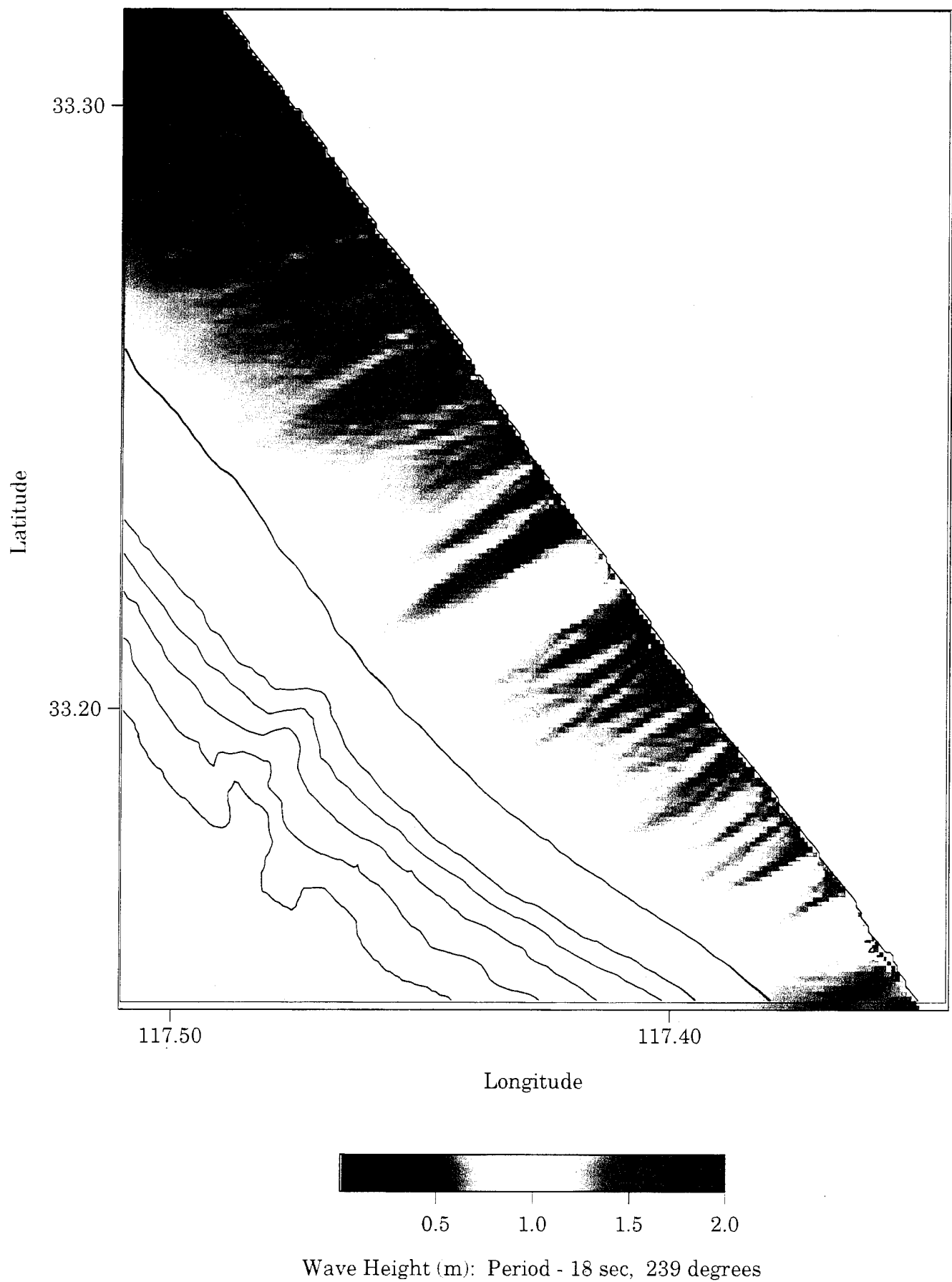


Figure 3-25. Nyquist test for 18-second deep water swells  
3-67

Wave Height Distribution - Nyquist Test, Camp Pendleton, CA

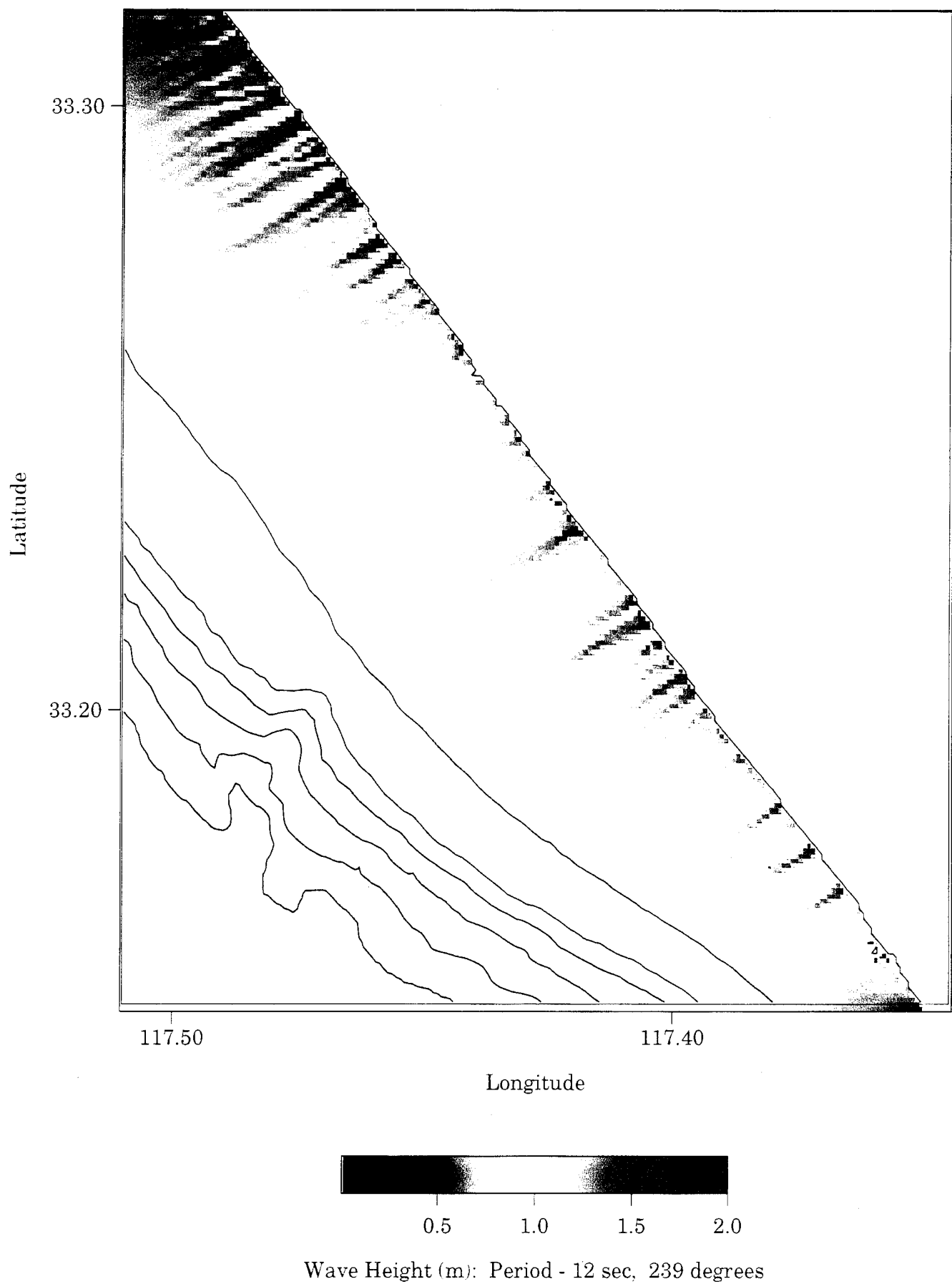


Figure 3-26. Nyquist test for 12-second deep water swells  
3-68

Wave Height Distribution - Nyquist Test, Camp Pendleton, CA

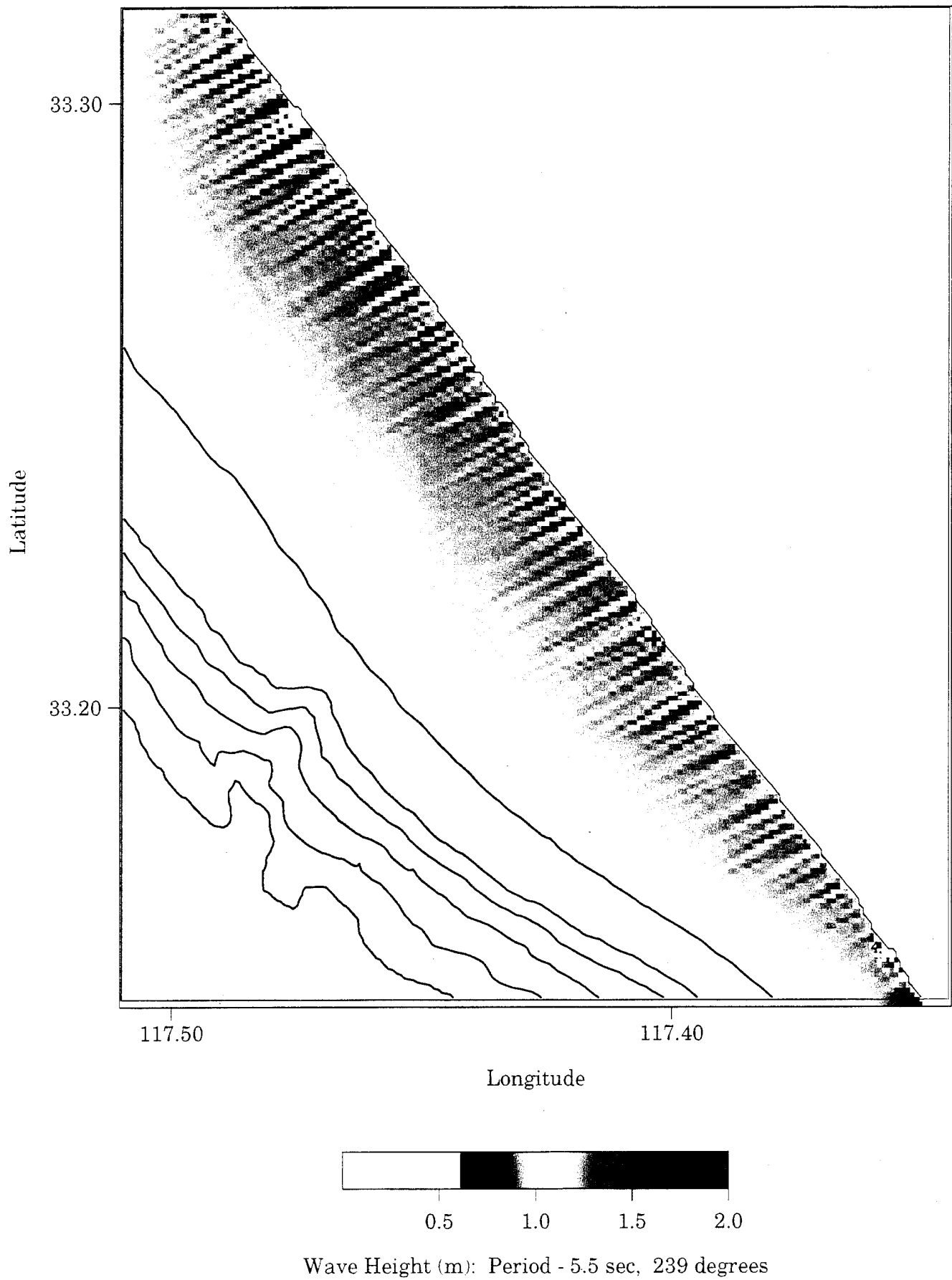


Figure 3-27. Nyquist test for 5.5-second deep water wind waves  
3-69

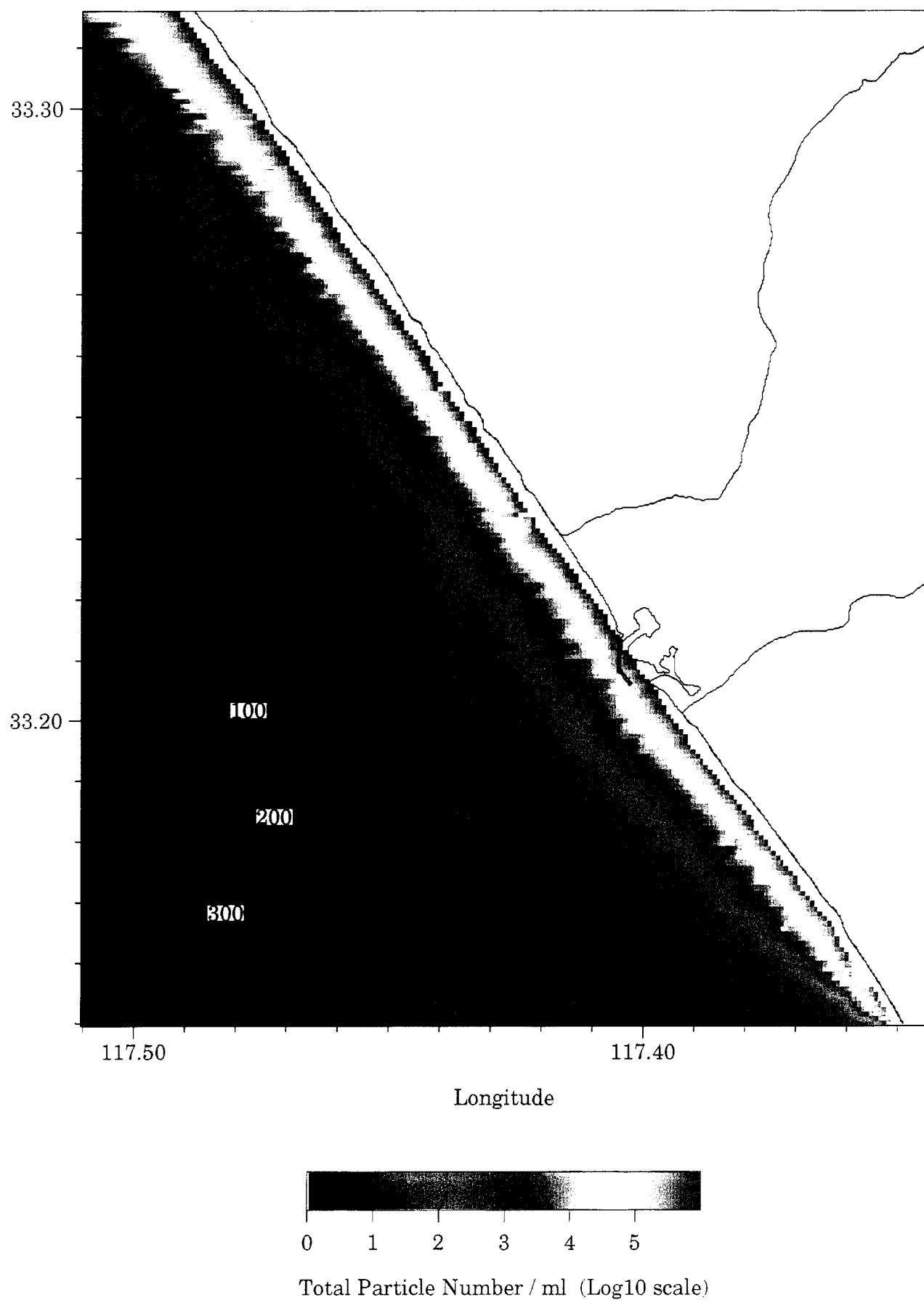


Figure 3-28. Suspended sediment at the surface for a  
uniform muddy/sand bottom  
3-70

knots. Doubling the wind again to 40 knots greatly accentuates these tendencies, deepening the initial value to 22 m, while reaching 40 m depth after 22 hours. The duration of the wind is obviously important in deepening the mixed layer at higher wind speeds. In Figure 3-29, the wind was monotonically increased to 40 knots and then relaxed over a 22-hour period. The mixed layer deepened to only 28 m and achieved that value 3 hours after reaching the maximum wind speed. The mixed layer depth relaxes very slowly with decreasing winds, 0 (days).

These variations in mixed layer depth, in response to wind speed and duration changes, exert a strong effect on the structure of the suspended sediment profile, as shown in Figure 3-30. River discharge and wave heights were held constant for all variations in wind speed. However, stronger winds were given more duration to reach maximum strength, as indicated by the times in Figure 3-30. The suspended sediment profiles bear qualitative similarity to those in Figure 3-20, with an upper portion controlled by the downward mixing of river wash load, and a lower portion, due to resuspension by waves and currents, mixing upward from the bottom boundary layer. A discontinuity at the pycnocline interface (bottom of mixed layer) separates the upper and lower portions of the profile. As the wind speed increases, the mixed layer deepens and the profile discontinuity moves lower into the water column. The enhanced mixing at higher wind speeds causes the surface concentrations to drop, while the suspended particle distribution across the mixed layer becomes more uniform. For the zero wind speed case, most of the particulates in the river wash load remain near the surface in the buoyant low salinity lens of the river plume.

Figure 3-30 shows that mixing due to strong winds ( $> 20$  knots) can deplete surface concentrations of suspended sediments by an order of magnitude. However, wind mixing appears to only dilute particle concentrations by deepening the mixed layer. Wind mixing effects do not appear to penetrate the pycnocline, and consequently, do not effect bottom resuspension when the bottom depth is below the pycnocline depth. This is not the case when the bottom depths are less than the pycnocline depths. Figures 31 and 32 give surface and bottom visibility depths averaged over all grid cells having depths less than 60 meters. Three separate mixed layer depths are indicated, 20 m, 40 m, and 80 m. The visibility distance in shallow water is found to decrease at both the surface and the bottom with increasing mixed layer depth. Thus, wind mixing does augment bottom

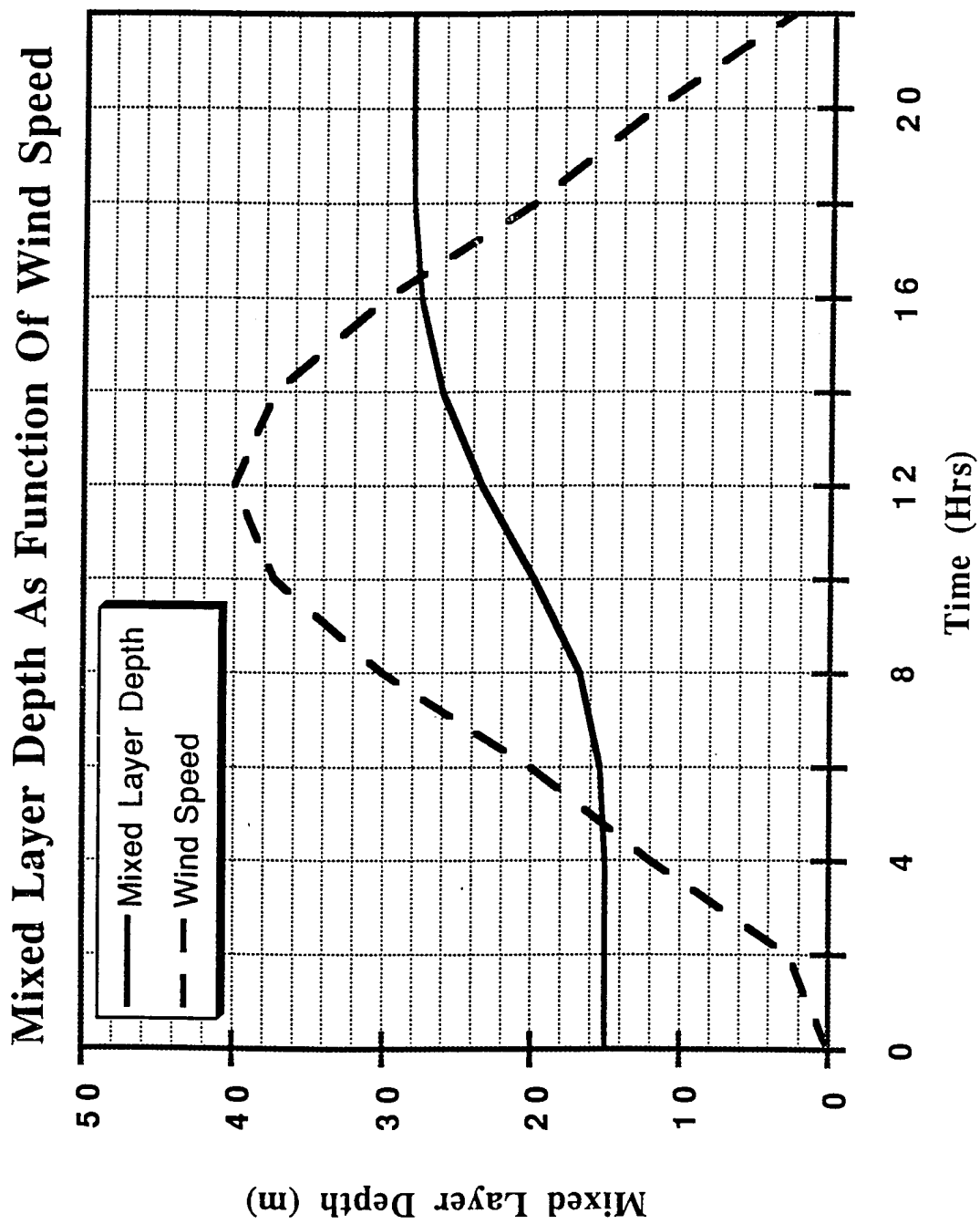


Figure 3-29. Mixed layer depth response to a diurnal 40-knot wind

SEDIMENT CONCENTRATION PROFILES AS A FUNCTION OF WIND SPEED  
 GRID CELL LOCATION: x=40, y=100  
 14:00 - 20:00 JANUARY 23, 1993 OCEANSIDE, CA

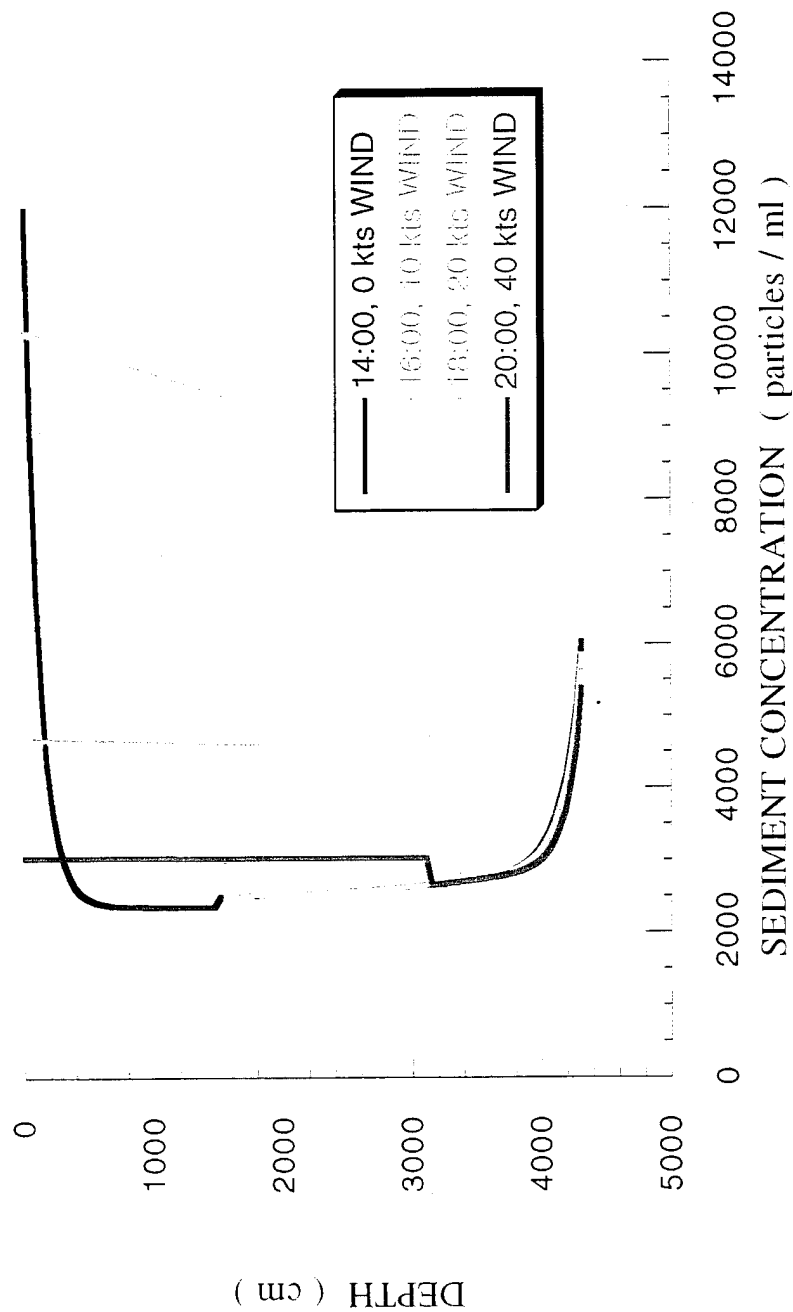


Figure 3-30. Sensitivity of suspended sediment profiles to variations in speed and duration of the wind.  
 River discharge = 80 cubic meters/sec., Wave height = 1 meter.

# **SURFACE VISIBILITY DISTANCE - MIXED LAYER DEPTH PARAMETER** **0-60 m DEPTH BAND: CAMP PENDELTON, CA**

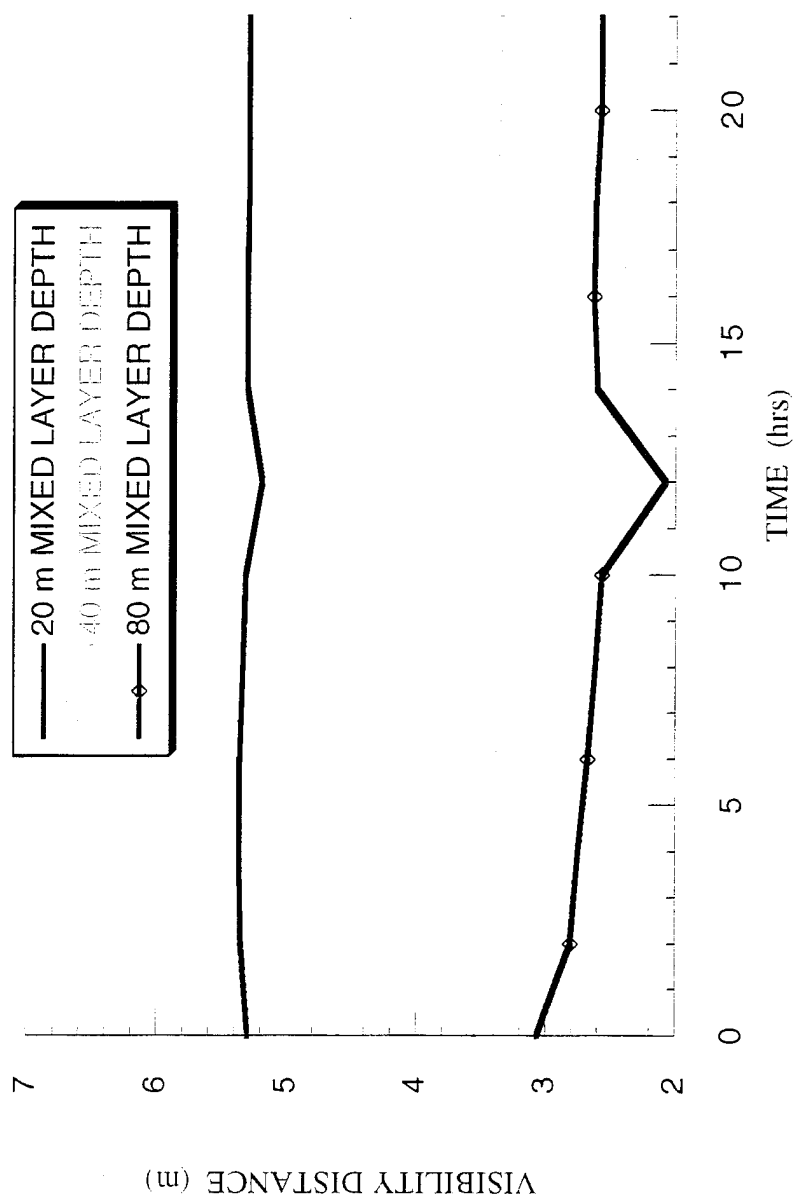


Figure 3-31. Surface visibility distance variations with mixed layer depth averaged over grid cells less than 60 m depth. Swells 3 feet at 12 seconds.



**BOTTOM VISIBILITY DISTANCE - MIXED LAYER DEPTH PARAMETER  
0-60 m DEPTH BAND: CAMP PENDELTON, CA**

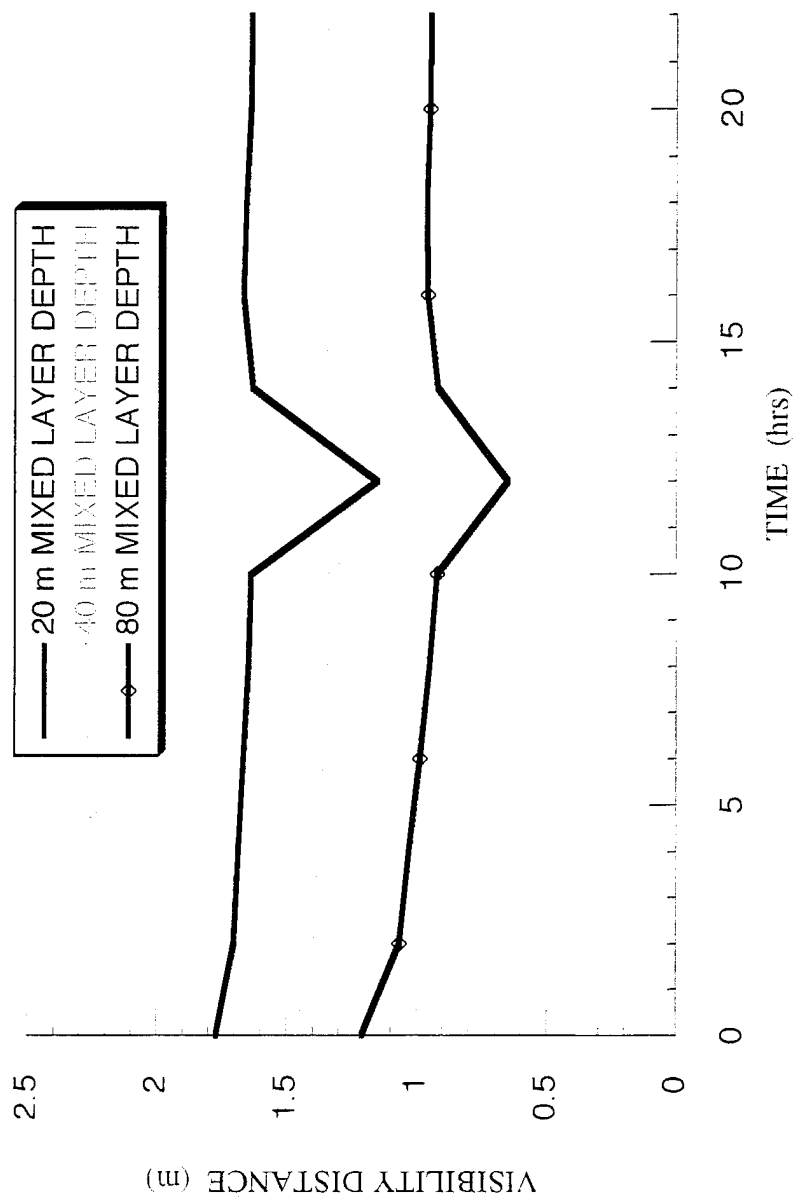


Figure 3-32. Bottom visibility distance variations with mixed layer depth averaged over grid cells less than 60 m depth. Swells 3 feet at 12 seconds.

resuspension when the bottom lies within the mixed layer. The diminished visibility distance occurring at 1200 hours corresponds with diurnal wind maximum, which increases bottom resuspension from wind stress mixing down to the bottom and thereby extending the threshold of motion depth to the 60 m depth contour. Similar findings in shallow water are shown in Figure 3-33, due to increasing wind stress in the absence of a pycnocline. The visibility distance at the surface has been averaged over all grid cells whose depth is less than 60 meters. Increased eddy diffusivity with increasing wind speed is found to increase the upward mixing of bottom resuspension when the pycnocline interface is not present, thereby diminishing surface visibility. The effect of the diurnal wind stress maximum at 1200 hours is also evident in diminished visibility according to Figure 3-33.

#### D. Sensitivity to Wave Height

Figure 3-34 shows the effect on suspended sediment profiles due to variations of wave height in shallow water whose depth is above the pycnocline. The river discharge was set to zero and the winds were run in a diurnal cycle with a 10 knot maximum occurring at 1200 hours. Accordingly, the pycnocline occurred at a depth of 15 m, whereas the local bottom depth in this figure was 10 m. In general, increasing wave height leads to increasing concentrations of suspended sediment at both the surface and the bottom, and at an incrementally increasing rate. In deeper water (Figure 3-35), where the bottom was at 43 m, the pycnocline was found to prevent suspended sediment from mixing upward to the surface. Consequently, increases in wave height led to only increases in suspended sediment below the pycnocline, while surface and mixed layer values remained unchanged.

The effects of wave height variations on shallow water visibility distance are shown in Figures 36 and 37. The visibility distance has been averaged over all grid cells where depth is less than 60 m. Consequently, the surface visibility changes only for those grid cells where depth is less than the pycnocline depth,  $z_m = 15\text{m}$ ; and the decreases in average surface visibility in Figure 3-36 is relatively small for increasing wave height. In contrast, the bottom visibility distance in Figure 3-37 shows significant decline with increasing wave height. In either instance, the abrupt decline in visibility distance at 1200 hours for the smaller waves was due to additional

**SURFACE VISIBILITY DISTANCE - WIND PARAMETER  
0-60 m DEPTH BAND: CAMP PENDELTON, CA**

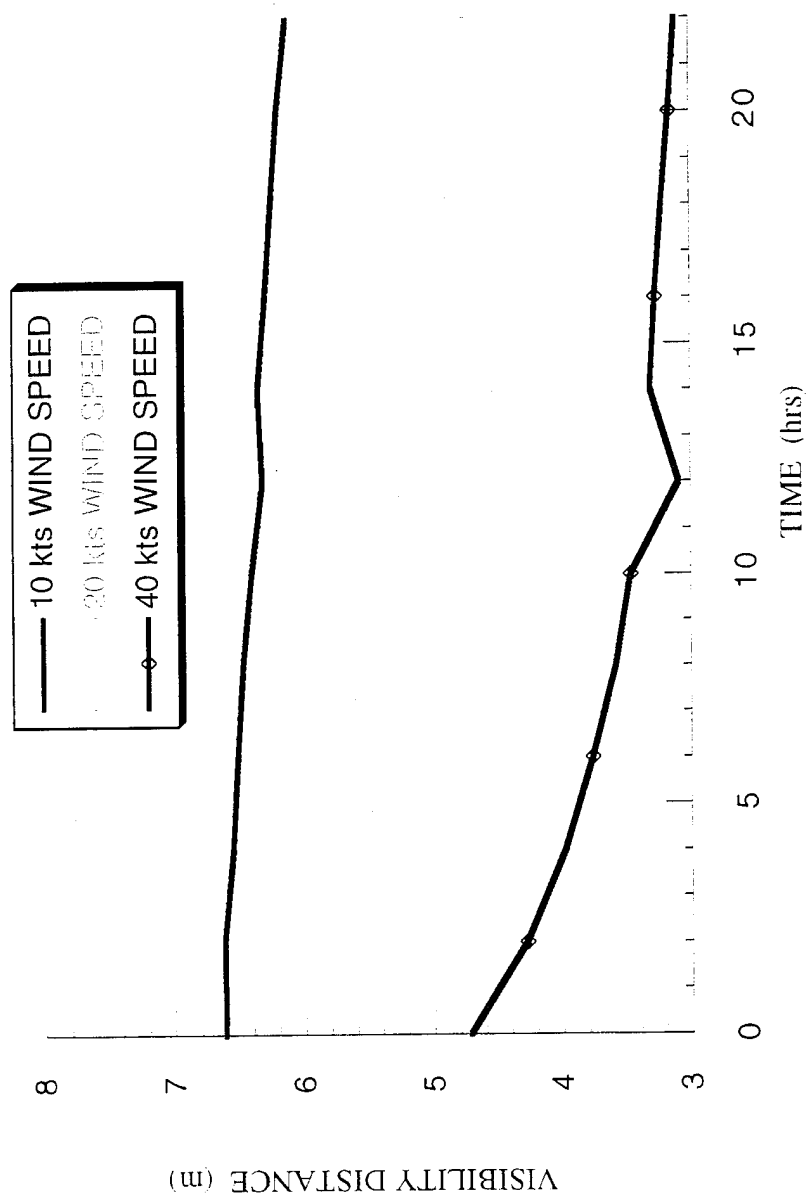


Figure 3-33. Surface visibility distance variations with wind speed and duration averaged over grid cells less than 60 m depth.  
No pycnocline. Waves 3 feet at 12 seconds.

**SEDIMENT CONCENTRATION PROFILES AS A FUNCTION OF WAVE HEIGHT**  
**GRID CELL LOCATION: x=100, y=100**  
**00:00 JANUARY 23, 1993 OCEANSIDE, CA**

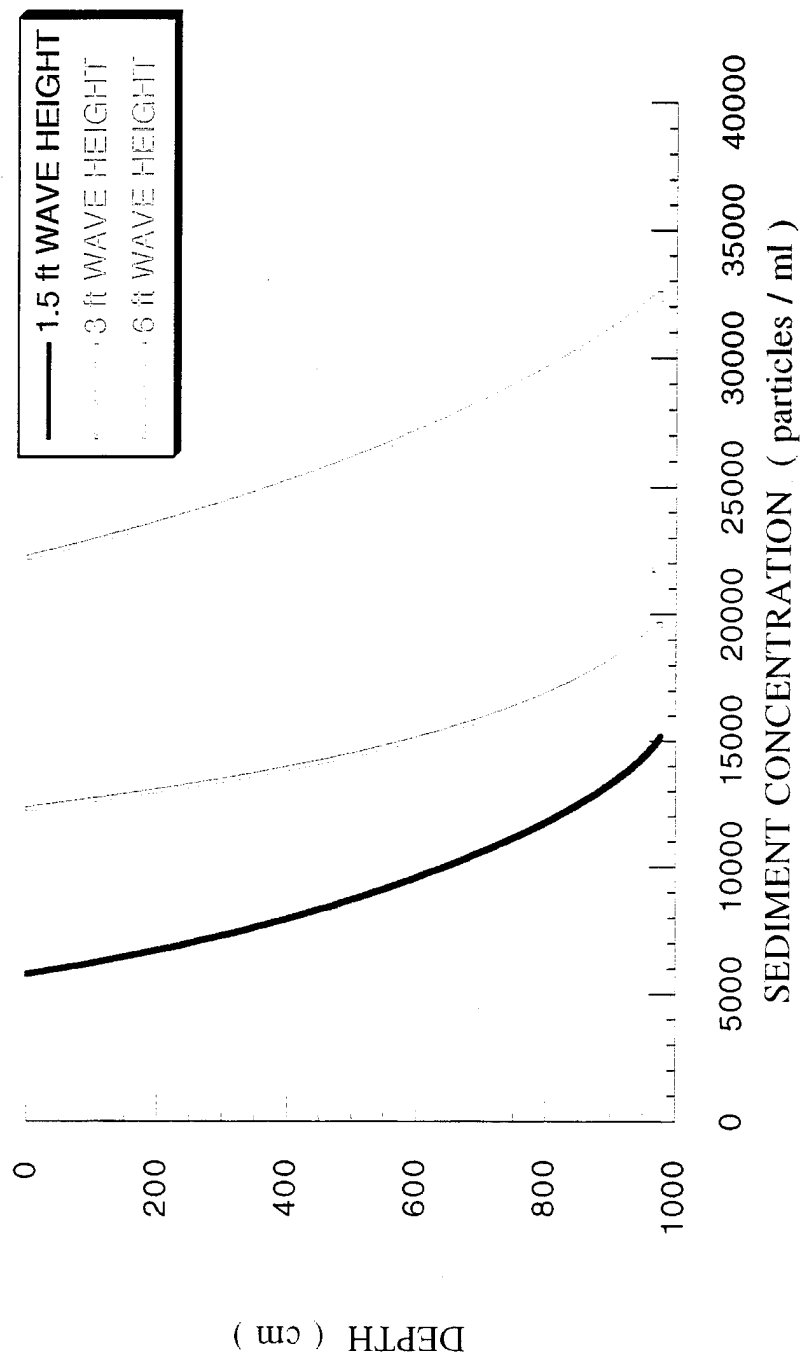


Figure 3-34. Suspended sediment profiles in 10 meters water depth (above the pycnocline) for wave height variations.  
 10-knot diurnal winds with no river discharge.

**SEDIMENT CONCENTRATION PROFILES AS A FUNCTION OF WAVE HEIGHT**  
**GRID CELL LOCATION: x=40, y=100; WIND SPEED = 10 kts**  
**00:00 JANUARY 23, 1993 OCEANSIDE, CA**

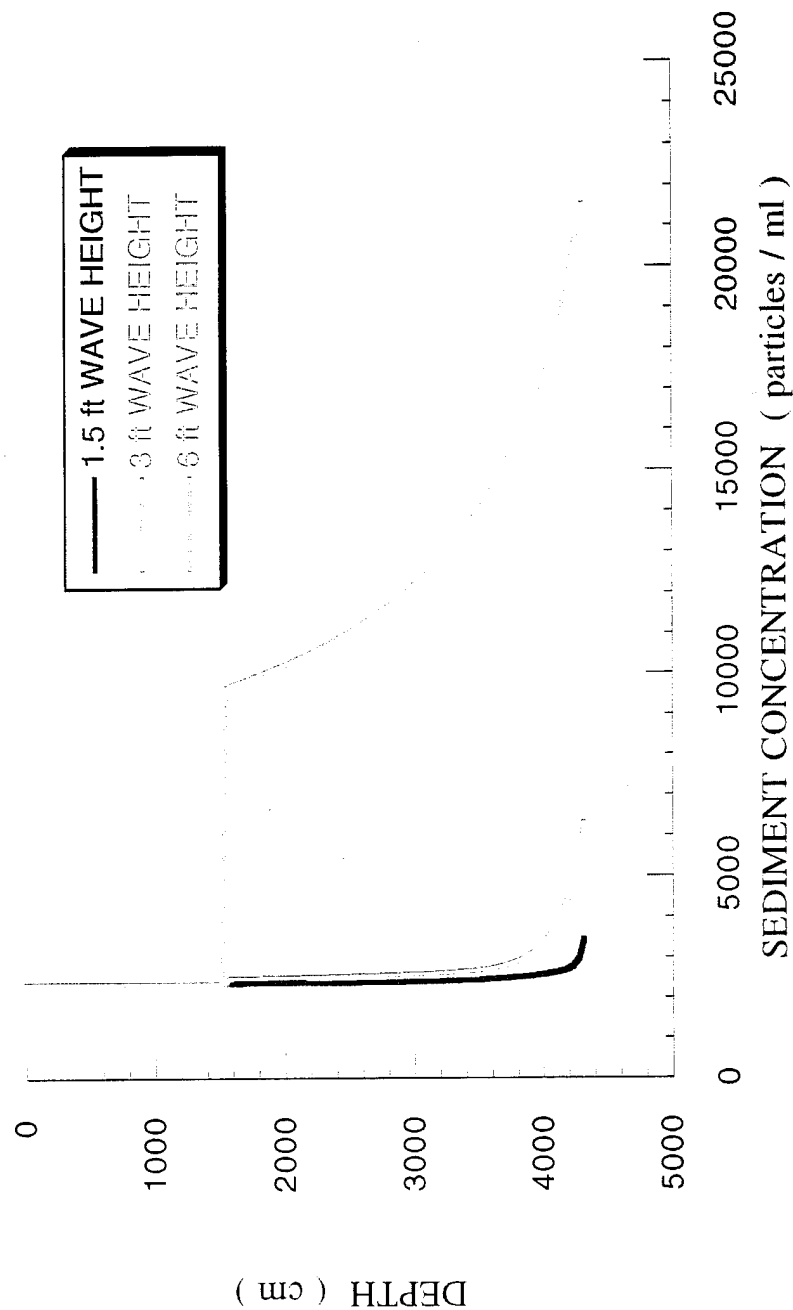


Figure 3-35. Suspended sediment profiles in 43 meters water depth (pycnocline depth at 15 meters) for wave height variations. 10-knot diurnal winds with no river discharge.

# MEAN SURFACE VISIBILITY DISTANCE AS A FUNCTION WAVE HEIGHT

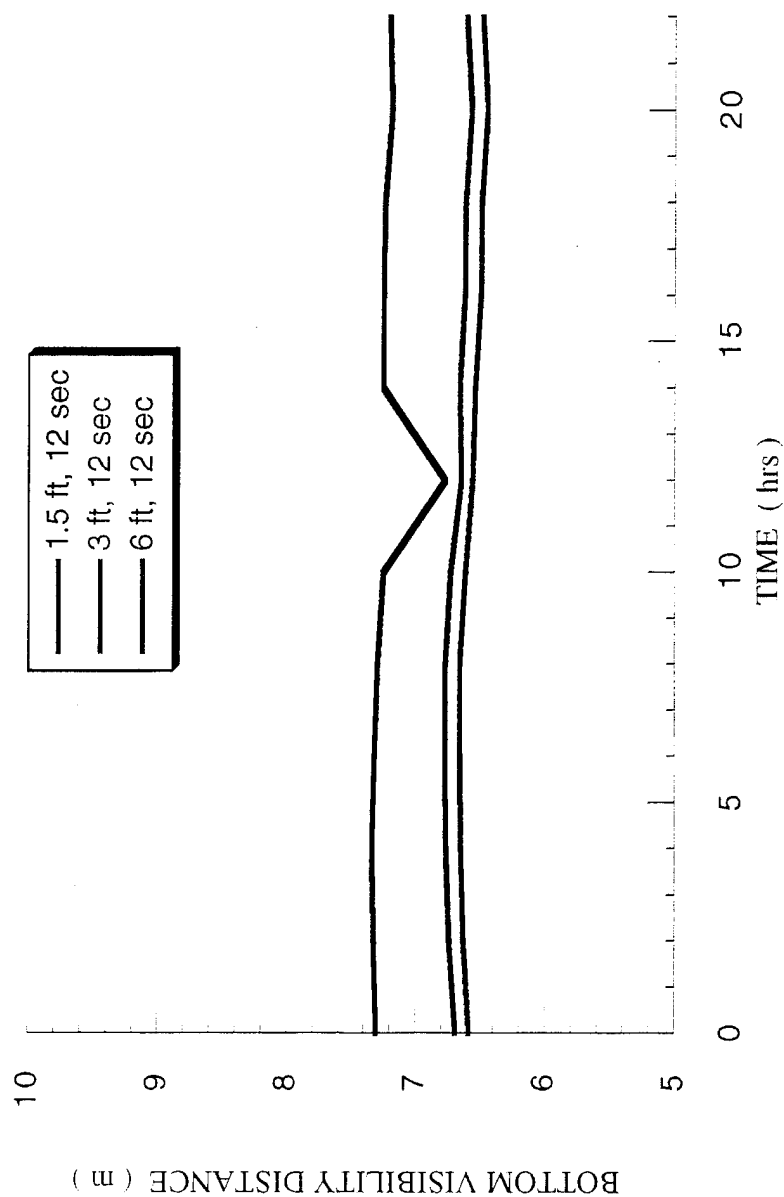


Figure 3-36. Shallow water surface visibility distance averaged over all grid cells less than 60 m depth for variable wave height and no river discharge.

# MEAN BOTTOM VISIBILITY DISTANCE AS A FUNCTION WAVE HEIGHT

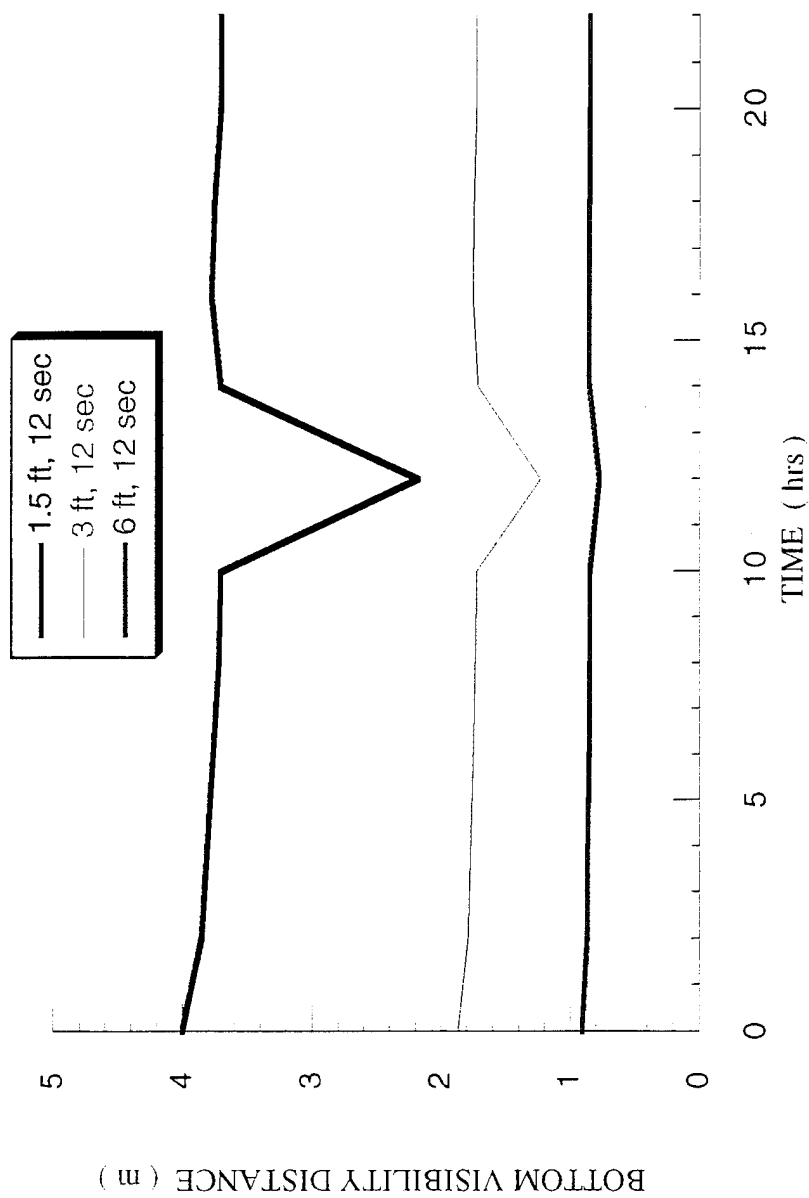


Figure 3-37. Shallow water bottom visibility distance averaged over all grid cells less than 60 m depth for variable wave height and no river discharge.

resuspension by the wind stress maximum, which caused significant reductions in visibility below the background level provided by wave action overwhelming amount of wave resuspension occurring under the largest waves. The duration of the waves was found to have not nearly the effect on visibility that the wind duration exerts, as in Figure 3-33. A slight decline in visibility is observed over the 22-hour simulation period, but this effect is primarily noticeable for the smaller waves.

#### E. Sensitivity to River Discharge

Figure 3-20 shows how the suspended sediment profiles at a grid cell seaward of the river mouth varied throughout the day of 23 Jan 93. During that period, the discharge of the Santa Margarita and San Luis Rey Rivers varied according to Figure 3-8, causing that wide variation in suspended sediment profiles above the pycnocline that are observed in Figure 3-20. Hindered settling at the pycnocline prevented little, if any, of this variability to mix down into the bottom resuspension layer.

Similar sensitivity to river discharge is shown in Figure 3-38, which is calculated for the same grid cell as Figure 3-20, but with a wider range of discharges for the Santa Margarita River and for the San Luis Rey River turned off. The profiles above the pycnocline reflect wind mixing from a constant 10-knot wind, rather than the variable winds used in the 24-hour simulation of Figure 3-20. Consequently, the mixed layer portion of the profile in Figure 3-38 appears more uniform. Nonetheless, both Figures 3-20 and 3-28 show that windmixing of river wash load sediments do not extend below the pycnocline, where the profiles in Figure 3-38 remain invariant for wave resuspension by the constant 3 foot, 12-second swells.

### 3.5 Discussion of Data Requirements

The clusters of modules which make up the suspended particle dispersion model are data intensive with respect to input files to drive the model, and require a number of internal calibration factors contained in the "super user." Only a few of these required input files are continuously "updated files" to provide the nowcast and forecast conditions to run the model in a predictive mode. The remaining are "inventory files" which can be compiled well in advance of any actual running of the model, and organized and dimensioned according to a coastal classification system.



**SEDIMENT CONCENTRATION PROFILES; VARIABLE RIVER FLOW RATE**  
**GRID CELL LOCATION: x=40, y=100; WIND SPEED = 5 kts**  
**00:00 JANUARY 23, 1993 OCEANSIDE, CA**

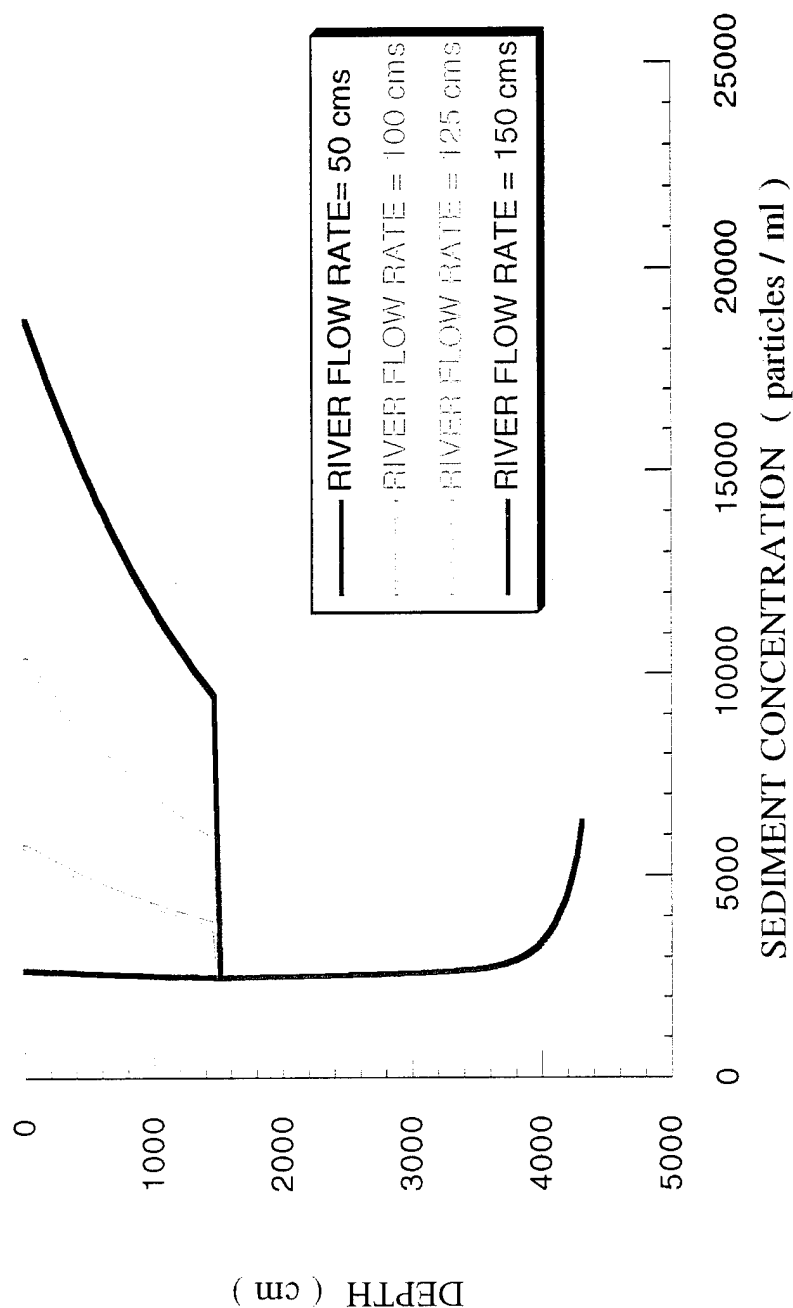


Figure 3-38. Suspended sediment profiles in 43 meters depth for variable river flow rates from the Santa Margarita River. Winds are constant at 10 knots. Swells are constant with 3-foot heights and 12-second periods.

#### A. Updated Files

These files contain nowcast and forecast conditions provided by Fleet Numerical Oceanographic Center (FNOC), or in some limited application, by the U.S. Army Hydrology Engineering Center (HEC). FNOC is relied upon primarily for site specific directional wave forecasts for swell and windwave components, ocean salinities, 24-hour precipitation forecasts, and pycnocline depths. The pycnocline forecasts are used as a diagnostic for assessing the suitability of the present mixed layer version of the particle dispersion model. Data from HEC is required only when multiple rain events precede the nowcast/forecast period and a residual hydrograph is needed to initialize the HEC-1 hydrology model.

#### B. Inventory Files

These files pertain to those input parameters which vary slowly or remain constant in time, and may, therefore, be compiled outside the nowcast/forecast time domain. It appears possible to organize these files into generic coastal classifications that are bracketed according to the properties outlined in Table 3-2. Worldwide, the coastal zone may be divided into five generic types, largely due to certain tectonic features. These are: 1) Collision coastlines with narrow shelves and steep coastal topography resulting from collisions between two or more continental and oceanic plates; 2) Trailing Edge coastlines with broad shelves and low relief coastal topography which rest in the interior of a continental plate; 3) Marginal sea coasts which are fetch limited by island arc systems resulting from tectonic hot spots; 4) Cryogenic coasts which are effected by ice processes; and 5) Biogenic coasts which are structured by fringing coral reef systems. The simulation in Section 3.3 is representative of a collision coastline. For a given coastal classification type, there exists a range of common sedimentary factors, hydrodynamic forcing, and transport factors (see Table 3-2), which may be exploited to develop a basket of data sets and calibration factors for use anywhere within that coastal type, if other more site specific data were not available.

Having an ensemble of input parameters according to a coastal classification system appears the only alternative for assigning calibration factors in the foreseeable future, since empirical data sets of sufficient detail to calibrate the model are rare. Among these calibration factors are: 1)

# PVM COASTAL CLASSIFICATION SYSTEM

Table 3-2. Coastal classification scheme for the structuring of inventory files, derived from the lecture notes of Douglas L. Inman.

SEDIMENTARY FACTORS				FORCING FACTORS		TRANSPORT FACTORS		
COASTAL TYPE	MORPHOLOGY	BEACH GRAIN SIZE	SHELF GRAIN SIZE	LATITUDE CLIMATE	FORCING	SOURCE	TRANSPORT PATH	SINK
A. COLLISION	NARROW SHELF MOUNTAINOUS	200 $\mu\text{m}$ to 300 $\mu\text{m}$	60 $\mu\text{m}$ to 100 $\mu\text{m}$	TEMPORAL/TROPICAL	WAVES 1-10 KW/M	RIVERS	LONGSHORE	CANYONS
B. TRAILING-EDGE	BROAD SHELF PLAINS	150 $\mu\text{m}$ to 200 $\mu\text{m}$	40 $\mu\text{m}$ to 80 $\mu\text{m}$	TEMPORAL TO TROPICAL	WAVES 1-2 KW/M	HEADLANDS AND SHELVES	LONGSHORE/ROLL OVER	BARRIER ISLANDS, SPITS, ROLL OVER SHOALS
C. MARGINAL SEAS (fetch limited)	1. NARROW-SHELF MTN	60 $\mu\text{m}$ to 150 $\mu\text{m}$	32 $\mu\text{m}$ to 60 $\mu\text{m}$	TEMPORAL TO TROPICAL TO ARCTIC	WAVES FETCH LIMITED	RIVERS	LONGSHORE	CANYONS
	2. WIDE-SHELF PLAINS	180 $\mu\text{m}$ to 210 $\mu\text{m}$	50 $\mu\text{m}$ to 90 $\mu\text{m}$		WAVES FETCH LIMITED		LONGSHORE	BEACHES & BARRIERS
	3. DELTAIC	40 $\mu\text{m}$ to 120 $\mu\text{m}$	1 $\mu\text{m}$ to 30 $\mu\text{m}$		TURBIDITY CURRENTS		ON/OFF SHORE	SHELF
D. CRYOGENIC	GLACIERS BERG ICE	100 $\mu\text{m}$ to 130 $\mu\text{m}$	1 $\mu\text{m}$ to 30 $\mu\text{m}$	ARCTIC	WAVES 0.1 KW/M & ICE PUSH	RIVERS & BERGE ICE PUSH	LONGSHORE SUMMER ONSHORE WINTER DUE TO ICE PUSH	SPIT EXTENSIONS & ICE RAFTING
E. BIOGENIC	CORAL REEF ISLAND OR SHOAL	250 $\mu\text{m}$ to 400 $\mu\text{m}$	80 $\mu\text{m}$ to 120 $\mu\text{m}$	TROPICS	WAVES 1-10 KW/M	REEF ORGANISMS	OVER THE REEF AND ALONG THE BEACH	POCKET BEACHES AND AWA CHANNEL

beach packing coefficients, akb; 2) surf zone suspended load efficiency factors, aks; and, 3) a variety of mixing length stretching factors, i.e., ak, ak2, ak3, ak3\_1, and ak4. These are contained in the super user files and can be selected as a group according to coastal type once calibration data sets from each coastal type are available to calibrate the model. The model is presently calibrated for the Collision Coastal Type, while data sets from SUPER DUCK experiments are anticipated for calibration of the Trailing Edge Coastal Type, and ongoing optical experiments in Florida, employed for calibrating the Marginal Sea Coastal Type.

Because of similarities in geomorphology within a coastal type, a great deal of sediment grain size and bottom composition input data may also be compiled and used on a default basis as representative input files if site specific data were not available. In particular, grain size distributions and bulk densities of the bottom sediments, and grain size distributions and bulk densities of river washload may be bracketed by this scheme, as suggested in Table 3-2. Because grain sizes and incident wave power have representative ranges for a given coastal class, beach slopes and bed forms could also be similarly categorized. Nearshore bathymetry is always site specific, but the similarities in wave power, shelf widths, and bed forms within a coastal class at least make it possible to categorize acceptable limits on bathymetry grid cell resolution.

The use of such baskets of input parameters according to coastal type must be carefully studied in subsequent sensitivity analysis to better understand potential errors associated with generic vs. site specific data. However, in many future applications, situations will undoubtedly arise when generic data is the only available kind, and the confidence limits on simulations resulting from such data must be well understood.

## 4.0 BIOLOGICAL COMPONENTS OF THE COASTAL WATER CLARITY MODELING FEASIBILITY STUDY

### INTRODUCTION

The Coastal Water Clarity (CWC) Model was conceived as a feasibility study to assess the adequacy of existing models for predicting optical properties in coastal waters. Concentrations of optically-important substances are predicted from the driving physical, chemical, and biological forcing functions. Optical properties are then predicted from these concentrations. Biological substances and processes with potential importance to coastal optical properties include phytoplankton, dissolved organic matter, zooplankton as grazers, or when swarming, particulate detritus, bacteria, and various activities by benthic organisms. Two questions must be considered before the modeling process is undertaken for any one of these substances: Does the biological component have a significant impact on optics? Do models exist for predicting both the concentration of the component and the optical properties of that component?

Phytoplankton biomass is the most thoroughly studied of these biological components. Models of various types exist: Empirical models relate phytoplankton biomass to some other measurable parameter. Ecosystem models describe factors controlling phytoplankton growth and loss rates, such as Kremer and Nixon's (1978) description of Narragansett Bay. A simplified ecosystem approach is used here, with phytoplankton biomass modeled as a function of irradiance, nitrate concentration, grazing, mortality, sinking, and mixing.

Previous studies of dissolved organic matter in the ocean have not attempted to create predictive models, but instead, examined spectral shapes of absorption (Carder *et al.*, 1989; Bricaud *et al.*, 1981), magnitude of absorption, or used absorption as a tracer of water mass dissolved material concentrations (Aminot *et al.*, 1990; Blough *et al.*, 1993). Since existing models for predicting dissolved organic matter are not available, a simple model is developed here. This model predicts absorption by colored dissolved organic matter (CDOM) produced by river, phytoplankton, and macrophyte sources, with loss to photodegradation.

Efforts to predict zooplankton concentrations and grazing processes lag those predicting phytoplankton concentrations. Existing models seem to require initialization with site- and season-specific zooplankton concentrations (*e.g.*, Marra and Ho, 1993; Franks *et al.*, 1986; Fasham *et al.*, 1990; Moloney and Field, 1991; and Hofmann and Ambler, 1988), which are not widely available for initialization of a generic coastal model. Zooplankton numbers are much smaller than phytoplankton numbers in the ocean. For example, Huntley *et al.* (1987) found 7 individuals per liter in the southern California Bight and Jimenez-Perez, and Lara-Lara (1988) found 10 individuals per liter in the Gulf of California. At these concentrations, zooplankton are not considered to be optically important. Swarms of zooplankton may be optically important, but understanding of the ecological processes leading to these swarms is not sufficient for modeling at this time. Huntley *et al.* (1987) suggested that the indirect influence of zooplankton on optics through removal of particles from the water column is more important than their direct effect. Zooplankton grazing is incorporated in this model as a loss of phytoplankton biomass, but zooplankton biomass itself is not modeled.

Potential sources of detrital particles in coastal waters include rivers, wetlands, estuaries, zooplankton or fish fecal pellets, dead phytoplankton, and macrophyte degradation. Studies of detritus have primarily focused on its role as a food source in marshes and estuaries (Mann, 1988; Duggins *et al.*, 1989; Newell, 1982; and Alongi and Christofferson, 1992) and its role in transporting organic carbon out of coastal systems (Newell and Field, 1983; and Walsh *et al.*, 1991). Studies measuring the phytoplankton component of particulate absorption sometimes estimated the detrital absorption (Cleveland, in press; Cleveland and Perry, 1994; Cleveland *et al.*, 1989; Morrow *et al.*, 1989; Bricaud and Stramski, 1990; Iturriaga and Siegel, 1988; Kishino *et al.*, 1985; and Nelson and Robertson, 1993), but none of these studies showed a predictable pattern between detrital absorption and phytoplankton absorption or chlorophyll *a* concentration that would form the basis of a predictive model. No predictive models for detrital concentrations or optical properties presently exist and detritus is not modeled here.

Benthic organisms influence optical properties of the water column, both positively and negatively, through diverse processes. Filter feeding clears the water column. Ejection of feces or pseudofeces, spawning, burrowing, or suspension of organisms directly adds particles to the water column. Indirect effects also occur as benthic organisms stabilize,

destabilize, and modify the bed form. The optical effects of these processes are discussed but not modeled.

Phytoplankton biomass is modeled from a series of coupled linear and nonlinear equations parameterizing processes known to be important to algal growth. Chlorophyll *a* concentration for two size classes (nanoplankton and netplankton) is calculated as a time-dependent function of incident irradiance, surface nitrate concentration, respiration, loss to grazing, and loss to cell mortality. A portion of new photosynthate is excreted as dissolved organic carbon. Phytoplankton cell numbers are calculated from chlorophyll concentration at depths of 1 m and the base of the euphotic zone (defined as the 1% irradiance level) from these local growth and loss terms; these values are passed to the mixing model.

Initial conditions required for modeling phytoplankton biomass are offshore mean surface concentrations of chlorophyll *a* and nitrate. For modeling purposes, both of these concentrations were obtained from archived data, but provision for using a remotely sensed (LANDSAT, aircraft sensors) initial chlorophyll *a* concentration is available as an optional model input. Incorporation of predictive relationships for nitrate as a function of temperature (Zentara and Kamykowski, 1977; and Kamykowski and Zentara, 1986) was investigated as an alternate method for obtaining initial nitrate concentration, but the available relationship did not agree with archived data for the test region. Input from other portions of the CWC Model includes surface irradiance (integrated over 400 to 700 nm; PAR) and the *in situ* diffuse attenuation coefficient at 490 nm.

Output from the module predicting phytoplankton biomass consists of files for the depth of the base of the euphotic zone (m); cell number concentration (cells ml<sup>-1</sup>) at 1 m and the base of the euphotic zone for both size classes; and nitrate concentration (μmol l<sup>-1</sup>) at 1 m and the base of the euphotic zone.

Absorption at 440 nm by colored dissolved organic matter from river sources is modeled as a linear function of salinity. A minimum value, representing absorption typical of local coastal seawater, is input to provide an offshore high salinity boundary condition. Colored dissolved organic matter released by "leaky" phytoplankton is added to the river source. Algorithms for estimating macrophyte sources of dissolved organic matter are presented but are not presently included in the CWC Model.

Values required for modeling absorption by colored dissolved organic matter are salinity and photosynthetic rates. These are both internally calculated within the CWC Model so that initial conditions are unnecessary. Output from the module predicting colored dissolved organic matter is absorption at 440 nm ( $\text{m}^{-1}$ ).

The site and time chosen for a model test case is nearshore Camp Pendleton, California, beginning on 23 Jan 1993. The spatial grid consists of 200 points in both the x and y directions, covering about 10 nautical miles on a side. Maximum bottom depth is approximately 300 m. Model runs begin at 00:00 hours. The integrated Coastal Water Clarity Model runs on a 2-hour time step. A 2-hour time step was chosen because tidal data is available on this time scale. However, photosynthetic rates change on a faster time scale, as incident irradiance changes. To increase the accuracy of modeled photosynthetic rates, light-dependent phytoplankton rate processes are calculated on a 30-minute interval and integrated over 2 hours.

#### **4.1 Phytoplankton Biomass Model**

Phytoplankton biomass is generally controlled by interacting physical, chemical, and biological factors. This model includes the major factors believed to influence phytoplankton biomass, basically following an ecosystem modeling approach. Growth rate depends on photosynthesis, which is a function of irradiance, nutrients, and size-dependent physiological characteristics, while loss rate is a function of grazing, mortality, sinking, and vertical mixing. Horizontal advection is not included in the present version of the BIOMASS/BIOXPORT distributed source model.

The following paragraphs describe the assumption and growth/loss and input/output required by the phytoplankton BIOMASS model.

##### **4.1.1 Model Structure**

Phytoplankton biomass is calculated by a program module entitled BIOMASS, which includes individual subroutines IRRAD, INPUT, INITIAL, and UPDATE. An additional subroutine, DOM, calculates the phytoplankton contribution to colored dissolved organic matter and adds it to the river source of CDOM. Fig. 4-1\* diagrams the interacting computer

---

\* Figures and tables are located at end of Section 4.0.



modules and subroutines involved in modeling the biomass and optical properties of phytoplankton. Required input to BIOMASS is obtained from LOWTRAN (surface irradiance) and OPTIC (diffuse attenuation at 490 nm). Subroutine IRRAD calculates *in situ* irradiance at depth from surface irradiance and diffuse attenuation. Subroutine INPUT reads parameters required for predicting phytoplankton biomass. Subroutine INITIAL reads values of initial or boundary conditions and extrapolates these values throughout the 200 by 200 horizontal grid space and vertically to 1 m and zeepar (the depth where irradiance attenuates to 1% of surface irradiance). INITIAL runs only during time step zero. Subroutine UPDATE reads cell number density (both size classes and both depths) and nitrate concentration files from the end of the previous time step as conditions for the beginning of a subsequent time step. UPDATE does not run during time step zero, but runs during all subsequent time steps.

Output from BIOMASS is utilized by BIOXPORT, which calculates vertical mixing of cells. Cell number concentrations are then passed to BIOOPTIC, where the optical properties of the phytoplankton are modeled. Output from subroutine DOM is passed directly to BIOOPTIC.

#### **4.1.2 Phytoplankton Size Classes**

Two size classes of phytoplankton are modeled; nanoplankton with an equivalent spherical diameter of 5  $\mu\text{m}$  and netplankton with an equivalent spherical diameter of 20  $\mu\text{m}$ . The presence of two size classes allows simulation of size-dependent physiological rates and consideration of size-dependent optical properties. A number of processes appear to be dependent on phytoplankton cell size. Maximum specific growth and photosynthetic rates decrease with increasing cell size (Langdon, 1988; Schlesinger *et al.*, 1981; Blasco *et al.*, 1982; and Banse, 1976). The maximum cell density for a particular species in culture or in nature decreases with increasing cell size (Agusti *et al.*, 1987; and Agusti and Kalff, 1989). Nutrient uptake may be diffusion-limited in large cells (Chisholm 1992; Morel *et al.*, 1991; and Eppley *et al.*, 1969). Field studies show size-dependent nitrogen uptake rates (Probyn, 1985; and Probyn and Painting, 1985). Grazers select food based on particle size (Bartram, 1980; and Paffenhöfer, 1984). Sinking rates vary with size (Smayda, 1970; Bienfang, 1980; and Eppley *et al.*, 1967).

The effects of phytoplankton cells on the optical properties of the water column vary with size. The specific absorption coefficient (*i.e.*, absorption normalized to chlorophyll *a* concentration) decreases as cell size increases for a constant pigment concentration per cell volume (Kirk, 1975 a, b, 1976; Morel and Bricaud, 1981; and Sathyendranath *et al.*, 1987). Scattering also varies with particle size (Bohren and Huffman, 1983).

Nanoplankton and netplankton represent two distinct size classes of phytoplankton that occur in coastal waters and are consistent with standard definitions of plankton size classes. Small cells dominate phytoplankton numbers in oligotrophic waters and form a background to which larger cells are added in more eutrophic waters. Chisholm (1992) pointed out that, beyond a threshold concentration, chlorophyll can only be added to a system by addition of a larger algal size class. This means that waters high in chlorophyll, typical of many coastal areas, will contain larger size classes of phytoplankton.

In a simulation model of the mid-Atlantic Bight, Gregg and Walsh (1992) defined two phytoplankton size classes that differed in maximum growth rates, light saturation intensities, specific absorption coefficients, and sinking rates. After a 70-day model run, results showed that nanoplankton dominated phytoplankton populations in deeper waters while netplankton dominated in shallower waters, similar to real distributions. Faster-sinking netplankton were lost from the surface layer in deep water but were resuspended and retained in the surface layer in areas of shallow water.

Separation of the phytoplankton community into nanoplankton and netplankton size classes in the present model allows variation in the size structure of the phytoplankton community as a response to changes in light, nutrients, mixing rate, or shoaling bottom. Size-dependent coefficients are specified for photoadaptive state, nitrate uptake kinetics, respiration rate, grazing losses, mortality, and sinking.

#### **4.1.3 Irradiance at Surface and Depth**

Irradiance at depth ( $E(z,t)$ ) is calculated from surface irradiance and the diffuse attenuation coefficient. All symbols are defined in Table 4-1. Surface irradiance is provided by LOWTRAN as an above-surface value in Watts  $m^{-2}$  integrated over PAR (photosynthetically available radiation, 400 to 700 nm). Watts  $m^{-2}$  are converted to  $\mu$ Einsteins  $m^{-2} s^{-1}$  using the factor  $2.77 \times 10^{-18}$  quanta  $s^{-1} watt^{-1}$  (Morel and Smith, 1974). For sun altitudes

from 22° to 90° and either clear or cloudy skies, this conversion factor is accurate within 2-3% percent (Morel and Smith, 1974).

Diffuse attenuation at 490 nm ( $K(490)$ ; provided by the optics module of the CWC Model) is converted to diffuse attenuation over PAR ( $K(PAR)$ ), utilizing the relationship between optical depth at 490 ( $\tau(490)$ ) and optical depth over PAR ( $\tau(PAR)$ ) developed by Zaneveld *et al.* (1993):

$$\tau(490) = K(490) * z \quad (1)$$

$$\tau(PAR) = 0.0085 + 1.6243 \tau(490) \quad (2)$$

$$K(PAR) = \tau(PAR) / z \quad (3)$$

This extrapolation assumes that Zaneveld's relationships, developed for open ocean waters of the North Pacific, are valid in coastal waters. Similar comparisons have not been made for attenuation in coastal waters. One goal of this project was to assess currently available models; a model predicting  $K(PAR)$  from  $K(490)$  is available for open ocean, but no model specific to coastal waters exists.

The compensation depth, where algal photosynthesis equals algal respiration, commonly occurs at the depth where irradiance attenuates to 1% of surface irradiance (Talling, 1957; and Sverdrup, 1953). This depth is used as the standard definition of the base of the euphotic zone (abbreviated here as *zeepar*), even though net photosynthesis has been shown to occur at lower light levels. For the purposes of the CWC Model, this definition provides a convenient reference depth for modeling phytoplankton biomass. Photosynthetic rates at depths greater than *zeepar* are very low due to low irradiance; neglect of photosynthesis occurring deeper than *zeepar* has no significant effect on modeled phytoplankton biomass.

$K(PAR)$  is assumed to be constant over the euphotic zone, which is a reasonable assumption in coastal waters with shallow euphotic zones. Irradiance is calculated from  $E(0,t)$  and  $K(PAR)$  at 30-minute intervals:

$$E(z,t) = E(0,t)e^{(-K(PAR) z)} \quad (4)$$

Irradiance and subsequent photosynthetic rates are calculated only at 1m and *zeepar*. The resolution of vertical profiles of phytoplankton biomass is limited by computational time and multi-layer computer storage requirements.

In order to conserve computational resources, incident irradiance is scaled relative to a selected wavelength (490 nm) in the CWC Model. If spectral computations were supported, diffuse attenuation at several wavebands could be calculated in the OPTIC module of the CWC Model at multiple depths ( $K(\lambda, z)$ ), with these values passed to the BIOMASS module for calculation of spectral irradiance at depth.

$$E(z, t, \lambda) = E(0, t, \lambda) e^{(-K(\lambda, z)) z} \quad (5)$$

Spectral irradiance at each depth would then be integrated over PAR for use in equations modeling photosynthetic rate. Incorporation of spectral attenuation coefficients would avoid the use of open ocean relationships between  $K(490)$  and  $K(\text{PAR})$  for coastal waters.

#### 4.1.4 Growth Terms

##### a. Photosynthesis as a Function of Irradiance

Photosynthetic rate at each depth for each size class is calculated using the photosynthesis vs. irradiance formulation developed by Platt *et al.* (1980). Several models are available but this formulation was chosen because it includes photoinhibition.

$$P_L^B(i, z, t) = P_{\max}^B(i) \left[ 1 - \exp\left\{ \frac{-\alpha^B(i) E(z, t)}{P_{\max}^B(i)} \right\} \right] \exp\left( \frac{-\beta(i) E(z, t)}{P_{\max}^B(i)} \right) \quad (6)$$

Symbols are defined in Table 4-1. Values for biological parameters are given in Table 4-2a. The symbol "i" denotes size class, with  $i=1$  referring to nanoplankton and  $i=2$  referring to netplankton. The parameters  $\alpha^B(i)$ ,  $P_{\max}^B(i)$ , and  $\beta(i)$  describe photosynthetic rate as a function of irradiance.

Values of  $\alpha^B(i)$  and  $P_{\max}^B(i)$  for the two size classes of phytoplankton were obtained from size-fractionated P vs. I measurements for coastal and estuarine waters of the Hudson River (Malone and Neale, 1981). Field data on size-fractionated P vs. I parameters are uncommon due to the difficulty in fractionating samples of the small volume typically used in P vs. I incubations and in detecting the radioactive label in a small sample volume. The photoinhibition factor for netplankton was obtained from the mean value found by Hood *et al.* (1991) for field experiments in the coastal transition zone of California. Since smaller phytoplankton have higher

specific absorption coefficients and are more sensitive to high irradiance, a slightly higher value was assigned to photoinhibition for nanoplankton.  $P$  vs.  $I$  relationships for nanoplankton and netplankton are shown in Fig. 4-2. The higher  $\alpha^B(i)$  and  $P_{\max}^B(i)$  coefficients for nanoplankton with respect to netplankton are evident in Fig. 4-2, as a more rapid increase in photosynthetic rate at low irradiance and a higher maximal rate.

### b. Influence of Nitrate on Photosynthetic Rate

A nondimensional nitrate limitation factor for each size class is calculated using Michaelis-Menten kinetics:

$$V_N(i, z, t) = \frac{[N(z)]}{K_N(i) + [N(z)]} \quad (7)$$

Size-dependent, half-saturation coefficients ( $K_N(i)$ ) were obtained from laboratory studies by Eppley *et al.* (1969). MacIsaac and Dugdale (1969) found similar values for natural populations. Nondimensional nitrate uptake as a function of nitrate concentration for both size classes is shown in Fig. 4-3.

This formulation of nitrate uptake allows application of a nondimensional nitrate limitation term as a reduction to photosynthetic rates initially calculated from irradiance alone (Eqn. 6). The nondimensional nitrate limitation term is compared to a nondimensional light limitation term, equal to  $P_L^B(i, z, t) / P_{\max}^B(i)$ . When the value for nitrate limitation is lower than that for light limitation, nitrate limitation is important, and this nondimensional limitation term is applied to decrease the light-dependent photosynthetic rate:

$$P_N^B(i, z, t) = V_N(i, z, t) P_L^B(i, z, t) \quad (8)$$

When the value for nitrate limitation is higher than that for light limitation, nitrate limitation is not significant and the nitrate limitation term is not applied.

$$P_N^B(i, z, t) = P_L^B(i, z, t) \quad (9)$$

This switching process allows for phytoplankton growth controlled by light alone or for growth controlled by both light and nitrate.

At the nitrate concentration specified in the initial conditions ( $0.5 \mu\text{mol l}^{-1}$ ), nitrate-limited photosynthetic rates for the nanoplankton are approximately 50% of the rate based on light alone at mid-day light level, while nitrate-limited photosynthetic rates for the netplankton are approximately 30% of the rate based on light alone (Fig. 4-3). In general, where either nitrate concentration is high or irradiance is low (*e.g.*, at zeepar), nitrate limitation of growth does not occur.

### c. Excretion of Photosynthate

"Leaky" phytoplankton release a portion of newly fixed organic carbon in the form of dissolved organic carbon. Disagreement exists among phytoplankton biologists regarding the magnitude of this excretion, whether it occurs only for cells under physiological stress, and the appropriate techniques for measuring this phenomenon (*e.g.*, Sharp, 1977; and Fogg, 1983). Baines and Pace (1991) evaluated studies on the extracellular release of dissolved organic carbon for consistency and reliable methodology. They concluded that an average of 13% of the photosynthate is excreted by phytoplankton as dissolved compounds.

Following calculation of photosynthetic rates influenced by nitrate limitation (Eqn. 8 or 9), 13% of the photosynthate (newly fixed carbon, not total biomass) is lost to extracellular excretion rather than utilized to create more particles, and a final photosynthetic rate is calculated ( $P^B(i,z,t)$ ):

$$P^B(i,z,t) = P_N^B(i,z,t) - 0.13P_N^B(i,z,t) \quad (10)$$

This dissolved organic carbon becomes part of the pool of colored dissolved organic matter and accumulates with time,

$$\text{DOM}_{\text{phyt}}(z,t) = \sum_{i=1}^2 0.13P_N^B(i,z,t)B(i,z,t). \quad (11)$$

Bacterial uptake of DOM is implicitly included in the rate of photosynthate release calculated by Baines and Pace (1991) because bacteria were not excluded from incubation experiments. An independent calculation of loss of phytoplankton-produced DOM to bacteria does not need to be made here.

#### d. Growth rate

Photosynthetic rates calculated in Eqns. 6, 8, 9, and 10 are already normalized to chlorophyll biomass because P vs. I parameters used here are normalized to biomass (Table 4-1). Calculation of growth rate from photosynthetic production of organic carbon employs the ratio of carbon to chlorophyll ( $\theta$ ), which typically varies between 20 and 100, depending on the nutrient and light history of the phytoplankton population. Cloern (1991) used a value of 50 for San Francisco Bay; Hofmann and Ambler (1988) used 40 for the southeastern U.S. continental shelf; Fasham *et al.* (1990) used 50 for the Sargasso Sea; and Marra *et al.* (1990) used 55 for the Sargasso Sea. An intermediate value of 50 is used here. Phytoplankton growth rate is calculated by dividing the photosynthetic rate by the assumed carbon to chlorophyll ratio,

$$\mu(i,z,t) = \frac{P^B(i,z,t)}{\theta} \quad (12)$$

Growth rates, calculated on a 30-minute interval, are then integrated over the two-hour time step.

#### 4.1.5 Nitrate Fluxes

As phytoplankton grow, they take up dissolved inorganic nitrogen and convert it to particulate organic nitrogen. Uptake rate is a function of light- and nitrate-limited photosynthetic rates (assuming that the excreted organic compounds include nitrogen), initial biomass, and the Redfield ratio:

$$U_N(i,z,t) = P_N^B(i,z,t)B(i,z,0) / (6.6 * 12). \quad (13)$$

Where  $U_N(i,z,t)$  is the uptake rate of nitrate, 6.6 is the Redfield ratio in mol C: mol N, and 12 is the molecular weight of carbon. The Redfield ratio is used here only to calculate nitrate removal from the water. Any variation in the C:N ratio of the phytoplankton or their uptake would have a small effect on modeled biomass. Changes in nitrate uptake caused by changes in the Redfield ratio would change the water column nitrate concentration; effects are dampened by a subsequent change in the nitrate gradient between surface and deep water. As part of the sensitivity analysis, it was found that a doubling of the Redfield ratio changed biomass in a 1-day model run by only

2%. Uptake rate is calculated on the same 30-minute time interval as photosynthetic rate, then integrated over the 2-hour time step.

Disappearance of nitrate through uptake is offset by a deepwater nitrate source. Nitrate influx to the mixed layer is a function of the vertical gradient in nitrate, the vertical diffusion coefficient, and the mixed layer depth. Nitrate influx is modeled as

$$\text{Inf} = A_v ((N_{\text{deep}} - N(z))/\text{pycno})/\text{MLD}. \quad (14)$$

Where Inf is influx of nitrate to the surface layer,  $A_v$  is the vertical eddy diffusivity;  $N_{\text{deep}}$  is the concentration of nitrate below the pycnocline;  $N(z)$  is the concentration of nitrate at depth (1 m or base of the euphotic zone), pycno is the thickness of the pycnocline, and MLD is the mixed layer depth. Assumed values are given in Table 4-2b. The initial mixed layer depth (50 m) was obtained from archived data. In this case, the mixed layer depth is based on the 9-year average for January, 1960-69, given in the CalCOFI Atlas (Wyllie and Lynn, 1971). The vertical eddy diffusivity used ( $0.3 \text{ cm}^2 \text{ s}^{-1}$ ) is the average of values used by Frost (1991), Moisan (1993), and Fasham *et al.* (1990). Values of 5 m for the pycnocline thickness and  $5 \mu\text{mol l}^{-1}$  for the deep water nitrate concentration are assumed. The current version of SEDXPORT (see section by Jenkins) models mixed layer depth, pycnocline thickness, and vertical diffusivity. Time-varying nitrate influxes can be calculated from these time-varying physical terms instead of using assumed values.

Nitrate concentration is calculated at the end of each time step from the concentration at the beginning of that time step, uptake, and influx. Nitrate concentration never reaches zero because supply is determined by both the vertical diffusivity and the nitrate gradient. As nitrate concentration in the surface layer decreases, the gradient increases and the influx increases. Under the assumed conditions, if no phytoplankton biomass is lost to mixing, nitrate uptake and influx reach a steady-state condition in 40 time steps (3.3 days). At this equilibrium nitrate concentration (approximately  $0.1 \mu\text{mol l}^{-1}$ ), nitrate-limited growth rates are approximately 17% and 8% of maximal growth rates for nanoplankton and netplankton, respectively.

#### 4.1.6 Losses

The following paragraphs discuss the three phytoplankton loss mechanisms presently included in the BIOMASS model, respiration,



mortality, and grazing, which combine with settling and vertical mixing to determine the equilibrium plankton population.

### **a. Respiration**

The basic dark rate of respiration measured for many species under varied growth conditions is approximately 10% of the maximal photosynthetic rate (McAllister *et al.*, 1964; Humphrey, 1975; Parsons *et al.*, 1984; and Langdon, 1988). The respiration rate utilized here is  $r(i) = 0.10 P^B_{\max}(i)$  for each size class. This respiration rate is applied as a loss of biomass in each time step.

### **b. Mortality**

Cell mortality represents death of phytoplankton through processes other than grazing, such as cell lysis or viral infection. Cell mortality is modeled as a constant proportion ( $m(i)$ ) of the biomass lost in each time step. Measurements on natural populations indicated mortality rates of  $0.07 \text{ d}^{-1}$  (Harris and Piccinin, 1977). In their models, Wroblewski (1977), Hofmann and Ambler (1988), and Franks *et al.* (1986) all selected mortality rates that decreased population size to  $e^{-1}$  after 10 days. A similar calculation for this model indicates a mortality rate of 6% or  $0.06 \text{ d}^{-1}$ . However, enhanced loss of phytoplankton biomass above that due to grazing, respiration, and mixing does not appear necessary for balancing growth and loss processes, so mortality is presently set to  $0.01 \text{ d}^{-1}$  or  $0.0004 \text{ h}^{-1}$  for both size classes. Fasham *et al.* (1990) used cell mortality as a free parameter for adjusting rate processes; cell mortality could be used in the same fashion in the CWC Model, if desired.

### **c. Grazing**

Grazing rates are represented simply as proportional losses per time step. A number of studies have indicated that zooplankton grazing occurs with a diel pattern. For example, Huntley *et al.* (1987) found that the 3 dominant zooplankton species in the Southern California Bight exhibited diel feeding rhythms even if the species did not vertically migrate. Diel vertical migration and grazing patterns by zooplankton were simulated using the approach of Gregg and Walsh (1992), where no grazing was allowed during daylight. In a model simulating temporal changes in phytoplankton biomass in San Francisco Bay, Cloern (1991) used a grazing rate of 10% of phytoplankton biomass per day, typical of zooplankton

grazing processes in this bay (Cloern, 1982). With the assumption that patterns from San Francisco Bay apply to other coastal areas, this rate was adopted for grazing loss of nanoplankton and adjusted to occur over a 12-hour grazing period ( $0.20 \text{ d}^{-1}$ ). Larger phytoplankton cells are available to fewer grazers, so a grazing refuge has been provided for netplankton by assigning a lower grazing rate ( $0.10 \text{ d}^{-1}$ ). These proportions remain constant but the absolute magnitude of phytoplankton biomass lost to grazing increases as the phytoplankton biomass increases, similar to the process of a zooplankton population responding to a spring increase in phytoplankton biomass.

This approach to grazing is, admittedly, simplistic. However, more sophisticated alternatives require site- and species-specific data on zooplankton biomass for initialization which are not available for a generic coastal optics model. For example, Huntley *et al.* (1987) modeled grazing losses of phytoplankton as a function of temperature, phytoplankton doubling rate, phytoplankton size-frequency distribution, zooplankton grazing efficiency on phytoplankton size classes, and zooplankton size-frequency distributions. Field data giving zooplankton abundance by size class was required for initialization. Marra and Ho (1993) modeled grazing losses of phytoplankton as a function of a maximum grazing rate, Ivlev constant for adaptive feeding (modified from Franks *et al.*, 1986), and zooplankton biomass. Data obtained from net tows was used to initialize zooplankton biomass. The parameterization of grazing by Fasham *et al.* (1990) implicitly requires an estimate of initial zooplankton biomass, but the source of values is not given. Moloney and Field (1991) specified initial standing stocks for bacteria and 3 size classes of zooplankton. For the southeastern continental shelf of the U.S., Hofman and Ambler (1988) utilized rate coefficients from selective feeding experiments with a local copepod to model grazing by 5 size classes of zooplankton and initialized with zooplankton biomass typical of the local concentration. These grazing models all require either data on initial concentrations of zooplankton biomass or species-specific rate information. This information is not widely available for global coastal areas in all seasons and is not amenable to remote sensing of initial conditions, making these types of models difficult to implement in the context of the Coastal Water Clarity Model.

In lieu of actual field data, initial zooplankton biomass might be calculated as some function of phytoplankton biomass or time of year. Based on published data from their model site, Walsh *et al.* (1988)

calculated grazing as a function of day number and day length in order to represent seasonal cycles of zooplankton. They imposed this grazing only at night in the upper and middle depth layers of their model. Wroblewski *et al.* (1988) used a grazing formulation similar to that of Marra and Ho (1993), but calculated initial zooplankton biomass by assuming that the system was in steady state with respect to nitrogen. Zooplankton initial concentration was calculated from phytoplankton and nitrogen concentrations and a known value for the total nitrogen in all compartments. Total nitrogen represents the nitrogen available to the phytoplankton via winter mixing, so that they set total nitrogen equal to the nitrate concentration at the local depth of the mixed layer in February. Despite inherent assumptions, one of these approaches may be useful for defining zooplankton initial conditions.

#### 4.1.7 Local Changes in Biomass

The change in biomass over time is formulated as a balance between growth rate and loss rate. Losses considered here as part of the local change in biomass are respiration, mortality, and zooplankton grazing. Sinking and vertical mixing are not local changes and are addressed in the physical transport module (see section by Jenkins), while horizontal advection is not part of the CWC Model at this time.

Growth, respiration, mortality, and grazing rates are expressed over a 2-hour time interval. The local change in chlorophyll biomass  $[\partial B(i, z, t) / \partial t]$  at the end of a 2-hour time step is calculated as

$$\frac{\partial B(i, z, t)}{\partial t} = [\mu(i) - r(i) - m(i) - G(i)] B(i, z, 0), \quad (15)$$

where  $B(i, z, 0)$  is the chlorophyll biomass at the beginning of the time step. Biomass at time  $t$  is the sum of initial biomass and this incremental change over the time step:

$$B(i, z, t) = B(i, z, 0) + \frac{\partial B(i, z, t)}{\partial t}. \quad (16)$$

When loss terms exceed growth terms,  $\partial B(i, z, t) / \partial t$  will be negative and biomass will decrease. This situation will occur at night when photosynthesis equals zero but respiration, mortality, and grazing continue to occur, or in turbid water where the *in situ* irradiance is very low.

In all the equations to this point in the model, phytoplankton biomass is represented as chlorophyll *a* concentration in each size class. Chlorophyll *a* provides an appropriate representation of phytoplankton biomass because it is unique to the living phytoplankton component of suspended particulate matter and is not present in zooplankton or detrital particles. The concentration of chlorophyll *a* is widely measured by oceanographers and is amenable to remote sensing for establishment of initial conditions. Parameters of the photosynthesis vs. irradiance relationship are typically normalized to chlorophyll *a* concentration, not some other measure of biomass such as cellular carbon or cell numbers. However, constraints of the modeling process for vertical mixing and sinking of phytoplankton require expression of biomass as cell number density (see section by Jenkins). Phytoplankton biomass as chlorophyll *a* concentration is converted to cell number density using the cellular concentration of chlorophyll *a* for each size class:

$$\text{cell}(i) = \frac{10^{-3} B(i, z, t)}{\text{chlcell}(i)} \quad (17)$$

where  $\text{cell}(i)$  is the cell number density of 5 or 20  $\mu\text{m}$  phytoplankton ( $\text{cells ml}^{-1}$ ),  $\text{chlcell}(i)$  is the internal concentration of chlorophyll *a* for the respective size class ( $\mu\text{g chl } a \text{ cell}^{-1}$ ), and  $10^{-3}$  converts from cells per liter to cells per milliliter to conform with the CGS system of units used for sediment particle concentrations.

$\text{Chlcell}(i)$  for the two size classes is determined from the relationship between chlorophyll *a* per cell volume and equivalent spherical diameter (Fig. 4-4) presented by Morrow (1988). Morrow developed this relationship utilizing published data from 3 laboratory studies (Blasco *et al.*, 1982; Davies-Colley, 1986; and Morel, 1987) and his analysis of data from the Biowatt Program in the Sargasso Sea. The laboratory data are based on chlorophyll *a* concentrations measured on acetone extracts and cell diameters measured microscopically for unialgal cultures. Field data are based on cellular chlorophyll *a* concentrations calculated from microphotometric measurements of absorption efficiency for single cells and microscopically-measured cell diameters. Field and culture data exhibit the same general relationship; chlorophyll *a* per cell volume decreases as cell volume increases. Scatter in the data represents real variability in the intracellular concentration of chlorophyll *a*, which varies with species or

adaptive responses to changing light or nutrient conditions. Fig. 4-4 summarizes this variability in cellular chlorophyll *a* by representing both field and laboratory conditions with one relationship based on numerous data points. Based on these data, average chlorophyll concentrations per cell are  $2.0 \times 10^{-5} \mu\text{g chl } a \text{ cell}^{-1}$  for 5  $\mu\text{m}$  cells and  $2.1 \times 10^{-6} \mu\text{g chl } a \text{ cell}^{-1}$  for 20  $\mu\text{m}$  cells (Table 4-2a).

#### 4.1.8 Sinking Rates

Sinking rates are not used in the calculation of local biomass changes, but are discussed here because sinking rates are specific to the two size classes and are controlled by a combination of physiological and physical factors. Smayda (1970; his Figure 1) presented measured sinking rates as a function of measured equivalent cell diameters for living phytoplankton cultures. Sinking rates could be calculated from Stokes' law using equivalent spherical diameters and specific gravity, but a number of factors other than cell diameter influence sinking rate, including cell density, chemical composition of cell coverings or internal constituents, presence of lipid-containing vacuoles, shape, presence of spines, and formation of chains. The empirical values in Smayda's Figure 1 implicitly include these factors, thus avoiding assumptions of sphericity that are required in calculating sinking rates from Stokes' equation. Smayda (1970) points out that small cells have greater densities (specific gravities), which is implicit in the empirical relationship between sinking rate and diameter. Based on these data, sinking rates assigned to the two size classes of phytoplankton are  $0.0001736 \text{ cm s}^{-1}$  ( $0.15 \text{ m d}^{-1}$ ) for nanoplankton and  $0.0009259 \text{ cm s}^{-1}$  ( $0.80 \text{ m d}^{-1}$ ) for netplankton.

#### 4.1.9 Initial Conditions

##### a. Biomass

Ecosystem models generally initialize with phytoplankton biomass at the beginning of the model time frame (Marra and Ho, 1993; Gregg and Walsh, 1992; Cloern, 1991; Frost 1991; Moloney and Field, 1991; Fasham *et al.*, 1990; Hofmann and Ambler, 1988; Wroblewski *et al.*, 1988; Walsh *et al.*, 1988; and Kremer and Nixon, 1978). Photosynthetic and growth rates depend on the concentration of living algal biomass present to perform photosynthesis and cell division; thus this

biomass must be specified initially. There is no real contradiction in requiring data on initial chlorophyll biomass in order to predict chlorophyll biomass when time scales are considered; the model is intended to forecast biomass (and optical properties) from this initial condition and the critical physical, chemical, and biological forcing functions over a time period of approximately 2 weeks. Phytoplankton concentrations can change considerably over a 2-week time frame, especially in physical conditions that favor bloom formation, making this predictive capability useful.

Initial phytoplankton biomass, as chlorophyll *a* concentration, is presently obtained from archived data. Contours of chlorophyll *a* concentration in the surface layer from the CalCOFI program indicate that nearshore levels in the winter are  $1.0 \mu\text{g chl } a \text{ l}^{-1}$  (Owen, 1974). This value is used to initialize the model. CalCOFI data for Jan., 1993, shows that chlorophyll concentration ranged between 1.1 and  $0.3 \mu\text{g chl } a \text{ l}^{-1}$  in the upper 30 m (Fig. 4-5), corroborating values obtained from archives. Gregg and Walsh (1992) divided initial chlorophyll *a* evenly between their two size classes; the same approach is used here.

Ecosystem models generally begin with homogeneous distributions of biomass, then allow phytoplankton growth and loss processes to distribute the biomass spatially in response to the controlling mechanisms (*e.g.*, Gregg and Walsh, 1992; Cloern, 1991; Frost 1991; and Kremer and Nixon, 1978). In early runs of the CWC Model, this approach was used and the initial concentration of chlorophyll was assumed to be homogeneously distributed in both the vertical and horizontal dimensions. However, in order to expedite attainment of horizontal and vertical distributions reflecting modeled forcing functions, the initial conditions were modified. Initial chlorophyll concentration is assumed to apply only at 0 m. The vertical distribution of chlorophyll is assumed to mimic the vertical distribution of PAR with depth, which would be true if light were the only factor controlling phytoplankton growth. Chlorophyll concentrations at 1 m and *zeepar* are calculated from the concentration at 0 m ( $B(i,0,0)$ ) and the diffuse attenuation coefficient for PAR ( $K(\text{PAR})$ ),

$$B(i,z,0) = B(i,0,0) \exp\{-K(\text{PAR}) z\}. \quad (18)$$

Thus at  $z = \text{zeepar}$ ,  $B(i,z,0)$  equals exactly 1% of  $B(i,0,0)$ . At 1 m,  $B(i,1,0)$  follows the spatial distribution of diffuse attenuation. Spatial distributions of nanoplankton at 1 m at the end of time step 0, reflecting these calculations of initial conditions, are shown in Fig. 4-6. Cell numbers are maximal

(approximately 2200 cells  $\text{ml}^{-1}$ ) in clear offshore water and minimal (approximately 20 to 50 cells  $\text{ml}^{-1}$ ) in turbid nearshore water. Cell numbers for netplankton (not shown) are lower but follow the same spatial pattern. Netplankton have higher cellular concentrations of chlorophyll *a* (Table 4-2a; Fig. 4-4), thus the division of initial chlorophyll evenly between the two size classes provides equal chlorophyll concentrations, but unequal cell number concentrations.

Results of two versions of a 10-day model run of only the phytoplankton growth (BIOMASS) and mixing (BIOXPORT) modules of the CWC Model confirm the appropriateness of this approach to evaluating initial biomass. The 10-day run allowed phytoplankton to approach dynamic equilibrium under both approaches to distributing initial biomass. Physical processes were the same each day; *i.e.*, this dynamic equilibrium condition is achieved by repeating the same physics each day. A 10-day run beginning with horizontally and vertically homogeneous initial biomass produced final biomass distributions that were similar to those for a 10-day run beginning with initial biomass based on diffuse attenuation.

The phytoplankton biomass portion of the CWC Model should, ideally, be run until biomass reaches a dynamic equilibrium so that initial biomass obtained from archives or remote sensing can respond to the modeled physical and chemical conditions. The full CWC Model has not been run for the time period required to reach dynamic equilibrium, but the coupled BIOMASS/BIOXPORT model has been run for an adequate time span. Output from this 10-day run could be used for initial phytoplankton distributions. Despite this quest for stability in the response of phytoplankton biomass, the model is not a true steady state model. Phytoplankton rate processes and, thus, biomass respond to time-varying physical, chemical, and biological forcing functions. As these forcing functions change, phytoplankton growth and biomass change. For example, an increase in river flow typically decreases light penetration into the water column which decreases phytoplankton growth. The balance between time-dependent growth and loss rates determines whether biomass accumulates or decreases in each time step.

The potential for obtaining initial chlorophyll concentration from remote-sensing data has been investigated by the Electro-Optics Organization, Inc. (EEO). EEO has processed one LANDSAT image for 23 Jan 1993, at 10:00 a.m., and produced images of sediment and chlorophyll

concentrations in the surface layer. These results have not been incorporated into the CWC Model.

### **b. Nitrate**

Initial nitrate concentration is presently obtained from archived data (CalCOFI; and Thomas and Seibert, 1974). Contours of nitrate concentration in the surface layer based on a 9-year average for January, 1960-69, indicate that nearshore levels in the winter are  $0.5 \mu\text{mol l}^{-1}$ . Nitrate concentration is set to  $0.5 \mu\text{mol l}^{-1}$  at 1 m throughout the horizontal grid. Nitrate at zeepar is set 20% higher than this to mimic vertical gradients in nitrate concentration. Nitrate concentrations from CalCOFI data for Jan., 1993, are similar, ranging from 0.5 to  $0.8 \mu\text{mol l}^{-1}$  (Fig. 4-5).

An alternative approach to the current process of obtaining initial nitrate concentration from archived data has been investigated. Zentara and Kamykowski (1977) analyzed relationships between temperature and nutrients for distinct regions in the Pacific Ocean. At temperate and tropical latitudes, they found that nutrient (nitrate, phosphate, and silicate) concentrations decreased with increasing temperature, as expected, considering that predominant nutrient sources are deep, cold water. The relationships vary with latitude. Zentara and Kamykowski (1977) presented scatter diagrams for nutrient concentration as a function of temperature for  $10^\circ$  latitudinal bands and suggested that these correlations could be useful for predicting surface nutrient concentrations from remotely sensed temperature data. These type of relationships have been used in several contexts and proposed as an approach for estimating nutrient concentrations from satellite data. Kamykowski and Zentara (1986) statistically analyzed relationships between nutrient concentration and temperature, or  $\sigma_t$  for a global data set. An example of their data and quadratic relationship is shown in Fig. 4-7a. Nitrate concentrations and fluxes in a tidal front were successfully modeled from region-specific, nitrate-temperature relationships and satellite-based temperature data (Morin *et al.*, 1993). Traganza *et al.* (1980) and Traganza *et al.* (1981) combined shipboard data on nutrients as a function of temperature with satellite thermal imagery to investigate chemical and biological interactions in coastal California fronts and upwelling areas. These studies indicate that nutrient concentrations can be predicted from temperature.



Kamykowski (personal communication) has provided a series of regression equations, based on data in Kamykowski and Zentara (1986), relating nitrate concentration to temperature for the Pacific Ocean. The relationship for nitrate concentration as a function of temperature within the  $10^\circ$  square centered at  $35^\circ\text{N}$ ,  $115^\circ\text{W}$  (which includes the position of the CWC Model test case), is shown in Fig. 4-7b. CalCOFI archives indicate that nearshore surface water temperature in January is typically  $15$  to  $16^\circ\text{C}$  (Wyllie and Lynn, 1971) and nitrate concentration is  $0.5\ \mu\text{M}$  (Thomas and Seibert, 1974). CalCOFI data from Jan., 1993, give a water temperature of  $14.8^\circ\text{C}$  and nitrate concentration of  $0.7\ \mu\text{M}$  (Fig. 4-5). The relationship provided by Kamykowski predicts a nitrate concentration of  $5.8\ \mu\text{M}$  for a temperature of  $15^\circ\text{C}$ . Because of the inconsistency between predicted and measured nitrate concentration, the nitrate-temperature relationship has not been incorporated into the CWC Model and archived data are used instead.

#### **4.1.10 Results of Phytoplankton Biomass Prediction Model**

##### **4.1.10.1 Local Growth and Loss Model**

A time course of photosynthetic rate over 1 day (Fig. 4-8a) illustrates the interactions of biological processes. Nanoplankton photosynthetic rate at 1 m in relatively clear water ( $K(\text{PAR})\ 0.20\ \text{m}^{-1}$ ) is shown as a function of the time of day. Surface irradiance was obtained from LOWTRAN for the model standard day, 23 Jan 1993. Standard parameter values (Table 4-2) and initial conditions (nitrate  $0.5\ \mu\text{mol l}^{-1}$ ; chlorophyll  $0.5\ \mu\text{g l}^{-1}$ , in each size class) were used. Photosynthetic rate was first calculated using Eqn. 6 without the photoinhibition term. Photosynthesis reached a maximum in late morning and remained at that maximum until late afternoon (Fig. 4-8a). Adding the photoinhibition term to the calculation of photosynthetic rate (complete form of Eqn. 6) caused a decrease of about 10% from that maximum (Fig. 4-8a). Consideration of nitrate limitation (Eqn. 8) reduced nanoplankton photosynthetic rates by 50-60% over light-dependency alone. When light is low in early morning and late afternoon, photosynthetic rate is determined by light availability alone. During mid-day, both light and nitrate availability influence photosynthetic rate.

Fig. 4-8b shows nanoplankton biomass at 1 m under the same standard conditions. The balance between growth and loss can be seen by comparing biomass calculated using different portions of the model.

Biomass calculated from the full series of local growth (light, nitrate) and loss (respiration, grazing, and mortality) terms shows a gradual decline during darkness as loss terms operate in the absence of photosynthesis, a gradual increase in daylight hours as photosynthetic increases exceed losses, and another decrease after sunset (Fig. 4-8b). Biomass calculated using only the growth terms of the model does not change during darkness and increases during daylight (Fig. 4-8b). The final biomass calculated in the absence of loss terms is more than double the biomass calculated when loss terms are included.

#### **4.1.10.2 Standard 24-hour Run of Integrated Model**

##### **a. Temporal Patterns**

Phytoplankton grow during periods of sunlight, are grazed during periods of darkness, and are lost to mortality, vertical mixing, and sinking at all times of day. Respiration occurs during all time periods. Fig. 4-9 shows the results for nanoplankton at 1 m depth at 1400 hours after growth, but before mixing, while Fig. 4-10 shows the results at 1400 hours after mixing. Biomass accumulates during each daylight time step as a consequence of photosynthesis (Fig. 4-9) and biomass is lost to mixing (Fig. 4-10) in each time step.

Time series of phytoplankton biomass can be examined in two fashions. The first approach looks directly at cell numbers as a function of time at one grid spot; this approach is used below in discussion of the 10-day model results. The second approach qualitatively follows changes apparent in the images over time. Using the second approach, we see that nanoplankton cell numbers at 1 m show a gradual increase from initial conditions (Fig. 4-6) to a maximum (Fig. 4-10) during the brightest part of the day (1400 hours). By the end of the day, cell numbers have decreases from this maximum as losses exceed growth during the night (Fig. 4-11). Nitrate limitation restricts the accumulation of biomass by decreasing photosynthetic rate through the brighter parts of the day (Fig. 4-8a). These results suggest that the temporal pattern in phytoplankton growth is primarily determined by the daily pattern in incident sunlight with a balance between light-dependent growth and mixing-dependent losses.

## **b. Spatial Patterns**

Spatial distributions of phytoplankton generally followed the distribution of diffuse attenuation, with some variation related to mixing. Lowest biomass levels occurred in the river plume where turbidity and diffuse attenuation were the greatest (values for  $K(\text{PAR})$  reached  $5.3 \text{ m}^{-1}$  during periods of highest river flow). The next lowest biomass levels occurred on the shelf, where  $K(\text{PAR})$  reached 1.5 to  $2.1 \text{ m}^{-1}$ . Highest biomass occurred where diffuse attenuation was low (approximately  $0.20 \text{ m}^{-1}$ ). In clear water areas, nitrate decreases the growth rate and accumulation of biomass, but this effect occurs evenly throughout the clear waters and is not apparent as spatial variability in the images. In areas of high light attenuation (*e.g.*, the river plume and shelf), nitrate supplies are adequate to support the light-dependent photosynthetic rates. In fact, nitrate influx exceeds uptake and nitrate concentration gradually increases. In areas of high attenuation, phytoplankton biomass is low because low light penetration into the water column limits growth. In relatively clear waters (*e.g.*, the southwest corner of the study area; Figs. 4-10 and 4-11), biomass is higher. Accumulation of biomass is also influenced by mixing processes, which move some phytoplankton biomass out of the surface layer. Comparison of nanoplankton distribution in Fig. 4-9 (before mixing) to Fig. 4-10 (after mixing) gives a qualitative description of the influence of mixing on phytoplankton populations. More cells are lost through mixing in deep water compared to mid-depths.

### **4.1.10.3 10-day Growth and Mixing Run**

A 10-day run, repeating the same 24-hour sequence of physical drivers (Irradiance, tides, wave, etc.) and the local biomass growth/loss (BIOMASS) and mixing (BIOXPORT) modules of the CWC Model to examine long-term temporal patterns and the balance between growth and mixing. During the course of each day, phytoplankton biomass accumulated gradually during the daylight hours and decreased gradually during nighttime hours. Images for this run are not shown, but a time course for nanoplankton cell numbers at one location (water depth approximately 280 m;  $K(\text{PAR}) 0.20 \text{ m}^{-1}$ ) is shown in Fig. 4-12. At this location, maximum cell numbers at 1 m were reached on day 2. Nitrate concentration had decreased to  $0.1 \mu\text{mol l}^{-1}$  by day 2, causing photosynthetic and growth rates to decrease to 18% of maximal rates. Accumulation of biomass slowed due to nitrate limitation while loss processes (mixing, grazing, mortality, and

respiration) continued, resulting in a net decline in biomass during following days. Concentrations and patterns were similar at the end of day 9 and day 10 (maximum difference 100 cells ml<sup>-1</sup>), indicating that a relatively steady state distribution had been achieved. At the base of the euphotic zone, the pattern in cell numbers differed from that at 1 m because light-dependent photosynthetic and growth rates were so low that nitrate supplies were adequate to support this growth. From the initial K-dependent cell density of 25, nanoplankton numbers gradually increased due to growth and mixing, until a maximum number was reached on day 4 and maintained afterwards.

During the course of the 10-day model run, netplankton and nanoplankton followed the same general patterns as their respective growth and loss rates responded to the same chemical and physical conditions (Fig. 4-13). Comparison of the two size classes is easier in terms of chlorophyll concentration in each size class rather than cell number concentration. From identical initial chlorophyll concentrations, netplankton and nanoplankton both increased for two days, then decreased as nitrate began to limit growth. Netplankton had slower growth and faster sinking rates compared to nanoplankton; final chlorophyll concentration for netplankton in the clear deep water example of Fig. 4-13 was about half that for nanoplankton.

#### **4.1.11 Sensitivity Analysis for Growth Model; Effects on Biomass**

Stage one of the sensitivity analysis examined the effects of variations in initial conditions and parameter values on phytoplankton biomass in the isolated local growth/loss model (light and nutrient dependent growth, respiration, mortality, and grazing terms; Eqn. 16). These results have been used to select the most important parameters for sensitivity analysis in the integrated CWC Model.

The local growth/loss model was run for 1 day under standard conditions (parameters given in Table 4-2; initial conditions as described in Section 4.1.9; surface irradiance from LOWTRAN for 23 Jan 1993). K(490) values were chosen to cover a range (0.1 to 2.5 m<sup>-1</sup>) representative of coastal waters, in general, and including most of the range found in the CWC Model test case. One parameter or initial condition was changed in each run for a total of 32 analysis runs. Parameter modifications are reported as percent change with respect to the standard value (Table 4-4). Resulting changes in biomass are reported as percent change in root-mean-square of output cell numbers compared to standard results (Table 4-4).

The parameters and initial conditions having the strongest effect on nanoplankton cell numbers at 1 m at the end of 1 day are initial chlorophyll, initial nitrate, grazing rate, respiration rate, chlorophyll per cell, and  $K(490)$ . Initial chlorophyll  $a$  concentration has a strong effect on modeled biomass. A doubling (or halving) of initial chlorophyll  $a$  results in nearly a doubling (or halving) of chlorophyll  $a$  and cell concentrations at the end of 1 day at both depths (Table 4-4). Nanoplankton and netplankton populations respond in identical fashions. At zeppar, growth is light-limited and parameters controlling nitrate concentrations or uptake (initial nitrate, half-saturation constant for uptake, vertical diffusivity, deep water nitrate concentration, and mixed layer depth) have no effect on growth. Changes in photoadaptive parameters ( $\alpha^B$ ,  $P_{\max}^B$ ,  $\beta$ ) have small effects (6 to 10%). The diversion of 13% of the photosynthate to DOM (Eqn. 11) decreases phytoplankton biomass by about 2% in each time step. A change in the assumed value for vertical diffusivity of 900% causes only a 41% change in nanoplankton cell numbers; this parameter may be more important over longer model runs, where influx of nitrate has a greater effect than initial nitrate concentration.

The results of two different approaches to extrapolation of initial biomass over the horizontal grid and vertically in the water column have been described in the section on initial conditions.

#### 4.1.12 Discussion of Phytoplankton Biomass Prediction Model

Spatial and temporal trends in the model results indicate that phytoplankton biomass is controlled by interactions of light, nitrate, and mixing. Sensitivity results indicate that grazing is also important. Phytoplankton growth and biomass are greatest in clear water areas of the test site, with photosynthetic rates reduced from light-dependent maximal rates by nitrate limitation. Biomass is lowest in areas of high *in situ* diffuse attenuation, such as the river plume, and adjacent to the surf zone. High diffuse attenuation coefficients decrease the *in situ* irradiance which results in low photosynthetic rates. Nitrate-limitation of photosynthetic and growth rates does not appear as a spatial or temporal variation in biomass but, instead, decreases growth rates from their potential maximum during the brightest part of the day.

The model test case occurs in winter in coastal California. Winter is a season of low sunlight and deeper mixed layer depths. During the model test, the mixed layer depth is deeper than the euphotic depth throughout the

entire spatial grid, meaning that the phytoplankton population is routinely and repeatedly mixed out of the sunlit surface zone and into deep water, where no net growth is possible. This situation is typical of winter. The relationships between mixed layer depth, critical depth (where community photosynthesis equals community respiration), and the initiation of the spring bloom were explained by Sverdrup (1953); when the mixed layer depth exceeds the critical depth, no net community growth occurs. When the mixed layer depth is shallower than the critical depth and adequate nutrients are present, net community growth occurs. The physical conditions during the CWC Model test, which represent environmental conditions in winter, make it impossible for significant phytoplankton growth to occur. Phytoplankton growth is greater during spring stratification when cells are held in the surface layer and during upwelling events when nutrient influx is high. For this test case, phytoplankton make only a small contribution to optical properties. This result would differ for a season of the year when significant phytoplankton growth occurs, such as a spring bloom or upwelling event. The effect of phytoplankton on modeled optical properties would be enhanced if this growth season coincided with a time of low rainfall and low river flow.

Time and space scales differ between this model and other ecosystem models. This model is designed to forecast over relatively short (days to weeks) time periods and small spatial scales (tens of kilometers). Other models discussed here include basin-scale estimates of primary productivity for the North Atlantic (Wroblewski *et al.*, 1988) and seasonal estimates of phytoplankton biomass for the Mid-Atlantic Bight (Gregg and Walsh, 1992). Marra and Ho (1993) considered the mixed layer as one single phytoplankton population, homogeneously distributed in the vertical. Fasham *et al.* (1990) modeled an annual cycle of plankton dynamics which required 3 years at a time step of 0.2 days to reach steady-state. Physical and biological processes in this model have been represented on shorter time scales and smaller spatial scales. In addition, published models for oceanic regions tend to be internally balanced (for example, total nitrogen in a system is considered constant and cycled between model components), with no terrestrial sources of nitrogen or organic matter. Ecosystem models are frequently developed as a tool for examining environmental forcing functions and explaining local controls of phytoplankton biomass. These models utilize site-specific biological information such as chlorophyll concentration, species identification, grazing rates, and population size-structure, or ignore processes considered unimportant in a particular

location. The CWC model is intended for application to coastal areas world-wide, without the luxury of site-dependent information. As a consequence, the model relies on simple formulations of important processes and initialization data available from archives or remote sensing rather than site-specific data.

Geographically-linked factors influencing phytoplankton growth include light, nutrient regime, horizontal and vertical transport, and depth of mixed layer; these factors are incorporated into the present model. In the absence of initialization data, nutrient regimes could be defined by habitat type, with default nutrient concentrations determined as a function of category. Category-specific grazing rate coefficients or initial zooplankton biomass might be advantageous also. Categories include temperate upwelling zones (high nutrients), temperate non-upwelling zones (low nutrients), polar/subpolar areas (low light), estuaries and bays (high nutrients), and oligotrophic tropics (low nutrients). At this time, there is no real basis for redefining size-dependent biological parameters for different categories.

## **4.2 Colored Dissolved Organic Matter Model**

The dissolved organic matter present in coastal waters originates on land with transport by rivers and run-off, in marshes or swamps, *in situ* as an exudation or degradation product of phytoplankton, or *in situ* as an exudation product of littoral vegetation. Only a portion of dissolved organic matter is "colored", *i.e.*, highly light absorbing. The term "colored dissolved organic matter" (CDOM), used to describe the light-absorbing dissolved organics, is adopted here.

### **4.2.1 Model Structure**

Calculation of CDOM from river sources presently occurs in the SEDXPORT module of the CWC Model, where salinity is modeled. Production of dissolved organic carbon through loss of phytoplankton photosynthate is presently calculated in the BIOMASS module. River and phytoplankton sources of CDOM are combined in a subroutine of BIOMASS called DOM (Fig. 4-1).

## 4.2.2 Sources of CDOM

### a. River Sources

Geochemists use dissolved organic matter as a tracer to indicate whether river water (high DOM source) conservatively mixes with ocean water (low DOM end-member), by examining the relationship between absorption by, or concentration of, dissolved organic matter and salinity. The high DOM signature of river water is progressively diluted with the low DOM signature of ocean water as the two mix. This type of relationship provides a simple method for estimating CDOM from river sources.

Several assumptions are implicit in this approach: 1) All rivers (*i.e.*, zero salinity) at all seasons have the same high CDOM end-member. This assumption does not hold for all rivers, but the published data are inadequate for creating a series of unique drainage-type algorithms. An improvement to this module would be assignment of varied CDOM end-members and construction of a series of relationships applicable to diverse drainage areas. 2) All coastal ocean waters (*i.e.*, high salinity waters) have the same low CDOM end-member. 3) Mixing of freshwater CDOM with marine water CDOM is conservative, with no sources of CDOM other than the two end-members and no sinks of CDOM. This assumption is valid for many rivers and estuaries (Laane, 1980; Aminot *et al.*, 1990; Mantoura and Woodward, 1983; and Blough *et al.*, 1993). Mantoura and Woodward (1983) summarized the literature on flocculation of dissolved organics when fresh and marine waters mix. They determined that it is primarily large molecular weight organics that flocculate and that the contribution of these molecules to the total DOC is small (1 to 11% of the total), supporting the conclusion that mixing is conservative.

Linear relationships between absorption by CDOM and salinity have been found for the Gulf of Maine (Fig. 4-14a; Yentsch *et al.*, 1979; Fig. 4-14d; Phinney and Yentsch, 1991), the Orinoco River and Gulf of Paria (Fig. 4-14b; Blough *et al.*, 1993), and Tampa Bay (Fig. 4-14c; Carder *et al.*, 1993). Data have been converted, when necessary, from the published wavelength to 440 nm using an exponential relationship with a slope of -0.014 (Bricaud *et al.*, 1981). Jerlov (1976) showed yellow substance (no units given) as a function of salinity for the Baltic (Fig. 4-14e, f). The two-part linear relationship implied that two different processes operate, one causing a rapid



decrease in CDOM at low salinity, and the other causing a slower reduction in CDOM as the freshwater source of CDOM is diluted by saltwater. The differences between the 6 relationships shown in Fig. 4-14 indicate that CDOM sources vary and a single relationship cannot adequately describe CDOM in all coastal regions. This conclusion is seconded by J.T.O. Kirk, who says that, "for any given system, the relationship between CDOM and salinity may well be predictable, but we cannot safely assume that the same relationship applies in other systems" (personal communication). Categorization of coastal areas by the type of drainage basin, *i.e.*, concentration of CDOM in the river source, and identification of basin-dependent regression models, may be necessary for extending the CDOM model to other regions. Adequate data sets for this categorization of coastal areas are not presently available, but data of the necessary type are being collected by a number of investigators.

The  $a_{\text{cdom}}(440)$ -salinity relationship of Yentsch *et al.* (1979),

$$a_{\text{cdom}}(440,z) = 2.266 - 0.0716 S(z), \quad (19)$$

was selected for predicting  $a_{\text{cdom}}(440)$  because both the CWC Model test site and the Gulf of Maine are temperate ocean areas. Furthermore, this relationship predicts intermediate, conservative values of  $a_{\text{cdom}}(440)$  for a given salinity compared to the other relationships shown in Fig. 4-14.

A minimum  $a_{\text{cdom}}(440)$  typical of oceanic water is used with this salinity-based relationship. Minimum  $a_{\text{cdom}}(440)$  values for coastal waters appear to be near 0.06 to 0.07  $\text{m}^{-1}$ . Absorption spectra for CDOM in coastal waters of California have a minimum value of 0.07  $\text{m}^{-1}$  at 440 nm (Monterey Bay, CA,  $n = 67$ , and coastal San Diego, CA,  $n = 1$ ; Cleveland, unpublished), suggesting that 0.07 represents a typical minimum for the California coast. For coastal waters of New Zealand,  $a_{\text{cdom}}(440)$  exhibited little variability with a mean value of 0.06  $\text{m}^{-1}$  (Davies-Colley, 1992), similar to the value for the California coast. Clear waters of the Sargasso Sea have lower  $a_{\text{cdom}}(440)$  (0.03  $\text{m}^{-1}$ ; Bricaud *et al.*, 1981), but higher values are expected in coastal waters which are more productive and are closer to river and terrestrial sources of CDOM.

This two-part model predicts  $a_{\text{cdom}}(440)$  from river sources (Fig. 4-14g). At a salinity of 30.67 ppt, the relationship described by Eqn. 19 reaches the coastal marine water minimum  $a_{\text{cdom}}(440)$  of 0.07  $\text{m}^{-1}$ . At

salinities greater than 30.67 ppt,  $a_{\text{cdom}}(440)$  is set to a constant value of  $0.07 \text{ m}^{-1}$ .

### b. Phytoplankton Sources

Baines and Pace (1991) summarized the controversial literature on extracellular release of dissolved organic carbon (DOM) by phytoplankton. Representing extracellular release as a function of primary production, they estimated the average release of DOM to equal 13% of photosynthate. The fraction released is a function of photosynthetic rate not biomass. The concentration of DOM (in units of  $\text{mg C m}^{-3} \text{ h}^{-1}$ ) released by the two size classes of phytoplankton is calculated from the photosynthetic rates calculated in the BIOMASS module (Eqn. 11).

Not all dissolved organic materials in the ocean absorb light strongly. Assuming that 50% of this DOM is light-absorbing, colored matter (CDOM) (Harvey *et al.*, 1983; and Walsh *et al.*, 1992), and assuming a specific absorption coefficient of  $0.07 \text{ m}^2 (\text{g C})^{-1}$  or  $7.0 \times 10^{-5} \text{ m}^2 (\text{mg C})^{-1}$  at 440 nm (Carder *et al.*, 1989), the contribution of phytoplankton to the light-absorption by CDOM at 440 nm is calculated for a 2-hour time step:

$$a_{\text{cdomphyt}}(440, z) = 0.50 \text{ DOM}_{\text{phyt}}(z) (7.0 \times 10^{-5}). \quad (20)$$

The CDOM contributed by phytoplankton accumulates gradually, with a portion contributed and photodegraded during each daylight time step.

### c. Macrophyte Sources

Data regarding rates or concentrations of dissolved organic matter produced by marine macrophytes are scarce in the literature. Newell and Field (1983) estimate that *Ecklonia maxima* and *Laminaria palida* kelp beds off the coast of South Africa release  $250 \text{ gC m}^{-2} \text{ y}^{-1}$  as  $\text{DOM}_{\text{kelp}}$ . Assuming a constant release rate over the year and day, this rate converts to  $29 \text{ mg C m}^{-2} \text{ h}^{-1}$ . CDOM per volume of water can be calculated from

$$\text{DOM}_{\text{kelp}}(z) = 29.0 A H V, \quad (21)$$

where A is the area of the kelp bed, H is the water column depth, and V is the volume of water over which the DOM is distributed. Assuming the ratio of colored organic matter to total organic matter and same specific absorption coefficient as for phytoplankton exudation, the contribution of kelp ( $a_{\text{cdomkelp}}(440)$ ) to absorption can be calculated as an hourly rate:

$$a_{\text{cdomkelp}}(440,z) = 0.50 \text{ DOM}_{\text{kelp}}(z) (7.0 \times 10^{-5}). \quad (22)$$

This value will be constant vertically if the DOM release is spread evenly over the depth of the water column.

Release of DOM from kelp or any other macrophyte is likely to vary with age of the kelp bed, water temperature, nutrient stress, and water motion, but predictive relationships based on these environmental parameters are not available in the literature.

Required inputs from other parts of the CWC Model are a real coverage of kelp beds (in  $\text{m}^2$ ) and bottom depth (in m). Horizontal transport of this material must be modeled in the physical transport section of the CWC Model.

### 4.2.3 Losses of CDOM

#### a. Photodegradation

The time-dependent photobleaching rate for natural dissolved organic matter estimated by Keiber *et al.* (1990) can be used to represent photodegradation of CDOM in the ocean. Their incubations were performed at sea surface irradiance levels, thus the rate implicitly applies to approximately the upper attenuation length ( $z = 1/K$ ). Keiber *et al.* (1990) give a photodegradation rate of  $0.00305 \text{ mg C h}^{-1}$  for natural dissolved organic matter. This rate was applied to phytoplankton sources of CDOM, but this loss completely prevented accumulation of phytoplankton CDOM. In the absence of other published rate estimates, photodegradation was reduced to  $0.001 \text{ mg C h}^{-1}$ .

Photodegradation is not applied to river sources of CDOM because it is implicitly included in the empirical relationship between CDOM and salinity. The samples on which absorption were measured had naturally been subjected to photodegradation in the environment.

## **b. Bacterial Consumption**

Bacteria were not excluded from incubation experiments measuring the phytoplankton release of DOM, and no corrections for bacterial uptake were included. Bacterial uptake of DOM is implicitly included in the rate of photosynthate release calculated by Baines and Pace (1991), and an independent calculation of loss of phytoplankton-produced CDOM to bacteria does not need to be made here.

The conservative mixing of DOM or  $a_{\text{cdom}}(\lambda)$  between river and marine waters indicates that no significant loss, including microbial degradation, of river DOM occurs (Mantoura and Woodward, 1983; and Blough *et al.*, 1993). In this case, it is not necessary to estimate loss of river  $a_{\text{cdom}}(440)$  to bacterial consumption. In general, DOM is highly refractory and unavailable as a food source for bacteria. The portion of the DOM released by photosynthesis that bacteria seem to utilize is the smaller molecular weight, less refractory component.

### **4.2.4 Results of CDOM Prediction Module**

The temporal and spatial variability of  $a_{\text{cdom}}(440)$  are controlled entirely by river flow (Fig. 4-15). At times of high river flow, the freshwater plume, coincident with high  $a_{\text{cdom}}(440)$ , extends the farthest seaward. The spatial distribution of  $a_{\text{cdom}}(440)$  shows maximum absorption in the river mouth, where salinity is lowest, with a steep gradient in  $a_{\text{cdom}}(440)$  in the area of the river plume, until the oceanic end-member is reached.

Phytoplankton contribute approximately  $0.00009 \text{ m}^{-1}$  to the  $a_{\text{cdom}}(440)$  signal during a mid-day time step and nothing during darkness. The phytoplankton contribution to  $a_{\text{cdom}}(440)$  is small compared to the river contribution and the oceanic background. At this production rate, it would take 65 days for phytoplankton to produce the oceanic minimum  $a_{\text{cdom}}(440)$  signal. The phytoplankton contribution to CDOM is indistinguishable from the river contribution in Fig. 4-15.

## **4.3 Benthic Sources and Effects**

Optical properties of seawater may be influenced by the addition or removal of particulate and dissolved materials and gases from the water column.

Most organisms living on the bottom, from the smallest bacterium to the largest kelp plant, interact with the overlying water column in some way. In many instances, these interactions involved either passive or active processes that input material to, or remove material from, the water column. Release of reproductive products or photosynthate, ejection of feces or pseudofeces, migrations, passive sloughing of cells, tissues or larger parts, or resuspension of living organisms are examples of processes that introduce materials from benthic systems. Suspension feeding, and hydrodynamic modifications associated with enhanced particle deposition, are examples of processes that remove material from the water to the benthos. Indirect effects of benthos on substrate properties so as to increase or reduce erodability are widespread, and can substantially affect turbidity in shallow waters. Light penetration can be altered from shading by benthic organisms that inhabit portions of the water column. All of these processes and others will be reviewed below.

Many benthic effects on the water column are limited to the viscous sublayer (usually a mm or less from the bottom), or the log layer (some cm to < 1 m above the bottom). Others influence the entire benthic boundary or nepheloid layer (many m), or the whole water column. Benthic organisms found in coastal water include bacteria, protists, vascular plants (mangroves, seagrasses, and salt marsh plants), macroalgae, microalgae, infauna (meio-, macro- and megafauna inhabiting sediments), endolithofauna (organisms within rock), and epifauna (corals, bottom fishes, many mollusks, and echinoderms). Very often, the types and intensity of benthic exchange with the water column will be controlled by physico-chemical properties of the water and the sea floor. These include bottom water oxygen concentration, bottom flows (tidal, wind-driven, and waves ), nutrient levels, and substrate properties such as composition, density, porosity and particle size.

#### **4.3.1 Release of Material from the Seafloor**

##### **a. Active release**

##### **1. Sediments**

Many large (megafaunal-sized) organisms eject suspended particulates into the water column as a consequence of burrowing and deposit-feeding activities. Taxa known to introduce sediments to the water in this manner (termed bioresuspension) include the bivalves *Yoldia*

*limatula* and *Macoma tenta*, the polychaete *Pectinaria gouldi* (Davis, 1993), a variety of thalassinid and stomatopod shrimp.

Early work on the contribution of benthic resuspension was carried out by Rhoads and co-workers. They noted an extensive near-bottom ( $\leq 9$  m) turbidity zone in Central Long Island Sound (LIS) that exhibits seasonal and tidal variations in intensity. This seasonality, with increasing turbidity in spring and highest levels from May to July (10-40 mg/l), was attributed to changing abundances and activities of bioturbating organisms and to variation in pelagic primary production (Rhoads et al., 1978; Yingst and Rhoads, 1978; and Rhoads et al., 1984). The benthic influences in LIS appear to include direct introduction of sediments into the water, as well as effects of bioturbation on sediment erodability by tidal currents. Rhoads et al. (1984) demonstrate experimentally that the benthic turbidity zone in LIS can support rapid growth of commercially valuable mussels such as *Mytilus edulis*, if they are elevated above the bottom during culture.

Figure 4-16 shows a sediment-profile photograph taken with the Rhoads-Cande sediment profile camera. This optical instrument is used to obtain high resolution information about structures and processes in the upper 20 cm of the seafloor. This image was taken south of the Rappahannock River mouth on the western side of the lower Chesapeake Bay. Large areas of the seafloor were mapped with this system showing structures present in this typical image. The dark area at the top of the image is the water overlying the bottom. The surface boundary roughness is ca. 1 cm. The water-filled excavations at 10 to 15 cm below the sediment surface were produced by maldanid polychaetes which feed head-down and pass sediment upward to the surface. The high reflectance of the image indicates that the sediment (muddy fine to medium sand) is low in sedimentary sulfides. A vertical burrow structure is seen to the right. Increased pore-water pressure from the penetrating optical prism is forcing water and fine-grained sediment out of the burrow (plume). Similar spontaneous ejections exert a continuous, as yet unquantified, influence on bottom optical properties.

There have been very few quantitative studies of the material ejected into the water by benthic organisms and its optical properties. A recent study by Davis (1993) examined light attenuation in water as it was passed through small experimental jars containing single individuals of several common bivalve, polychaete, and decapod species. Distinct, rhythmic patterns of light attenuation, occurring at 15-20, 20-25, and 25-30 min. intervals in

*Macoma*, *Yoldia*, and *Pectinaria*, respectively (Figure 4-17), were taken to represent pseudofeces ejection events. Pseudofeces are technically non-ingested sediments removed through burrowing, however, Davis notes some fecal pellets were included. Active surface browsing in the decapod *Pagurus* sp. produced nearly continuous resuspension of sediment in the same experiments (Davis, 1993). The height the ejected material reaches in the water column is dependent on the taxon, the size of the animal, shear, water turbulence, and the water content of the material. The bivalve *Yoldia* ejected material several cm into the water column and a shear of 2 dyne/cm<sup>2</sup> was required to maintain the material in suspension, whereas the resuspended sediment of *Pagurus* was distributed only as high as its mouth parts.

## 2. Reproductive Products

A large fraction of benthic invertebrate taxa release some type of reproductive products into the water. Eggs and sperm are spawned as dense clouds of gametes in many coelenterates, annelids, mollusks, echinoderms, and fish. Though adjacent individuals often spawn at once, the gametes usually dilute fairly quickly, thus optical effects would normally be highly localized and short-lived. The same is true for release of developing larvae by benthic organisms. However, mass spawning of gametes or larvae that create long-lived, cloudy parcels of water have been reported for corals (Willis and Oliver, 1990), polychaetes (Schroeder and Hermans, 1975), and decapod larvae (Christy, 1982, pers. obs.). Many of these incidences occur during a few days or weeks of the year and their timing, location, and extent can be predicted in advance. Mass spawning of corals occurs on the Great Barrier Reef over 2-4 nights in the austral spring (Babcock et al., 1986; and Harrison et al., 1984). Resulting aggregations of eggs and larvae are visible by aerial survey and LANDSAT imaging. Slicks generated under hydrodynamic influence are concentrated near the surface and form linear features 3-10 m wide and up to a km in length. These may persist for up to 20 hours (Willis and Oliver, 1990).

Polychaetes, including the Palolo worms (*Eunice viridis*, *E. schemacephala*), and many syllids and nereids swarm during gamete release on a single night of the year, or on a lunar cycle (Schroeder and Hermans, 1975). Sometimes luminescence is involved, as in the syllid *Odontosyllis phosphorea*. There is a crinoid that spawn en mass, once a year. Decapod larvae, such as zoea of the genus *Uca*, are released together during specific

phases of the moon and tide (usually just after nocturnal high tides) (Christy, 1982). At the time of release, estuarine and coastal waters can become a veritable zoea soup.

Plant reproductive products such as spores, or gametes are released into the water column as well. However, they are small and no mass spawning likely to influence optics have been reported.

Despite the ephemeral nature of spawning aggregations, larvae of benthic invertebrates (defined as meroplankton) often accumulate in large numbers in shallow embayments (particularly in spring and summer). They can be among the most abundant components of the zooplankton, and are often found behaviorally concentrated within particular depth strata (Forward, 1985; and Thiebaut et al., 1992) or at fronts (Epifanio, 1987).

### **3. Adults, Waste Products, and Dissolved Substances**

Sometimes benthic adults enter the water column, as well as their reproductive products. This often takes place to facilitate feeding (in the case of demersal zooplankton) or mating. Demersal zooplankton in varied habitats such as coral reefs, sandy shelves, kelp holdfasts, and seagrass beds often migrate up into the water nocturnally to feed near the bottom or throughout the water column (Porter, 1974; Aldredge and King, 1977, 1980; Robertson and Howard, 1978; Hobson and Chess, 1979; Ohlhorst, 1982, and Snider, 1985). These organisms are adding large particles to the water at night (themselves, feces, and possibly reproductive products), but are also removing material through ingestion. I am not aware that the actual effects of particulate concentrations or optical properties have been quantified.

Organic wastes are released by animals that molt (exoskeletons), by sloughing of cells (most algae), or by release of epibionts. In most instances, these are unlikely to occur in concentrations sufficient to alter water optical properties. However, release of dissolved materials such as tannins (by mangroves) or humic substances may discolor estuarine waters. Salt marsh grass (*Spartina alterniflora*) contributes about half the humic substances present on the southeastern U.S. continental shelf (Moran and Hodson, 1994).

Macroalgae often release water soluble mucilaginous materials containing dissolved organics (mannitols, sugars, alginates, and lipids) and



surface active agents (Percival and McDowell, 1967; Velimirov, 1980; and Lucas et al., 1981). This release is enhanced during fragmentation (Lucas et al., 1981). These compounds contribute to the formation and stabilization of surface slicks and surface foam in kelp (*Ecklonia* and *Laminaria*) beds (Velimirov, 1979, 1980, 1982). The slicks and foam promote significant bacterial growth and may ultimately influence light penetration and water clarity. Off South Africa, foam accumulations are reported to be stable for up to 2 days in nearshore waters after the cessation of onshore winds (Velimirov, 1980).

#### **b. Passive Resuspension of Benthic Organisms**

A range of benthic organisms, from bacteria to clams are known to enter the water column from the bottom through passive resuspension. Microalgae are resuspended or entrained into the water column by waves, tidal currents, heavy rainfall (intertidal only), or by supersaturation bubbles resulting from high primary productivity (Shaffer and Sullivan, 1988). However, few studies have quantified the importance of this phenomenon. Both the number of benthic diatoms in the water column and the chlorophyll content of these waters have been related to tidal currents (Baillie and Welsh, 1980) and wind-induced currents (Lukatelich and McComb, 1986).

Examination of diatoms collected in Mugu Lagoon plankton revealed that over 90% of them consisted of benthic diatoms commonly found in the lagoon sediments. Common genera include *Achnanthes*, *Amphiprora*, *Amphora*, *Gyrosigma*, *Navicula*, *Nitzschia*, *Rhaphoneis*, and *Surirella* (Schaffer and Sullivan, 1980). Oceanic waters entering Mugu Lagoon exhibited significantly higher productivity 3 h later, and it was concluded from this that benthic diatoms contribute significantly to the gross primary productivity of the lagoon water column. During spring tides, the benthic microalgae are scoured and primary productivity in the water rises. During neap tides, associated with low current speeds, the benthic standing crop increases and is negatively related to water column productivity in the lagoon.

Similar studies in Barataria Bay revealed 70% of water column diatoms to be benthic species. However, relationships between water column and benthic primary production were more variable. Schaffer and Sullivan (1980) predict that the coupling between the benthos and the water column should be highly dependent on estuarine morphology, and that

coupling should be strongest in shallow, well-mixed estuaries, weakest in deep, stratified estuaries.

The same processes that resuspend benthic diatoms may introduce bacterial mat into the water column. In shallow and intertidal estuaries, thick mats of sulfur oxidizing *Beggiatoa* form and are eroded. Grant and Bathmann (1987) have shown that resuspension of these mats introduce large amounts of sulfur into the water column, producing a flux into the water two orders of magnitude greater than that of sulfate reduction or sulfide oxidation by benthic bacteria.

Wind-induced waves and tidal currents commonly resuspend meiofauna such as harpacticoid copepods and nematodes (Palmer, 1988), and macrofauna (Tamaki, 1987). Passive resuspension and transport of newly settled clams on sandflats is particularly well documented (Emerson and Grant, 1991; and Committo et al., in press). However, the optical effects of these faunal resuspension events are likely to be minor relative to the turbidity caused by associated sediment transport.

#### **4.3.2 Benthos as a Sink**

##### **a. Active Removal of Material from the Water by Benthos**

The benthos can act as an important sink for particulates in the water column, effectively removing them in ways that alter turbidity and light attenuation. Active removal of particles results from consumption by infaunal and epifaunal suspension feeders or by collection of particles for other purposes (e.g., tube or test construction). For example, at high densities, bivalves can form phytoplankton-depleted regions above beds in tidal boundary layers and may even remove a significant fraction of daily primary production in shallow bays (Peterson and Black, 1987; Frechette and Bourget, 1985; and Asmus and Asmus, 1991). The extent to which filter feeding by bivalves can control phytoplankton biomass in the overlying water column is governed by phytoplankton transfer to the bivalves as determined by the dynamics of concentration boundary layers (O'Riordan et al., in press). Cloern (1982) estimated that suspension feeding bivalves in South San Francisco Bay can filter a volume equivalent to the South Bay at least once daily, and suggested that grazing by benthos exerts primary control on phytoplankton biomass during summer and fall. Effects of this magnitude are less likely in deeper, coastal waters. More local depletion of

suspended particles within the log layer (a few cm from the bed) is probably a more common condition (O'Riordan, 1993, in press).

The changes in particle concentration in and near dense beds of bivalves have been modeled and examined experimentally for mussels (Wildish and Kristmanson, 1979; Frechette and Bourget, 1985; and Frechette et al., 1989) and clams (O'Riordan, 1993, in press), and one study has been carried out in dense beds of the facultative filter feeding polychaete, *Nereis diversicolor* (Vedel et al., 1994). Mussels and clams differ because clams have siphons which can project above the seabed interacting with flow and injecting high vertical momentum fluid into the boundary layer. Oysters, which form similar dense beds, might be expected to behave like mussels. Flume experiments using mimic bivalve siphons at natural densities clearly illustrate effects of suspension feeding on nearbottom water properties (O'Riordan, 1993, in press). For the siphonate clam species, *Tapes japonica* and *Potamocorbula amurensis*, which are common in San Francisco Bay, near bed phytoplankton concentration gradients are affected by (1) siphon height, which influences bed roughness (2) animal density, which affects multiple jet interactions, (3) boundary layer shear, affecting mixing and food availability to the bed, and (3) siphon pumping velocity, which affects jet/crossflow interactions (O'Riordan, in press).

#### **b. Passive Removal of Material from the Water by Benthos**

Passive removal of particles from the water by reduction of flow can occur on many space scales, from km to mm. The most dramatic instances occur inside vegetated stands such as kelp forests and seagrass beds. The plants bend in currents or waves, deflecting the flow over or around vegetation. Also, the shoots and blades reduce current speeds by extracting fluid momentum, creating low energy microenvironments that enhance deposition of suspended particles (Gambi et al., 1990). Current reductions are documented for kelp (*Macrocystis*) beds (Jackson and Winant, 1983) and seagrass stands (Harlin et al., 1982, Fonseca et al., 1982, Fonseca and Fisher, 1986, and Gambi et al., 1990). These often are sites of reduced erosion and sediment resuspension relative to non-vegetated areas (e.g., Harlin et al., 1982). Eckman et al. (1989) suggest that higher rates of particle deposition documented beneath kelp canopies may be caused by longer particle residence times and higher redeposition probabilities rather than by greater particle import.

Similar flow alterations and enhanced particle deposition occurs within or near biogenic structures formed of sediments such as tubes (Eckman et al. 1981), burrows (DePatra and Levin, 1989), pits (Yager et al., 1993) or tracks (Reimers and Wakefield, 1989), but the effects are limited to water within mm to cm of the bottom and are unlikely to alter particle concentrations above the log layer.

#### **4.3.3 Light Attenuation by Shading**

Dense macroalgal or seagrass vegetation also causes extensive light attenuation and waters within these stands are often dark (Reed and Foster, 1984). Studies in a South African kelp bed dominated by *Ecklonia maxima* revealed that phytoplankton production under the kelp canopy is reduced by 95%. Over the entire study area, extending to 20m depth 500 m offshore, *Ecklonia* cover, which was 13% of the surface area, was estimated to reduce total phytoplankton production by 12% (Borchers and Field, 1981). Shading by upright and table corals also occurs (Stimson, 1985), and undoubtedly affects light penetration and phytoplankton production.

#### **4.3.4 Indirect Effects of Benthos**

##### **a. Sediment Stability**

Many of the burrowing, feeding, defecation, and irrigation activities of infaunal organisms that do not introduce sediments into the water column directly, are known to modify the stability of marine sediments and thus the ease with which they are eroded by tidal, storm, or other currents (Rhoads et al., 1978, Rhoads and Boyer, 1982; and Grant et al., 1982). These effects translate into greater or lesser turbidity, depending on whether sediments are stabilized or destabilized by benthos. Jumars and Nowell (1984) describe 4 ways in which organisms affect sediment flux. These are (1) modification of fluid momentum by biogenic structures, (2) alteration of particle exposure, (3) changes to adhesive-cohesive bonding properties of particles, and (4) alteration of particle momentum associated with deposition (described above). Items 1-3 are discussed below.

The effects of biogenic structures such as tubes, mounds, and pits on fluid momentum have been examined in detail. It is clear that the collective effects of these structures on sediment resuspension depends on the size and

density of the structures, ambient flow velocities, on particle properties, and on degree of mucous binding. Early experimental work in flumes by Rhoads and Boyer (1982), and by Eckman et al. (1981), demonstrated that sediment tubes (such as those made by polychaetes, phoronids, nematodes, and other infauna) could stabilize or destabilize sediments. Destabilization results from increased skin friction at the base of tubes, while stabilization, achieved only when tube areas cover more than 1/12 of the surface, results when flow is directed over the tops of the tubes (called skimming flow). Comparable hydrodynamic studies carried out for mound-shaped objects (e.g., sediment mounds and Mn Nodules) by Mullineaux (1988) have yielded similar inferences. However, the theoretical destabilizing effects of these structures inferred from flume studies are often absent in the field because the processes that generate these structures (e.g., tube building, defecation) also introduce copious quantities of sediment-binding mucous.

Other biogenic structures that have the potential to stabilize sediments include dense bivalve beds (e.g., mussels, oysters, scallops, or clams), as well as rhizome mats made by seagrasses, salt marsh plants, and mangroves (Orth, 1977; and Brenchley, 1981, 1982).

Sediment binding by mucous exudates produces stabilization and reduced resuspension of seabed material. This translates into reduced turbidity, thus greater water clarity. Sources of mucous include microorganisms, algal filaments, microalgae, or infaunal invertebrates (Probert, 1984, Rhoads et al., 1978, Yingst, and Rhoads, 1978). Laboratory experiments in which microorganisms were cultured on glass beads produced a 25 to 60% increase in critical rolling velocities of beads relative to aseptic beads (Rhoads et al., 1978). Flume experiments demonstrate the ability of purple sulfur bacterial mats to increase  $u_*$  critical (erosion threshold) as much as fivefold relative to control cores (Grant and Gust, 1987).

Diatom mucus is spread through interstices of surface and subsurface sediments by motile epipellic diatoms which migrate vertically within the sediments. This stabilizes sediments by increasing cohesion between sediment grains and decreasing skin friction (Grant, 1988). Diatom binding affects size and morphology of sediment ripples and the supply of fine- and coarse-grained sediment available for transport. Stabilization effects are best developed in diatom patches at cm scales and rarely occur uniformly. Grant (1988) provides an excellent review of the subject. Benthic microalgae have been shown experimentally to stabilize sediment in shallow subtidal areas

lacking tidal influence. Polysacharrides content of sediment can be used to give a qualitative prediction of sediment stability (Madsen et al., 1993).

Alteration of particle exposure, as occurs with deposition of feces and pseudofeces may increase or reduce susceptibility of particles to resuspension. Deposition of fecal pellets can increase effective particle size when pellets are cohesive (reducing erosion), or it can reduce cohesion and effective particle size in the case of unconsolidated pseudofeces (increasing the likelihood of erosion). In both cases, particles are often transported from subsurface to the sediment-water interface, making erosion possible. Accompanying changes in particle water content or cohesion will also determine ultimate effects on sediment stability. Jumars and Nowell (1984) point out that these effects are not always predictable. Burrowing and feeding activities of animals vary seasonally (Rhoads et al., 1978) and even tidally (Fuller et al., 1991), affecting temporal fluctuations in nearbottom turbidity.

#### **b. Solutes and Gases**

Biogenic structures in sediments may alter solute exchange in addition to modifying sediment stability. Huettel and Gust (1992) demonstrate that many different forms of biogenic sediment microtopography (termed bioroughness) contribute to interfacial solute fluxes in permeable seabeds. A field experiment involving rhodamine dye injected into sandy sediments revealed strong porewater replacement down to 5 cm depth, caused by small aggregations of mussel shells exposed to boundary layer flows. In flume experiments, bioroughness elements such as tubes, mounds, and crabs on the sediment surface increased porewater fluxes in sandy sediment from 5- to 7-fold.

Microcosm experiments suggest macroinfaunal activities (at natural abundances) typically elevate molecular diffusion 2 to 10 times (up to 100x), effecting extensive solute exchange at the sediment water interface (Aller, 1982, and Aller and Yingst, 1985). However, faunal irrigation activities are not accurately described by the one-dimensional equations used to calculate molecular diffusion. Comparable studies for meiofauna indicate they increase solute transport coefficients in surface sediments by 1.3 to 2 times the molecular diffusion values over length scales of a few mm (Aller and Aller, 1992). Nematodes, juvenile bivalves, and polychaetes appear to have the greatest effects.

Most solutes emitted from porewaters absorb in the UV range and probably have little effect on optical properties of seawater. Exceptions might include groundwater, which, when mixed with seawater, as occurs on the North Carolina shelf, for example, alters the refractive index of the water. Also, DOC might contain humic substances that absorb in the 210 nm range (mostly far UV, N. Blair, person.com.).

While the majority of infaunal effects on solutes act to promote exchange between porewaters and overlying waters, oxygenation that results from animal irrigation and burrowing minimizes methane bubbling in organic-rich sediments. Release of methane bubbles occurs in low-oxygen or anoxic areas where infauna are rare (i.e., Cape Lookout, Martens, 1976). These bubbles are likely to alter acoustic properties of water. The presence of infauna leads to methane oxidation within the sediments, suppressing the production and release of methane gas (N. Blair, unpublished data).

#### **4.3.5 Summary Remarks**

The potential effects of benthic organisms, populations, and communities on water clarity and other optical properties are potentially far-ranging, but few of these effects have been quantified. The interactions likely to be of greatest magnitude and spatial extent are those involving: (a) infaunal effects on particle resuspension and deposition in soft-bottom habitats, and (b) kelp and seagrass bed shading, flow attenuation, and DOM release. Accordingly, additional research on these topics should benefit efforts to model the optical properties of the coastal zone.

Clearly, not all possible types of benthos-water column interactions are important in all habitat types. Any attempt to incorporate benthos effects into coastal zone optical models will necessitate the use of habitat or ecosystem categories, within which significant interactions are specified. Relevant categories might include (a) tidal wetlands (salt marsh, mangrove, seagrass, and mudflats), (b) subtidal soft-bottom, fine sediments, (c) subtidal sands, (d), subtidal rock reef and hardgrounds, (e) kelp forests, and (f) coral reefs. Table 4.7 summarizes the optically relevant processes likely to be important in different benthic systems.

## 4.5 SUMMARY AND RECOMMENDATIONS

Interactions between growth through photosynthesis and loss through mixing appear to be important controlling factors in phytoplankton biomass distribution modeling. Initial conditions of chlorophyll and nitrate concentrations are significant factors due to the relatively short run-time of this model. The format provided by existing models developed for specific sites has been successfully adapted for modeling the diurnal variation of phytoplankton biomass with the several caveats discussed below. Relationships used for evaluating the conservative nature of mixing between river and ocean waters were adapted for use here as a predictive model for absorption by colored dissolved organic matter. Models do not presently exist for predicting concentrations of some of the biological components that can be optically-important.

1) The portions of the Coastal Water Clarity model that predict phytoplankton biomass and absorption by colored dissolved organic matter could be improved with some simple changes. 1) Mixed layer depth, vertical eddy diffusivity, and pycnocline thickness are used in BIOMASS to calculate influx of nitrate to the surface layer. Values for the physical terms are in the present version of BIOMASS and these values are modeled in SEDXPORT and will be incorporated in future versions of the CWC. Use of modeled rather than assumed physical variables would no doubt improve the realism of this calculation and allow for variation time dependent.

2) Horizontal advection of phytoplankton, not included in the initial calculations, must be included in BIOXPORT after site specific compatible parameters for vertical equilibrium are established.

3) As discussed above, the grazing model used here is simplistic. Sensitivity analysis shows that a 2-fold change in grazing rate causes approximately a 0.4-fold change in biomass, implying that this rate is a somewhat important constraint on biomass. A modification of the adaptive-feeding model (Marra and Ho, 1993; and Franks *et al.*, 1986) would be useful if a tractable scheme for zooplankton biomass estimation can be developed.

4) It is widely known that chlorophyll per cell varies with species, photoadaptive state, nutritional state, and other physiological variables. Conversion from chlorophyll to cell number is not required for calculating



mixing losses of phytoplankton in any of the cited models; a potential source of error would be avoided if this conversion were unnecessary.

5) Phytoplankton respond to physical, chemical, and biological forcing functions. A model run-time of only one day results in phytoplankton biomass determined primarily by the initial chlorophyll concentration and the assumptions about initial patterns of distribution. Initializing with a homogeneous chlorophyll distribution in both the horizontal and vertical (as done by Gregg and Walsh, 1992) and a longer run-time from the model start (Fasham *et al.*, 1990, ran their model for 3 years) would allow this assumed initial biomass to distribute according to the modeled forcing functions.

6) In the absence of models predicting  $K(\text{PAR})$  from  $K(490)$  for coastal waters, this model uses a relationship developed for oceanic waters (Zaneveld *et al.*, 1993). Given the different nature of absorbing and scattering materials in coastal vs. oceanic waters, this relationship is probably not accurate. It would be relatively simple to propagate irradiance spectrally with depth, using  $K(\lambda)$ , and integrate over PAR at depth in order to calculate photosynthetic rate.

7) Due to computer, the model presently calculates phytoplankton biomass at only two depths, 1 m and the depth of the 1% irradiance level. This limits the model to a single specified functional shape for all chlorophyll profiles. Profiles showing a deep chlorophyll maximum result from an interaction of between light availability near the surface and nutrient availability at depth. These types of profiles are common in coastal waters and are present in CalCOFI data for the demonstration site for other seasons. Phytoplankton biomass needs to be calculated at more depths to allow for this vertical variability. In the BIOMASS module, depth resolution can be increased simply by calculating irradiance and related photosynthetic rates at the desired depths.

8) The linear relationships between  $a_{\text{cdom}}(440)$  and salinity shown in Fig. 4-14 provide reassurance that the mixing process between high CDOM freshwater and low CDOM seawater is conservative. However, the variation in slopes and intercepts for the different ocean regions suggests that the freshwater, high CDOM end-member of this relationship is not identical for all river sources of CDOM. Extension of these data sets over a greater range of salinity and compilation of a data base describing river sources by their

drainage basin-type would allow creation of a series of regression equations for different drainage areas.

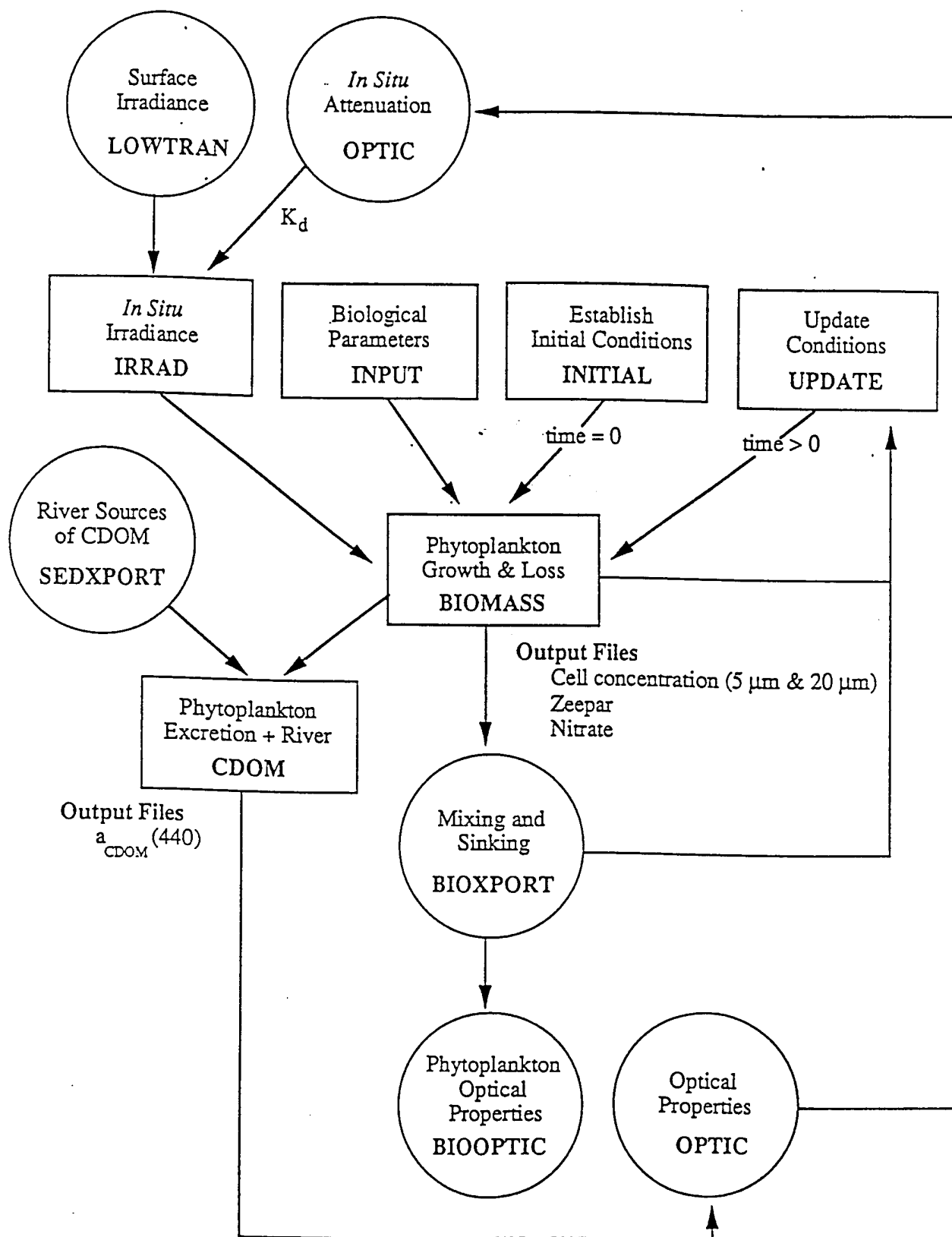


Figure 4-1. Schematic of computer modules and subroutines utilized in modeling phytoplankton BIOMASS and absorption by colored dissolved organic matter. Modules in squares are subroutines of BIOMASS; modules in circles are other portions of the CWC Model.

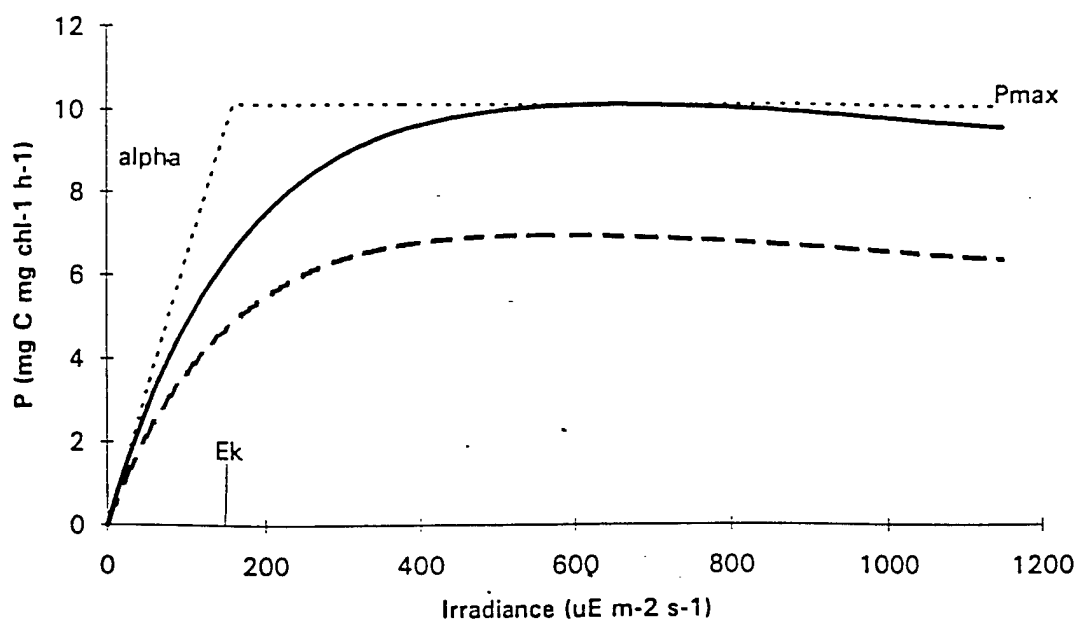


Figure 4-2. Photosynthesis as a function of irradiance for nanoplankton (solid line) and netplankton (dashed line). Dotted line defines alpha (light-limited slope of relationship);  $P_{\max}$  (maximal light-saturated photosynthetic rate);  $E_k$  (irradiance at which  $P_{\max}$  is reached). Illustrated  $P_{\max}$  differs from the parameter due to photoinhibition.

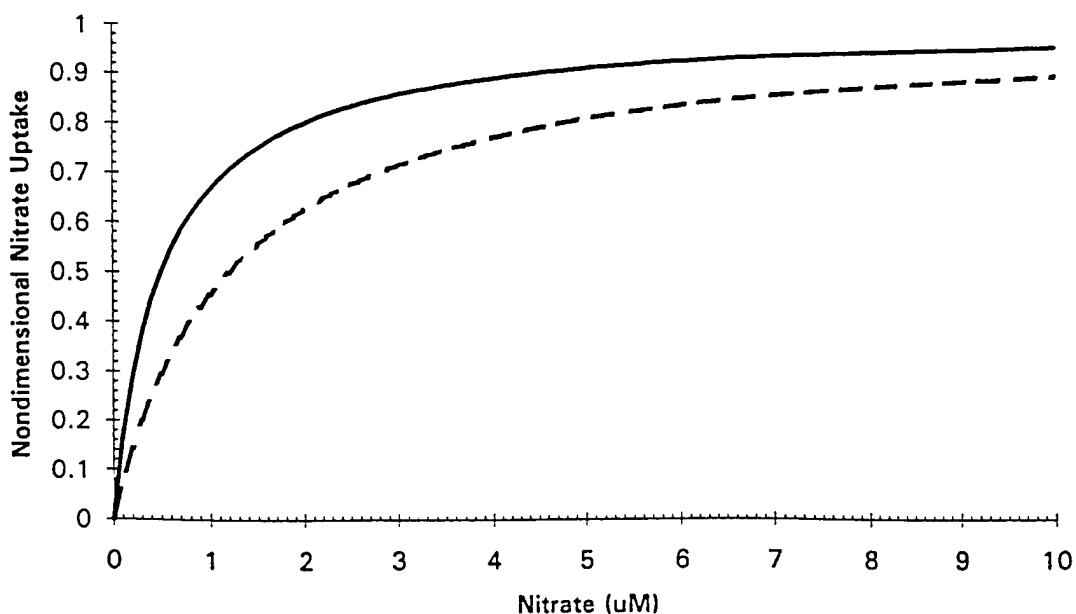


Figure 4-3. Nondimensional nitrate uptake, modeled from Michaelis-Menten kinetics, for nanoplankton (solid line) and netplankton (dashed line).

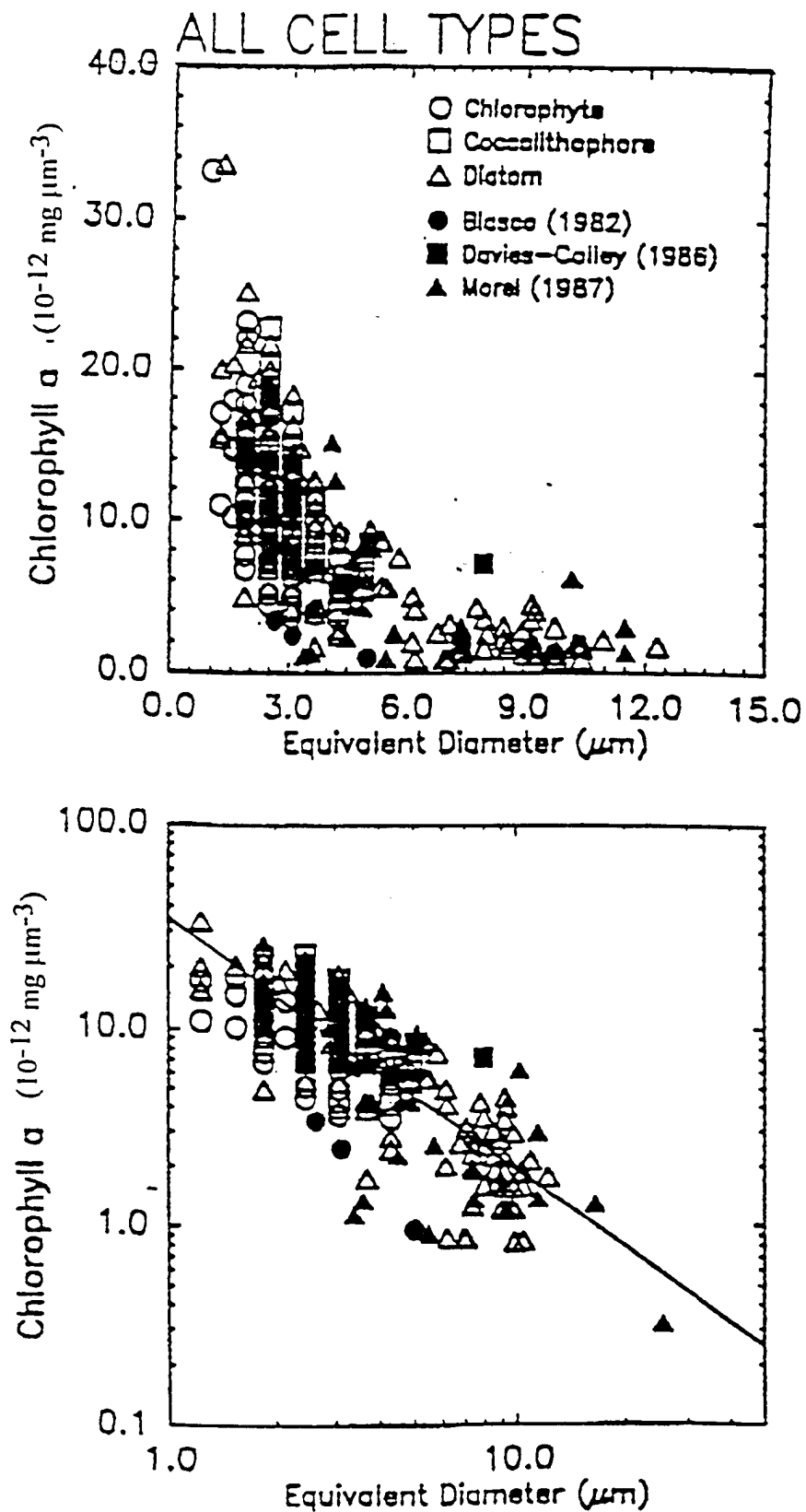


Figure 4-4. Chlorophyll *a* concentration per cell volume as a function of equivalent spherical diameter for laboratory-grown cultures (solid symbols) and natural field samples (open symbols). From Morrow (1988) with permission.

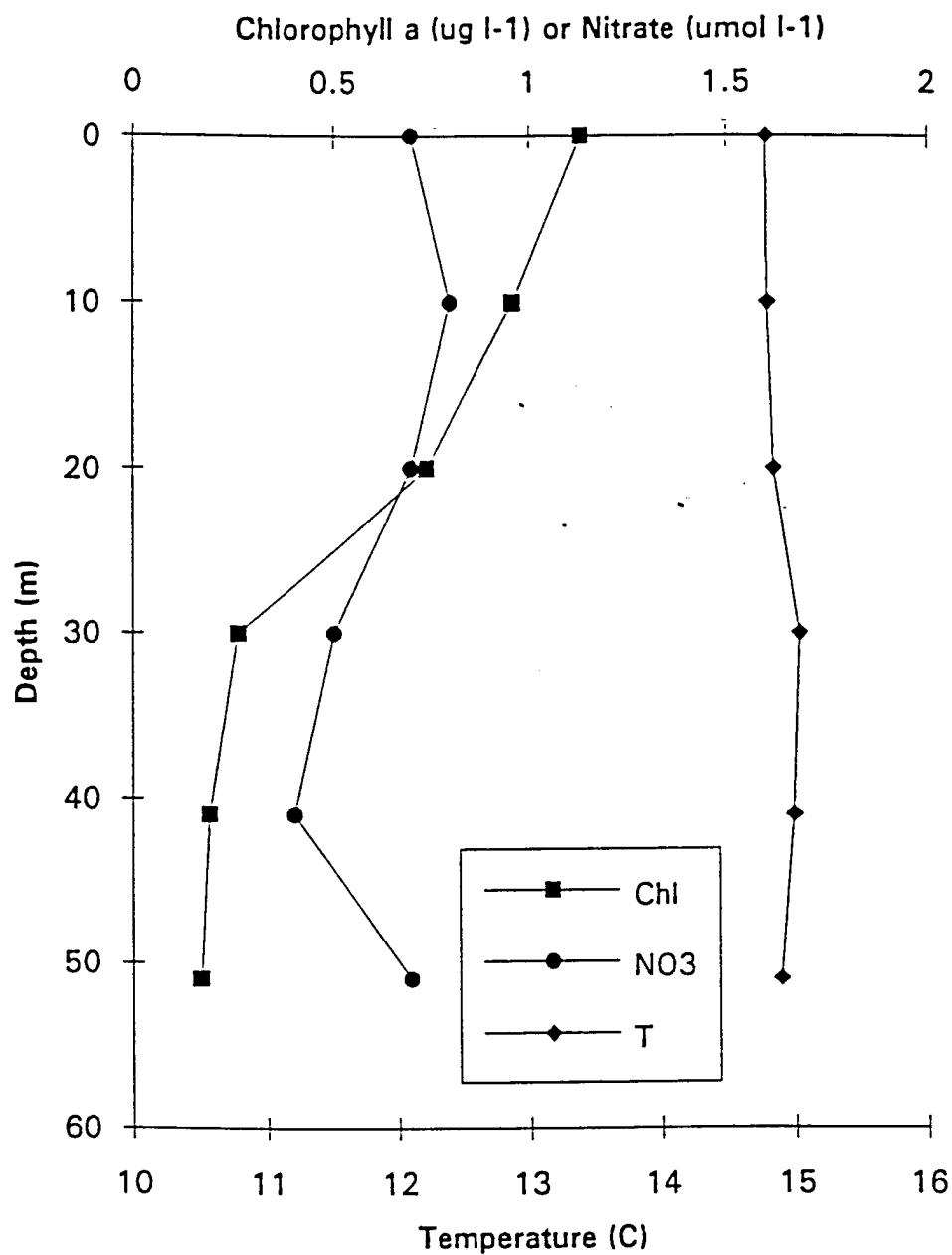


Figure 4-5. Depth profiles of chlorophyll *a* (squares), nitrate (circles), and temperature (diamonds) for 12 Jan 1993 at 32-57.5 N, 117-18.3 W; CalCOFI data, Scripps Institution of Oceanography.

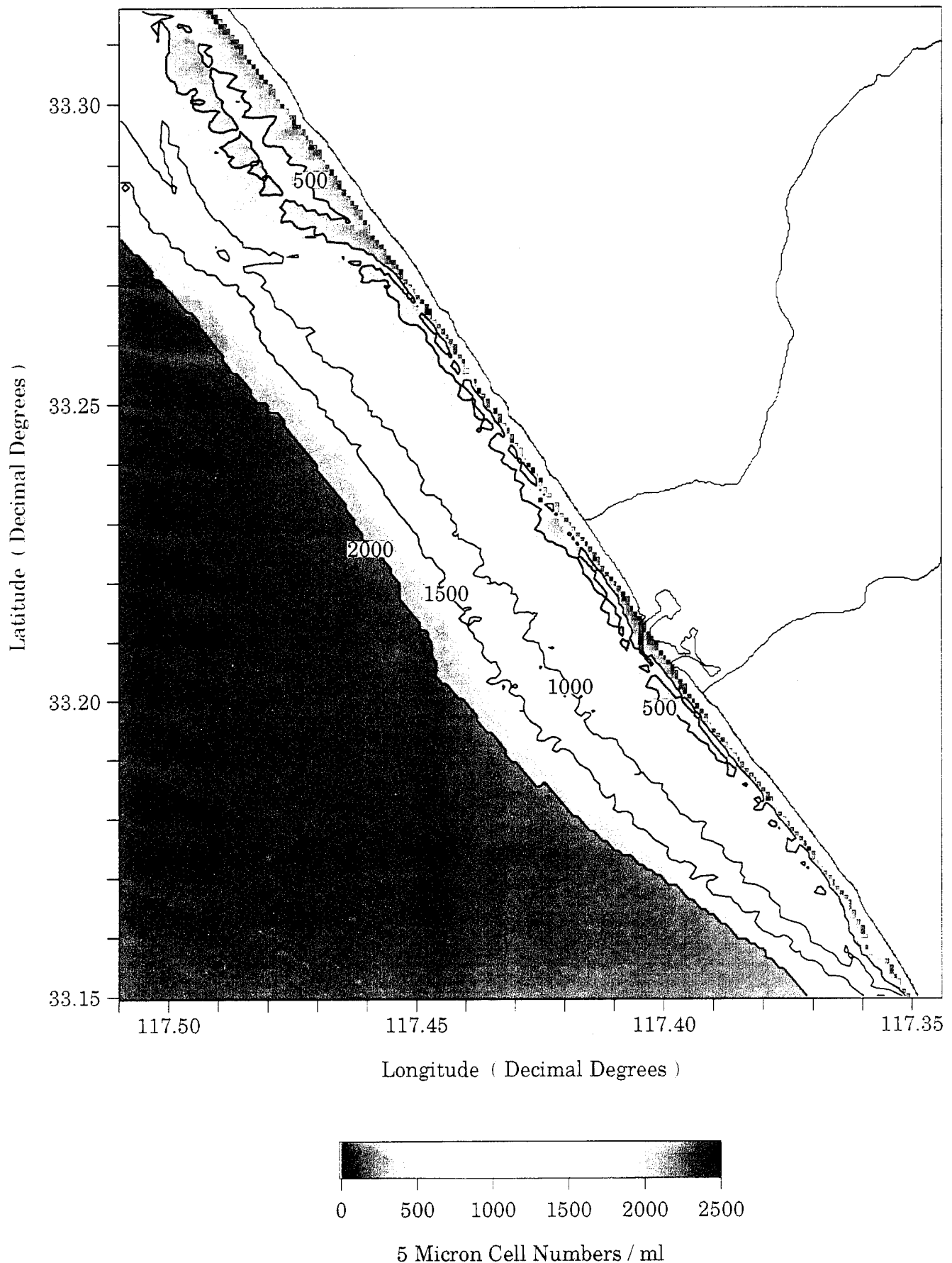


Figure 4-6. Modeled distribution of nanoplankton at 1 m depth at 00:00 on 23 Jan 1993. Initial distribution determined by spatial distribution of *in situ* diffuse attenuation ( $K(\text{PAR})$ ).

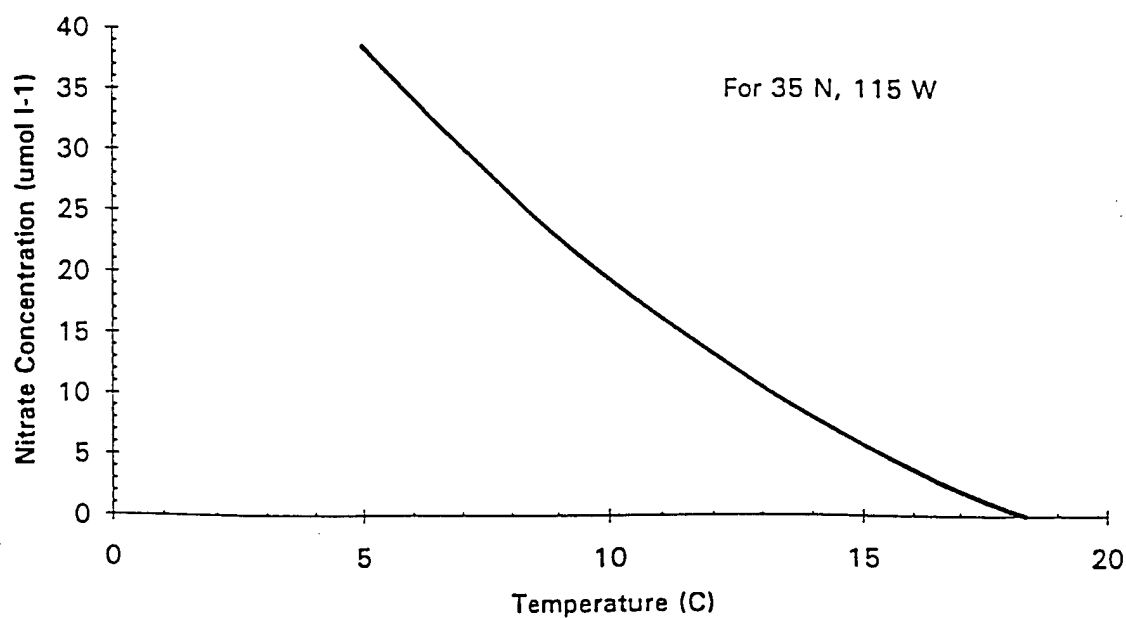
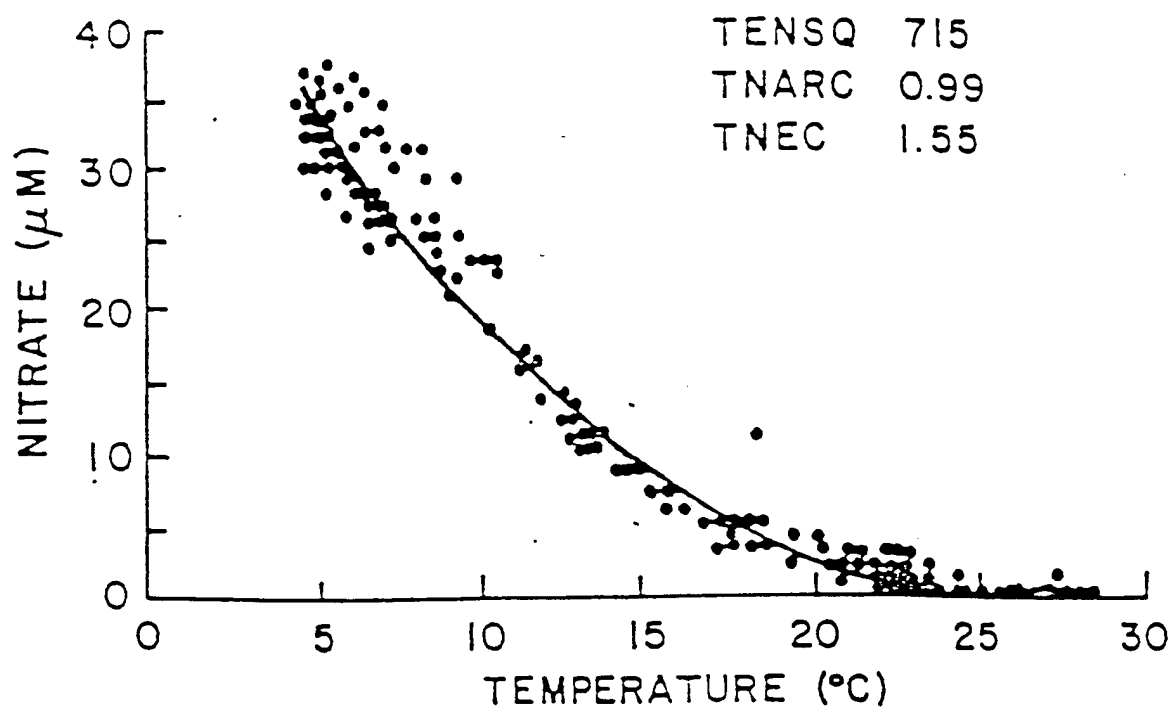


Figure 4-7. Cubic regression fits to nitrate concentration as a function of temperature for a 10-degree square centered on a) 15 S, 123 W (Kamykowski and Zentara, 1986), and b) 35 N, 115 W, which includes the CWC site (Kamykowski, personal communication).



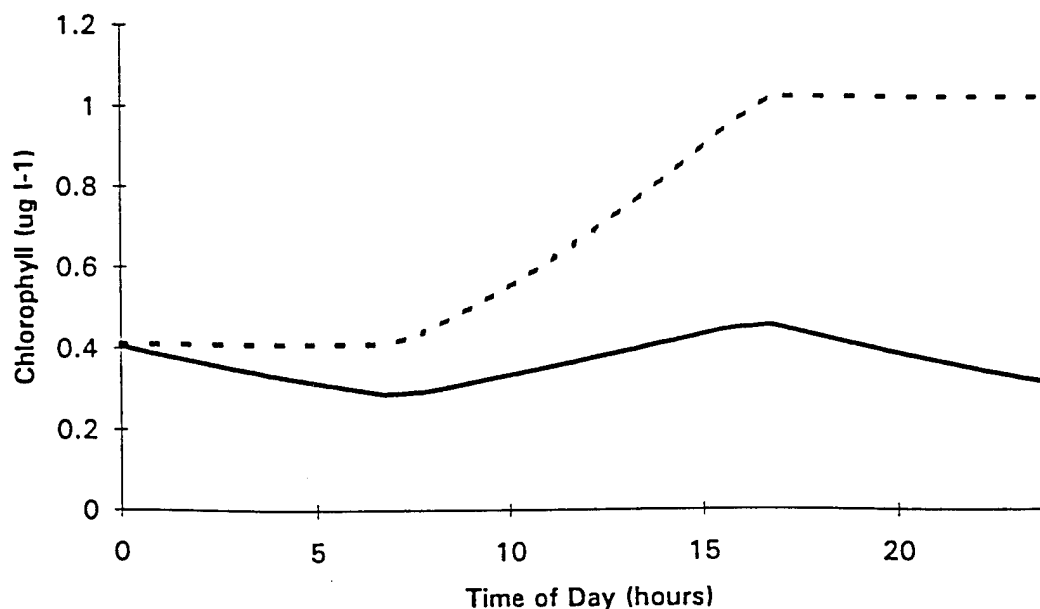
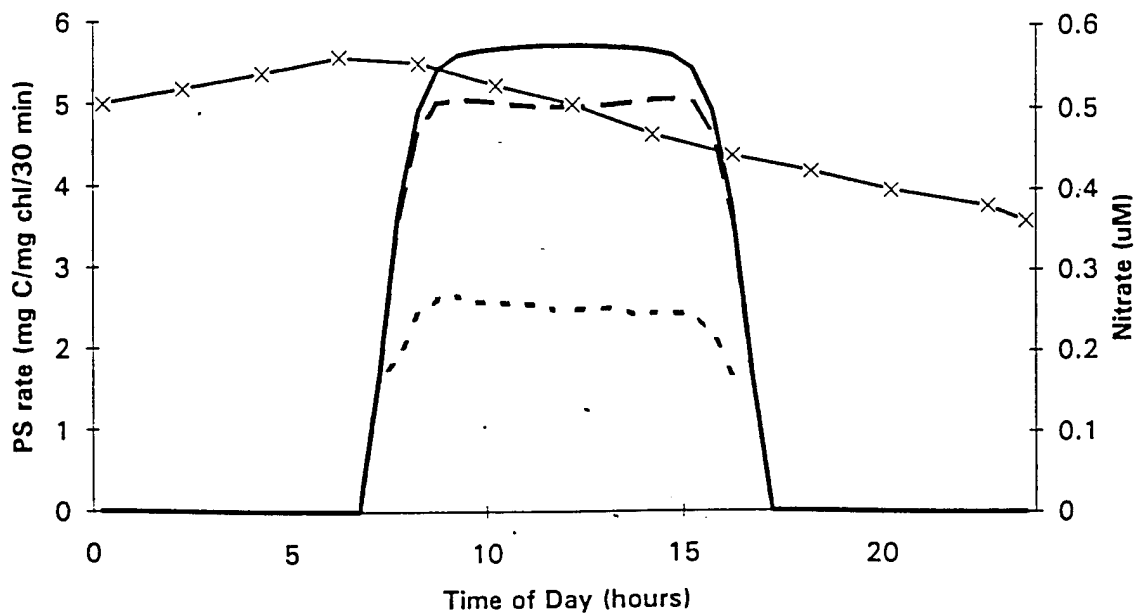


Figure 4-8. a) Photosynthetic rates over 1 day for nanoplankton at 1 m,  $K(\text{PAR}) = 0.20 \text{ m}^{-1}$ , calculated with no photoinhibition and no nitrate limitation (solid line), photoinhibition but no nitrate limitation (dashed line), and both photoinhibition and nitrate limitation (dotted line), and mean nitrate concentration (X); b) Nanoplankton biomass modeled with both local growth and loss terms (solid line) and with growth terms only (dashed lines).

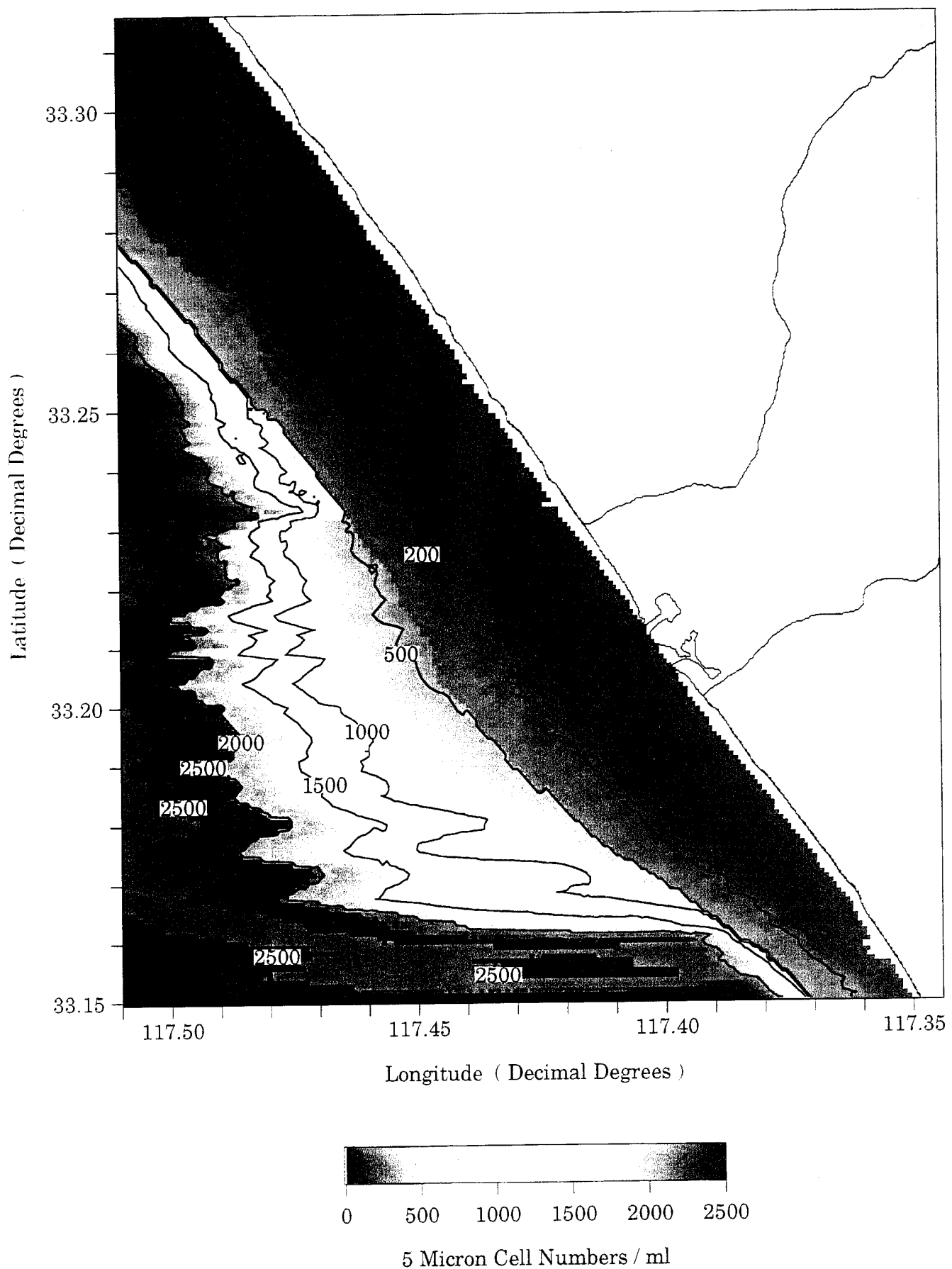


Figure 4-9. Modeled distribution of nanoplankton at 1 m depth at 1400 hours on 23 Jan 1993, at end of BIOMASS module. Local growth and loss have been calculated but mixing has not been calculated.

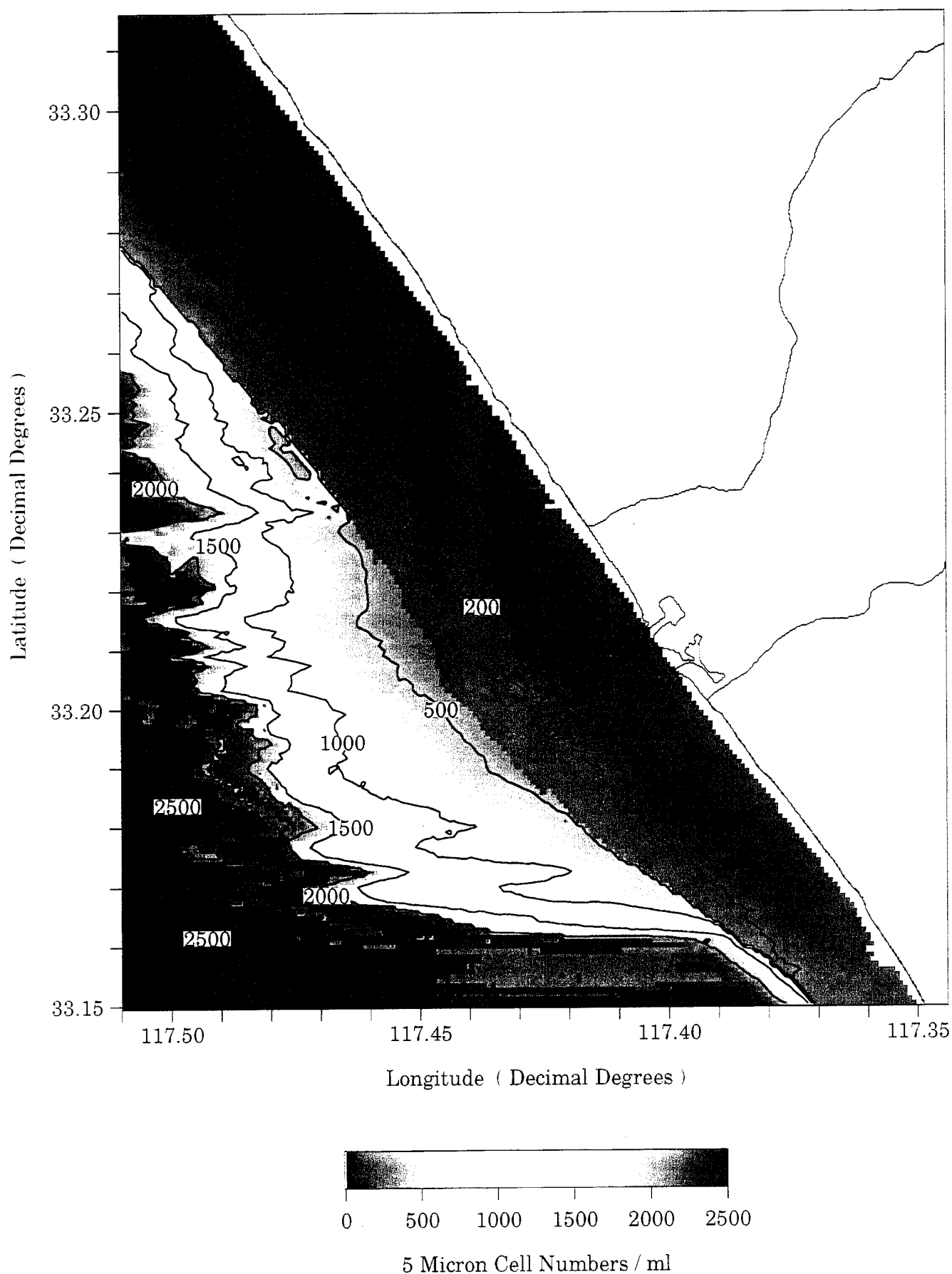


Figure 4-10. Modeled distribution of nanoplankton at 1 m depth at 1400 hours on 23 Jan 1993, at end of BIOXPORT module. Mixing has been calculated.

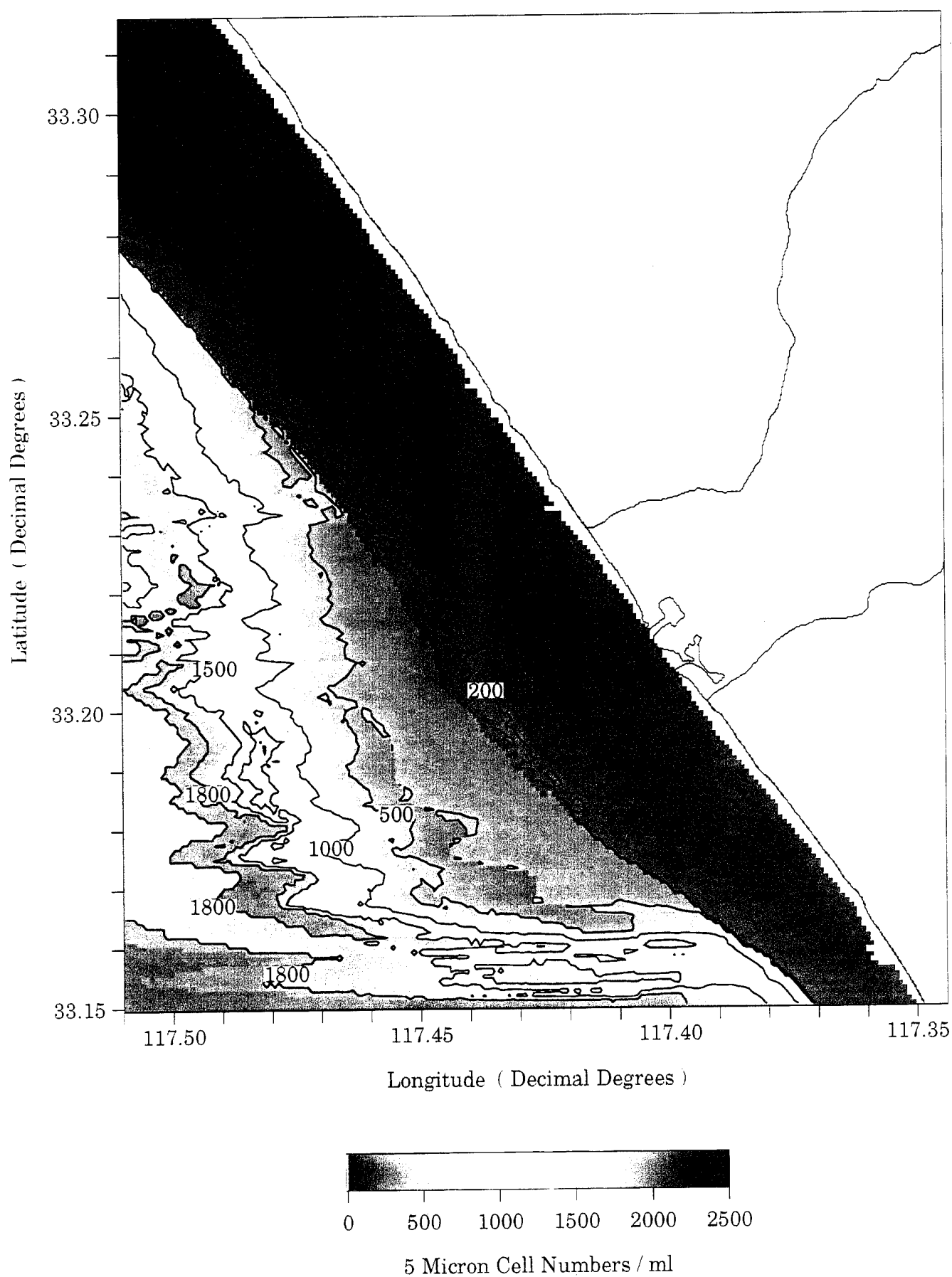


Figure 4-11. Results of full day model run showing distribution of nanoplankton at 1 m depth at 2200 hours on 23 Jan 1993.

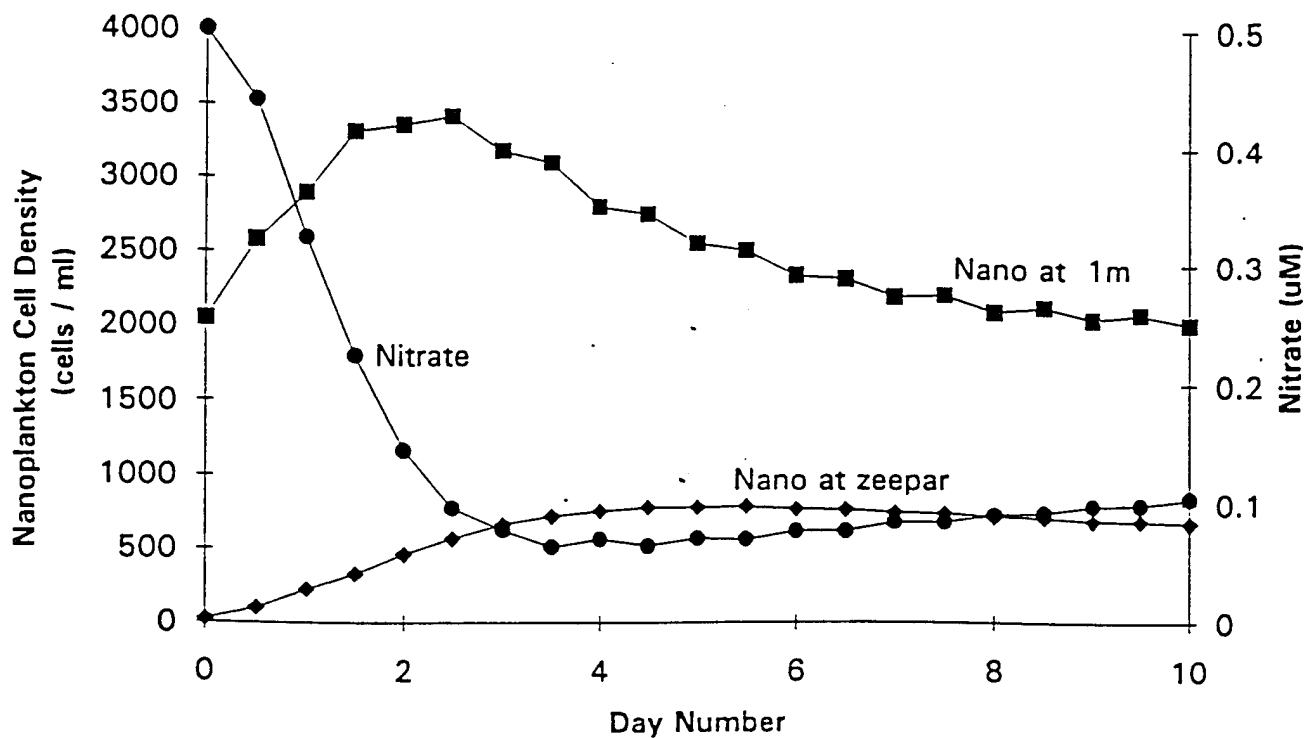


Figure 4-12. Nanoplankton cell numbers at 1 m (squares) and zeepar (diamonds), and nitrate concentrations for 10-day time course.

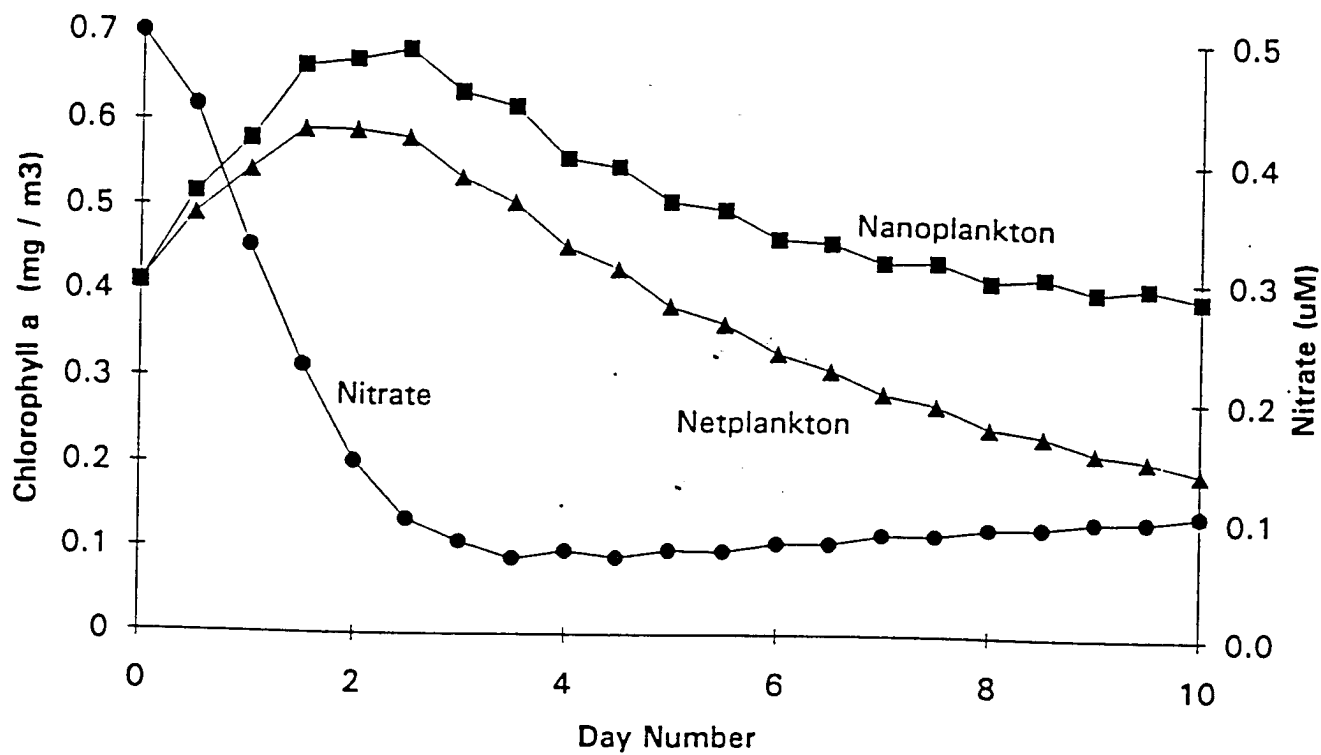


Figure 4-13. Chlorophyll concentration for nanoplankton (squares) and netplankton (triangles), and nitrate concentration (circles) at 1 m for 10-day time course.

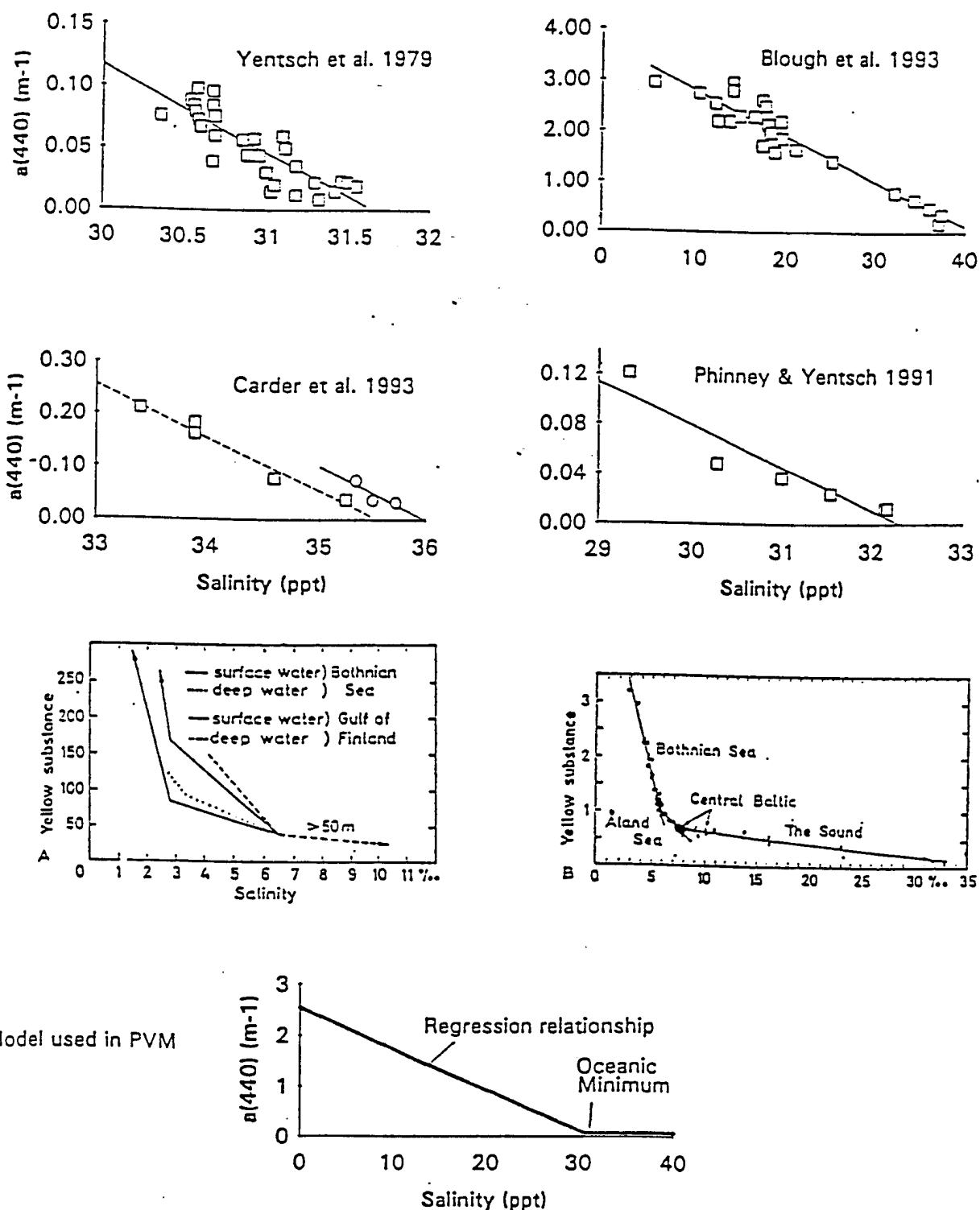


Figure 4-14. Relationship of  $a_{\text{cdom}}(440)$  with salinity for a) the Gulf of Maine; b) the Orinoco River and Gulf of Paria; c) Tampa Bay; d) the Gulf of Maine; e and f) the Baltic Sea; and g) the regression model with seawater end-member equal to 0.07 m<sup>-1</sup>.

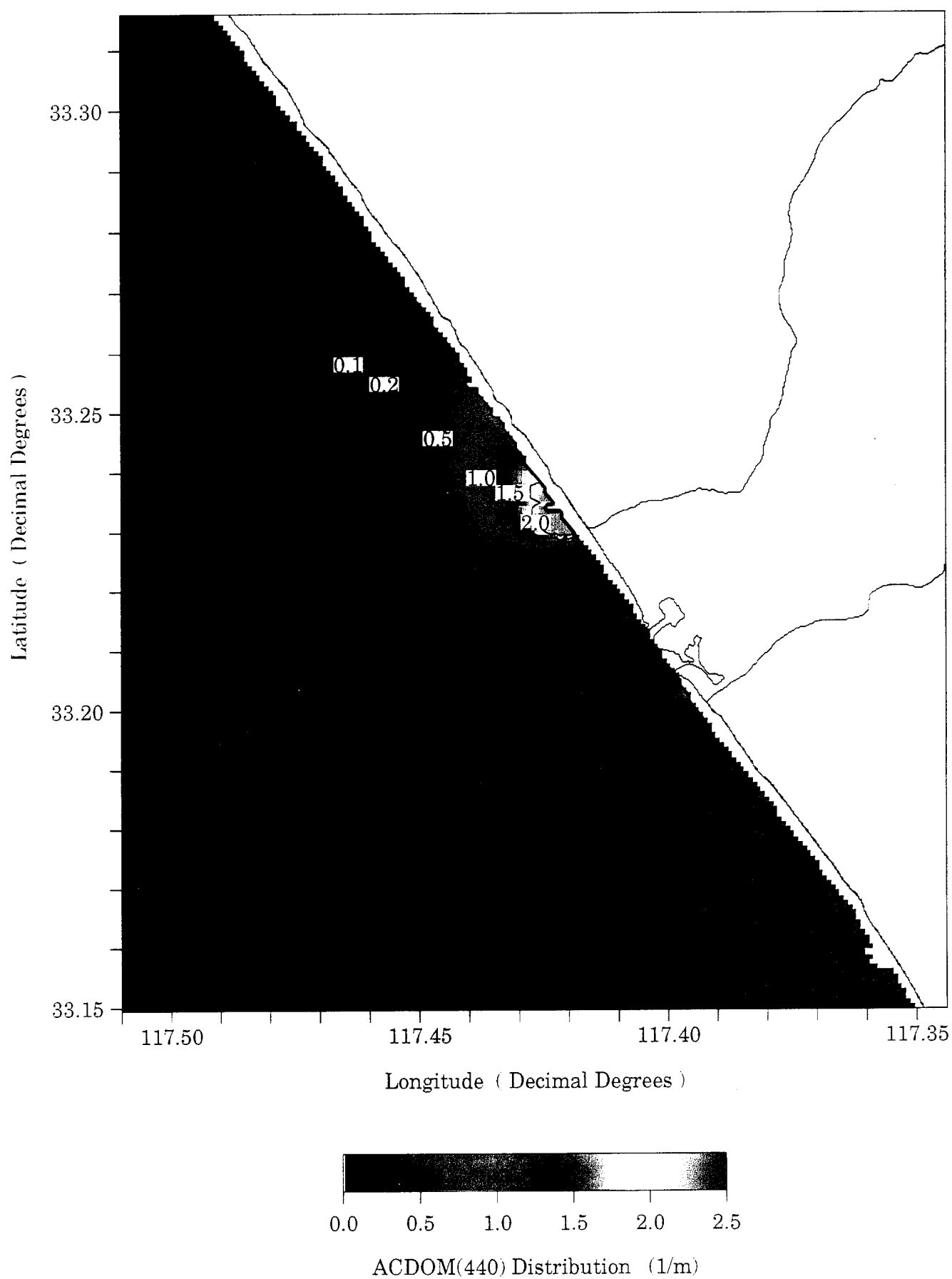


Figure 4-15. Modeled distribution of  $acdom(440)$



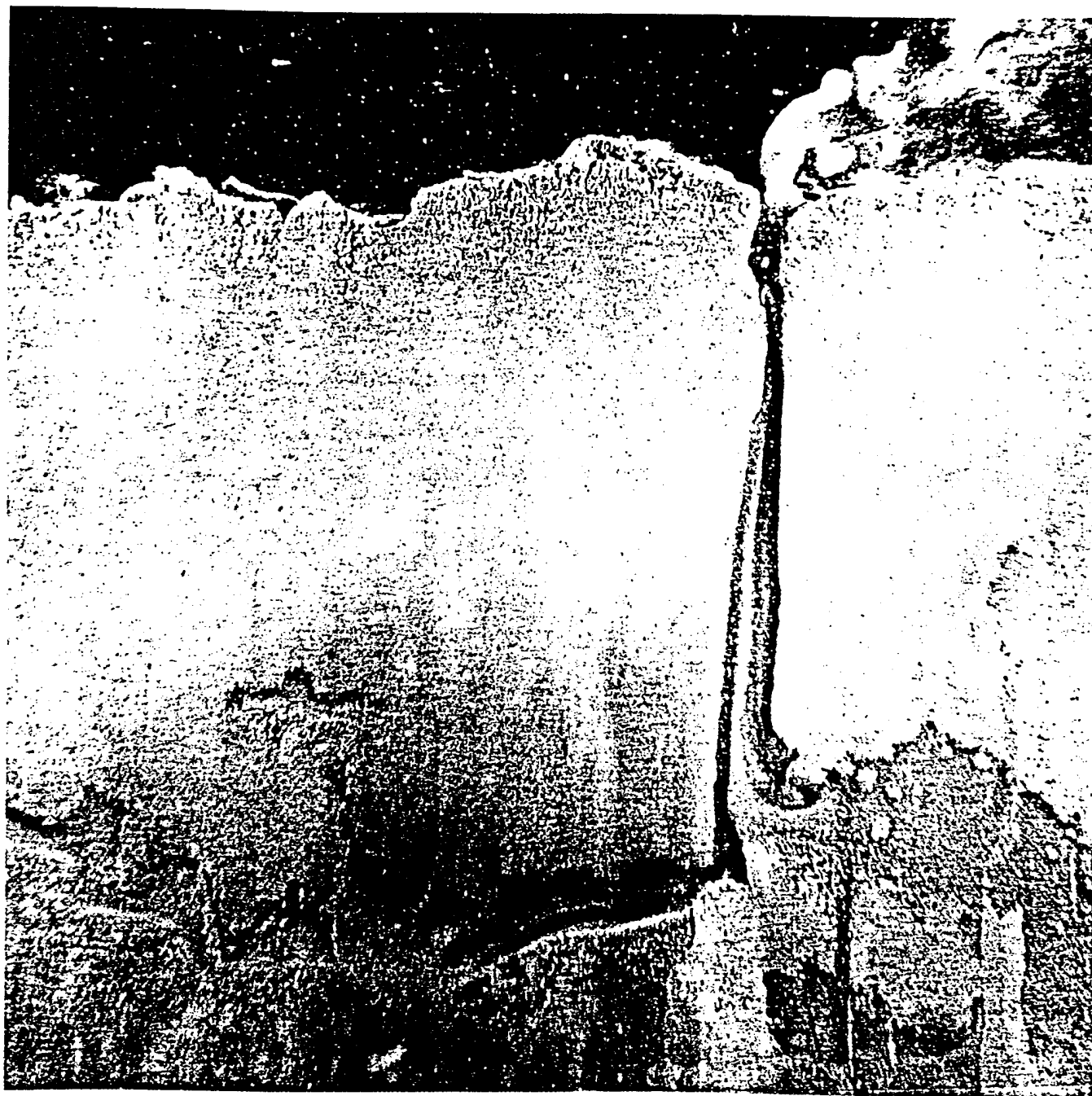


Figure 4-16. Biological sediment resuspension (Klemas et al., 1987)

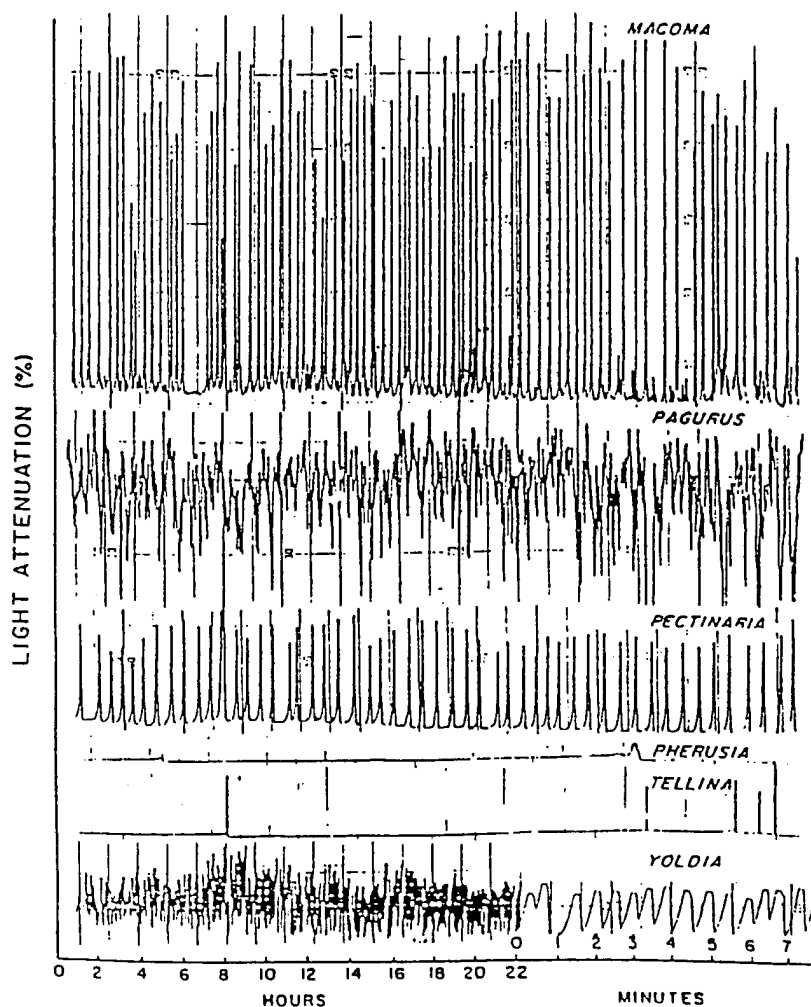


Figure 4-17. Light attenuation variation with bio-resuspension. From Davis, 1993 (Fig. 3). Measurements were made in jars containing single individuals. Peak values represent maximum light attenuation and, therefore, maximum suspended solids concentration. *Macoma*, *Yoldia*, and *Tellina* are bivalves; *Pagurus* is a crab, and *Pectinaria* and *Pherusa* are polychaetes.

Table 4-1. Symbols and units for parameters and variables used in BIOMASS

Symbol	Property	Units
$z$	depth	m
$t$	time	h
$E(z,t)$	irradiance over PAR (400 to 700 nm)	$\mu\text{E m}^{-2} \text{s}^{-1}$
$\tau(\lambda)$	optical depth	nondimensional
$K(\lambda)$	diffuse attenuation	$\text{m}^{-1}$
$i$	phytoplankton size class	no units
$z_{\text{ee}}^{\text{par}}$	depth of 1% light level	m
$PBL(i,z,t)$	light-limited photosynthetic rate	$\text{mg C mg chl}^{-1} \text{h}^{-1}$
$\alpha^B(i)$	light-limited slope of P vs. I relationship	$\text{mg C mg chl}^{-1} \text{h}^{-1} (\mu\text{E m}^{-2} \text{s}^{-1})^{-1}$
$P_{\text{max}}^B(i)$	maximal photosynthetic rate	$\text{mg C mg chl}^{-1} \text{h}^{-1}$
$\beta(i)$	photoinhibition term	$\text{mg C mg chl}^{-1} \text{h}^{-1} (\mu\text{E m}^{-2} \text{s}^{-1})^{-1}$
$V_N(i,z,t)$	nitrate uptake rate	nondimensional
$K_N(i)$	half-saturation constant for nitrate uptake	$\mu\text{mol l}^{-1}$
$PBN(i,z,t)$	nitrate-limited photosynthetic rate	$\text{mg C mg chl}^{-1} \text{h}^{-1}$
$PB(i,z,t)$	final photosynthetic rate	$\text{mg C mg chl}^{-1} \text{h}^{-1}$
$DOM_{\text{phyt}}(i,z,t)$	dissolved organic matter excreted by phytoplankton	$\text{mg C m}^{-1} \text{h}^{-1}$
$\mu(i,z)$	growth rate, integrated over 2 hour time step	$\text{h}^{-1}$
$\theta$	carbon to chlorophyll ratio	$\text{mg C mg chl}^{-1}$
$U_N(i,z,t)$	nitrate uptake rate	$\mu\text{mol l}^{-1} \text{h}^{-1}$
$B(i,z,t)$	biomass	$\mu\text{g chl l}^{-1}$
$I_{\text{nf}}$	nitrate influx concentration	$\mu\text{mol l}^{-1} \text{h}^{-1}$
$A_v$	vertical diffusivity	$\text{m}^2 \text{s}^{-1}$
$N_{\text{deep}}$	nitrate concentration in deep water	$\mu\text{mol l}^{-1}$
$N(z)$	nitrate concentration	$\mu\text{mol l}^{-1}$
$\text{pycno}$	thickness of pycnocline	m
$MLD$	mixed layer depth	m
$r(i)$	respiration rate	$\text{d}^{-1}$
$m(i)$	cell mortality rate	$\text{d}^{-1}$
$G(i)$	grazing rate	$\text{d}^{-1}$
$\text{chlcell}(i)$	cellular chlorophyll <i>a</i> concentration	$\mu\text{g chl cell}^{-1}$
$\text{cell}(i)$	cell number concentration	$\text{cells ml}^{-1}$

Table 4-2a. Values for size-dependent biological parameters  
used in BIOMASS

Parameter	Nanoplankton	Netplankton	Units
cell diameter	5	20	$\mu\text{m}$
$\alpha^B(i)$	0.064	0.050	$\text{mg C mg chl}^{-1} (\mu\text{E m}^{-2} \text{s}^{-1})^{-1}$
$P_{\text{max}}^B(i)$	11.5	8.0	$\text{mg C mg chl}^{-1} \text{h}^{-1}$
$\beta(i)$	0.00175	0.00155	$\text{mg C mg chl}^{-1} (\mu\text{E m}^{-2} \text{s}^{-1})^{-1}$
$r(i)$	$0.10 * P_{\text{max}}(i) / \theta$	$0.10 * P_{\text{max}}(i) / \theta$	$\text{h}^{-1}$
$G(i)$	0.10	0.05	$\text{d}^{-1}$
$\text{chlcell}(i)$	$0.2 * 10^{-6}$	$2.1 * 10^{-6}$	$\mu\text{g chl cell}^{-1}$
$m(i)$	0.01	0.01	$\text{d}^{-1}$
$K_N(i)$	0.5	1.2	$\mu\text{mol l}^{-1}$
$\theta$	50	50	$\text{mg C mg chl}^{-1}$
Sinking rate	0.0001736	0.0009259	$\text{cm s}^{-1}$

Table 4-2b. Values for physical constants assumed in BIOMASS

Parameter	Value	Units
$A_v$	0.0003	$\text{m}^2 \text{s}^{-1}$
MLD	50	m
pycno	5	m
$N_{\text{deep}}$	5.0	$\mu\text{mol l}^{-1}$

Table 4-3. Properties required by phytoplankton BIOMASS prediction module from other parts of the CWC Model or as initial conditions

Property	Units	Source	Data Type
surface irradiance	Watts m <sup>-2</sup>	Lowtran	Variable
diffuse attenuation at 490 nm	m <sup>-1</sup>	Optics Module	Variable
initial nitrate	μmol l <sup>-1</sup>	Archive, Remote Sensing	Initial Condition
initial chlorophyll	μg l <sup>-1</sup>	Archive, Remote Sensing	Initial Condition

Table 4-4. Results of sensitivity analysis for nanoplankton cell numbers at 1 m and zeepar modeled in BIOMASS module. Mean cell numbers were 1192 cells ml<sup>-1</sup> at 1 m and 10.9 cells ml<sup>-1</sup> at zeepar at the end of 24 hours for the standard run.

- 1) % change in parameter calculated as 100\*(modified-standard)/standard.
- 2) RMS difference calculated as  $\left\{ \frac{\sum_m (y_m - \bar{x})^2}{n} \right\}^{0.5}$  where m = cell numbers in successive grid locations and n = total number of grid locations.
- 3) % change in cell # calculated as 100\*(RMS/mean).

Parameter	Modified Value	Change in Parameter	Change in Cell # at 1 m	Change in Cell # at Zeepar
initial chlorophyll	2.0	+100	87	97
initial chlorophyll	0.5	-50	53	50
initial nitrate	1.0	+100	28	0
initial nitrate	0.01	-98	44	0
$\alpha^B$	0.128	+100	6	7
$\alpha^B$	0.032	-50	11	4
$P_{max}^B$	22.0	+91	10	42
$P_{max}^B$	5.2	-55	10	38
$\beta$	0.0035	+100	6	0
$\beta$	0	-100	6	0
C:chl	100	+100	10	27
C:chl	20	-60	23	55
grazing rate	0.6	+200	44	41
grazing rate	0.07	-65	19	17
respiration rate	0.20	+100	41	41
respiration rate	0.005	-50	46	46
mortality rate	0.1	+900	10	10
mortality rate	0	-90	1	0
chl / cell	$0.4 \times 10^{-6}$	+100	55	51
chl / cell	$0.1 \times 10^{-6}$	-50	109	97
$K_N$	1.0	+100	22	0
$K_N$	0.025	-50	84	0
adv	0.003	+900	41	0
adv	0.0006	+100	6	0
adv	0.0001	-67	5	0
deep nitrate	30.0	+500	29	0
deep nitrate	0.50	-90	10	0
MLD	100	+100	4	0
MLD	20	-60	10	0
Redfield ratio	13.2	+100	2	0
K(490)	2 times	+100	43	0
K(490)	half	-50	37	45

Table 4-5. Input to CDOM Model

Property	Units	Source
salinity	ppt	Sedxport
photosynthetic rates	mg C mg chl <sup>-1</sup> h <sup>-1</sup>	Biomass
kelp bed area	m <sup>2</sup>	
bottom depth	m	Isite.grd file

Table 4-6. Parameters in CDOM Model

Parameter	Value	Units
intercept of salinity model	2.266	m <sup>-1</sup>
slope of salinity model	-0.0716	m <sup>-1</sup> (ppt) <sup>-1</sup>
a <sub>cdom</sub> (440) minimum	0.07	m <sup>-1</sup>
specific absorption for CDOM	7.0*10 <sup>-5</sup>	m <sup>2</sup> mg C <sup>-1</sup>
kelp release rate of DOM	29.0	mg C m <sup>-2</sup> h <sup>-1</sup>

Table 4-7. Benthos-water column interactions with potential optical consequences

HABITAT	PROCESS	EFFECT
Tidal Wetlands (Salt marshes, mangroves, seagrasses, mudflats)	Vascular plant fragmentation Reduced water flow  Shading Sediment stabilization by rhizomes Release of tannins, humic substances Suspension feeding (bivalves, tunicates)	Increased turbidity Higher deposition rates, reduced resuspension, longer particle residence Lower phytoplankton production Reduced resuspension, erosion Change in water color Reduced turbidity
Sub-tidal Soft Bottom-Fines	Ejection of feces, pseudofeces  Resuspension of microalgae, bacteria, infauna Suspension feeding (bivalves)  Bioturbation (polychaetes, bivalves, crustaceans, echinoderms) Biogenic structure formation Mass release of larvae	Increased turbidity, light attenuation " "  Reduced turbidity, increased transmission Altered erodibility, stability Altered solute and gas fluxes Altered erodability, stability Turbidity, acoustic targets
Sub-tidal Soft Bottom-Sands	Resuspension of microalgae, bacteria, infauna Nocturnal migration of demersal and benthic forms Suspension feeding (bivalves)	Increased turbidity, light attenuation Acoustic targets  Reduced turbidity
Sub-tidal Hardgrounds, Reefs	Suspension feeding (octocorals, sponges, bryozoans, etc.)	Reduced particulates, turbidity
Kelp Forests	Reduced flow  Shading  Release of dissolved organics Suspension feeding (bryozoans)	Longer particle residence times Higher particulate deposition rate Less sediment resuspension Lower light intensity, phytoplankton production Foam and slick formation Reduced turbidity
Coral Reef	Mass spawning  Nocturnal migration of demersal zooplankton Suspension feeding (corals, sponges, bryozoans, tunicates, crinoids) Shading	Increased turbidity, slick formation " "  Reduced particulates, turbidity  Less light penetration, reduced phytoplankton production



## **5.0 OPTICS MODULE FOR THE PREDICTIVE VISIBILITY MODEL**

### **INTRODUCTION**

Coastal water clarity modeling has the objective of predicting the inherent underwater optical properties required for interpreting the performance of optical systems in the complicated shallow coastal region. It is not expected that predictions for these high sediment (Morel "Case II," 1977) coastal regions will be as accurate as those achievable for extensively studied open ocean waters (Case I), because of the close proximity to a multitude of intense and highly variable constituent sources. The initial goal of the Predictive Visibility Model (PVM) is the prediction of relative and episodic changes in the optical environment. Improvements in absolute accuracy will be sought only after feasibility has been established and the dominant driving mechanisms identified. The computer architecture for the PVM is sub-divided into modules related to: 1) the sources of water column constituents critically affecting optical propagation; 2) the mixing and advection of these constituent concentrations in the dynamic coastal environment; and 3) the scattering and absorption which converts these concentrations into inherent optical properties.

The sources of optical variability are presently limited to sediments, phytoplankton, and colored dissolved organic materials (CDOM). Other source modules may be added for specific locations if they are determined to be significant. The source modules numerically estimate the concentration of these constituents based on geospecific bathymetry/topography and water characteristics, quasi-empirical inputs from contemporary remote-sensing data, and/or climatic observations-forecasts. These estimations are made through a sequence of 2-hour time steps representing fractions of the tidal cycle. The hydrodynamic mixing and advection module estimates the spatial distributions on a nominal 100-meter grid, selected to approximate the scale of available coastal

bathymetry (3 arcseconds). The optical scattering and absorption module uses these inputs to estimate spatially and temporally varying optical properties.

The integrated response of optical properties to principal drivers such as tidal currents, ocean swell, phytoplankton growth, and episodic changes in storm-related land runoff are believed to be within modeling capability. It is essential that all inputs be adequately defined and parametrically investigated to determine their relative effects on optical property estimates. A simplified approach to the PVM utilized the most obvious controlling factors first. The goal was to develop a multi-tiered framework for testing interactions and alternative approaches. This provides a continually improving model in an evolving state of sophistication. The optical scattering and absorption modeling procedures and assumptions are described in terms of preliminary laboratory experiments (Schoonmaker et al., 1994). This approach provides a baseline for generic classification of water constituents applicable for the very nearshore area (0-100 meters). Laboratory and *in situ* optical and constituent concentration measurements are compared with modeled values to give a preliminary demonstration of optical coefficient prediction capability.

## **5.1 Optics Module Development**

A high discrimination technique must be used to account for the space and time dependence of optical properties on constituents in the coastal water column. It has been hypothesized, but not conclusively demonstrated, that optical properties of individual constituents can be linearly combined to estimate the optical properties of diverse mixtures. The separation is important due to the necessity to independently model the generation of additive sources to describe individual concentrations within the mixture. Initial input parameters for the optics module include sediment and phytoplankton concentrations, and a single absorption at 440 nm for the CDOM. These concentrations are characterized in terms of

variable size distributions and indices of refraction for similar particle groupings. Using these input parameters, absorption and scattering coefficients for the assemblage are determined along with the angular scattering dependence. This is done through the use of the Mie theory of light scattering by small particles (van de Hulst, 1981).

In order to apply Mie theory to particles of all sizes, it will be necessary to assume that the particles are either spherical in shape or that their effect on light can be described using an "equivalent spherical diameter." This assumption has been used extensively in the literature and has been supported by experimental verification of Mie theory with a number of different types of solid crystalline materials in suspension, and does not lead to serious error (Burt, 1952; and Kirk, 1981). With this in mind, the particles in suspension are considered as a dispersoid of equivalent spheres of varying sizes with a single complex index of refraction adjusted to produce angular volume scattering compatible with measured data. Another restriction is that the number concentration of particles must be low enough to justify use of a single scattering model; this assumption can be tested by evaluating linearity as concentrations increase in the laboratory. While descriptions of these procedures abound in the literature (Brown & Gordon, 1974; Morel, 1975; and Kitchen & Zaneveld, 1992), the single scattering assumption could become restrictive in turbid coastal regimes. However, at the point when multiple scattering and shadowing become important, the optical properties will already be outside the range of immediate interest. The assumptions that have been mentioned allow an exact solution for absorption and scattering cross sections which includes scattering angle-dependence using only a few input parameters.

A comprehensive data set is required to validate this procedure. There is an absence of this concurrent data which should include: segregated particle size distributions for plankton and sediments, CDOM concentrations, segregated optical absorption and scattering coefficient measurements, and  $0^{\circ}$ - $180^{\circ}$  volume scattering function measurements. Because of this, laboratory measurements and a limited coastal data set

were used together with Scripps Visibility Laboratory data (Petzold, 1972) for the parametric trade-offs presented here. The laboratory measurements and procedures are described in Schoonmaker et al., 1994.

Water samples consisting of various mixtures of phytoplankton, sediment, and filtered seawater were prepared and analyzed in the laboratory. The samples included phytoplankton and sediment concentrations characteristic of nearshore coastal waters. For each sample, the number of suspended particles and their size distribution were measured before and after mixing, along with their inherent optical properties. Using the measured particle data and the known concentrations of phytoplankton and sediment as inputs to the optical model, the inherent optical properties were calculated and compared with the measured values to develop a set of spectral calibration coefficients. The scattering and absorption contributions for pure ocean water (Smith & Baker, 1981) were initially removed to simplify absorption data comparison and reintroduced in the final coefficient calculations. Selected spectral values for coefficients of pure ocean water are presented in Table 5-3.

## 5.2 Particle Size Distribution

The particles which occur in natural waters have a continuous size distribution which is roughly hyperbolic; the number of particles being defined in terms of the total number,  $N_l$ , with diameter greater than  $d > 1$ , as shown in Equation (1) (Junge, 1963; and Bader, 1970). The exponent,  $\gamma$ , is constant for a particular body of water, but varying between 0.7 to 6.0 for different water bodies (Kirk, 1983). The constants  $N_l$  and  $\gamma$  are herein referred to as the "concentration" and "slope," respectively. This is done because they are routinely plotted as cumulative number concentrations versus particle diameter on log-log scale where gamma is the slope. Morel (1975) suggests a value of  $\gamma > 3$ , and Apel (1987), an average of 2.5 for offshore ocean areas. Different values are expected near the coastline due to the variety of particulate sources and increasing particulate size. Temporal changes in particulate concentration on the order of a factor of

ten routinely follow the shallow water tidal current cycle (Joseph, 1955; & Jenkins et al., 1981). These tidally driven particulate variations can dominate visibility distance and therefore represent a critical planning factor for many subsurface applications.

$$N = N_1 d^{-\gamma}, \quad \gamma = 0.7 \text{ to } 6.0 \quad (1)$$

A hyperbolic distribution predicts many more small particles than large ones, however, their summed interaction cross sections are small. Large particles have large summed interaction cross sections but, due to the hyperbolic distribution, are typically smaller in number. Thus, intermediate-sized particles, with diameters between 1  $\mu\text{m}$  and 5  $\mu\text{m}$ , can dominate the scattering process (Jerlov, 1976; and Morel, 1975). The slope,  $\gamma$ , and concentration,  $N_1$ , are the parameters supplied by the source models which must be experimentally determined for optical model calibration. A value of  $\gamma = 2.1$  was derived by fitting the scattering model described below to Petzold's volume scattering function measurements (1972). This slope value appears appropriate for a wide range of offshore coastal waters when compared to his data. Indeed, most measurements for coastal waters produce values over 2.0. Further offshore, higher values are expected where number concentrations are dominated by sub-micron particulate, and phytoplankton in the low to sub-micron size range. Open ocean optical properties are primarily responsive to the phytoplankton, detrital fragments, and particles from terrestrial runoff small enough to remain suspended over long periods, i.e., slow settling velocities. Whereas, nearshore areas exhibit an increasing particulate size due to the proximity of the sources of rivers, surf, and bottom resuspension. Phytoplankton typically increase in size (Gregg & Walsh, 1992) which is a response to proximity to nutrient sources.

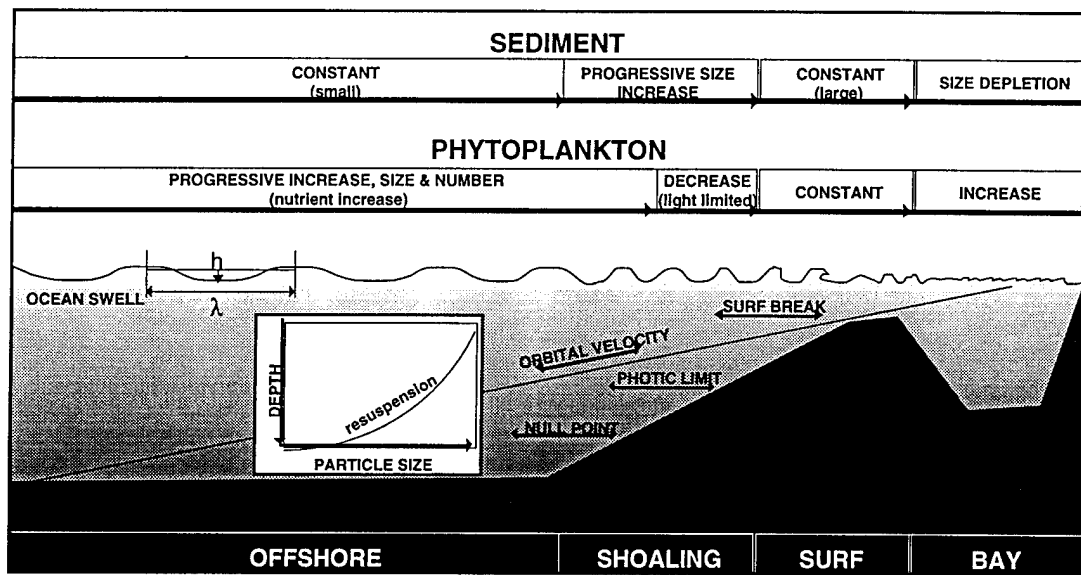


Figure 5-1. Hypothetical sublittoral particle size distribution trends

As shoreline particulate sources are approached, the number concentration is expected to shift toward larger sediment particles (Figure 5-1). Bottom resuspension creates a continuous source of sediments as the nearbottom components of tidal current and surface wave orbital velocities exceed the "Shields" entrainment criterion (Dyer, 1986), which is dependent on grain size and the density. This is labeled the Null Point in Figure 5-1. The largest sediment particles quickly fall out and are absent further off shore because of their higher settling velocities (Sverdrup, et al., 1942). However, particles below the size parameter of  $1.0 \mu\text{m}$  have small settling velocities (Table 5-1), with the size parameter being defined as  $k = d/2\lambda$ . These velocities are on the order of 1.0 mm to 7.4 cm per day for particles in the range of  $0.1 \mu\text{m}$  to  $1.0 \mu\text{m}$ , with the effects of local turbulence and density gradients reducing the settling rate even further. A certain amount of the extremely fine-grained particles may be formed in the sea, but probably most of it comes from land, where the agencies of mechanical and chemical weathering are much more effective, i.e., rivers, rainwash, shoreline erosion, terrestrial winds, volcanic activity, glacier, etc..

Table 5-1. Settling velocity of quartz spheres in distilled water at 20°C, (Sverdrup et al., 1942)

	Particle Diameter	Size Parameter	Time to Fall 10cm				Settling Velocity
	( $\mu\text{m}$ )	$k_{530}$ ( $\mu\text{m}$ )	(days)	(hours)	(minutes)	(seconds)	(m/day)
clay	0.12	0.11	87	3	19		0.001
	0.25	0.23	21	18	50		0.004
	0.49	0.45	5	10	42		0.018
	0.98	0.91	1	8	41		0.074
	1.95	1.81		8	10		0.3
silt	3.9	3.9		2	2	32	1.2
	7.8	7.2			30	38	4.7
	15.6	14.5			7	40	18.8
	31.2	29			1	55	75.2
	62.5	58				29	301
very fine sand	125	116				8.3	1040
fine sand	250	232				2.7	

In locations where rivers and coastal runoff sources are present, a continuous sequence of point and surf-energy modulated sources exist which reduce  $\gamma$  as the bottom or surfzone are approached; surf break line (Figure 5-1). In fetch-limited waters such as quiescent bays, these trends may reverse in favor of smaller sediments due to decreased resuspension and diffusivity.

Simultaneously, the relative abundance of nutrients increases the phytoplankton size as the coastline is approached (Gregg and Walsh, 1992), but this increase can be reversed at the photic limit as subsurface photosynthetically available radiation (PAR) dwindles, due to the increased particulate attenuation (Figure 5-1). This increase would also reduce  $\gamma$  while increasing the biological fraction of the particulate concentration,  $N_I$

Our best fit to Petzold's,  $\beta(\theta)$ , measurements was with a slope of  $\gamma = 2.1$  and an index of refraction of  $\eta = 1.2 - j0.015$ . This fit to selected water types will be discussed in the particulate scattering Section 5.3.1. Since this includes offshore measurements where large particulate is diminished as well as more turbid San Diego Bay water, it will be assumed that this  $\gamma$  value can be used to maintain a coastal ocean background level

for the 0.1  $\mu\text{m}$  - 1.0  $\mu\text{m}$  particle size decade. Therefore, the distribution used in future model calculations will employ a modified hyperbolic distribution which maintains a  $\gamma = 2.1$  in the lower decade of the particle size distribution, while allowing the second and third decades to vary as described by the sediment transport modules. It is important to maintain a background level of these small particles because of their importance to optical backscatter.

Plots were constructed of the volume scattering function for each particle size decade and their sum. This was done for three  $\gamma$ 's of 1.0, 2.1, and 3.0, while holding  $N_I$  constant at 1000 particles. The plots (Figure 5-2) demonstrate the shifting of importance of each size decade to particular scattering angles. The large particle size decade from 10  $\mu\text{m}$  - 100  $\mu\text{m}$  dominates the forward scatter for all values of  $\gamma$ . However, the relative scattering effectiveness is reduced as  $\gamma$  increases, which is simply due to the decrease in the number of larger particles. In the backscatter region, particle sizes of 0.1  $\mu\text{m}$  - 1.0  $\mu\text{m}$  and 1.0  $\mu\text{m}$  - 10  $\mu\text{m}$  are important at all  $\gamma$ 's, but increasingly so at larger slopes. Hyperbolic distributions are parameterized (Equation 1) in terms of the number of particles greater than 1.0  $\mu\text{m}$ ,  $N_I$ . This creates a hinge point that increases the number of particles less than 1.0  $\mu\text{m}$ , if the slope is allowed to increase. The resulting backscatter would be driven to unrealistically high values due to the dominance by the smallest particles. Inversely, when  $\gamma$  is decreased by the addition of larger particulate, the backscatter would be underestimated.

### 5.3 Optical Property Estimation Procedures

The calculation of optical properties splits naturally into absorption, scattering, and backscattering calculations for sediment and phytoplankton designated by the customary interaction coefficients:  $a_{sed}$ ,  $a_{bio}$ ,  $b_{sed}$ ,  $b_{bio}$ ,  $bb_{sed}$ , and  $bb_{bio}$ . The method used to calculate these parameters employs Mie scattering calculations for suspended particles along with calibration coefficients. The calibration coefficients  $A_{sed}$ ,  $A_{bio}$



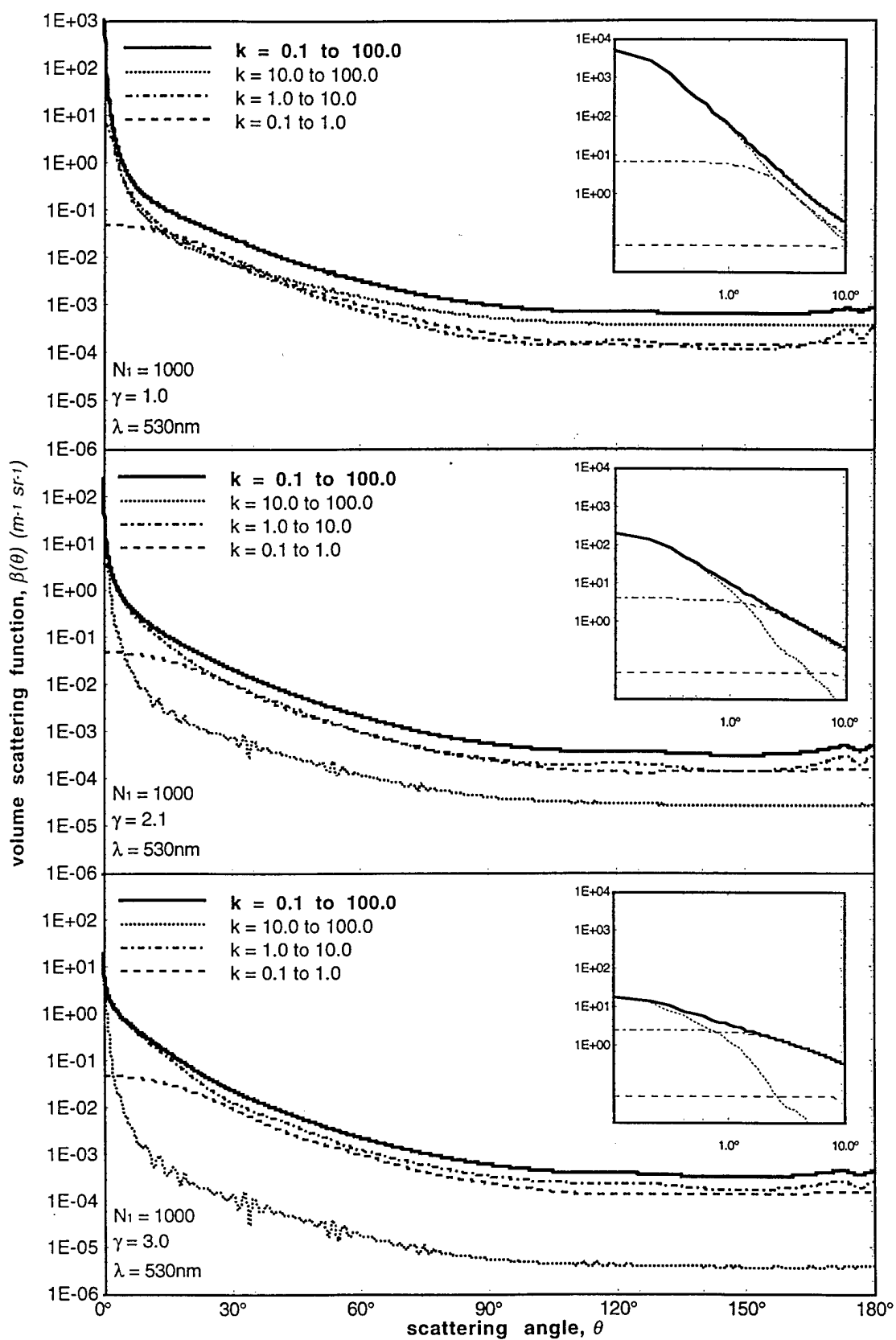


Figure 5-2. Volume scattering as functions of index of refraction and size parameter bin

and  $B_{sed}$ ,  $B_{bio}$ , are applied to the modeled coefficients to obtain the absorption coefficients  $a_{sed}$  and  $a_{bio}$  and the scattering coefficients  $b_{sed}$ ,  $bb_{sed}$ ,  $b_{bio}$ ,  $bb_{bio}$  for the sediment and biological water constituents, respectively.  $a_{sed}$  and  $a_{bio}$  are summed to give particulate absorption and  $b_{sed}$  and  $b_{bio}$  are summed to give particulate scattering. The particulate values are then combined with their corresponding clear seawater (Smith and Baker, 1981) and CDOM values as appropriate.

$$a(\lambda) = a_{sed}(\lambda) + a_{bio}(\lambda) + a_{water}(\lambda) + a_{CDOM}(\lambda) \quad (2)$$

$$b(\lambda) = b_{sed}(\lambda) + b_{bio}(\lambda) + b_{water}(\lambda) \quad (3)$$

$$bb(\lambda) = bb_{sed}(\lambda) + bb_{bio}(\lambda) + bb_{water}(\lambda) \quad (4)$$

The process requires laboratory and coastal measurements to determine the calibration coefficients for generic types or assemblages of optically significant constituents. In this way, they can be applied for predictions in "similar" coastal regions (Schoonmaker et al., 1994). Five geologically similar classifications of sediment constituents,  $j$ , are envisioned for the PVM, along with a yet to be determined number of biological classifications,  $i$ . Biological classifications might cover generic chlorophytes, chromophytes, and cyanobacteria, for example. Different species could also be combined depending on the precision required for a specific application. However, at any given time, one phytoplankton species is usually dominant, while another is fading and still another is beginning to bloom. Any one of a number of species can be dominant, (Duntley et al., 1974). A generic species may prove to be the most logical selection simply due to the turnover of specific dominant species. Initial calibrations for just one sediment category ( $j=1$ ) and one biological category ( $i=1$ ) are provided here.

The CDOM values used are calculated spectrally using Equation (5a) in terms of a single parameter,  $DOM_{440}$ , the absorption at 440 nanometers. The exponential dependence is included as a spectral calibration coefficient,  $[A_{DOM}]$  in Table 5-3, to illustrate the relative effect for selected wavelengths. Equation (5b) provides an estimate of the diffuse attenuation coefficient, an apparent optical property required for biological growth in PVM water constituent source models. This expression was developed specifically for turbid waters, using Petzold's San Diego Bay volume scattering data (Kirk, 1981).

$$a_{CDOM}(\lambda) = DOM_{440} \exp[-0.014(\lambda - 440)] \quad (5a)$$

$$k(\lambda) = [a(\lambda)^2 + 0.256a(\lambda)b(\lambda)]^{1/2} \quad (5b)$$

### 5.3.1 Particulate scattering

Petzold (1972) provides the most comprehensive and most quoted angular scattering data ( $\beta(\theta)$ ) available in the literature. Figure 5-3 shows Petzold's data for eight locations normalized by their respective scattering coefficients,  $b$ , to produce a normalized volume scattering function independent of particulate concentration.

At most, these curves deviate by a factor of  $\pm 2.5$ , predominantly at small forward angles, and, more broadly, in the backscatter direction in response to changes in the slope of the particle size distribution. This agreement seems somewhat amazing since the data cover extreme differences in water types from a shallow enclosed bay to clear deep ocean water.

Mie theory provides the solution for the scattering matrix of homogenous spheres in the form of two complex amplitude functions,  $S_1(\theta)$  and  $S_2(\theta)$ , of an axially symmetric scattering angle,  $\theta$ , (Hansen and Travis, 1974). These functions involve spherical Bessel functions which are

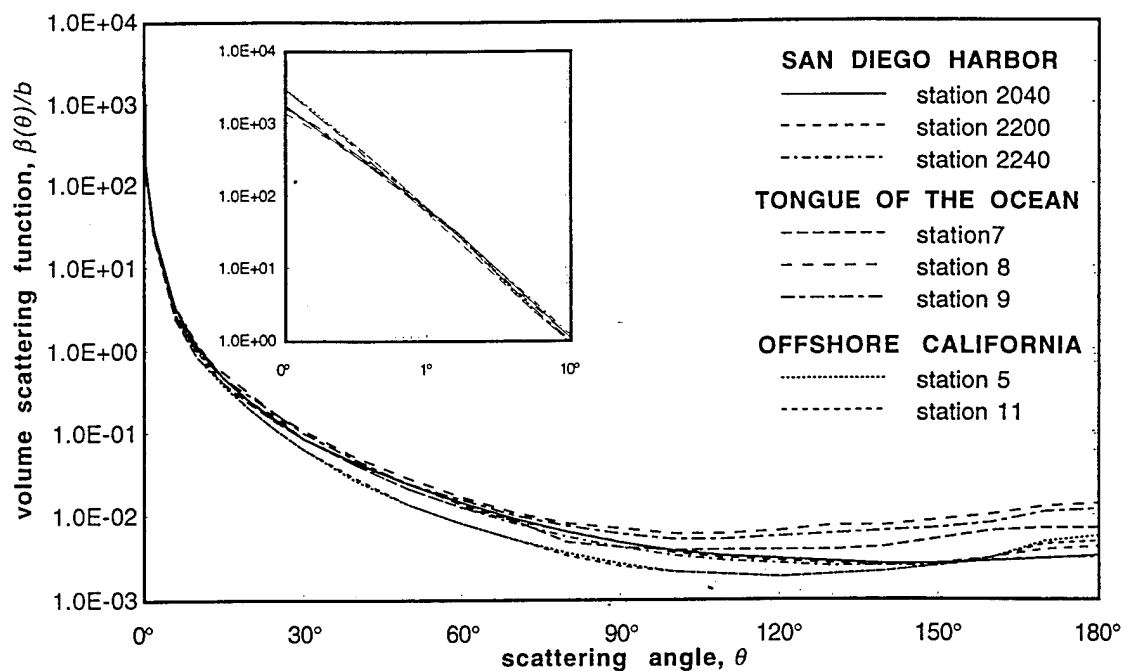


Figure 5-3. Concentration independent volume scattering functions normalize to  $b$  for various waters

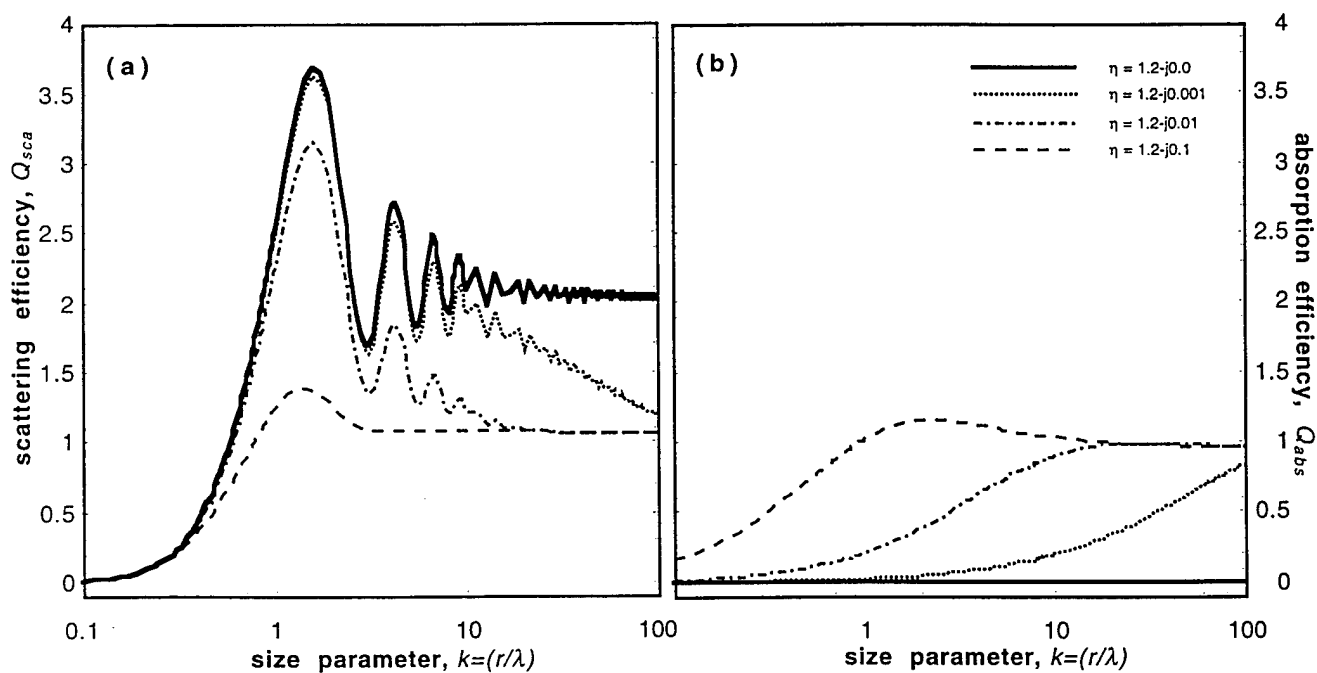


Figure 5-4. Efficiencies vs. particle size for a) scattering, and b) absorption

computed using recursion relationships (van de Hulst, 1957). The functions,  $S_1(\theta)$  and  $S_2(\theta)$ , provided by the Mie code are, in turn, used to calculate the directional scattering function,  $\beta(\theta)$ , and the spectral absorption and scattering coefficients,  $a_{model}$  and  $b_{model}$ , in terms of a non-dimensional parameter,  $k = r/\lambda$ , where  $r$  is the equivalent spherical radius and  $\lambda$ , the optical wavelength. The size parameter factor of  $2\pi$ , used in the Mie calculations, has not been included in plots to facilitate comparisons. The scattering model integrates bulk particles over three decades of  $k$ , covering particle sizes from  $0.1\lambda$  to  $100\lambda$ , roughly  $0.05$  to  $50 \mu\text{m}$ , using a particle size distribution parameter,  $2k = \text{diameter}/\lambda$ . Phytoplankton cell scattering and absorption are treated as discrete particle sizes independently.

Scattering efficiency,  $Q_{sca}$ , and absorption efficiency,  $Q_{abs}$ , for dielectric spherical particles as a function of  $k$ , are shown in Figure 5-4, with the imaginary part of the index of refraction,  $\eta''$ , as a parameter. Scattering efficiency is multiplied by geometric cross section,  $\pi r^2$ , to obtain interaction cross section. For the transparent sphere case, with the imaginary part of the index of refraction equal to zero, the scattering efficiency oscillates above  $k = 1$ , due to interference between the diffracted and transmitted light, and approaches a value of two as  $k$  increases. As the absolute value of the imaginary component increases, the oscillation is damped and the value tends to 1.0 as particle size increases. This is because the imaginary part corresponds to the internal absorption,  $a_{int}$ , of the particle substance as given by  $\eta'' = a_{int}\lambda/4\pi$  (van de Hulst, 1957), which, when totally absorbing, leaves only the diffractive interaction contribution to the cross section. The real parts of indices of refraction reported in the literature for the water to quartz interface are  $1.15 < \eta' < 1.2$ , and values of  $\eta''$  vary between 1.005 and 1.03 for the water to chloroplast interface. The imaginary indices are expected to vary with outer shell thickness, and the location and amount of chlorophyll in the cell. Since these terms also vary with cell size (Beardsley et al., 1970), species, and ambient light, variable imaginary parts were used in the spherical model, both with and

without concentric shells, in order to achieve agreement with available absorption measurements.

Figure 5-5a shows data for San Diego Harbor and offshore California, and Figure 5-5b, the mean and standard deviation of five of Petzold's volume scattering curves, selected for near coastal water characterization, along with the modeled Mie scattering approximation. Efforts to fit the Mie scattering model output to the shape of Petzold's data for shallow waters (Figure 5-5a) using plausible values for the particle distribution parameters and the refractive index followed the approach of Morel (1975) and Brown and Gordon (1974). This effort involves only three variables since varying the concentration,  $N_l$ , simply moves the scattering curve up and down in amplitude without altering its shape. The volume scattering functions have been normalized to the scattering coefficient,  $b$ , to provide a means of comparison. The parameters which control the shape of the function are the slope,  $\gamma$ , of the size distribution discussed above and the real and imaginary coefficients of the refractive index,  $\eta = \eta' - j\eta''$ . These parameters were investigated over the range of values quoted in the literature. The fit to the coastal volume scattering data, including measurements inside San Diego Bay (Petzold, 1972), is shown in Figure 5-5b. Petzold's measurements were all made at 530 nm.

This fit was achieved using  $\gamma = 2.1$  and  $\eta = 1.2 - j0.015$ . The imaginary index required for a smooth match over the backscatter region gives rise to a high particulate absorption. If a smaller, more realistic, imaginary part of the index of refraction is used, forward scattering can be modeled, but the backscatter displays the rainbow ( $120^\circ$ - $130^\circ$ ) and glory ( $180^\circ$ ) effects (Figure 5-6), which results from the use of perfect spherical shapes when particles are larger than  $\lambda$ , (Hansen and Travis, 1974).

The spherical particle's scattering effects can be better described through illustrating the different contributions (Figure 5-7). The light rays which pass near the particle, without intersecting, correspond to  $l=0$ , and are diffracted into the particle's geometrical shadow. The specular reflection, or reflection from the outside of the sphere, corresponds to  $l=1$ .

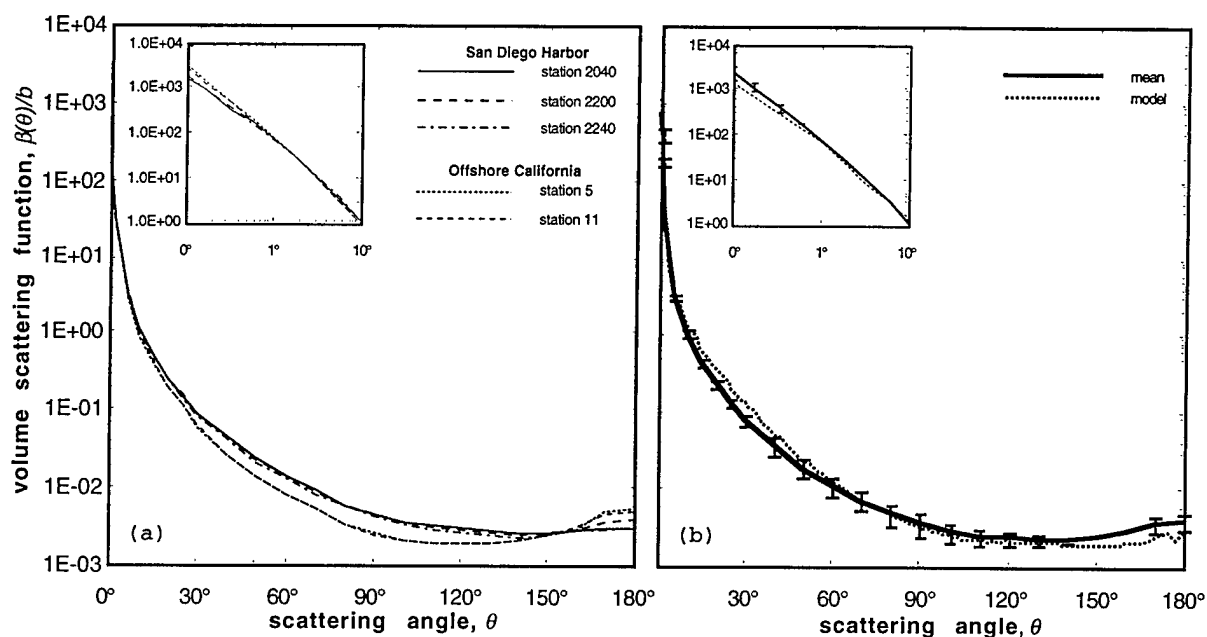


Figure 5-5. Concentration independent volume scattering functions for offshore California and San Diego bay and the optical model: a) measurements, and b) statistical fit

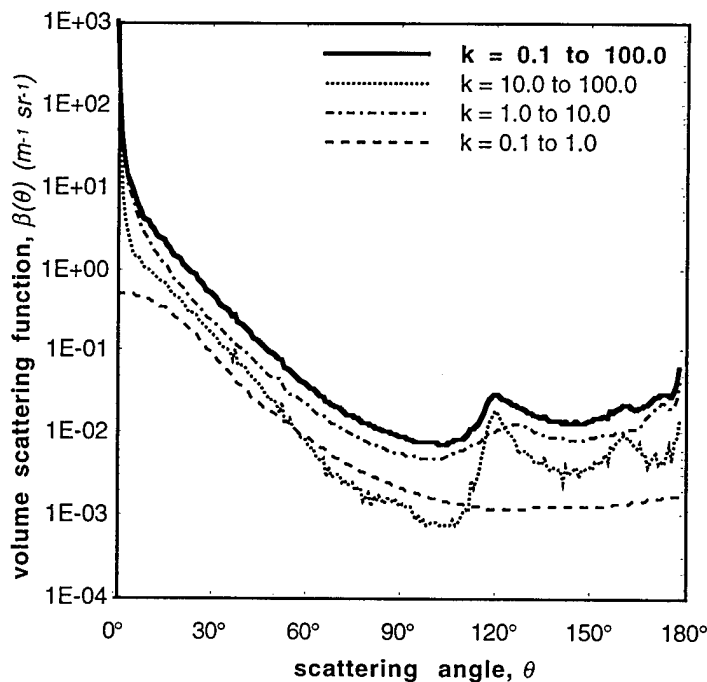


Figure 5-6. Size and angle dependent scattering w/o an imaginary index of refraction demonstrates rainbow and glory effects for particles  $\geq l$ .

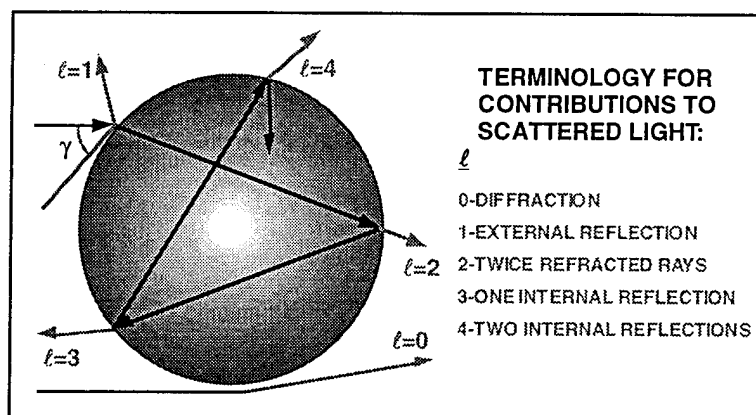


Figure 5-7. Features of light scattered by a sphere of size  $\lambda$

Light which is refracted twice without an internal reflection corresponds to  $l=2$  and makes up a large fraction of the scattered light for partially transparent spheres. The light which is internally reflected ( $l \geq 3$ ) represents no more than a few percent of the scattered light. However, for spheres, the energy in the  $l=3$  and  $l=4$  terms is sufficiently concentrated in angle to give rise to rainbow effects.

The features in Figure 5-6, near  $120^\circ$ - $170^\circ$ , are the rainbow effects which occurs when the scattering angle,  $\theta$ , has an extremum as a function of the incident angle of the sphere,  $\phi$ . The enhanced intensity in the backscattering direction,  $180^\circ$ , is the glory effect which is the result of shape-dependent focusing of energy. This is caused specifically by the spherical shape (Bryant and Jarmie, 1974), unlike the rainbow, which requires that the particle have a circular cross section. The use of a large imaginary index provides a fit to the measurements, however, this results in a reduced slope, which slightly increases forward scattering (Figure 5-5a) by very small increases in the fraction of larger particles. A slope of 3 for the size distribution (Morel, 1975) may be closer to physical measurements and give a better fit in the forward scattering area if rainbowning is neglected, ( $\eta'' = 0.0$ ). Since available volume scattering data



indicate that seawater-suspended materials do not strongly display the rainbow effect, we suggest that spherical particulate shapes are not important constituents of seawater. However, the artificially high  $\eta''$  is required if the spherical assumption is to be used to accurately match empirical scattering data at all angles. This appears true for the open ocean, coastal, and bay waters, which all fit closely using identical parameters. The assumption of spherical particles is a simple controlled approach to sediment scattering that provides good results which can easily be adapted to empirical data as it becomes available. A more complex approach, such as randomly shaped and oriented particles composed of layered indices and different distribution functions, would only serve to further complicate the first order approach. These variables could be included as refinements, if deemed necessary after exercising the model through multiple scenarios.

It should be noted that even though particle concentration values are not available for Petzold's scattering measurements, the concentrations required to match Petzold's San Diego Bay data are in reasonable agreement with recent San Diego Bay particle measurements (Schoonmaker et al., 1994). Model estimates of particulate concentrations for Petzold's scattering data are shown in Table 5-2.

Table 5-2. Estimated particle concentrations and scattering coefficients for Petzold's data

Offshore California		San Diego Bay		Tongue of the Ocean	
$N_I$	$b(m^{-1})$	$N_I$	$b(m^{-1})$	$N_I$	$b(m^{-1})$
1627	0.275	10800	1.824	692	0.117
1296	0.219	9368	1.583	254	0.043
		7131	1.205	219	0.037

Due to the many uncertainties involved and the absence of data covering the many possible variables, a single index of refraction was selected for use on all materials. As shown by the statistical curve in

Figure 5-5b, a satisfactory fit was obtained using  $\eta = \eta' - \eta'' = 1.2 - j1.015$ , even though biological materials were clearly present. A satisfactory procedure for spectral compensation of the modeled scattering coefficient,  $b_{model}$ , fit to the 530 nm volume scattering data is given by Equations (6) and (7). The hemispherical backscatter coefficient,  $bb_{sed}$ , can also be calculated as shown in Equation (8).

$$B_{sed}(\lambda) = \left( \frac{\lambda}{530} \right)^2 \quad (6)$$

$$b_{sed} = \sum_{j=1}^{j_{max}} B_{sed}(\lambda) b_{model}(j, \lambda, N_j, \gamma) \quad (7)$$

$$bb_{sed} = \sum_{j=1}^{j_{max}} B_{sed}(\lambda) \left[ 2\pi \int_{\pi/2}^{100} \int_{0.1} N_j(k) \beta_j(\theta, k) \sin(\theta) dk d\theta \right] \quad (8)$$

Values of  $B_{sed}(\lambda)$  vary by the square of the wavelength (van de Hulst, 1957) and are included in Table 5-3 for selected wavelengths. The  $j$  in Equation (7) refers to the sediment category which presently is restricted to one type, pending further measurements. The concentrations for laboratory samples, together with the  $\gamma = 2.1$  and the above index of refraction, combined to produce accurate values at 530 nm and accurate spectral values for combined sediment and phytoplankton laboratory samples, as shown in Figure 5-8.

Table 5-3. Laboratory-derived corrections parameters  
(Schoonmaker et al., 1994)

$\lambda(nm)$	Seawater (Smith&Baker, 1981)		NRaD Lab Measurement Calibration/Corrections			
	$b(m^{-1})$	$a(m^{-1})$	$B_{sed}$	$B_{bio}$	$A_{sed}$	$a_{lab}$
412	0.00666	0.01602	0.6043	2.4902	0.1529	12.8205
440	0.00490	0.01450	0.6892	2.5543	0.1317	14.5447
488	0.00316	0.01920	0.8478	2.6327	0.1006	12.0498
515	0.00250	0.04170	0.9442	2.7058	0.0831	5.5483
532	0.00218	0.05172	1.0076	2.7142	0.0752	3.0719
550	0.00190	0.06380	1.0769	2.7065	0.0673	2.6708
650	0.00100	0.34900	1.5041	2.6253	0.0384	7.5583
676	0.00074	0.44200	1.6268	2.1460	0.0355	11.2663
715	0.00065	1.00400	1.8200	2.7852	0.0159	0.4989

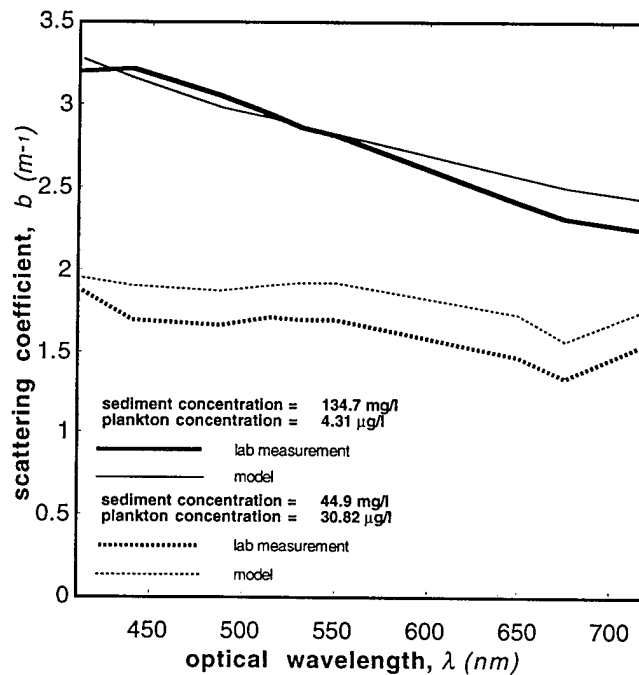


Figure 5-8. Comparison of model calculations with laboratory estimates  
for selected particulate concentrations

Biological particulate scattering requires unique calibration coefficients if the local water column communities exhibit significantly different optical properties. Mean cell size and shape may affect this coefficient, so the procedure is posed in terms of multiple constituents, even though only one phytoplankton species is presently included. For each biological constituent,  $i$ , the particulate scattering scaling factor,  $B_{bio}$ , is given in terms of the mean laboratory-measured spectral scattering coefficient,  $b_{meas}(i, \lambda)$ , as expressed in Equation (9). The preliminary calibration coefficients shown in Table 5-3 are based on one representative chlorophyte species ( $i = 1$ ). Calibration coefficients ( $i$ ) for additional species or generic plankton categories will be necessary, depending on the optical precision required.

$$B_{bio}(i, \lambda) = \left\{ \frac{b_{meas}(i, \lambda)}{b_{model}(i, \lambda)} \right\} \quad (9)$$

The combined biological scattering coefficient are,

$$b_{bio} = \sum_{i=1}^{i_{max}} N_i B_{bio}(i, \lambda) b_{model}(i, \lambda), \text{ and} \quad (10)$$

$$bb_{bio} = \sum_{i=1}^{i_{max}} N_i B_{bio}(i, \lambda) \left[ 2\pi \int_{\pi/2}^{\pi} \beta_i(\theta) \sin(\theta) d\theta \right]. \quad (11)$$

Figure 5-8 illustrates these results and the reduced scattering near 676 nm, where the chlorophyll absorption peak reduces the scattering interaction cross section ( $Q_{sca} = Q_{ext} - Q_{abs}$ ). Similar reductions in scattering at pigment absorption peaks were seen in laboratory measurement of phytoplankton scattering (Bricaud et al., 1983).

### 5.3.2 Particulate absorption

The scattering model was run with the above parameters to produce values for both scattering and absorption coefficients. For the sediments, the absorption value includes the artifact discussed above to correct for the mathematical convenience of using spherical particles. Since sediment samples tested in the laboratory are composed of real coastal sediment materials, they contain an unknown fraction of biological material, which is evidenced by a small chlorophyll or pheopigment absorption increase at 676 nm. In addition, laboratory mix water from the coastal region contains variable amounts of dissolved organics. This makes it difficult to determine the relative contributions to the total absorption.

To circumvent determining these fractions, the optical model was calibrated to adjust the sediment absorption coefficients to coincide with laboratory measured values as a function of optical wavelength,  $\lambda$ , and sediment concentration,  $N_s$ . It must be emphasized that these calibration coefficients are presently only available for a single classification of sediment; nearshore southern California. The number of sediment classifications required to model a wide variety of sublittoral visibility conditions must be determined by sensitivity comparisons for samples covering the range of optical constituents. As suggested later, it is advisable to include the slope of the particle concentration as a variable in all future constituent calibrations. Laboratory dilution with mix water changes the concentration, but the relative number of particles of each size remains constant. It was determined that  $N_s$  did not appreciably affect the sediment absorption scaling constant,  $A_{sed}$ , which has only been evaluated at one constant slope,  $\gamma$ . For each optical constituent,  $j$ , the sediment absorption scaling coefficient is given by;

$$A_{sed}(j, \lambda) = \left\{ \frac{a_{meas}(j, \lambda, N_I, \gamma)}{a_{model}(j, \lambda, N_I, \gamma)} \right\} \quad (12)$$

Note that  $a_{model}$  for sediment is calculated using the same index of refraction,  $\dot{\eta}$ , and slope,  $\gamma$ , as used in the calculation of  $b_{model}$ . The sediment absorption scaling coefficient [ $A_{sed}$ ], shown in Table 5-3, has been calibrated for quartz sand beaches and offshore coastal particulate ( $j = 1$ ). In terms of available volume scattering data (Petzold, 1972), this optical category (index of refraction) should provide optical estimates for a wide range of coastal situations, but other environments (coral sand, etc.) may require recalibration for additional sediment categories ( $j$ ).

The weighted optical constituent for sediment absorption is given by

$$a_{sed} = \sum_{j=1}^{j_{max}} A_{sed}(j, \lambda) a_{model}(j, \lambda, N_j, \gamma), \quad (13)$$

where  $N_j$  is the number concentration of the sediment constituent,  $j$ .

For biological absorption, the matter is approached differently due to the unique spectral absorption properties of many materials. Since modeling of detailed spatial variations demands treatment of particle dynamics, it is assumed that absorption can be estimated as the product of phytoplankton concentration and a mean absorption per cell. A phytoplankton community would be treated as a single biological classification or evaluated as a combination of independent constituents ( $i$ ), for which calibration coefficients must be determined, depending on the accuracy required for a specific application.

For phytoplankton, *Dunaliella tertiolecta*, the preliminary biological constituent for which the calibration coefficients were determined, we make the following assumptions (cell = particle):

1. Spectral absorption is proportional to chlorophyll present
2. Chlorophyll per ml is proportional to (cells per ml) x (chlorophyll per cell)

3. The absorption per unit chlorophyll concentration,  $a_{lab}(i, \lambda)$  [ $m^{-1}$  per  $\mu g/ml$ ], is given by the slope of the laboratory-measured spectral absorption as a function of chlorophyll concentration. Laboratory measured values are shown in Table 5-3 for category  $i=1$  (*Dunaliella tertiolecta*).

The laboratory determined value for the chlorophyll per cell ( $A_{bio} = 4.96 \times 10^{-6} \mu g/cell$ ) is slightly higher than naturally occurring phytoplankton, (Morrow, 1988). This is attributed to the limited lighting conditions of the laboratory, which, in turn, gets compensated by a higher production of chlorophyll per cell. This and the number of cells per ml determined, either by measurement or modeling, gives the spectral absorption coefficient, such that

$$a_{bio} = \sum_{i=1}^{i_{max}} N_i A_{bio}(i) a_{lab}(i, \lambda). \quad (14)$$

Laboratory absorption measurements of  $a_{bio}$  are compared with the modeled values (Figure 5-9).

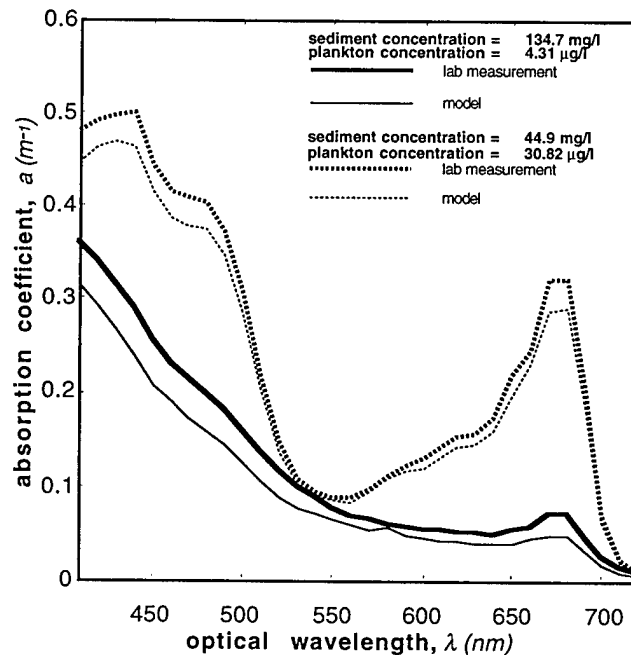


Figure 5-9. Comparison of modeled absorption with laboratory measurements

Combining the sediment and biological scattering and absorption terms given by Equations (2), (3), (5), (7), (13), and (14) provides the required estimates of total absorption and scattering coefficients. A technique for unfolding this from measured data is included in the next section.

#### 5.4 Oceanside Nearshore Example

The optics model presented here has yet to be evaluated due to the absence of nearshore data. However, two nearshore samples were available to support order-of-magnitude comparisons and search out problem areas.

For these measurements, the winds were calm but there was a long (12-14 sec) swell of approximately 1 meter height stimulating abundant bottom resuspension and a well developed Bottom Turbid Layer (BTL). Water samples were collected in nominally 20-meter deep water, approximately one half mile north of the breakwater at Oceanside, California, for subsequent laboratory-size distribution determination. *In situ* absorption and total attenuation measurements were made using the WetLabs absorption/attenuation meter used in the laboratory measurements of Schoonmaker, 1994. Figure 5-10 compares modeled and measured values of spectral absorption and scattering coefficients for the surface and mid depths shown in Table 5-4. Optical data in close proximity to the bottom was also measured, but with total attenuation coefficients around ten ( $c_{532} \approx 10$ ), single scattering calculation comparisons with the 20 cm long optical path in the instrument were deemed inappropriate.

Table 5-4. Particle parameters for Oceanside water

depth (m)	slope $\gamma$	particle number > $1\mu\text{m}$		
		$N_l$	$N_s$	$N_b$
2.5	1.9	2930	2422	508
10.0	1.7	7143	6572	571
Bottom	1.3	16190	—	—



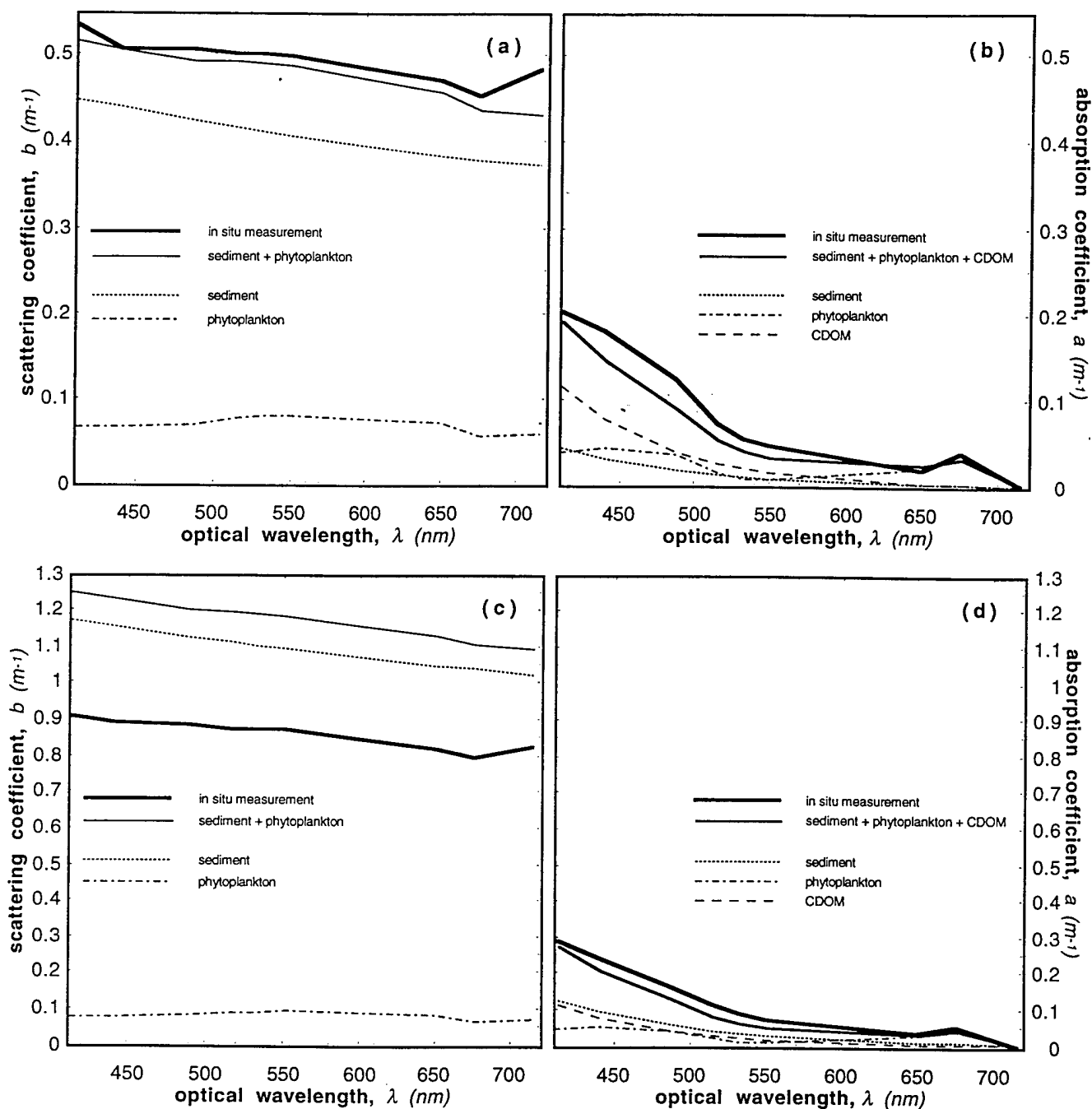


Figure 5-10. Oceanside scattering and absorption comparison of measurements vs. modeled: a) surface layer scattering, b) surface layer absorption, c) mid depth scattering, and d) mid depth absorption

PVM source models estimate  $N_s$  and  $N_b$  separately, but ocean measurements are presently limited to total particles,  $N_t$ . This requires splitting the measured  $N_t$  into phytoplankton and sediment particle numbers, in order to reconcile the data and model predictions. Schoonmaker et al. (1994) accomplished this using an approximation suggested by Zaneveld (personal communication, 1994), wherein the observed absorption at 676 nm above the line connecting 650 nm and 715 nm in the data is attributed to chlorophyll a. The contribution of dissolved organics at 676 nm is assumed to be negligible. The chlorophyll absorption determined in this way corresponds to a specific  $N_b$  in the laboratory-calibrated model. Subtracting this value of  $N_b$  from the measured total particulate gives  $N_s$ . Table 5-4 shows the measured  $N_t$ , and calculated  $N_s$  and  $N_b$  for the surface (2.5 meters) and 10 meters. The calculated  $N_s$  and  $N_b$ , together with the laboratory calibration coefficients, were used in Equations (13) and (14) for the sediment and phytoplankton absorption calculations (Figures 5-10b and 5-10d). An estimate of the spectral absorption of CDOM,  $a_{CDOM}$ , was calculated scaling from the remaining absorption at 412 nm, after the sediment and biological contributions had been subtracted from the measured values. This procedure gave  $a_{CDOM}(440)$  values of approximately 0.07 for both depths. A mean phytoplankton cell diameter of 7.6  $\mu\text{m}$  was used in the calculations. This diameter, along with the calculated  $N_b$ , were used to estimate the biological scattering and  $N_s$  was used to estimate sediment scattering (Figures 5-10a and 5-10c).

The modeled spectral coefficients agree fairly well with the observed values for the surface layer (Figures 5-10a and 5-10b), but the scattering is overestimated by about 30 to 40% for the mid-depth observations. This is thought to result from deviation of the particle size distribution slope from the value ( $\gamma = 2.1$ ) derived from fitting Petzold's scattering phase function data for coastal and San Diego Bay surface water.

A final step would be required to adjust the slope of the particle size distribution (fraction of large particles) so that the spectral sediment

scattering curves fit the data. This step was unanticipated because  $\gamma$ , derived from Petzold's data, fit all of the observed water types reasonably well with a single value of 2.1. In shallow water, the sediment size distribution appears to be significantly modified by the addition of large particles resuspended from the bottom, as indicated in Table 5-4. For the hyperbolic distribution in Equation 1, a doubling of the number of particles in the 1 to 10  $\mu\text{m}$  band will decrease  $\gamma$  from 2.1 to 1.8.

The PVM model will calculate this slope variation directly from sediment source model inputs and provide spatially and temporally varying values as input to the optics module. A nearshore increase in large particles could result in the shift towards forward scattering shown in Figure 5-2. Recalling that we have defined  $k = d/2\lambda$  so that in the center of the visible spectrum (0.5 $\mu\text{m}$ ),  $k$  is approximately equal to the particle diameter. The Mie scattering solution shows the contribution of particle sizes to angular scattering, grouped in three decades in Figure 5-11, replotted from the middle plot ( $\gamma = 2.1$ ) in Figure 5-2. The smaller particle numbers in the Rayleigh scattering decade ( $k = 0.1$  to  $1.0$ ) compose 99.2% of total particle number, but contribute little to  $\beta(\theta)$  in the forward direction due to their small optical cross sections and isotropic scattering. Inversely, the largest particles, while less than 1% of total, dominate forward scattering and point spread functions (Baker & LaVelle, 1984), but make only a very small contribution to backscatter. Note that the calculations for Figure 5-2 are based on the index of refraction fit to Petzold's data ( $\eta = 1.2 - j0.015$ ) in the absence of scattering phase function data essential for adequate description of these important situations.

Table 5-5 summarizes Mie scattering estimates of particulate scattering as a function of changing size distribution slope,  $\gamma$ , with a constant number of particles greater than 1  $\mu\text{m}$ . Decreases in  $\gamma$  increase the relative number of large particles. The effects of this relative increase in large particles are clearly evident as an increase in the front-to-back scatter ratio,  $b_{fwd}/b_{bck}$ , and an increase in the contribution of large particles to total scatter. This suggests that the larger difference between modeled

and measured scattering at mid-depth is due to the presence of larger particles.

Table 5-5. Scattering fraction variations with slope

slope $\gamma$	$b_{\text{decade}}/b_{\text{total}}$			$b_{\text{fwd}}/b_{\text{bck}}$ 0.1-100 $\mu\text{m}$
	0.1-1 $\mu\text{m}$	1-10 $\mu\text{m}$	10-100 $\mu\text{m}$	
1.5	5.40%	40.83%	53.77%	96.6995
1.8	10.99%	52.79%	36.22%	81.2036
2.1	19.07%	59.74%	21.19%	64.9435
2.4	28.84%	60.17%	10.98%	50.3499
2.7	39.34%	55.49%	5.18%	37.9628

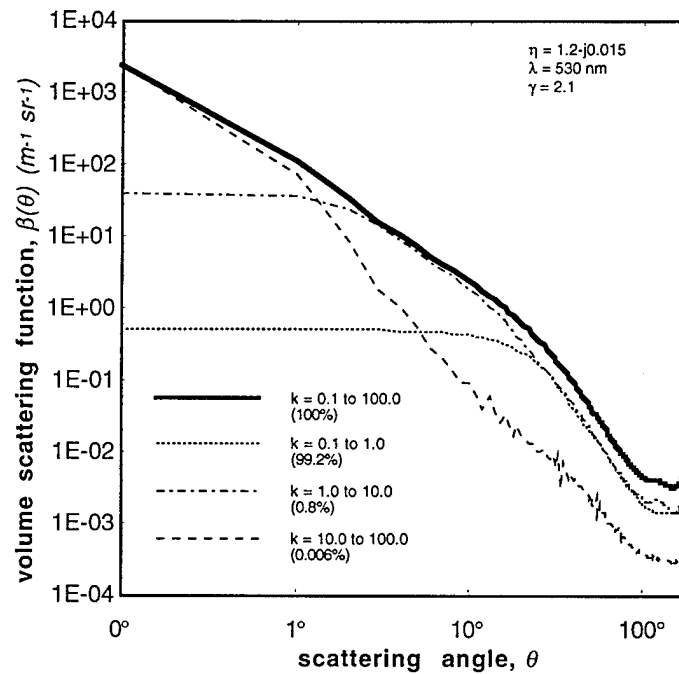


Figure 5-11. Three decade volume scattering function

Clearly, there is a need for laboratory measurements to characterize scattering,  $\beta(\theta)$ , and calculate the sediment absorption correction factors,  $A_{\text{sed}}$ , in Table 5-3 as a function of  $N_s$ ,  $\gamma$ , and refractive index ( $\eta$ ). This is

essential for the description of the optical properties near the bottom for shallow coastal areas subject to bottom sediment resuspension. The estimated scattering of phytoplankton cells was relatively small compared to the total particles in the Oceanside area, and can probably be neglected in many nearshore regions (see Figure 5-10).

Visibility distance can be characterized by multiples of the reciprocal of the total beam attenuation coefficient,  $c$ . Three times  $c$ . is used as a convenient rule of thumb for PVM visibility distance estimates. Values of  $c$ . are shown in Figure 5-12a for the Oceanside surface layer. The measured spectral values for the shallow water sample follow the modeled values closely. However, identical treatment for the mid-depth sample produces an offset of approximately 25%. This spread between measured and modeled attenuation may result from the change in the size distribution close to shore, which was discussed above. More data is required to resolve the problems associated with the large particle cases.

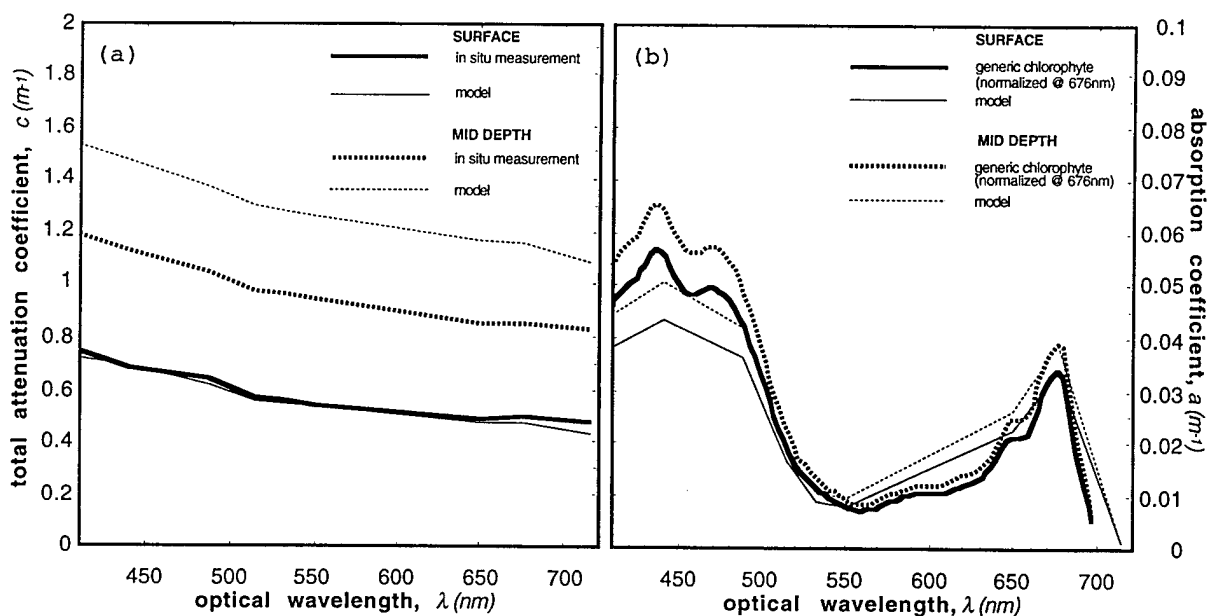


Figure 5-12. Oceanside nearshore data comparison: a) total attenuation, and b) phytoplankton absorption

Figure 5-12b compares a generic chlorophyte spectral absorption curve (Cleveland and Perry, 1994) with modeled biological absorption for the Oceanside surface and mid-depth samples. The curves have been normalized at 676 nm. The normalized modeled absorption spectrum, which is based on one phytoplankton species, generally resembles the normalized chlorophyll spectrum. Differences in spectral peak ratios are probably due to different ratios of chlorophyll *b* to chlorophyll *a* in the model assumptions compared to the generic chlorophyte. Nearshore data includes absorption by other phytoplankton pigments, organic detritus, and sediment particles. These particles give rise to differences between modeled and "generic" absorption. All of the phytoplankton absorption values are small relative to the scattering coefficients, and could almost be neglected without seriously impacting total attenuation in this Oceanside case.

### **5.5 Sensitivity To Sediment & Biological Parameters**

The optical estimation procedures presented in Section 5.3 rely on the use of calibration coefficients covering biological categories (*i*) and sediment categories (*j*). While all particulate scattering is based on fundamental Mie calculations, biological calculations, and, in particular, spectral absorption estimates require calibration coefficients for each category of material. Operating on the particulate number concentrations ( $N_1$ ,  $N_5$ , and  $N_{20}$ ) and size distribution slopes ( $\gamma$ ) provided from the hydrodynamic transport modules, these calibration coefficients determine the local optical properties. PVM accuracy is directly dependent on the accuracy and precision with which these coefficients are determined for each biological and sediment category. In addition to calibration coefficients, there are several constants used in the calculations which must be assumed or selected from the literature. The relative effects of these constants and calibration coefficients on optical estimates are the subject of this section.

The biological description is in terms of two discrete sizes, or pseudo-categories, since they use the same optical calibration coefficients in

the absence of measurements. Scattering coefficient calibrations,  $B_{bio}(i, \lambda)$ , must be determined in the laboratory for plankton cells representative of each of these biological categories ( $i$ ). The assumed scattering constants for biology are limited to the two coefficients of the complex index of refraction ( $\eta'$ ,  $\eta''$ ). This is because particulate sizes are fixed with only two discrete particle sizes ( 5 & 30  $\mu\text{m}$ ,  $i = 1$  & 2), and a slope parameter is not required.

For sediment scattering, the slope of the size distribution ( $\gamma$ ) and the complex index of refraction ( $\eta'$ ,  $\eta''$ ) are the constants which must be selected. The "best fit" values (  $\gamma = 2.1$  and  $\eta' = 1.2$  ), selected for the nearshore environment in Section 5.2, fall in between the plankton-dominated Case I clear ocean water (  $\gamma \geq 3$  ,  $\eta' = 1.02$  ) and the sediment case (  $\gamma \leq 2$ ,  $\eta' = 1.2$ ) typical of San Diego Bay. The "best fit" index was used with modeled concentration and slope for the sediment-dominated Oceanside example in Section 5.4. These default values are the basic optical parameters (  $\gamma = 2.1$  and  $\eta' = 1.2 - j0.015$ ) referred to as sediment category ( $j = 1$ ). The fact that the steeper slope and decreasing index of refraction both result in increased forward scattering may contribute to the similarity of the volume scattering functions for such diverse water types. It is assumed here that as the shoreline is approached (Figure 5-1), combinations of ( $\gamma$ ) and ( $\eta'$ ) will fall between these boundaries, and are well represented by the "best fit" values selected (see Figures 5-2 and 5-5b).

The same complex coefficient which corresponds to internal particulate absorption ( $\eta'' = 1.015$ ) is used in all cases to remove the rainbowing and glory effects, exacerbated by the spherical assumption, not observed in Petzold's 1972 measurements. Absorption calibration coefficients,  $A_{sed}(j, \lambda)$ , are required to relate the Mie-calculated absorption to laboratory-determined values for each category ( $j$ ) to compensate for artificially elevated absorptions.

Additional sediment index of refraction categories ( $j$ ) could be introduced to accommodate constituents like coral, calcium carbonate, or

other variations of the most common clay-silt-sand component, iron-stained quartz. How many sediment categories are required depends on local variations and the optical estimation accuracy required. At present, there is insufficient data to support any additional categories over and above the ubiquitous quartz material for which scattering and absorption coefficients were measured by Schoonmaker (1993).

For biological absorption, the situation is somewhat more complicated. There can be significant spectral absorption differences between plankton which vary between the open ocean and coastal species, and other local environmental factors (Parsons et al., 1984). As discussed in Section 5.4, the calibration constants were determined for *Dunaliella Tertiolecta*, used here as a representative chlorophyte. Representative chromophyte and cyanobacteria are generic candidates for biological category additions (Cleveland & Perry, 1994). It is the view of marine biologists that one species dominates at any given time (Duntley et al., 1974), and models which attempt to predict the temporal variation of species mixtures are beyond present capabilities.

The biological input category parameters used in the calculation of phytoplankton absorption are the specific spectral absorption ( $\text{m}^{-1}$  per  $\mu\text{g/ml}$ ) and the chlorophyll per cell ( $\mu\text{g/ml}$ ). These inputs must also be determined in the laboratory for each separate biological category ( $i$ ). At present, specific absorption values determined, using *Dunaliella Tertiolecta*, have been applied to both the biological categories (5 & 30  $\mu\text{m}$ ,  $i = 1$  & 2), and values from the literature used to accommodate variations between cell sizes.

Spectral sensitivity for the particulate mixtures of sediment and plankton, which are modeled in the hydrodynamic and plankton growth modules of the PVM, vary as shown in Figure 5-13, where the parameter ( $F$ ) is the biological fraction. Here, the total number of particles is held constant at 1000 and ( $F$ ) is the fraction of biological particles [ 0 - 100% ]. Since two sizes of plankton were included in the PVM biological growth module, the approximate ratio of 10:1 nanoplankton to netplankton



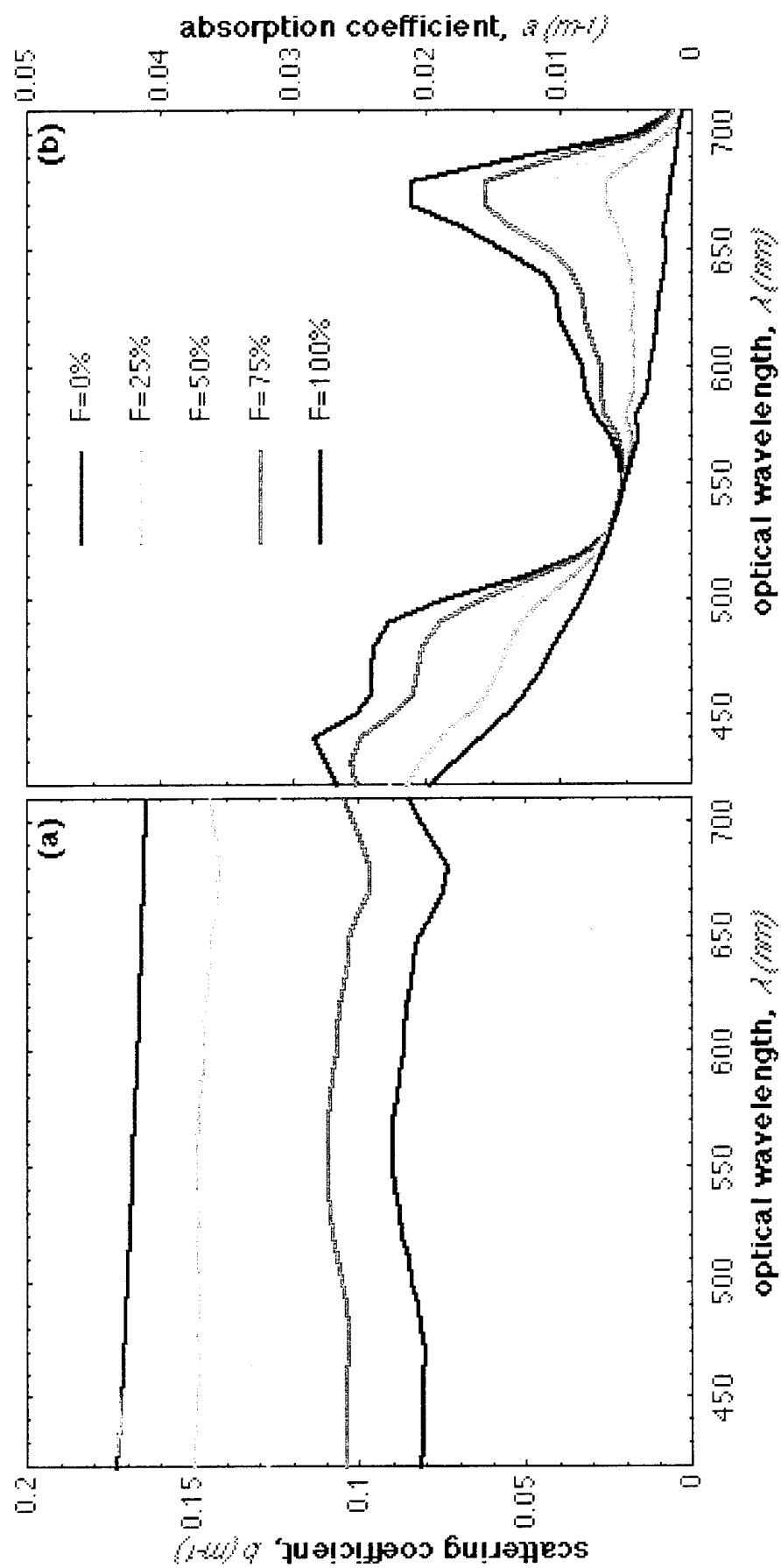


Figure 5-13. Spectral sensitivity as a function of biological fraction (F)

observed in extended biological runs was assumed. Additionally, the offshore concentration of small particulate (0.1 to 1  $\mu\text{m}$ ), contributing ubiquitously in the nearshore regime to the optical coefficients, was held constant using a reference  $N_1$  of 1000.

These plots are very sensitive to chlorophyll per cell ( $\mu\text{g}/\text{ml}$ ) estimates, and to enhance the peak at 676 nm, the higher values used in this plot are were four times the value currently resident in the model (literature consensus), twice the laboratory value used in the Oceanside example (*Dunaliella Tertiolecta*), but close to those suggested in Kirk, 1983. Using the consensus values, the 0.1 to 1  $\mu\text{m}$  particulate in the offshore background dominates the ( $F = 100\%$ ) spectral absorption up to 630 nm. This indicates that further calibrations are required to accommodate large particulate effects. Recall that the (*Dunaliella Tertiolecta*) coefficients used alone matched the Oceanside observations reasonably well. Figure 5-13 clearly indicates that further efforts are required to obtain size-dependent calibration coefficients for separated biological constituents.

## 5.6 Model Status & Recommendations

The results of the Bohren-Huffman-based Mie scattering code calculations agree remarkably well with the laboratory measurements and one nearshore surface water sample. The internal absorption coefficients, introduced to fit Petzold's angular scattering data and compensate for the mathematical convenience of spherical particles, also provide tractable representations for the laboratory sediment data and the nearshore surface water example. Modeled attenuation, which is the sum of the absorption and scattering also agreed with nominal *in situ* attenuation measurements for surface waters.

The modeled sediment plus phytoplankton absorption compare favorably to the measured *in situ* absorption for both depths in the coastal example. The modeled phytoplankton spectral shape resembled the spectral

shape for generic chlorophyte. This spectral shape is fixed by the reference water corrections. The generic chlorophyte curve appears reasonably close for the Oceanside case, but the number of biological reference classifications required to cover the range of desired coastal conditions depends on phytoplankton community variations, and the optical accuracy required. Additional laboratory calibrations covering additional "representative species" and/or for generic chlorophytes, chromophytes, and cyanobacteria categories will be essential for wide ranging worldwide estimates.

Colored dissolved organic materials (CDOM) are additive-absorbing constituents which employ an offshore concentration based on historic or remotely sensed observations. The method used to extract the initial offshore concentration of CDOM is critical since this value forms the permanent baseline for this quantity on which river and other local source and models are superimposed.

Remote sensing algorithms for simultaneous extraction of offshore CDOM in the presence of sediment and phytoplankton need to be rigorously tested and verified *in situ*. SeaWiFS will include new spectral bands designed expressly for this purpose, although it will be spatially constrained to waters further offshore ( $\approx 10\text{km}$ ), with resolution too crude ( $\approx 1\text{km}$  pixels) for resolving kilometer scale coastal eddy structures. Optical property variation with depth, and, in particular, the steep gradients in properties near the bottom, can be expected to complicate the unfolding of layered contributions to aerospace passive remote sensing estimation.

In the bottom turbid layer (BTL), prediction of optical properties may require size-dependent calibration coefficients to be responsive to the larger particles which strongly affect the front-to-back scattering ratio, and, hence, extinction length and diffuse attenuation in different ways. Due to the computational burden of the repetitious Mie scattering calculations, this has been taken off-line and interpolated look-up table values used within the PVM computational sequence. Precalculated particulate

scattering, absorption, and back-scattering coefficients are included in this table as a function of optical wavelength ( $\lambda$ ) and sediment distribution slope ( $\gamma$ ).

In the BTL, it may also be expedient to neglect biological effects entirely since the absorption term may be overwhelmed by sediment scattering. This suggestion is based on very limited data and more laboratory and *in situ* measurements will be required to validate this approach. The primary optical parameters for bottom visibility are extinction in the BTL, and perhaps diffuse attenuation coefficient,  $K_d$ , of the upper waters, which reduce the light available for passive bottom visibility. Figure 5-14 provides an example of the effects of spatially varying surface sediment and phytoplankton concentration on surface visibility distance and diffuse attenuation coefficients. These types of estimates are on two-hour time intervals for surface (1 m deep) and bottom (1 m elevation) and for vertical profiles within the PVM computational region.

The apparent divergence of the "best fit" parameters for particle distributions heavily burdened with large particles requires further investigation. The absorption correction coefficients were determined from a sediment-size distribution, but the size distribution is significantly altered when current and wave action doubles the relative concentration of larger particles. Sediment samples, including these large particles, need to be measured in the laboratory to obtain sufficient data to fully characterize the scattering, and update the slope variable as a parameter in both the scattering and absorption calculations. Spatial and temporal slope variations are a routine output of the PVM sediment source models.

Referenced laboratory measurements demonstrated small decreases in the combined sum of particle numbers when mixtures of sediment and/or phytoplankton concentrations are combined.

This decrease may be due to unknown effects like agglomeration or flocculation. The absence of significant changes in particle number is

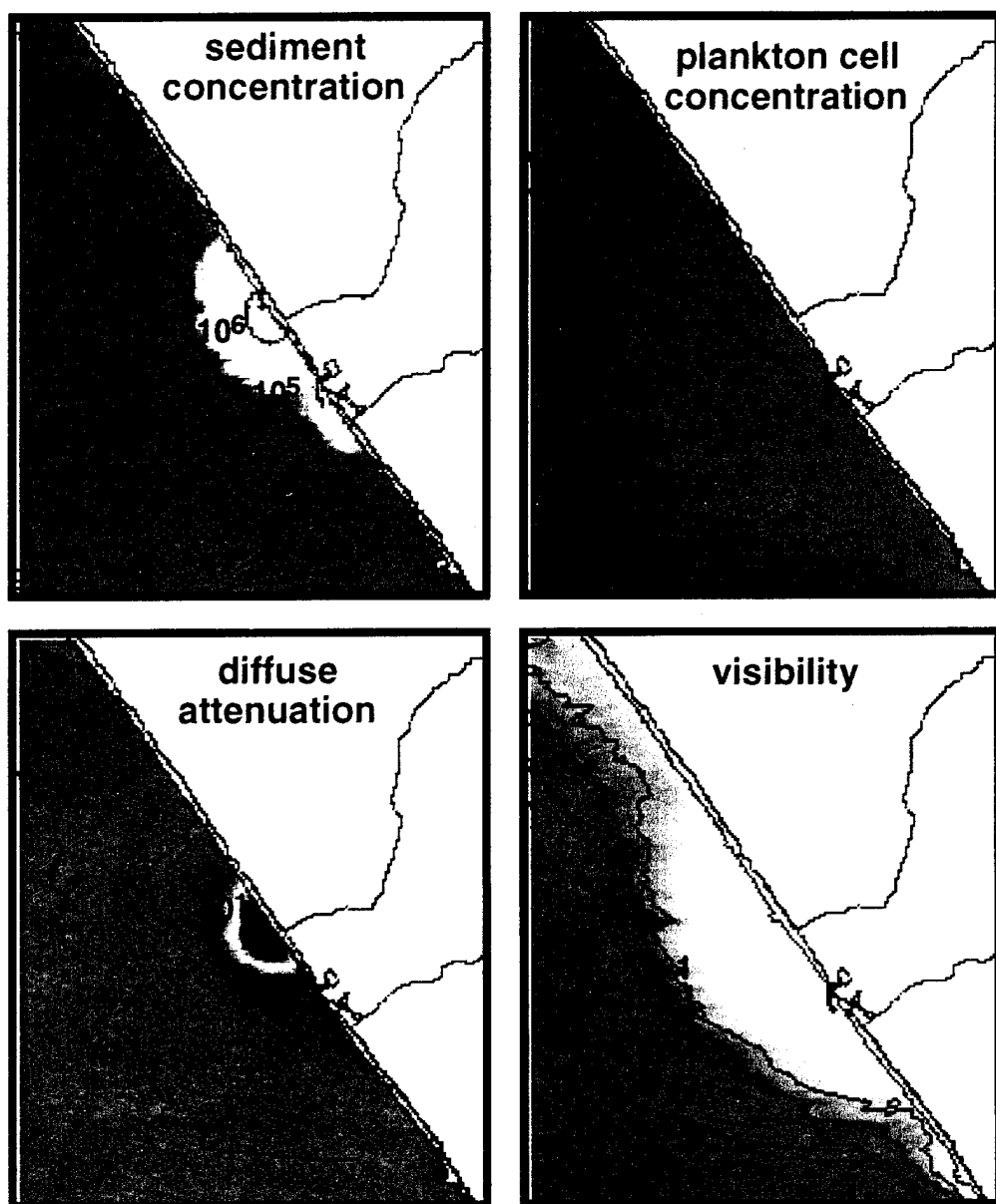


Figure 5-14. Surface sed.-plankton-visibility-diffuse atten. quad chart example

critical for optical modeling which independently combines the absorption and scattering contributions of particulate concentrations. The preliminary optical model calibration constants presently used in the optical calculations were established using a single-sediment sample (size-number distribution) and mix water (salinity/CDOM). Slope variations and possible salinity effects require further investigation when data becomes available.

Hyperspectral remote sensing is rapidly advancing in its ability to extract terrestrial data from the 3-D "data cube," two space, and one spectral dimension. For nearshore waters complications must be anticipated in extracting data on the fourth and fifth dimensions, depth, and time, which are essential in describing the dynamic nearshore environment treated by the PVM. The initialization values of surface chlorophyll, sediment, and CDOM concentrations used in PVM determine the number of time steps required for conditions to converge to a dynamic equilibrium representative of existing spatial and temporal distributions, and these values directly effect optical parameter estimates. The closer the estimates, the more rapidly these parameters and the optical properties will converge. When one considers this five-dimensional data space, the ocean truth data collection problem becomes insurmountable without a model framework in which to conduct the sensitivity analysis which identifies and prioritizes the dominant parameters for the planning and execution of algorithm validation experiments. When calibrated for a definitive set of sediment, biological, and optical categories, the optical algorithms presented above are intended to develop into a ubiquitous predictive capability.

## 6.0 CONCLUSIONS AND RECOMMENDATIONS

All of the following conclusions and recommendations are based on preliminary CWC model calibrations established for the Camp Pendleton, California, coastline. Reasonable agreement was demonstrated between modeled values and the very limited number of observations available. Extrapolations for other worldwide coastal locations await calibration and testing for a minimum set of coastal categories. Modeling of an arbitrary beach location is predicated on an adequate choice from "similar" calibrated locations residing in the model data base. At least five coastal-type categories, based on geology, will be required to cover the range of coastal circumstances with an undetermined number of additional independent categories to describe the coastal runoff, plankton, and benthic contributions.

Suspended sediments exerted the strongest influence on subsurface optical properties in the Camp Pendleton nearshore regime. The addition of fine-grained sediment particulate (diameter 1-10  $\mu\text{m}$ ) to the water column results in an increase in scattering to larger angles relative to open ocean waters. As the coastline is approached and coarser particulate is introduced, Mie scattering calculations reveal a significant return to very narrow angle scattering about the forward direction. *In situ* verification of Mie-derived optical scattering phase functions for nearshore and turbid bottom layer particulate distributions will be essential in removing the uncertainties associated with specific instrument performance estimates.

Suspended sediments also limit the growth of plankton by limiting the available light in the upper layers. Thus, absorption due to both the biological particles and the dissolved organic materials they release can ultimately be a function of suspended sediment concentration.

The relative concentration of suspended sediment in the water column is controlled by bottom resuspension through wave and current action in dry weather, and, locally, by river flow in wet weather.

Accurate forecasts of suspended sediment effects on optical properties during dry weather depend on four critical environmental input descriptors.

1. Wave height, period, and direction estimates
2. Bathymetric resolution
3. Bottom composition estimates
4. Episodic current events

The prediction of wave resuspension on the inner shelf is only as good as the sea, and swell wave forecasts and bathymetry used to construct the nearshore wave field from refraction/diffraction computations. For shallow fetch-limited environments like the Gulf of Mexico in the Persian Gulf, the standard digital bathymetry available with 3 arc-second pixel spacings is inadequate to resolve the wave fields, because much of the wave energy is associated with spatial scales less than the Nyquist length corresponding to 1.5 arc-second pixel spacings, i.e., less than 50 meters at 30 degrees latitude.

The bottom composition is equally critical in this calculation. While the smallest particle sizes represent a small mass fraction in the total bottom composition, they dominate the total particle number concentration and have a disproportionate effect on optical scattering. Errors in small particle mass fraction estimates lead to large errors in optical properties. Furthermore, when bottom resuspension adds large silt particles, grain size distribution shifts effect the calculated slope of the hyperbolic approximation, which results in order of magnitude changes in forward scattering coefficients. Particle distribution variations change the threshold of motion, and, hence, the size of the shelf area where optical properties are degraded by sediment water constituents. Bottom composition variability data is presently one of the most critical deficiencies in the input parameters list.

It is suggested that bottom reflectivity will vary in time at any specific location with environmentally-driven changes in the sediment size distribution. These temporal reflectivity variations and their optical significance are outside the scope of this study, but require careful investigation.

For the Camp Pendleton computational region used in the demonstration example presented here, bottom current was modeled as the vector sum of wave orbital and prevailing offshore velocity components. In the dominant case, where only the progressive tidal components were used, optical properties were more strongly degraded by wave resuspension than current resuspension. This observation, however, cannot be expected to be universal in areas where strong currents such as inertial eddies, wind-driven circulation, or tidal resonances are present. The inclusion of a nearshore eddy model based on coastline curvature is a high priority effort for the future, but comprehensive nowcasting of coastal current structures is probably best handled with direct remote sensing input. When these events



give rise to bottom stresses exceeding the threshold of motion of local sediment sizes, rapid degradation of optical properties by current resuspension is expected. Biological activity within the sediment bed also has an unquantified, but probably smaller, effect.

Accurate forecasts of the suspended sediments and optical properties during wet weather depend on accurate assessment of river hydrology and the land use factors which control the constituents of the washload. They require the following critical input data:

1. Accurate precipitation estimates
2. Sufficient topographic data to delineate river drainage basins and networks
3. Accurate soil and stratigraphic data estimates to define spatial variability in soil infiltration, permeability, and Manning's roughness coefficients
4. Accurate land use estimates for the determination of dissolved organic material (DOM) in the washload

Quantitative precipitation estimates must be accurate in time of arrival, volume, and duration to facilitate precise computation of critical river flood hydrographs (flow rate vs. time). This is one of the weakest prediction areas in meteorological forecasting, especially for storms approaching the coastline from the open ocean. Generally, precision in this type of estimates relies on the availability of, and the forecaster's experience with the interpretation of, infrared satellite imagery.

Flood hydrographic computations for any river require complete delineation of the total watershed and/or high quality time/volume estimates for other separable contributing river basins. For many coastal rivers, particularly along trailing edge coasts, basin size could require topography and digital elevation maps over computational regions many times larger than the coastline of interest. Further, quantitative soil and vegetation data in the form of maps or exploitable imagery product must be included to allow for computation of the spatial dependence of the soil infiltration parameter. Failure to properly delineate the complete river drainage basin or the infiltration parameter can lead to order of magnitude errors in the river flow rates (see Appendix B, Figure 7) and similar errors in the supply of sediment washload to the coastal waters. Drainage network assessment and soil variations require the type of precise registration which is best treated in an automated GIS data base. The hydrology model used for PVM calculations operates on GIS registered layers integrated within the same GRASS software package used to set up the BASEMAP and processed

image data layers required to initiate the PVM modeling process. These procedures are summarized in Appendix B.

At present, there are no quantitative models for calculating the dissolved organic material (DOM) content of the washload. These are related to land use factors, but presently only regionally specific "rules of thumb" are available with which to make order of magnitude estimates. Hence, there is significant uncertainty in the DOM optical absorption computations in the neighborhood of a river mouth during wet weather. Similarly, active benthic releases of both sediment and organic material constitute an unquantified source of potentially significant optical constituents to the water column. Fortunately for the normally arid Camp Pendleton coastline, DOM and probably benthic releases are of minor importance; a circumstance which will not be true for many other locations.

The wind speed and duration exert a strong influence on the surface to bottom suspended sediment gradient which significantly influences optical visibility distance. The decisive factor is the wind-induced mixed layer depth relative to the local bottom depth. If the bottom depth is less than the mixed layer depth, then bottom resuspended sediment can be mixed upward into the surface waters, and surface visibility degrades significantly. Similarly, river discharge rapidly mixes downward under these conditions to further degrade bottom visibility. On the other hand, where bottom depths exceed the mixed layer depth, hindered settling near the pycnocline separates surface and bottom sources of suspended sediment and there is high likelihood of significant differences between surface and bottom visibility distances. Under these conditions, the bottom visibility near or under a fresh water river plume may be significantly better than surface visibility. In dry weather, when rivers are not discharging, the surface visibility can remain comparable to clear offshore waters due to its isolation from bottom resuspension sources.

Wind speed is the primary factor in deepening the mixed layer and producing these effects. Winds greater than 20 knots increase these effects at an accelerating rate, while layer depth effects are markedly lessened at speeds below 20 knots. At all speeds, duration has a second order effect, although sustained winds over 24-hour periods produce noticeable enhancement over diurnal winds.

Phytoplankton particulate exerted a second order effect on coastal optical properties relative to sediment particulate at the Camp Pendleton demonstration site. In general, phytoplankton effects were not significant over the middle and inner shelf, from the threshold depth of bottom resuspension shoreward; nominally 30 meters for the observation interval.

This was due to light limitations to growth caused by suspended sediment and the mixing and sinking losses induced by wave and current action. On the outer shelf, however, where significant amounts of suspended sediment particles do not, in general, remain at the surface, plankton growth proceeds subject to sunlight, nutrient availability, grazing activity, and mixing depth limitations. In this case, plankton particulate becomes the controlling factor in determining optical properties which display less dramatic spatial gradients than the sediment rich areas on the inner shelf.

The extreme influence of sediment and parameters external to the plankton module tended to overwhelm the more subtle influences of internal constants at the Camp Pendleton site. Calibration of this module for a plankton dominated coastline is therefore essential for further fine tuning and overall validation.

The critical factors in accurate modeling of plankton populations and their associated effects on coastal optical properties are:

1. Internally consistent initialization parameters
2. Nutrient source limitations
3. Vertical diffusivity
4. Mixed layer depth

Nutrient source limitations are difficult to assess, especially near terrogenous sources, for the same reasons that DOM is intractable in river washloads. The initial plankton population can be most accurately established using aerospace spectral imaging sensor data, processed to provide the offshore chlorophyll concentrations required as model input. Use of historic data must at least account for mean monthly variability in nutrient availability which must, in turn, be consistent with the observed chlorophyll concentration and the existing local mixing situation. Unfortunately, archived mean values are always parametrically inconsistent when applied to a varied set of local conditions. This results in estimation errors in the initial plankton population variation, which depends on the compatibility of the initialization parameters and the variability of the scene to which they are applied. Simultaneously measured parameters should yield initialization data sets which more rapidly approach dynamic equilibrium with other driving mechanisms.

Definitive assessment of the impact of the plankton growth/dispersion models on optical properties must await its application to a high productivity location (new biological category) where plankton population factors are dominant. Even in the deeper offshore waters of the demonstration area, the biological model responded more sensitively to extreme variations in the

PVM-modeled inputs than to the selection of internal biological rate constants. This may not hold true for other locations where these internal constants might become significant optical variables.

Recommendations for continuing PVM improvement are as follows:

1. Effective use of the PVM requires comprehensive calibration in a wider variety of areas to establish additional categories describing additional coastal locations. At each calibration site, it will be necessary to obtain the full range of data required to calibrate each separate module of the PVM, and tune the overall model response to principle physical drivers. The concurrent measurement of optical properties, particle abundance, and bottom composition are the most critical deficiencies in existing data sets. Hence, dedicated PVM seatruth field measurements are essential. This effort would also make extensive use of hindcast data where direct observations are input to isolate and evaluate individual module performance. The versatility of the PVM is entirely dependent on the selection and number of generic categories in its data bank and on the accuracy with which each is calibrated. Note that since the BASEMAP inputs are already compiled and a preliminary calibration has been accomplished for Camp Pendleton, this site represents the most cost-effective location for additional module checkout and testing. Other high priority PVM calibration and checkout sites include a marginal seas, Gulf coast with refined bathymetry, and a clear water location where plankton dominates the optical properties.
2. After the PVM is thoroughly calibrated at any site, a validation of its performance under a wider range of local weather conditions, and an evaluation of PVM prediction capabilities using varied external meteorological forecasts should be carried out. Predictions can be no more accurate than the forecasted environmental parameters used as PVM input. These forecasts can be based on distant wide area analysis or on locally obtained soundings and measurements, thus providing important feedback for PVM applications.
3. Several areas were identified in which insufficient data was found to exist for making confident decisions on physical mechanisms. As would be expected, these cover the range of practical measurements for immediate attention, as well as wish

list capabilities, deferred for future long term projects. These include (a) optical scattering phase function determination for variable bottom turbid conditions, (b) bottom composition variability measurements and (c) washload characterization for sediment size and dissolved organic content. Several important, high leverage experimental areas which could answer critical questions in the immediate future, without extensive funding, have been described in this section. These should be addressed as soon as possible.

4. Other efforts which expand the flexibility of the PVM in terms of its ability to support optical predictions on curved irregular coastlines and enclosed bays, and to contribute to the full range of environmental applications like effluent, contaminant, and thermal plume monitoring, should also be pursued.

## 7.0 REFERENCES

- Ackleson, S. G. and R. W. Spinrad: 1988, Size and refraction index of individual marine particulates: a flow cytometric approach, *Applied Optics*, Vol. 27, No. 7.
- Agusti, S. and J. Kalff. 1989. The influence of growth conditions on the size dependence of maximal algal density and biomass. *Limnol. Oceanogr.* **34**, 1104-1108.
- Agusti, S., C.M. Duarte and J. Kalff. 1987. Algal cell size and the maximum density and biomass of phytoplankton. *Limnol. Oceanogr.* **32**, 983-986.
- Aijaz, S. and S.A. Jenkins, 1994, "On the electrokinetics of shear stress behavior in fluid-mud suspensions," *Jour. Geophys. Res.*, Vol. 99, No. C6, pp. 12697-12706.
- Aijaz, S. and S.A. Jenkins: in press, On the Electrokinetics of Shear Stress Behavior in Fluid-Mud Suspensions, *J. Geophys. Res.*, pp 20.
- Aldredge A. L. and J.M. King. 1977. Distribution, abundance and substrate preferences of demersal reef zooplankton at Lizard Island Lagoon, Great Barrier Reef. *Mar. Biol.* **41**: 317-333.
- Aldredge, A.L. and J.M. King. 1980. Effects of moonlight on the vertical migration patterns of demersal zooplankton. *J. Exp. Mar. Biol. Ecol.* **44**: 133-156.
- Aller, R.C. 1982. The effects of macrobenthos on chemical properties of marine sediment and overlying water, p. 53-102 In: P.L. McCall and M.J.S. Tevesz (eds), *Animal-Sediment Relations*. Plenum Press.
- Aller, R.C. and J.Y. Aller. 1992. Meiofauna and solute transport in marine muds. *Limnol. Oceanogr.* **37**: 1018-1033.
- Aller, R.C. and J.Y. Yingst. 1985. Effects of the marine deposit-feeders *Heteromastus filiformis* (polychaeta), *Macoma balthica* (bivalvia) and *Tellina texana* (bivalvia) on averaged sedimentary solute transport, reaction and microbial distributions. *J. Mar. Res.* **43**: 615-643.
- Alongi, D.M. and P. Christofferson. 1992. Benthic infauna and organism-sediment relations in a shallow, tropical coastal area: Influence of

- outwelled mangrove detritus and physical disturbance. *Mar. Ecol. Prog. Ser.* 81, 229-245.
- Aminot, A., M.A. El-Sayed and R. Kerouel. 1990. Fate of natural and anthropogenic dissolved organic carbon in the macrotidal Elorn Estuary (France). *Mar. Chem.* 29, 255-275.
- Apel, J. R.: 1987, *Principles of Ocean Physics*, Academic Press, pp. 511-605.
- Armi, L.A., 1979, "Effects of variations in eddy diffusivity on property distributions in the oceans," *Journal of Marine Res.*, Vol. 37, No. 3, pp. 515 to 530.
- Asmus, R.M. and H. Asmus. 1991. Mussel beds: limiting or promoting phytoplankton? *J. Exp. Mar. Biol. Ecol.* 148: 215-232.
- Babcock, R.C., G.D. Bull, P.L. Harrison, A.J. Heyward, J.K. Oliver, C.C. Wallace and B.L. Willis. 1986. Synchronous spawning of 105 scleractinian coral species on the Great Barrier Reef. *Mar. Biol.* 90: 379-394.
- Bader, H.: 1970, The Hyperbolic Distribution of Particle Sizes, *J. Geophys. Res.*, Vol. 75, pp. 2822-2830.
- Bailard, J.A., 1981, "An energetics total load sediment transport model for a plane sloping beach," *Jour. Geophysical Res.*, Vol. 86, No. C11, pp. 10,938-10,954.
- Baillie, P.W. and B.L. Welsh, 1980. The effect of tidal resuspension on the distribution of epipelagic algae in an estuary. *Est. Coastal and Shelf Sci.* 10: 165-180.
- Baines, S.B. and M.L. Pace. 1991. The production of dissolved organic matter by phytoplankton and its importance to bacteria: Patterns across marine and freshwater systems. *Limnol. Oceanogr.* 36, 1078-1090.
- Baker, e.t. and J.W. LaVelle: 1984, The Effect of Particle Size on the Light Attenuation of Natural Suspensions, *J. Geophys. Res.*, Vol.89, No. C5, pp. 8197-8203.
- Banase, K. 1976. Rates of growth, respiration, and photosynthesis of unicellular algae as related to cell size - A review. *J. Phycol.* 12, 135-140.

- Bartram, W.C. 1980. Experimental development of a model for the feeding of neritic copepods on phytoplankton. *J. Plankton Res.* **3**, 25-51.
- Battjes, J.A. and J.P.F.M. Janssen, "Energy loss and set-up due to breaking of random waves," in Proceedings 16th International Conference Coastal Engineering, pp. 569-587, ASCE, New York, 1978.
- Battjes, J.A. and M.J.F. Stive, "Calibration and verification of a dissipation model for random breaking waves," in Proceedings 19th International Conference Coastal Engineering, ASCE, New York, 1984.
- Berkoff, J.C.W., "Computation of combined refraction-diffraction," Proc. 13th Coastal Eng. Conf., pp. 471-490, 1972.
- Berkoff, J.C.W., N. Booij, and A.C. Radder, "Verification of numerical wave propagation models for simple harmonic linear water waves," Coastal Engineering **6**, pp. 255-279, 1982.
- Bienfang, P.K. 1980. Phytoplankton sinking rates in oligotrophic waters off Hawaii, USA. *Mar. Biol.* **61**, 69-77.
- Blasco, D., T.T. Packard and P. Coble. 1982. Size-dependence of growth rate, respiratory electron transport system activity, and chemical composition in marine diatoms in the laboratory. *J. Phycol.* **18**, 58-63.
- Blough, N.V., O.C. Zafiriou and J. Bonilla. 1993. Optical absorption spectra of waters from the Orinoco River outflow: Terrestrial input of colored organic matter to the Caribbean. *J. Geophys. Res.* **98**, 2271-2278.
- Bohren, C.F. and D.R. Huffman. 1983. *Absorption and Scattering of Light by Small Particles*. J. Wiley and Sons, New York. 530 pp.
- Borchers, P. and J.G. Field. 1981. The effect of kelp shading on phytoplankton production. *Botanica Marina* **XXIV**: 89-91.
- Bowen, A.J. and J.C. Doering, 1984, "Nearshore sediment transport: Estimates from detailed measurements of the nearshore velocity field," Proc. 19th Coastal Engineering Conf., Amer. Soc. Civil Engin., New York, Vol. 2, pp. 1703-14.
- Brenchley, G.A. 1981. Disturbance and community structure: an experimental study of bioturbation in marine soft-bottom environments. *J. Mar. Res.* **39**: 767-790.



- Brenchley, G.A. 1982. Mechanisms of spatial competition in marine soft-bottom communities. *J. Exp. Mar. Biol. Ecol.* 60: 17-33.
- Bricaud, A., A. Morel and L. Prieur: 1983, Optical efficiency factors of some phytoplankters, *Limnol. Oceanogr.* 28, 816-832.
- Bricaud, A. and D. Stramski. 1990. Spectral absorption coefficients of living phytoplankton and nonalgal biogenous matter: A comparison between the Peru upwelling area and the Sargasso Sea, *Limnol. Oceanogr.* **35**, 562-582.
- Bricaud, A., A. Morel, and L. Prieur. 1981. Absorption by dissolved organic matter of the sea (yellow substance) in the UV and visible domains. *Limnol. Oceanogr.* **26**, 43-53.
- Brown, O. B. and H. R. Gordon: 1974, Size-Refraction Index Distribution of Clear Coastal Water Particulates from Light Scattering, *Applied Optics*, Vol. 13, No. 12.
- Bryant, H. C. and N. Jarmie: 1974, *Scientific American*, Vol. 231, p. 60.
- Burt, W. V.: 1952, *Scattering of Light in Turbid Water*, University of California, Los Angeles graduate dissertation.
- Carder, K. L., R. D. Tomlinson and G. F. Beardsley, Jr.: 1972, A Technique for the Estimation of Indices of Refraction of Marine Phytoplankters, *Limnol. Oceanogr.*, Vol. 17, No. 6.
- Carder, K.L., R.G. Steward, G.R. Harvey, and P.B. Ortner. 1989. Marine humic and fulvic acids: Their effects on remote sensing of ocean chlorophyll. *Limnol. Oceanogr.* **34**, 68-81.
- Carder, K.L., R.G. Steward, R.F. Chen, S. Hawes and Z. Lee. 1993. AVIRIS calibration and application in coastal oceanic environments: Tracers of soluble and particulate constituents of the Tampa Bay coastal plume. *Photogrammetric Eng. Rem. Sens.* **59**, 339-344.
- Chisholm, S.W. 1992. Phytoplankton size. In: *Primary Productivity and Biogeochemical Cycles in the Sea*. P.G. Falkowski and A.D. Woodhead (eds.), pp 213-237.

- Christy, J.H. 1982. Adaptive significance of semilunar cycles of larval release in fiddler crabs (Genus *Uca*): test of an hypothesis. *Biol. Bull* 163: 251-263.
- Cleveland, J. S. and A. D. Weidemann: 1993., Quantifying absorption by aquatic particles: A multiple scattering correction for glass-fiber filters. *Limnol. Oceanogr.* 38, 1321-1327.
- Cleveland, J. S., M. J. Perry, D. A. Kiefer, and M. C. Talbot. 1989. Maximal quantum yield of photosynthesis in the northwestern Sargasso Sea. *J. Mar. Res.* 47, 869-886.
- Cleveland, J.S. and M.J. Perry. 1994. A model for partitioning particulate absorption into phytoplanktonic and detrital components. *Deep-Sea Res. I* 41, 197-221.
- Cleveland, J.S. in press. Regional models for phytoplankton absorption as a function of chlorophyll *a* concentration. *J. Geophys. Res.*
- Cloern, J.E. 1982. Does the benthos control phytoplankton biomass in South San Francisco Bay (USA)? *Mar. Ecol. Prog. Ser.* 9, 191-202.
- Cloern, J.E. 1991. Tidal stirring and phytoplankton bloom dynamics in an estuary. *J. Mar. Res.* 49, 203-221.
- Commito, J.A., C.A. Currier, L.R. Kane, K.A. Reinsel, and I.M. Ulm. 1994. Dispersal dynamics of the bivalve *Gemma gemma* in a patchy environment. *Ecol. Monogr.* In press.
- Davis, W.R. 1993. The role of bioturbation in sediment resuspension and its interaction with physical shearing. *J. Exp. Mar. Biol. Ecol.* 171: 187-200.
- Davis-Colley, R.J. 1992. Yellow substance in coastal and marine waters around the South Island, New Zealand. *New Zealand J. Mar. Freshw. Res.* 26, 311-322.
- Davis-Colley, R.J., R.D. Pridmore and J.E. Hewitt. 1986. Optical properties of some freshwater phytoplanktonic algae. *Hydrobiologia* 133, 165-178.
- DePatra K.D. and L.A. Levin. 1989. Evidence of the passive deposition of meiofauna into fiddler crab burrows. *J. Exp. Mar. Biol. and Ecol.* 125: 173-192.

- Duggins, D.O., C.A. Simenstad and J.A. Estes. 1989. Magnification of secondary production by kelp detritus in coastal marine ecosystems. *Science* **245**, 170-173.
- Duntley, S.Q., R. W. Austin, W. H. Wilson, C. F. Edgerton and S. E. Moran: 1974, Ocean Color Analysis, Scripps Institution of Oceanography, SIO Ref. 74-10.
- Durst, C.S., "The relationship between current and wind," *Quart. J. R. Met. Soc.*, Vol. 50, p. 113 (London), 1924.
- Dyer, K. R.: 1986, Coastal and Estuarine Sediment Dynamics, Wiley & Sons, New York, pp.342
- Eckman, J.E. and A.R. M. Nowell. 1984. Boundary skin friction and sediment transport about an animal-tube mimic. *Sedimentology* 31: 851-862.
- Eckman, J.E., A.R. M. Nowell and P.A. Jumars. 1981. Sediment destabilization by animal tubes. *J. Mar. Res.* 39: 361-374.
- Eckman, J.E., D.O. Duggins, and A.T. Sewell. 1989. Ecology of understory kelp environments. I. Effects of kelp on flow and particle transport near the bottom. *J. Exp. Mar. Biol. Ecol.* 129: 173-187.
- Emerson, C.W. and J. Grant. 1991. The control of softshell clam (*Mya arenaria*) recruitment on intertidal sandflats by bedload sediment transport. *Limnol. and Oceanogr.* 36: 1288-1300.
- Epifanio, C. 1987. The role of tidal front in maintaining patches of brachyuran zoeae in estuarine waters. *J. of Crustacean Biology* 7: 513-517.
- Eppley, R.W., J.N. Rogers and J.J. McCarthy 1969. Half-saturation constants for uptake of nitrate and ammonium by marine phytoplankton. *Limnol. Oceanogr.* **14**, 912-920.
- Eppley, R.W., R.W. Holmes, and J.D.H. Strickland. 1967. Sinking rates of marine phytoplankton measured with a fluorometer. *J. exp. mar. Biol. Ecol.* **1**, 191-208.

- Fasham, M.J.R., H.W. Ducklow and S.M. McKelvie. 1990. A nitrogen-based model of plankton dynamics in the oceanic mixed layer. *J. Mar. Res.* **48**, 591-639.
- Fogg, G.E., C. Nalewajko and W.D. Watt. 1965. Extracellular products of phytoplankton photosynthesis. *Proc. R. Soc. Lond., Ser. B.* **162**, 517-534.
- Fonseca, M.S. , J.S. Fisher, J.C. Zieman, and G.W. Thayer. 1982. Influence of the seagrass, *Zostera marina* L. on current flow. *Est. Coast. Shelf Sci.* **15**: 351-364.
- Fonseca, M.S. and J.S. Fisher, 1986. A comparison of canopy friction and sediment movement between four species of seagrass with reference to their ecology and restoration. *Mar. Ecol. Progr. Ser.* **29**: 15-22.
- Forward, R.B. 1985. Behavioral responses of larvae of the crab *Rhithropanopeus harrisii* (Brachyura: Xanthidae) during diel vertical migration. *Mar. Biol.* **90**: 9-18.
- Franks, P.J.S., J.S. Wroblewski and G.R. Flierl. 1986. Behavior of a simple plankton model with food-level acclimation by herbivores. *Mar. Biol.* **91**, 121-129.
- Frechette, M. and E. Bourget. 1985. Food limited growth of *Mytilus edulis* L. in relation to the benthic boundary layer. *Can. J. Fish. Aquat.Sci.* **42**: 1166-1170.
- Frechette, M. C.A. Butman and W.R. Geyer, 1989. The importance of boundary layer flows in supplying phytoplankton to the benthic suspension feeder, *Mytilus edulis* L. *Limnol. and Oceanogr.* **34**: 19-36.
- Frost, B.W. 1991. The role of grazing in nutrient-rich areas of the open sea. *Limnol. Oceanogr.* **36**, 1616-1630.
- Fuller, C.M., C.A. Butman and N. Conway. 1991. Periodicity in fecal pellet production by the capitellid polychaete *Mediomastus ambiseta*, throughout the day. *Proc. Second Int'l. Polychaete Conference.*
- Gambi, M.C., A. R. M. Nowell and P.A. Jumars. 1990. Flume observations on flow dynamics in *Zostera marina* (eelgrass) beds. *Mar.Ecol. Progr. Ser.* **61**: 159-160.

- Grant, J. 1988. Intertidal bedforms, sediment transport and stabilization by benthic microalgae. pp 499-510 In: P.L. de Boer et al., eds. Tide-influenced sedimentary environments and facies. D. Reidel Publishing Co.
- Grant, J. and G. Gust. 1987, Prediction of coastal sediment stability from photopigment content of mats of purple sulfur bacteria. *Nature* 330: 244-246.
- Grant, J. and U.V. Bathmann, 1987. Swept away: Resuspension of bacterial mats regulates benthic-pelagic exchange of sulfur. *Science* 236: 1472-1474
- Grant, W.D., L.F. Boyer and L.P. Sanford, 1982. The effects of bioturbation on the initiation of motion on intertidal sands. *J. Mar. Res.* 40: 659-677.
- Gregg, W.W. and J.J. Walsh, 1992, "Simulation of the 1979 spring bloom in the Mid-Atlantic Bight: a coupled physical/biological/optical model," *J. Geophys. Res.* 97(C4): 5723-5743.
- Hansen, J. E., and L. D. Travis: 1974, Light Scattering in Planetary Atmospheres, submitted to Space Science Reviews.
- Harlin, M.M. B. Thorne-Miller and J.C. Boothroyd. 1982. Seagrass-sediment dynamics of a flood-tidal delta in Rhode Island (USA) *Aquatic Botany* 14: 127-138.
- Harris, G.P. and B.B. Piccinin. 1977. Photosynthesis by natural populations. *Arch. Hydrobiol.* **80**, 405-457.
- Harrison, P.L., R.C. Babcock, G.D. Bull, J.K. Oliver, C.C. Wallace and B.L. Willis. 1984. Mass spawning on tropical reef corals. *Science* 233: 1187-1189.
- Harvey, G.R., D.A. Boran, L.A. Chesal and J.N. Takar. 1983. The structure of marine fulvic acid and humic acids. *Mar. Chem.* **12**, 119-133.
- Hobson, E.S. and J.R. Chess. 1979. Zooplankters that emerge from the lagoon floor at night at Kure and Midway Atolls, Hawaii. *Fish. Bull. US* 77: 275-280.

- Hofmann, E.E. and J.W. Ambler. 1988. Plankton dynamics on the outer southeastern U.S. continental shelf. Part II: A time-dependent biological model. *J. Mar. Res.* **46**, 883-917.
- Hood, R.R., M.R. Abbott and A. Huyer. 1991. Phytoplankton and photosynthetic light response in the coastal transition zone off Northern California in June 1987. *J. Geophys. Res.* **96**, 14,769-14,780.
- Horikawa, K., 1988, *Nearshore Dynamics and Coastal Processes*, University of Tokyo Press, 522 pp.
- Huettel, M. and G. Gust. 1992. Impact of bioroughness on interfacial solute exchange in permeable sediments. *89*: 253-267.
- Humphrey, G.F. 1975. The photosynthesis: Respiration ratio of some unicellular marine algae. *J. Expl. Mar. Biol. Ecol.* **18**, 111-119.
- Huntley, M.E., V. Marin and F. Escritor. 1987. Zooplankton grazers as transformers of ocean optics: A dynamic model. *J. Mar. Res.* **45**, 911-945.
- Inman, D.L. and R.A. Bagnold, 1963, "Littoral processes," p. 529-553 in M.N. Hill (ed) The Sea, V. 3f, The Earth Beneath the Sea, Interscience (John Wiley & Sons), New York, London, 963 pp.
- Inman, D.L., J.A. Zampol, T.E. White, D.M. Hanes, B.W. Waldorf, and K.A. Kastens, "Field measurements of sand motion in the surf zone," Proc. of the 17th Coastal Engineering Conf., Amer. Soc. Civil Engin., New York, Vol. 2, p. 1215-34, 1980.
- Ippen, A.T. and P.S. Eagleson, 1955, "A study of sediment sorting by waves shoaling on a plane beach," U.S. Army Corps of Engineers, Tech Memo #63, 83 pp.
- Iturriaga, R.H. and D.A. Siegel. 1988. Determination of absorption properties of individual marine particulates: A microphotometric approach. *SPIE, Ocean Optics IX.* **925**, 277-287.
- Jackson, G.A. and C.D. Winant. 1983. Effect of a kelp forest on coastal currents. *Cont. Shelf Res.* **2**: 75-80.
- Jeffrey, S.W. and G.F. Humphrey : 1975, New spectrophotometric equations for determining chlorophylls a, b, c1 and c2 in higher plants, algae, and natural phytoplankton. *Biochem. Physiol. Pflanzen* **167**: pp. 191-194.

- Jenkins, S. A. and D. L. Inman, 1985, "On a submerged sphere in a viscous fluid excited by small amplitude periodic motions," Jour. Fluid Mech., Vol. 157, pp. 199-124.
- Jenkins, S. A., D. L. Inman and W. G. Van Dorn: 1981, The evaluation of sediment management procedures; Phase IV-VI Final Report, Scrip Institution of Oceanography, SIO Reference 81-22
- Jenkins, S.A. and J. Wasyl, 1990, "Resuspension of Estuarial Fine Sediments," Journal of Coastal Research, Vol. 6, No. 4, pp. 961-980.
- Jerlov, N.G. 1976. *Marine Optics*. Elsevier, Amsterdam. 231 pp.
- Jimenez-Perez, L.C. and J.R. Lara-Lara. 1988. Zooplankton biomass and copepod community structure in the Gulf of California during the 1982-1983 El Niño event. *CalCOFI Rep.*, **XXIX**, 122-128.
- Joseph, J.:1955, Extinction measurements to indicate distribution and transport of watermasses, In; *Proc. UNESCO, Symp. Phys. Oceanogr.*, Tokyo, pp. 59-75.
- Jumars, P.J. and R.R. M Nowell. 1984. Effects of benthos on sediment transport: difficulties with functional grouping. *Cont. Shelf. Res.* 3: 115-130.
- Junge, C.E.: 1963, *Air Chemistry and Radioactivity*, Academic Press, New York, p. 382.
- Kamykowski, D. and S.J. Zentara. 1986. Predicting plant nutrient concentrations from temperature and sigma-*t* in the upper kilometer of the world ocean. *Deep-Sea Res.* **33**, 89-105.
- Keiber, R.J., X. Zhou, and K. Mopper. 1990. Formation of carbonyl compounds from UV-induced photodegradation of humic substances in natural waters: Fate of riverine carbon in the sea. *Limnol. Oceanogr.* **35**, 1503-1515.
- Kirby, J.T., "Higher-order approximations in the parabolic equation method for water waves," J. Geophys. Res., **91** (C1), pp. 933-952, 1986a.
- Kirby, J.T., "Open boundary condition in the parabolic equation method," J. Waterway, Port, Coastal, and Ocean Eng. **112** (3), pp. 460-465, 1986c.

- Kirby, J.T., "Rational approximations in the parabolic equation method for water waves," Coastal Engineering 10, pp. 355-378, 1986b.
- Kirk, J. T.O.: 1983, Light and photosynthesis in aquatic ecosystems, Cambridge University Press, New York, p. 72.
- Kirk, J.T.O. 1975a. A theoretical analysis of the contribution of algal cells to the attenuation of light within natural waters. 1. General treatment of suspensions of pigmented cells. *New Phytol.* **75**, 11-20.
- Kirk, J.T.O. 1975b. A theoretical analysis of the contribution of algal cells to the attenuation of light within natural waters. II. Spherical cells. *New Phytol.* **75**, 21-36.
- Kirk, J.T.O. 1976. A theoretical analysis of the contribution of algal cells to the attenuation of light within natural waters. III. Cylindrical and spheroidal cells. *New Phytol.* **77**, 341-358.
- Kirk, J.T.O.: 1981, Monte Carlo study of the nature of the underwater light field in, and the relationships between optical properties of, turbid yellow waters, *Aust. J. Freshwater Res.*, 32, pp. 517-532.
- Kishino, M., M. Takahashi, N. Okami and S. Ichimura. 1985. Estimation of the spectral absorption coefficients of phytoplankton in the sea. *Bull. Mar. Sci.* **37**, 634-642.
- Kitchen, J. C. and J. R. V. Zaneveld: 1992, A three-layer sphere model of the optical properties of phytoplankton, *Limnol. Oceanogr.*, Vol. 37, No. 8, pp. 1680-1690.
- Klemas, V., J. thomas, J. Zaitzeff, 1987, Remote Sensing of Estuaries, Proceedings of a Workshop, Washington, D.C., NOAA, Estuaries Programs Office, 250 pages.
- Kremer, J.N. and S.W. Nixon. 1978. *A Coastal Marine Ecosystem. Simulation and Analysis*. Springer-Verlag, Berlin. 210 pp.
- Krone, R.B.: 1978, Aggregation of Suspended Particles in an Estuary, In: *Estuarine Transport Process*, B. Kjerfve, (ed.), Univ. of So. Carolina Press, Columbia, SC, pp. 177-190.
- Laane, R.W.P.M. 1980. Conservative behaviour of dissolved organic carbon in the Ems-Dollart estuary and the western Wadden Sea. *Neth. J. Sea Res.* **14**, 192-199.



- Lamb, H., 1932, *Hydrodynamics*, Dover.
- Lambermont, J. and Lebon, G., "Erosion of fine soils," Journal of Hydraulic Research, 16, pp. 27-33, 1978.
- Lamoure, J. & Mei, C.C., 1977, "Effects of horizontally two-dimensional bodies on the mass transport near the sea bottom," J. Fluid Mech., **83**, pp. 415-433.
- Langdon, C. 1988. On the causes of interspecific differences in the growth-irradiance relationship for phytoplankton. II. A general review. J. Plankton Res. **10**: 1291-1312.
- Lee, Z., K. L. Carder, S. K. Hawes, R. G. Steward, T. G. Peacock and C. O. Davis: 1994, J. Appl Optics (in press).
- Longuet-Higgins, M.S., 1953, "Mass transport in water waves," Phil. Trans. R. Soc. Lond. A **245**, pp. 535-581.
- Longuet-Higgins, M.S., 1970, "Steady currents induced by oscillations around islands," J. Fluid Mech., 42, pp. 701-720.
- Lucas, M.I., R.C. Newell, and B. Velimirov. 1981. Heterotrophic utilization of mucilage released during fragmentation of kelp (*Ecklonia maxima* and *Laminaria pallida*). II. Differential utilization of dissolved organic components from kelp mucilage. Mar. Ecol. Progr. Ser. 4: 43-55.
- Lukatelich, R.J. and A.J. McComb. 1986. Distribution and abundance of benthic microalgae in a shallow southwestern Australian estuarine system. Mar. Ecol. Progr. Ser. 27: 287-97.
- MacIsaac, J.J. and R.C. Dugdale. 1969. The kinetics of nitrate and ammonia uptake by natural populations of marine phytoplankton. Deep-Sea Res. **16**, 45-57.
- Madsen, K.M., P. Nilsson and K. Sundback. 1993. The influence of benthic microalgae on the stability of a subtidal sediment. J. Exp. Mar. Biol. Ecol. 170: 159-177.
- Malone, T.C. and P.J. Neale. 1981. Parameters of light-dependent photosynthesis for phytoplankton size fractions in temperate estuarine and coastal environments. Mar. Biol. **61**, 289-297.

- Mann, K.H. 1988. Production and use of detritus in various freshwater, estuarine, and coastal marine ecosystems. *Limnol. Oceanogr.* **33**, 910-930.
- Mantoura, R.F.C. and E.M.S. Woodward. 1983. Conservative behavior of riverine dissolved organic carbon in the severn Estuary: Chemical and geochemical implications. *Geochim. et Cosmochim.* **47**, 1293-1309.
- Marra, J. and C. Ho. 1993. Initiation of the spring bloom in the northeast Atlantic (47 N, 20 W): A numerical simulation. *Deep-Sea Res. II* **40**, 55-73.
- Marra, J., R.R. Bidigare, and T.D. Dickey. 1990. Nutrients and mixing, chlorophyll and phytoplankton growth. *Deep-Sea Res.* **37**, 127-143.
- Martens, C.S. 1976. Control of methane sediment-water bubble transport by macrofaunal irrigation in Cape Lookout Bight, North Carolina. *Science* **192**: 998-1000.
- McAllister, C.D., N. Shah, and J.D.H. Strickland. 1964. Marine phytoplankton photosynthesis as a function of light intensity: A comparison of methods. *J. Fish. Res. Bd. Canada* **21**, 159-181.
- Moisan, J.R. 1993. *Modeling Nutrient and Plankton Processes in the California Coastal Transition Zone*. Ph.D. Dissertation. Old Dominion University. 214 pp.
- Moloney, C.L. and J.G. Field. 1991. The size-based dynamics of plankton food webs. I. A simulation model of carbon and nitrogen flows. *J. Plankton Res.* **13**, 1003-1038.
- Moran, M.A. and R.E. Hodson. 1994. Dissolved humic substances of vascular plant origin in a coastal marine environment. *Limnol. and Oceanogr.* **39**: 762-771.
- Morel, A. 1987. Chlorophyll-specific scattering coefficient of phytoplankton. A simplified theoretical approach. *Deep-Sea Res.*, **34**, 1093-1105.
- Morel, A. and A. Bricaud. 1981. Theoretical results concerning light absorption in a discrete medium, and application to specific absorption of phytoplankton, *Deep-Sea Res.* **28A**, 1375-1393.
- Morel, A. and L. Prieur: 1977, Analysis of variations in ocean color., *Limnol. Oceanogr.* Vol. 22, pp. 709-722.

- Morel, A. and R.C. Smith. 1974. Relation between total quanta and total energy for aquatic photosynthesis. *Limnol. Oceanogr.* **19**, 591-600.
- Morel, A.: 1975, The scattering of light by seawater; Experimental results and theoretical approach., NATO Advisory Group for Aerospace Research and Development, AGARD Lecture Series No. 61, "Optics of the Sea, Interface and in-water transmission and imaging."
- Morel, F.M.M., R.J.M Hudson and N.M. Price. 1991. Limitation of productivity by trace metals in the sea. *Limnol. Oceanogr.* **36**, 1742-1755.
- Morin, P., M.V.M. Wafar, and P. Le Corre. 1993. Estimation of nitrate flux in a tidal front from satellite-derived temperature data. *J. Geophys. Res.* **98**, 4689-4695.
- Morrow, J.H. 1988. *Light absorption in naturally occurring marine phytoplankton communities*. Ph.D. Dissertation. University of Southern California, Los Angeles. 161 pp.
- Mullineaux, L. S. 1988. Vertical distributions of the epifauna on manganese nodules: implications for settlement and feeding. *Limnol. and Oceanogr.* **34**: 1247-1262.
- Nelson, J.R. and C.Y Robertson. 1993. Detrital spectral absorption: Laboratory studies of visible light effects on phytopdetritus absorption, bacterial spectral signal, and comparison to field measurements. *J. Mar. Res.* **51**, 181-207.
- Neumann, G., "Ober die komplexe Natur des Seeganges, Teil 1 and 2," *Deut. Hydrogr. Zeit.*, Vol. 5, No. 2/3, pp. 95-110, No. 5/6, pp. 252-277, 1952.
- Newell, R.C. 1982. The biological role of detritus in the marine environment. *Proc. NATO Adv. Res. Inst. Bombannes, May 1982*. Plenum Press. pp 317-343.
- Newell, R.C. and J.G. Field. 1983. The contribution of bacteria and detritus to carbon and nitrogen flow in a benthic community. *Mar. Biol. Lett.* **4**, 23-26.
- Nielsen, P., I.A. Svendsen and C. Staub, "Onshore-offshore sediment movement on a beach," in Proceedings 16th International Conference Coastal Engineering, pp. 1475-1492, ASCE, New York, 1978.

- Nielsen, P., "Some basic concepts of wave sediment transport," Series paper No. 20, Institute of Hydrodyn. and Hydr. Eng., Techn. Univ. of Denmark, 1979.
- O'Riordan, C.A. , S.G. Monismith and J.R. Koseff. in press. The effect of bivalve excurrent jet dynamics on mass transfer in a benthic boundary layer. *Limnol. and Oceanogr.*
- O'Riordan, C.A., S.G. Monismith, and J.R. Koseff. 1993. An experimental study of concentration boundary layer formation over a bed of model bivalves. *Limnol. and Oceanogr.* 38: 1712-1729.
- Ohlhorst, S.L. 1982. Diel migration patterns of demersal reef zooplankton. *J. Exp. Mar. Biol. Ecol.* 60: 1-15.
- Orth, R.J. 1977. The importance of sediment stability in seagrass communities. p. 281-300 In: B.C. Coull (ed). *Ecology of marine benthos*. Univ. of South Carolina Press. Columbia.
- Owen, R.W., Jr. 1974. Distribution of primary production, plant pigments and Secchi depth in the California Current region. 1969. California Cooperative Oceanic Fisheries Investigations, Atlas No. 20.
- Paffenhöfer, G.-A. 1984. Calanoid copepod feeding: Grazing on small and large particles. In: *Trophic Interactions within Aquatic Ecosystems*, D.G. Meyers and J.R. Strickler, (eds.), pp 75-95.
- Palmer, M.A. 1988. Dispersal of marine meiofauna: a review and conceptual model explaining passive transport and active emergence with implications for recruitment. *Mar. Ecol. Progr. Ser.* 48: 81-91.
- Parsons, T.R., M. Takahashi, and B. Hargrave. 1984. *Biological Oceanographic Processes*. Pergamon, New York. 332 pp.
- Percival, E. and R. McDowell. 1967. Chemistry and enzymology of marine polysaccharides. 219 pp. London. Academic Press.
- Peterson, C.H. and R. Black. 19487. Resource depletion by active suspension feeders on tidal flats: influence of local density and tidal elevation. *Limnol. Oceanogr.* 32: 143-166.
- Petzold, T. J.: 1972, Volume Scattering Functions for Selected Ocean Waters, Scripps Institution of Oceanography, SIO Ref. 72-78.

- Phinney, D.A. and C.S. Yentsch. 1991. On the contribution of particles to blue light attenuation in the sea. *J. Plankton Res.* **13**, 143-152.
- Platt, T., C.L. Gallegos and W.G. Harrison. 1980. Photoinhibition of photosynthesis in natural assemblages of marine phytoplankton. *J. Mar. Res.* **38**, 687-701.
- Porter, 1974. Zooplankton feeding by the Caribbean reef-building coral *Montastrea cavernosa*. *Proc. 2nd Int. Coral Reef. Symp. Brisbane* 1: 111-125.
- Probert, P.K. 1984. Disturbance, sediment stability and trophic structure of soft-bottom communities. *J. Mar. Res.* **42**: 893-921.
- Probyn, T.A. 1985. Nitrogen uptake by size-fractionated phytoplankton populations in the southern Benguala upwelling system. *Mar. Ecol. Prog. Ser.* **22**, 249-258.
- Probyn, T.A. and S.J. Painting. 1985. Nitrogen uptake by size-fractionated phytoplankton populations in Antarctic surface waters. *Limnol. Oceanogr.* **30**, 1327-1332.
- Radder, A.C., "On the parabolic equation method for water-wave propagation," *J. Fluid Mech.*, **95**, Part 1, pp. 159-176, 1979.
- Rashid, M. A., D. E., Muckley and K. R. Robertson: 1972, Interactions of a marine humic acid with clay minerals and a natural sediment, *Geoderma*, Vol. 8, pp.11-27.
- Reed, D.C. and M.S. Foster. 1984. The effects of canopy shading on algal recruitment and growth in a giant kelp forest. *Ecology* **65**: 937-948.
- Rhoads D.C. and L.F. Boyer, 1982. The effects of marine benthos on physical properties of sediments: A successional perspective. p3-52, In: In: P.L. McCall and M.J.S. Tevesz (eds), *Animal-Sediment Relations*. Plenum Press.
- Rhoads, D.C., J.Y. Yingst, and W. Ullman. 1978. Seafloor stability in central Long Island Sound: I. Temporal changes in erodability of fine-grained sediment. Pages 221-224 in M.L. Wiley ed, *Estuarine Interactions*. Academic Press. NY.

- Rhoads, D.C., L.F. Boyer, B.L. Welsh, and G.R. Hampson. 1984. Seasonal dynamics of detritus in the benthic turbidity zone (BTZ); Implications for bottom-rack molluscan mariculture. *Bull. Mar. Science* 35: 536-549.
- Robertson, A.I. and R.K. Howard. 1978. Diel trophic interactions between vertically migrating zooplankton and their fish predators in an eelgrass community. *Mar. Biol.* 48: 207-213.
- Sathyendranath, S., L. Lazzara, and L. Prieur. 1987. Variations in the spectral values of specific absorption of phytoplankton. *Limnol. Oceanogr.* 32, 403-415.
- Schaffer, G.P. and M.J. Sullivan. 1988. Water column productivity attributable to displaced benthic diatoms in well-mixed shallow estuaries. *J. Phycology* 24: 132-140.
- Schlesinger, D.A., L.A. Molot, and B. Shuter. 1981. Specific growth rates of freshwater algae in relation to cell size and light intensity. *Can. J. Fish. Aquat. Sci.* 38, 1052-1058.
- Schmidt, W., "Wirkungen der ungeordneten Bewegungen im Wasser der Meere und Seen," *Ann. d. Hydr. u. Marit. Meteorol.*, Vol. 45, pp. 367-381 and 431-445 (Berlin), 1917.
- Schoonmaker, J. S., R. R. Hammond, A. L. Heath and J. S. Cleveland: 1994, A Numerical Model for Prediction of Sub-littoral Optical Visibility, SPIE Ocean Optics XII, pp. 18.
- Schoonmaker, J. S.: 1993, Unpublished data.
- Schroeder, P.C. and C.O. Hermans 1975. Ch.1. Annelida: Polychaeta in *Reproduction of Marine Invertebrates Volume III. Annelids and Echiurids.* ed. by A.C. Giese and J.S. Pearse. Boxwood Press
- Sharp, J.H. 1977. Excretion of organic matter by marine phytoplankton: Do healthy cells do it? *Limnol. Oceanogr.* 22, 381-399.
- Smayda, T.J. 1970. The suspension and sinking of phytoplankton in the sea. *Oceanogr. Mar. Biol. Ann. Rev.* 8, 353-414.
- Smith, R.C. and K.S. Baker: 1981, Optical properties of the clearest natural waters (200- 800 nm). *Appl. Opt.* 20, pp. 177-184.

- Snider, 1985. Demersal zooplankton of the giant kelp *Macrocystis pyrifera*: Patterns of emergence and the population structure of three gammarid amphipod species. PhD Thesis. Scripps Inst. of Oceanography, La Jolla, CA
- Stimson, J. 1985. The effect of shading by the table coral *Acropora hyacinthus* on understory corals. *Ecology* 66: 40-53.
- Sverdrup, H. U., M. W. Johnson and R. H. Fleming: 1942, *The Oceans*, Prentice-Hall, Englewood Cliffs, N. J. , pp 1087.
- Sverdrup, H.U. 1953. On conditions for vernal blooming of phytoplankton. *J. Const. int. Explor. Mer.* **18**, 287-295.
- Talling, J.F. 1957. Photosynthetic characteristics of some freshwater plankton diatoms in relation to underwater radiation. *New Phytol.* **56**, 29-50.
- Tamaki, A. 1987. Comparison of resistivity to transport by wave action in several polychaete species on an intertidal sand flat. *Mar. Ecol. Progr. Ser.* **37**: 181-189.
- Tassan, S.: 1988, The effect of dissolved 'yellow substance' on the quantitative retrieval of chlorophyll and total suspended sediment concentrations from remote measurements of water colour, *International Journal of Remote Sensing*, Vol. 9, No. 4, pp. 787-797.
- Thiebaut, E., J.C. Dauvin, and Y. Lagaduec. 1992. Transport of *Owenia fusiformis* larvae (Annelida-Polychaeta) in the Bay of Seine. I. Vertical distribution in relation to water column stratification and ontogenic vertical migration. *Mar. Ecology Progr. Ser.* **80**: 29-39.
- Thomas, W.H. and D.L.R. Seibert. 1974. Distribution of nitrate, nitrite, phosphate and silicate in the California Current region. 1969. *California Cooperative Oceanic Fisheries Investigations*, Atlas No. 20.
- Thorade, H., "Die Geschwindigkeit von Triftströmungen und die Ekman'sche Theorie," *Ann. d. Hydr. u. Marit. Meteorol.*, Vol. 42, p. 379, 1914.
- Traganza, E.D., D.A. Nestor and A.K. McDonald. 1980. Satellite observations of a nutrient upwelling off the coast of California. *J. Geophys. Res.* **85**, 4101-4106.

- Traganza, E.D., J.C. Conrad and L.C. Breaker 1981. Satellite observations of a cyclonic upwelling system and giant plume in the California current. *Coastal Upwelling*. Coastal and Estuarine Sciences 1. pp 228 - 241.
- van de Hulst, H. C.: 1957, *Light Scattering by Small Particles*, John Wiley & Sons, New York, pp. 857.
- Vedel, A., B.B. Anderson and H. U. Riisgard. 1994. Field investigations of pumping activity of the facultatively filter-feeding polychaete *Nereis diversicolor* using an improved phototransducer system. *Mar. Ecol. Progr. Ser.* 103: 91-101.
- Velimirov, B. 1979. Fatty acid composition of kelp on the west coast of South Africa and some ecological implications. *Botanica Marina* XXII: 237-240.
- Velimirov, B. 1980. Formation and potential trophic significance of marine foam near kelp beds in the Benguela upwelling system. *Mar. Biol.* 58: 311-318.
- Velimirov, B. 1982. Sugar and lipid components in sea foam near kelp beds. *P.S.Z.N. I. Marine Ecology*. 3: 97-107.
- Walsh, J.J., D.A. Dieterle and J.R. Pribble. 1991. Organic debris on the continental margins: A simulation analysis of source and fate. *Deep-Sea Res.* 38, 805-828.
- Walsh, J.J., D.A. Dieterle and M.B Meyers. 1988. A simulation analysis of the fate of phytoplankton within the Mid-Atlantic Bight. *Continental Shelf Res.* 8, 757-787.
- Walsh, J.J., K.L. Carder, and F.W. Müller-Karger. 1992. Meridional fluxes of dissolved organic matter in the North Atlantic Ocean. *J. Geophys. Res.* 97, 15,625-15,637.
- Wildish, D.J. and D.D. Kristmanson. 1974. Tidal energy and sublittoral macrobenthic animals in estuaries. *J. Fish. Res. Board. Can.* 1197-1206.
- Willis, B.L. and J.K. Oliver. 1990. Direct tracking of coral larvae: implications for dispersal studies of planktonic larvae in topographically complex environments. *Ophelia* 32: 145-162.
- Wroblewski, J.S. 1977. A model of phytoplankton plume formation during variable Oregon upwelling. *J. Mar. Res.*, 35, 357-393.



- Wroblewski, J.S., J.L. Sarmiento and G.R. Flierl. 1988. An ocean basin scale model of plankton dynamics in the north Atlantic 1. Solution for the climatological oceanographic conditions in May. *Global Biogeochemical Cycles* **2**, 199-218.
- Wyllie, J.G. and R.J. Lynn. 1971. *Distribution of Temperature and Salinity at 10 Meters. 1960-1969, and Mean Temperature, Salinity and Oxygen at 150 meters. 1950-1968, in the California Current*. California Cooperative Oceanic Fisheries Investigations, Atlas No. 15. 187 pp.
- Yager, P.L., A.R. M. Nowell and P.A. Jumars. 1993. Enhanced deposition to pits: a local food source for benthos. *J. Mar. Res.* **51**: 209-236.
- Yentsch, C.S., Skea, W., J.C. Laird, and T.S. Hopkins. 1979. Ocean Color Observations. In: *The Apollo-Soyuz Test Project Report Volume II*. F. El-Baz and B.M. Warner (eds). NASA SP-412. pp 441-454.
- Yingst, J.Y. and D.C. Rhoads. 1978 Seafloor stability in central Long Island Sound: Part II. Biological interactions and their potential importance for seafloor erodability. PP 245-260. In *Estuarine Interactions*, M. Wily, ed. Academic Press, Inc. New York.
- Zaneveld, J.R.V., J.C. Kitchen and J.L. Mueller. 1993. Vertical structure of productivity and its vertical integration as derived from remotely sensed observations. *Limnol. Oceanogr.* **38**, 1384-1393.
- Zentara, S.-J. and D. Kamykowski. 1977. Latitudinal relationships among temperature and selected plant nutrients along the west coast of North and South America. *J Mar. Science* **35**, 321-337.

**APPENDIX A**

**User Manual  
for the  
Predictive Visibility Model (PVM)**

## 1.0 INTRODUCTION

The Predictive Visibility Model (PVM) estimates the spatial and temporal distributions of environmental drivers in coastal waters required to predict 1) subsurface scattering, absorption, and diffuse attenuation coefficients within a factor of two, and 2) to forecast episodic changes of operational and environmental significance. The model inputs nowcast and forecast values of wave statistics and river discharge flow rates, and computes suspended particle distributions in successive two-hour time steps between the nowcast and forecast conditions. The model creates selectable display maps of the vertical visibility distributions for viewing the output from the current time step, or the output from any other time step, provided that output files are uncompressed.

At the end of each time step, the output files are copied from the work directory to a subdirectory under the working directory. This subdirectory is given a name that corresponds to the current time step. For a full-day run, there will be 12 subdirectories corresponding to the two-hour time steps throughout the day. The files in these sub-directories are compressed using the UNIX "compress" routine, to save disk space.

## 2.0 ARCHITECTURE

The software architecture for the PVM, as shown in Figure A-1, has four main components: (1) the Executive, (2) the Physics Models, (3) the Data Display package, and (4) the Geographical Information System (GIS) package. Each component is a separate executable or is composed of a set of executables.

The Executive is the central controller, data manager, and user interface for what is commonly referred to as the "on-line" system. The Executive provides an X-Windows menu interface for selecting site locations, setting model parameters, executing models, and invoking data or GIS displays. The data management consists of archives of basemap data and predetermined geological and biological "category" parameters. Each site location has its own database of parameters and data files. In addition, a user may completely configure and populate a private database. Output from the physics models are compressed and archived into directories at the end of each time step.

## System Architecture

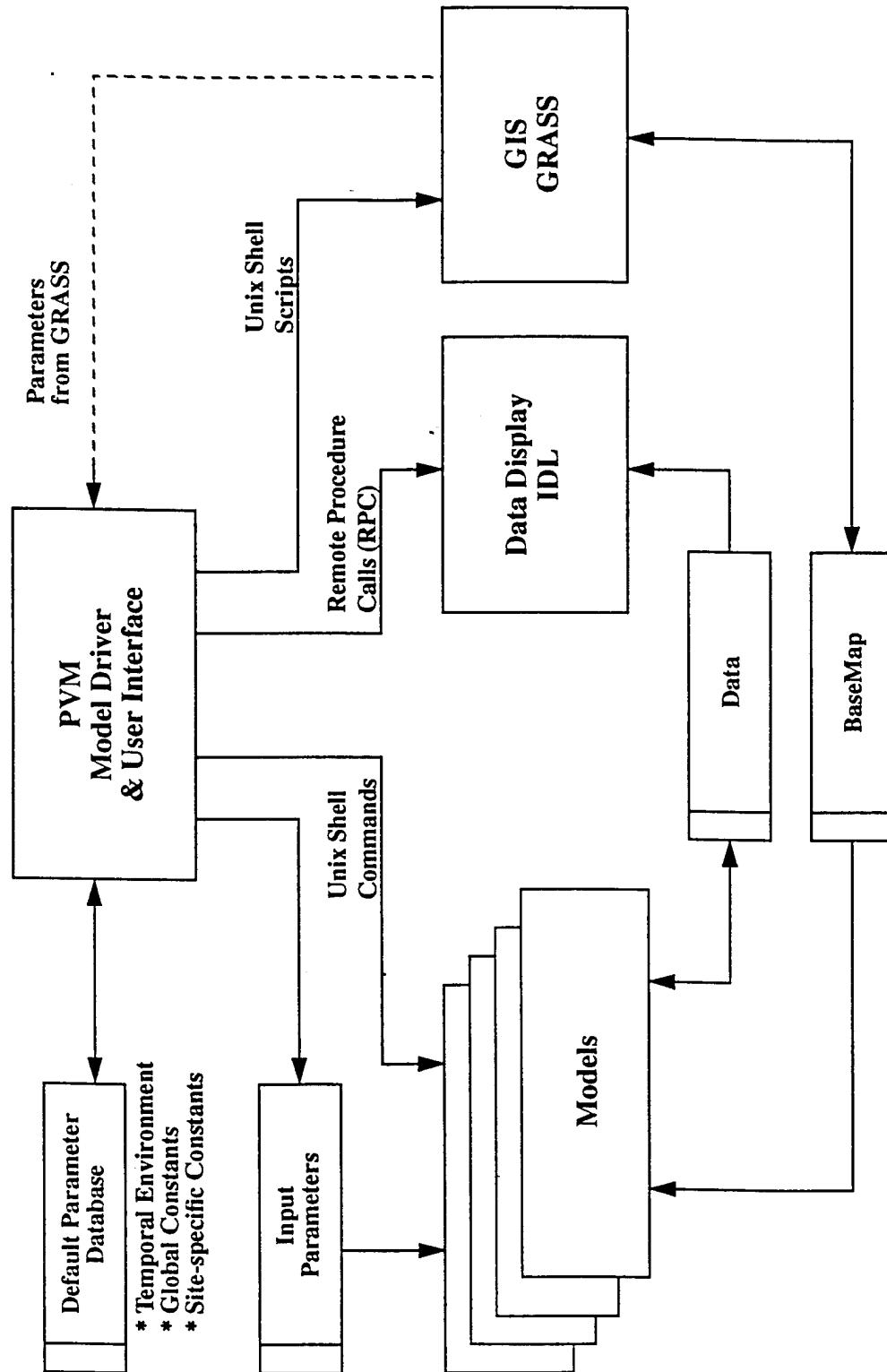


Figure A-1. System Architecture  
A-3

The Physics Models are a set of stand-alone FORTRAN programs. These programs are the calculation engines for the PVM. Each program is controlled by a set of input parameters. The Executive manages input and output data files for each program. The models do not talk directly to each other, rather their input parameters and data files are managed by the Executive. The Executive presents output data from one model to the next model, as appropriate.

The models fall into two categories, Initialization models and Time Step models. Initialization models are executed once per day and generate data in the form of values vs. time of day. Time Step models are executed once per time step, where a time step is a two-hour time period. Some models depend on data from the previous time step; that is, they require "feedback" data. Each of the models that use feedback data have a mode switch which tells it if this is the time-zero (t0) time step, or if it is to use the feedback data.

The Data Display package is IDL, a widely used Commercial Off-the-Shelf (COTS) display package from Research Systems, Inc. (RSI). IDL is operated as a server. The Executive connects to IDL as a client and sends instructions through Remote Procedure Calls (RPC) used to bring up display windows and specify the paths of data files. Special Coastal Water Clarity (CWC) display routines have been written in the IDL language to present the bit mapped data with appropriate scales, axes, colors, and contour overlays.

The GIS package is GRASS, a public domain system from the U.S. Army Corp. of Engineers. GRASS is used off-line to generate a digitized map database, register satellite images, and extract data from remote sensors. The processes performed using GRASS are done in an interactive mode, and setting up the BASEMAP for a particular site is labor intensive. Once the site has been set up, it is archived and accessible to the Executive for presentation to the physics models. On-line displays of basemap data and satellite images are controlled by the executive through GRASS shell commands.

## **2.1 System Requirements**

This section describes the platform and disk storage requirements for operating the PVM.

## **Required Platform**

SunOS (Solaris 2.3) workstation

## **Disk Space Requirements**

### **Installation**

The disk space required for installing the PVM project tree is 78,521 kilobytes: 63,632K for the prj/pvm directory, 14,296K for the cwc\_data directory, and 1,093K for the models directory.

### **Model Execution**

The disk space requirements for storing the output of a single time step is 51 megabytes: 44 megabytes for the output directory, and 7 megabytes for an archived compressed time step directory. The table below shows the storage requirements for both a one- and two-day run.

output directory size	44M
1 archived time step	7M
12 archived time steps	84M
one day:	$44\text{M} + 84\text{M} = 128\text{M}$
two day:	$44\text{M} + 2 \times 84\text{M} = 212\text{M}$

Note: The size of the output directory remains constant.

## **2.2 Installation Procedures**

This section describes the installation procedures which consists of five steps, as shown below. Step 1 lists the products that should already be installed. Step 2 shows the information to be added to the (.cshrc) file. Step 3 shows the command line instruction required to invoke the modified (.cshrc) file. Step 4 shows an example of the required modifications to the configure.mk file. Step 5 lists the command line instructions that perform the actual installation.

Step 1. The following products should already be installed.

<u>Product</u>	<u>Version</u>
Motif	1.2
Wcl	2.4
IDL	3.5 w/RPC's
Xgrab	2.3

Step 2. Add the following to your (.cshrc) file.

```
setenv CWCHOME      <CWC executive installation directory>
setenv CWCMODELBIN <location of CWC model executables>
setenv CWCDATA      <location of CWC data directory>
setenv IDL_DIR       <IDL installation directory>
setenv IDL_PATH      +$IDL_DIR/lib:$CWCHOME/idl
setenv XGRABBIN      <location of xgrab executable>
setenv XUSERFILESEARCHPATH $CWCHOME/app-defaults/%N
setenv MANPATH       $CWCHOME/doc/man
```

```
set path = ($path $CWCHOME/bin $CWCMODELBIN $IDL_DIR/bin
$XGRABBIN)
```

Step 3. To invoke these modifications to your (.cshrc) file, type: source  
~/.cshrc

Step 4. Edit configure.mk to specify the locations of the headers and  
libraries for the products listed in Step 1.

### example of an configure.mk file

```
# Configuration file for the CWC projects. This file is included
# by other Makefiles in the project tree.
#
# SCCS ID: @(#)configure.mk.cwc 1.1 06 Oct 1994
#
# Location of IDL which has an installed rpc directory underneath
# Reset only if RPC's not compiled under the IDL_DIR in set in the
# environment
IDL_DIR    = /home/lrssi/public.sol/idl
# Location of WCL headers and libraries
WCLINCDIR  = /usr/include/X11
WCLLIBDIR  = /home/lrssi/public.sol/lib
OS         = __svr4__
RANLIB     = /bin/true
```

Step 5. Type the following in \$CWCHOME. <your group> is the group that is to have permissions on the files in \$CWCHOME.

```
make -f Makefile.cwc GROUP=<your group> includes
make -f Makefile.cwc GROUP=<your group> install
```

For example, if you belong to the UNIX group "staff," use the following:

```
make -f makefile.cwc GROUP=staff includes
make -f makefile.cwc GROUP=staff install
```

### 3.0 PROJECT TREE

The PVM project tree, shown in Figure A-2, has eight subdirectories: one containing the executable, six containing data, and one containing the source for cwc executive. The executables are located in the model/bin subdirectory, and the data files are located in the bio\_cat, optical sed\_cat, sitedirs, and tidal subdirectories.



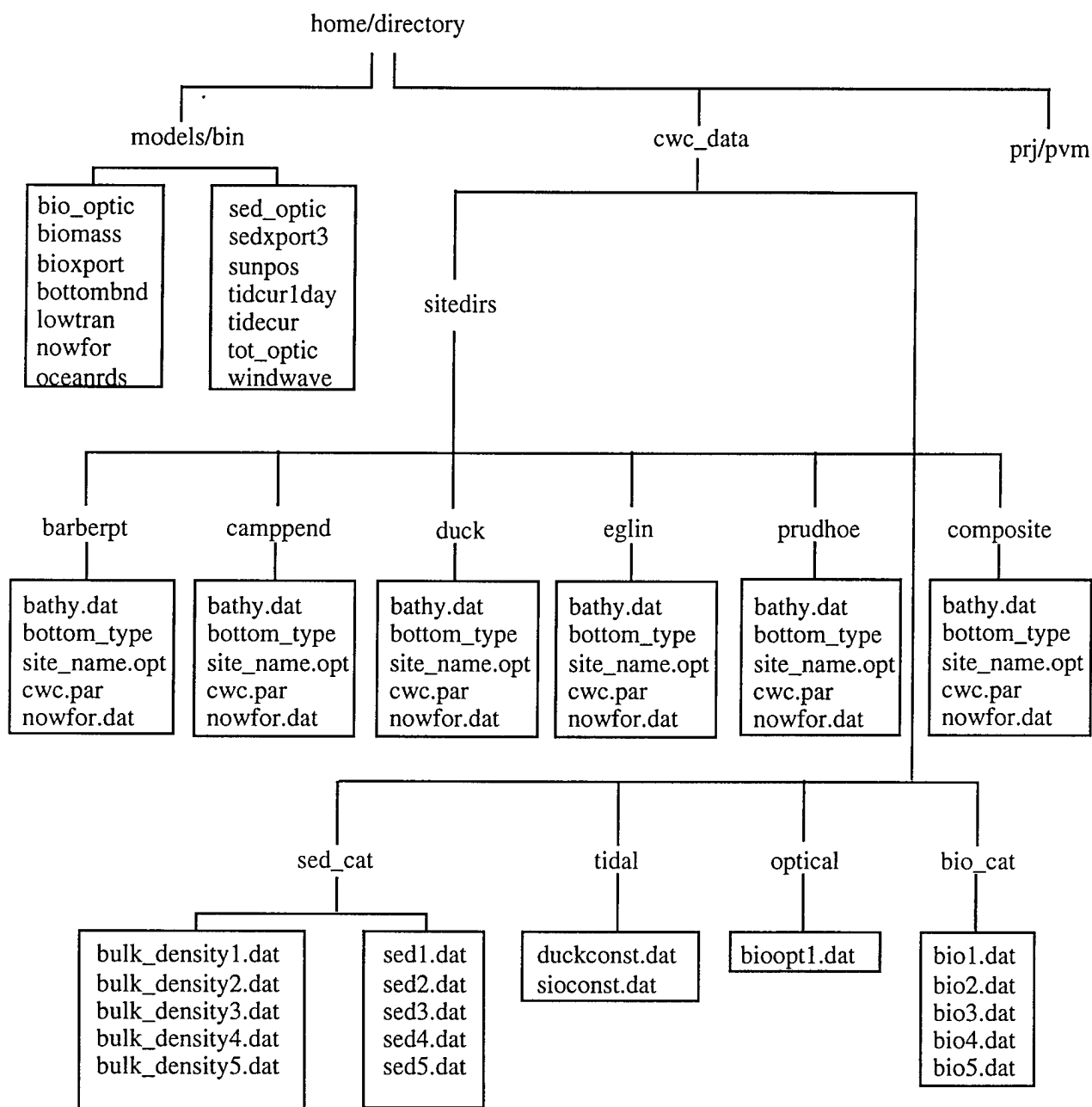


Figure A-2. Description of the PVM Project Tree

The bin/subdirectory contains 14 executables. The executables in alphabetical order are: biomass, bio\_optic, lowtrans, oceanrds, sedxport, sed\_optic, sunpos, tidcur1day, tidecur, tot\_optic, and windwave. A description of each model and their execution sequence is given in Section 4.1. A detailed description of the input and output parameters for each model are listed in Section 5.0.

The bio\_cat/subdirectory contains biological data files of the five generic coastlines. The plankton is modeled as a site-dependent, bi-modal distribution.

The optical/subdirectory contains a file of optical parameters called bioopt1.dat, which is the biological optical scattering matrix for the region of the site being modeled.

The tidal/subdirectory contains harmonic tidal constituents for each site location to be modeled. For example, sioconst.dat would be the tidal constituent file used to model the tides at Camp Pendleton, California.

The sitedirs/subdirectory contains separate subdirectories for each of the five site locations, which include Camp Pendleton, CA; Duck, NC; Barber Point, HI; Prudhoe Bay, AK; and Eglin Air Force Base, FL. Each site subdirectory contains a bathy.dat, bottom\_type.dat, cwc.par, nowfor.dat, and site\_name.opt file.

- bathy.dat contains the site specific bathymetry map data generated off-line in GRASS.
- bottom\_type.dat contains map array of the bottom types that are used to vary the bottom sediment size distribution. This is also generated in GRASS.
- cwc.par contains default input parameters for each site, except time-dependent variables.
- nowfor.dat contains the run time dependent variables. These values can be manually entered from direct observation and/or interpolated from initial and forecast values for Cloud Cover, Air Temperature, Sea Surface Temp, Sea Surface Pressure, 24-hour Precipitation, Surface Wind Speed, Sea Period, Sea Direction, Sea Height, Swell Period, Swell Direction, Swell Height, and Offshore Current Velocity parameters usually obtained from Fleet Numerical Oceanography Center (FNOC).

- site\_name.opt/subdirectory contains the sediment optical scattering matrix also generated off line for the material present at the site being modeled.

The sed\_cat/subdirectory contains the sediment data files for the five generic coastline categories, bulk\_densityx.dat. and sedx.dat.

The tidal/subdirectory specifies the tidal constituent files for each site location.

#### **4.0 MODEL DESCRIPTION AND EXECUTION SEQUENCE**

The execution sequence is performed in two steps called Initialization and Time Step Loop. Initialization generates the environmental and boundary values parameters for the full day, where the models in the Time Step Loop then uses the Initialization output and calculates optical properties of the water column at each two-hour time step. Below is a description of the models in their order of execution.

##### **Initialization**

- 1) **tidcur1day** calculates the water elevation relative to MSL and a single mean offshore tidal current and direction for each of the 12, 2-hour, time steps, and stores the information in a file called "tidcur1day.dat."
- 2) **sunpos** calculates the elevation and azimuth of the sun at 6-minute intervals for the full day.
- 3) **lowtran** uses angular information from "sunpos" to calculate the solar irradiance array for the full day and stores the information in "irad.dat."
- 4) **nowfor** performs a linear interpolation between the initial and forecast values of the Cloud Cover, Air Temperature, Sea Surface Temp, Sea Surface Pressure, 24-hour Precipitation, Surface Wind Speed (sinusoidally varied between midnight and noon), Sea Period, Sea Direction, Sea Height, Swell Period, Swell Direction, Swell Height,

and Offshore Current Velocity obtained from the National Oceanographic Data Distribution System (NODDS), and generates the temporal parameters matrix of values to be used in the simulation. Values in this matrix can be edited.

### Time Step Loop

- 5) **oceanrds** performs refraction-diffraction of the swell component of the wave spectra with input conditions for initial and forecast values of wave period, height, and direction, received from the TPM, bathymetry from "bathy.dat," and water elevation from tidcurlday. Outputs are wave height, direction, and wave numbers for each of the 200 x 200 grid cells; files are called "camppend.wh1," "camppend.an1," and "camppend.wn1."
- 6) **windwave**, by tracking the high frequency component of the wave spectra (rather than the overall component used in "oceanrds") from the TPM, performs a similar refraction-diffraction calculation as "oceanrds," and after interpolation estimate values for each 2-hour time step. Outputs of "windwave" are "camppend.wh2," "camppend.an2," "camppend.wn2," and the combined wave height, "camppend.wht."
- 7) **tidecur** calculates the local currents from the mean-offshore-tidal current, the bathymetry ("bathy.dat"), and any inertial current and direction specified by the TPM matrix. The local current information for each of the 200 x 200 grid cells is resolved into x and y vectors, (true east, true north), and stored as "xcur.xpt," and "ycur.xpt" files.
- 8) **bottombnd** uses wave, current, and bathymetry files to calculate the bottom resuspension to the top of the bottom boundary layer. It uses, as a fundamental input, the sediment size distribution and mass fraction from the data file, "masstotal.dat." "bottombnd" treats each size fraction independently and outputs the bulk density for each fraction at each grid cell. The total sediment distribution is modeled as nine separate size bins.

- 9) **sedxport** advects the inorganic sediment from each of four sources: offshore bottom boundary layer, surfzone, river 1, and river 2. The hydrodynamic forcing parameters (North & East current vectors, wave height, wave angle, and wave number) are read in, and total particle numbers/ml for each grid cell at the four layers are output.
- 10) **sedoptic** inputs sediment particle number and slope files from "sedxport", and calculates optical coefficients over the 200 x 200 point. These coefficient files (for the first time step, due only to the presence of the sediment) are then throughput to a Plankton growth model, "biomass."
- 11) **biomass** computes the growth of nanoplankton (5 microns) and netplankton (20 microns) over a two-hour growth period, and outputs 200 x 200 point arrays of plankton populations for the surface, and for the depth of the 1% light level  $1/(Z_{par})$  to the advection-mixing model, "bioexport."
- 12) **bioexport** advects and mixes plankton numbers using the identical hydrodynamic forcing parameters as "sedxport". Files for plankton number/ml are read from biomass for two plankton sizes (5 & 20 mm) at two vertical layers; 1 meter below the surface, and at the depth of the 1% light level (z-par).
- 13) **bio\_optic** is where optical coefficient computations on the "bioexport.f" files for both discrete cell size bins are done. Output of "bio\_optic" is then throughput to "totoptic."
- 14) **totoptic** is where the optical properties arising from both the sediments and from the biology are combined to yield final outputs of absorption, volume scattering function, backscatter coefficient, diffuse attenuation coefficient, and visibility distance.

## 4.1 Tutorial

This section gives step-by-step instructions on operating the PVM. The sequence of operational procedures are also graphically presented in Figure A-3.

### 4.1.1 Setting Up A New Run

One begins the model execution by typing "cwc," and pressing return. "cwc" is the front-end driver for the PVM. This will bring up a terminal window CWC, which can be iconified, and the main model window (as shown in Figure A-4). In order to proceed, it is first necessary to select a site and name the output directory.

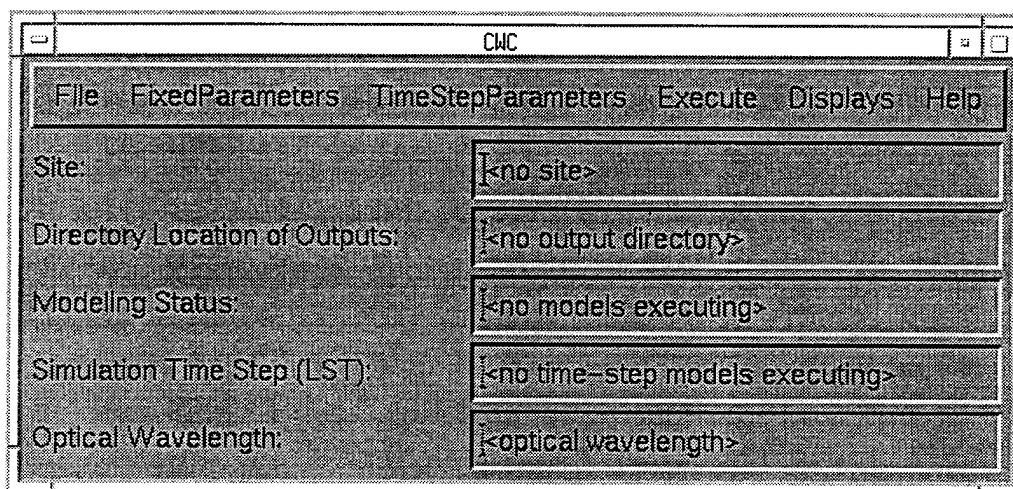


Figure A-4. Main Model Window before Selection of Output Directory

The PVM operates from the point of view of a working directory. All input and output files from a run are stored in this directory. Generally, the first thing that needs to be done when using CWC is to create a working directory. This is done through the "New" option under the File pull down bar.

Selecting this option will bring down a File Selection Window, which is used to select the name of an existing directory or the name of a new working directory. The box on the left allows the user to traverse the existing directories in the file system. The box on the right shows the directory names already in use at the present location.

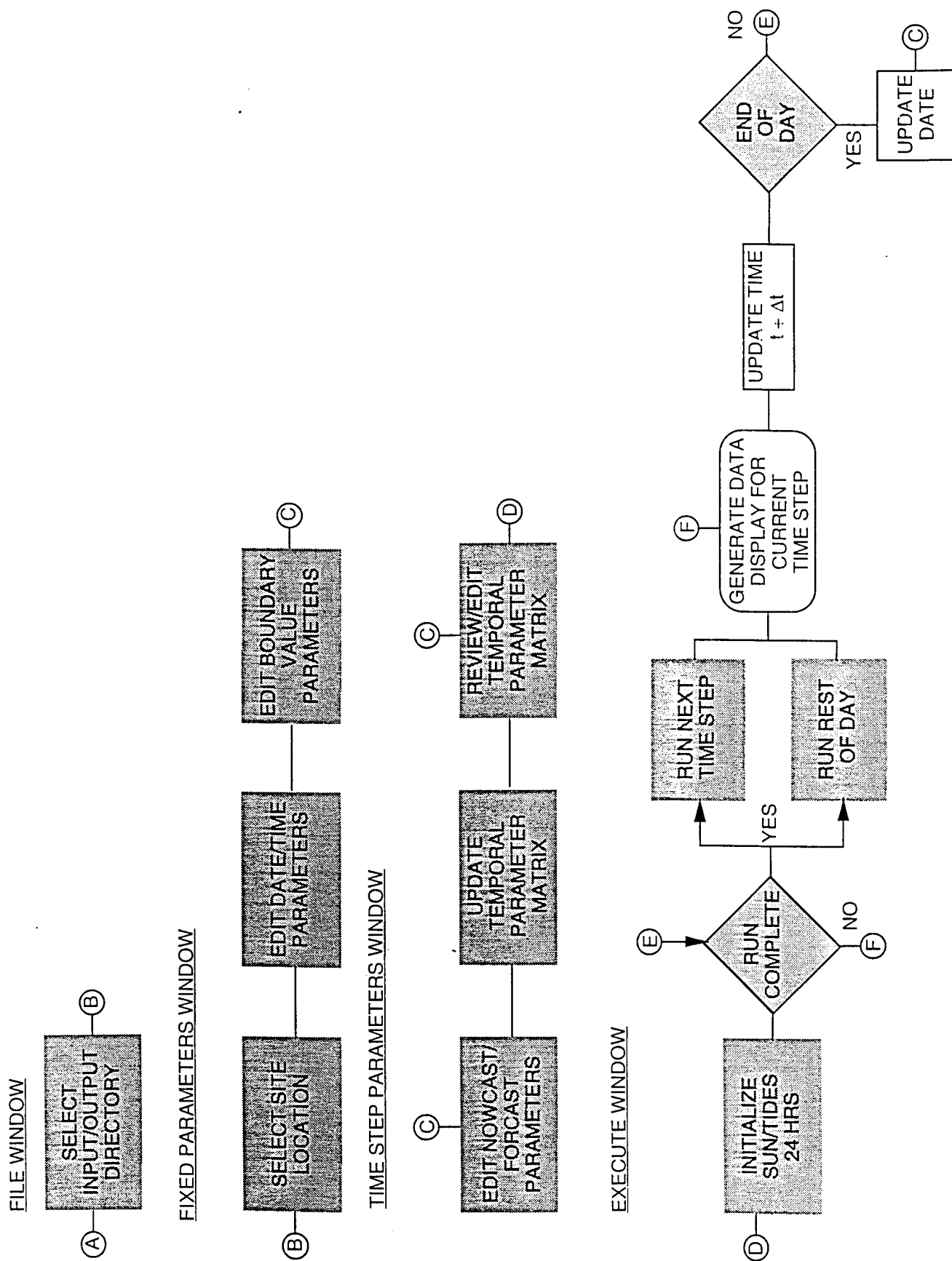


Figure A-3. The PVM Operational Flow Chart

Click on the "File" option and select "New." Enter the name "test," as shown in Figure A-5. When done, press "OK." This creates an output directory called "test." Next, press "cancel." This deactivates the file browser.

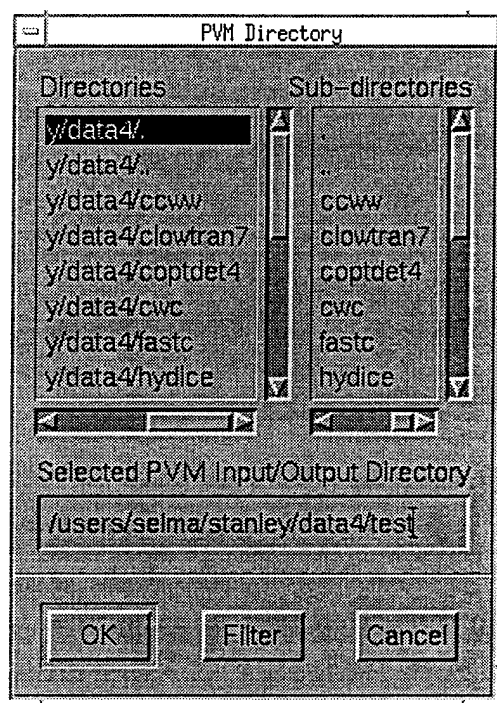


Figure A-5. File Browser Window

The name of the output directory will appear in the "Directory Location of Outputs" box in the model window (as shown in Figure A-6).

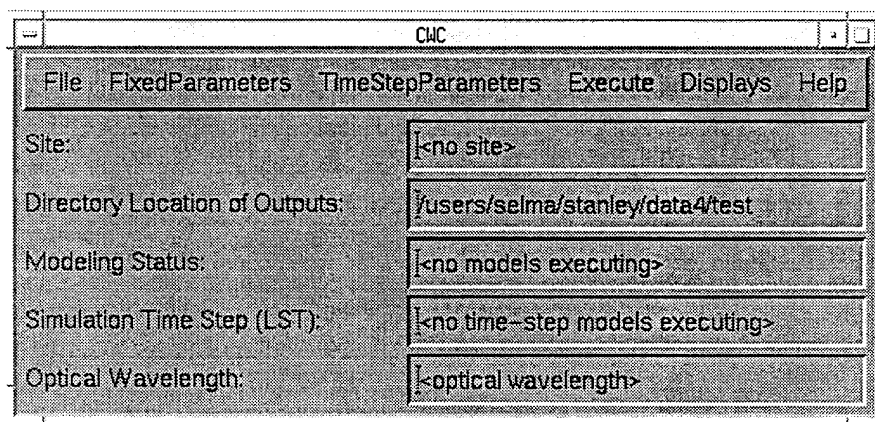


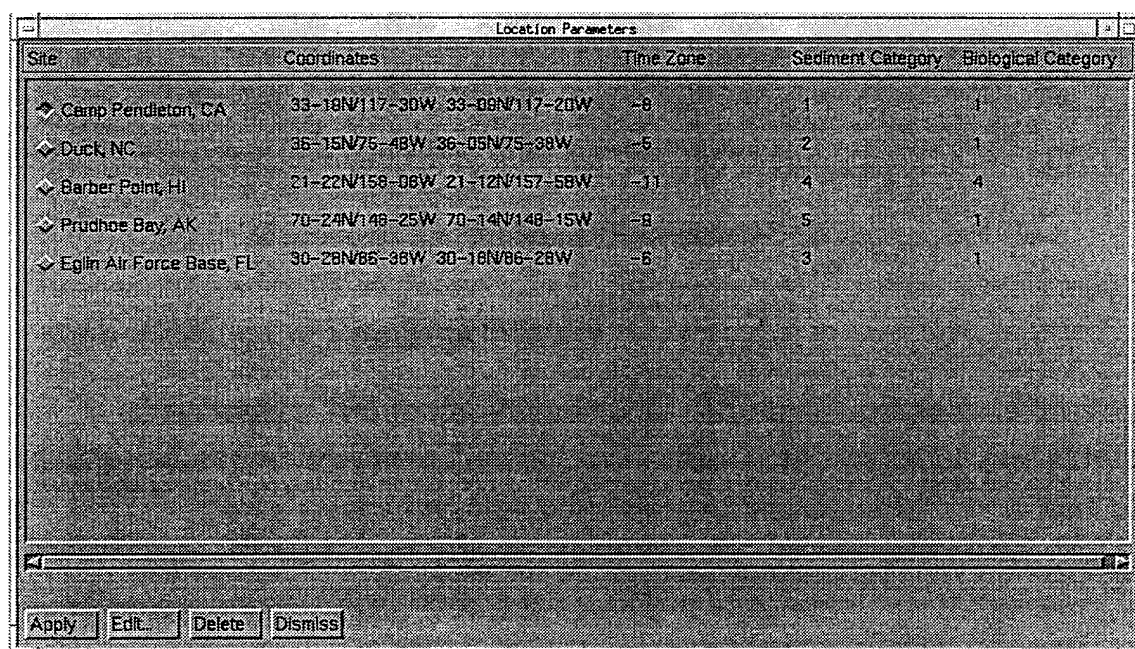
Figure A-6. Main Model Window after Selection of Output Directory



Now that the working directory has been chosen, the next step is the input parameters. When the model is first started, the input parameters are given hard-wired default values. In addition, certain sets of parameters are provided that correspond to different sites. Choosing a site will load in the set of parameters for the specific site chosen.

### 4.1.2 Choosing A Site Location

To input a site, click on the "Fixed Parameters" option and select "Location." This window shows the names, coordinates, time zones, sediment, and biological categories which correspond to the five generic coastal types (sediment categories). To run the demo case, select "Camp Pendleton, California," as shown in Figure A-7, then press "Apply." This step initializes the model (loads in model default values). Next, press "Dismiss" to deactivate the "Location Parameters" window. Creating a new composite site will be discussed in Section 4.1.11.



The screenshot shows a window titled "Location Parameters" with a table containing five rows of site data. Each row has a diamond icon to its left. The columns are labeled: Site, Coordinates, Time Zone, Sediment Category, and Biological Category. At the bottom of the window are four buttons: Apply, Edit, Delete, and Dismiss.

Site	Coordinates	Time Zone	Sediment Category	Biological Category
◆ Camp Pendleton, CA	33-18N/117-30W 33-09N/117-20W	-8	1	1
◆ Duck, NC	35-15N/75-48W 36-05N/75-38W	-6	2	1
◆ Barber Point, HI	21-22N/159-08W 21-12N/157-58W	-11	4	4
◆ Prudhoe Bay, AK	70-24N/148-25W 70-14N/148-15W	-8	5	1
◆ Eglin Air Force Base, FL	30-28N/86-38W 30-18N/86-28W	-6	3	1

Figure A-7. Location Parameters Window

The model window now contains the site name, output directory, and optical wavelength (see Figure A-8).

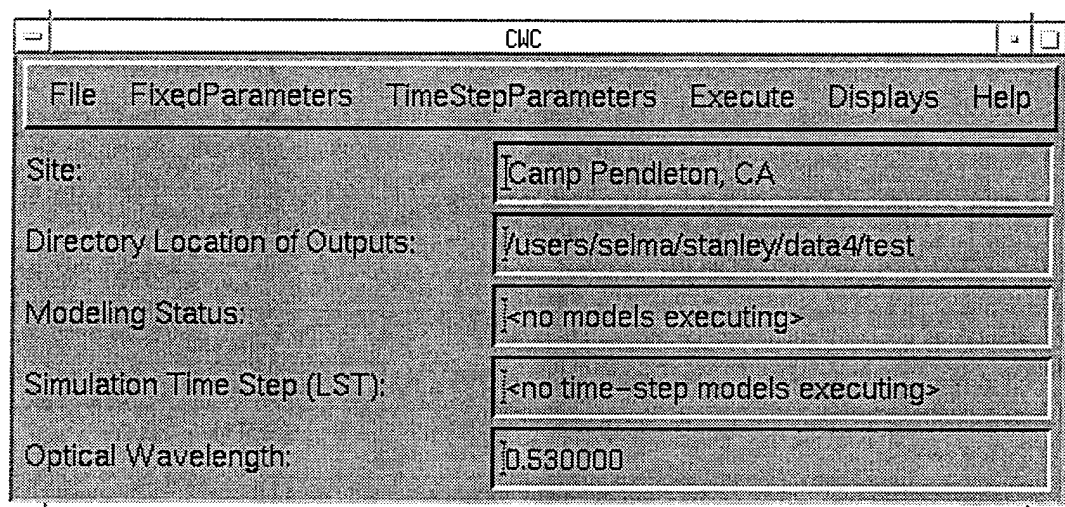


Figure A-8. Main Model Window after Selection of both Site Location and Output Directory

#### 4.1.3 Selecting "Simulation Start Date & Time/Vertical Profile Location"

Next, select "Simulation Start Date & Time/Vertical Profile Location" under the "Fixed Parameters" option (as shown in Figure A-9). This window shows the time and date of the collected data, start and stop times, time increment, first time step, and optical wavelength. There are two important parameters, the "Start Hour" and "Stop Hour," which give the first and final step times. The default start & stop times are midnight (2400 hours) and 10 p.m. (2200 hours), respectively. The start time can be any even hour during the day and the stop time must be at least 2 hours later on the same day. If the stop hour is left at its default hour (2200 hours), the execute options discussed later will facilitate stopping after each 2-hour increment to view outputs or running through 2200 hours, at which time a new day can be initiated. Current time step is displayed in the "Simulation Time Step" box in the main model window during a run. Press "Dismiss" when finished.

Parameter	Value
Year	1993
Month (1-12)	1
Day (1-31)	23
Start Hour (LST) (0, 2, 4, ..., 22)	0
Stop Hour (LST) (0, 2, 4, ..., 22)	22
Time Increment (hrs)	2
First Time Step (y, n)	y
Optical Wavelength (nm)	650000

Apply Dismiss

Figure A-9. Data/Time Parameters Window

#### 4.1.4 Selecting "Fixed Boundary/Outer Boundary Values"

Select "Fixed Boundary/Outer Boundary Values" under the "Fixed Parameters" option, as shown in Figure A-10. This window displays the names, units, range, default values, and editable values of each boundary parameter. The default values are from the cwc.per file corresponding to the generic site selections, and may be used as is or edited, if local values are known. If image files are available, boundary values can be selected from the image displays under the map display window; if not, archived values must be entered. The mixed layer depth (MLD) entered remains constant during the entire run or (optionally) varies with wind speed if a -1 is entered. Press "Dismiss" when finished.

Parameter	Units	Range	Default	Value
Sediment	mg/l	0-10	10	10
Sediment (lower layer)	mg/l	0-10	10	10
DOM Absorption (440 nm)	m <sup>-1</sup>	0-0.5	0.070000	0.070000
Chlorophyll a	mg m <sup>-3</sup>	0.5-50.0	1.000000	1.000000
Nitrate	micromolar	0-45	0.200000	0.200000
Deep Water Nitrate	micromolar	0-45	5.000000	5.000000
Phosphate	micromolar	0-5	0.750000	0.750000
Mixed Layer Depth	m	0-1000	50.000000	50.000000
Peak Precipitation Time	hr	0.0-23.9	12.000000	12.000000
Ground Saturation Factor	fraction	0.0-1.0	0.500000	0.500000

Apply Dismiss

Figure A-10. Boundary Parameters Window

Now, the last window under the "Fixed Parameters" option shows the super user categories. This window permits global access to additional, non-time dependent, input parameters. A detailed description of super user parameters is available upon request. **All values should only be changed by experienced users since they represent an internally consistent set of calibration constants used to match data.** The "Local Tidal Corrections" category is included for constrained bodies of water where amplitude and phase lag departures from coastal ocean variations are required. This option is not currently activated.

#### 4.1.5 Setting Up The Matrix

Now that a site location has been selected and boundary values set, the next step is specifying time step parameter variations. Click on the "TimeStepParameters" option and select "Nowcast/Forecast." This will bring up the "Nowcast/Forecast" window (as shown in Figure A-11). This window facilitates entry of nowcast and forecast values for the various environmental quantities for a 24-hour period. The default values are also from the generic cwc.par file chosen. The initial and forecast parameters may be obtained from "NODDS," local observations, or any other data source. When the "Update Temporal Parameters Matrix" button is pressed, the model performs an interpolation between the initial and forecast parameters generating a matrix of environmental parameters called the "Temporal Parameters" matrix. The

interpolation is currently linear, except for "Surface Wind Speed," which varies sinusoidally between ) at midnight and reaches its input maximum value at noon. Pressing this button also generates a new "nowfor.dat" file, which is used by the model driver later when the oceanographic models are being run.

The screenshot shows a window titled "Nowfore Parameters". At the top, it displays "Site: Camp Pendleton, CA" and "Simulation Time (LST): 1/23/1993 @0000". Below this, there are input fields for "ENOC Reference Coordinates (lat, lon):" with "33.000" and "117.000" entered, and "Mixed Layer Depth: 16404.995 ft".

Parameter	Units	Range	Source	Default	Initial Value	Forecast
Cloud Cover	%	0-100	NODDS	0	0	0
Air Temperature	degrees C	0-50	NODDS	20	20	20
Sea Surface Temperature	degrees C	0-35	NODDS	15	15	15
Sea Surface Pressure	mbars	814-1025	NODDS	1000	1013	1013
24 Hour Precipitation	10th inch	0-50	NODDS	0	0	16
Surface Wind Speed	knots	0-50	NODDS	5	5	5
Wind Wave Period	seconds	7-17	NODDS	8	8	8
Wind Wave Direction	degrees True	0-360	NODDS	255	255	255
Wind Wave Height	feet	0-50	NODDS	0.464000	0.464000	0.260000
Swell Period	seconds	7-17	NODDS	12	12	12

At the bottom of the window, there are three buttons: "Input Next Day", "Update Temporal Parameters Matrix", and "Dismiss".

Figure A-11. Nowcast/Forecast Window

#### 4.1.6 Editing the Run Time Matrix

Now select "Temporal Parameters." The temporal parameters matrix has 12 interpolated values at 2-hour intervals for each parameter (as shown in Figure A-12). These values are also editable so that actual hindcast values or alternative temporal variations can be dually input. If you edited the run time matrix, you must press "Apply" to invoke your modifications.



Temporal Parameters							
PARAMETER	0000	0200	0400	0600	0800	1000	1200
Cloud Cover	0.000000	0.000000	0.000000	0.000000	0.000000	0.000000	0.000000
Air Temperature	20.000000	20.000000	20.000000	20.000000	20.000000	20.000000	20.000000
Sea Surface Temperature	15.000000	15.000000	15.000000	15.000000	15.000000	15.000000	15.000000
Sea Surface Pressure	1013.000000	1013.000000	1013.000000	1013.000000	1013.000000	1013.000000	1013.000000
24 Hr Precipitation	0.000000	0.250000	2.500000	5.750000	5.000000	0.250000	0.500000
Wind Speed	5.000000	5.000000	5.000000	5.000000	5.000000	5.000000	5.000000
Wind Wave Period	6.000000	6.000000	6.000000	6.000000	6.000000	6.000000	6.000000
Wind Wave Direction	255.000000	255.000000	255.000000	255.000000	255.000000	255.000000	255.000000
Wind Wave Height	0.400000	0.400000	0.400000	0.400000	0.400000	0.400000	0.400000
Swell Period	12.000000	12.000000	12.000000	12.000000	12.000000	12.000000	12.000000
Swell Direction	230.000000	230.000000	230.000000	230.000000	230.000000	230.000000	230.000000
Swell Height	0.550000	0.550000	0.550000	0.550000	0.550000	0.550000	0.550000
Offshore Current Velocity	0.000000	0.000000	0.000000	0.000000	0.000000	0.000000	0.000000
Offshore Current Direction	142.000000	142.000000	142.000000	142.000000	142.000000	142.000000	142.000000
Ocean Salinity	33.000000	33.000000	33.000000	33.000000	33.000000	33.000000	33.000000
River 1 Throughput	0.000000	0.000000	0.000000	0.000000	0.000000	0.000000	0.000000
River 2 Throughput	0.000000	0.000000	0.000000	0.000000	0.000000	0.000000	0.000000

Figure A-12. Temporal Parameters Window

#### 4.1.7 Initialization Step

To begin executing the physics models, click on the "Execute" option and select "Initialize Daily Sun and Tides." This starts the initialization process described in Section 4.0. It takes approximately 2 minutes to complete this process. When this process is done, a message reading "Complete Initialization" will appear in the "Modeling Status" window.

#### 4.1.8 Running Single Time Step

Next, select "Run Next Time Step." This will start the time step loop process as described in Section 4.1. It takes approximately 16 minutes to complete this process; when finished, a message reading "Simulation Completed" will appear in the "Modeling Status" window.

### 4.1.9 File Compression

The output files are copied to a subdirectory under the working directory. This subdirectory is given a name that corresponds to the time label of the current iteration. For a full-day run, there will be 12 of these subdirectories corresponding to the 2-hour time steps throughout the day. The files in these subdirectories are compressed using the UNIX "compress" routine to save disk space.

### 4.1.10 Display Options

There are three options under the Displays menu that can be activated at any time: They include the Map Displays, Local Hourly Plot Displays, and Water Column Plot Displays (as shown in Figures A-13 through A-15). Not all buttons in these windows are connected for display at this time. To use, bring up the desired menu, select the desired displays, and press "Accept". If a specific button is mapped to a display file, and the input file is available, the desired display will come up on the screen. To cause an existing window to disappear, deselect it from the appropriate window, and press "Apply." Use "Dismiss" to make the Displays Menu windows disappear. Currently, these windows will only work with the files in the current working directory.

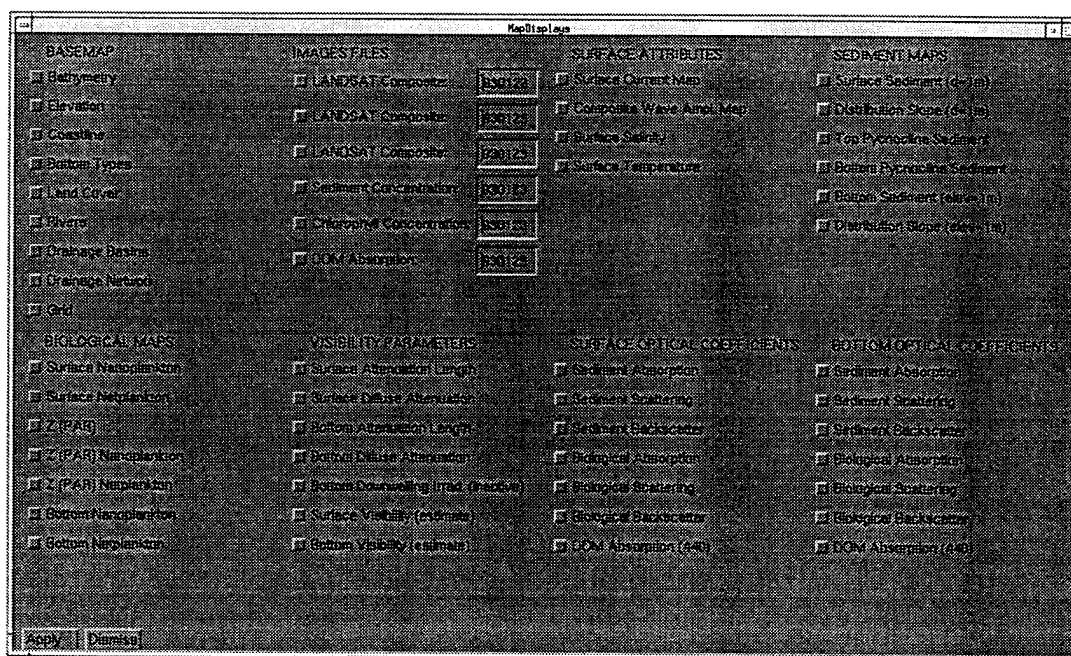


Figure A-13. Map Display Window

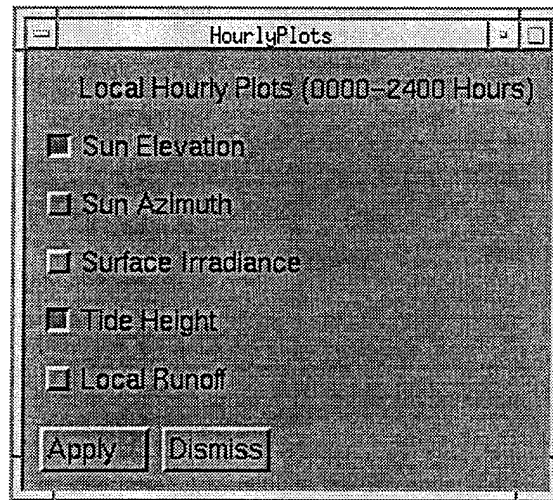


Figure A-14. Hourly Plots Window

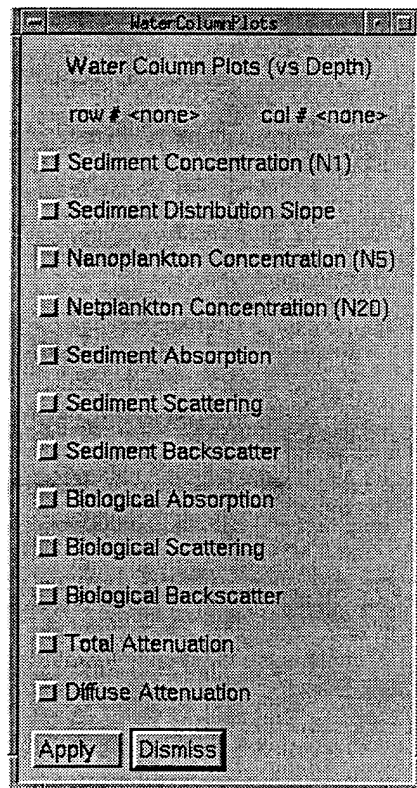


Figure A-15. Water Column Plots Window



#### **4.1.11 Running The Next Time Step**

To run a second time step, click on the "Execute" option and select **"Run Next Time Step."** Again, the run will take about 16 minutes to complete.

#### **4.1.12 Running "Reach of Day Next"**

To run a full day, click on the "Execute" option and select **"Run Reach of Day Next."** This process will take about 3 hours to complete.

#### **4.1.13 Running A Second Day**

To run a second day, click on the "TimeStepParameters" option, select "Nowcast/Forecast," and press the "Input Next Day" button. This copies the forecast to the nowcast. One can enter new forecast values. When done, press "Update Temporal Parameters Matrix." This creates a new "Temporal Parameters" matrix. Since it is a new day, you must run the "Tides/Sun" models, or press the "Tides/Sun" button, prior to executing either of the two run options.

#### **4.1.11 Creating a New Site Location**

To create a new site location, click on the "FixedParameters" option and select "Location." Now press "Edit;" this will bring up the "Edit Location" window. Enter "Composite site" location. You can specify the Site Name, Tidal Constituents File, Time Zone, Sediment and Biological Categories, Optical Sediment Base Matrix File, Grass Location, and the name of the new Site/Directory.

For this example, enter "Composite site" for the Site Name, and enter "compos\_site" for the name of the site directory (as shown in Figure A-16). Press Save. This creates a new site directory named "compos\_site," copies the input files in the current site directory ("camppend") to the new site directory, and updates the "Location" window with the new site name ("Composite site")(as shown in Figure A-17). Important note: The Tidal Constituents and Optical Sediment Base Matrix files are site specified.

The 'Edit Location' window contains the following parameters and values:

Parameter	Value
Site Name	Composite site
Tidal Constituents File	tsioconst.dat
Time Zone	-8
Sediment Category	1
Biological Category	1
Optical Sediment Base Matrix File (under \$CWCDATA/sitedi	camppend.opt
GRASS Location (under \$GISDBASE)	pendleton
Name of Site / Directory (under \$CWCDATA/sitedirs)	compos_site

Buttons: Save, Cancel

Figure A-16. "Edit Location" Window for Creation of a New Site Location

The 'Location Parameters' window displays a table of site locations with the following data:

Site	Coordinates	Time Zone	Sediment Category	Biological Category
◆ Camp Pendleton, CA	33-19N/117-30W 33-09N/117-20W	-8	1	1
◆ Duck, NC	36-15N/75-48W 36-05N/75-38W	-5	2	1
◆ Barber Point, HI	21-22N/158-08W 21-12N/157-58W	-11	4	4
◆ Prudhoe Bay, AK	70-24N/148-25W 70-14N/148-15W	-9	6	1
◆ Eglin Air Force Base, FL	30-28N/86-38W 30-18N/86-28W	-6	3	1
◆ Composite site	33-19N/117-30W 33-09N/117-20W	-8	1	1

Buttons: Apply, Edit, Delete, Dismiss

Figure A-17. Location Parameters Window After Creation of a New Site Location

## 5.0 DESCRIPTION OF INPUT AND OUTPUT PARAMETERS BY MODEL

### DESCRIPTION OF PARAMETERS FOR BIOMASS

Input Files & Parameters				
File Name	Description	Units	Default Value	Parameter Type
bioconst.dat	initialization constants for the biology	N/A	-----	-----
Parameter Names				
adv	vertical advection	$\text{m}^2 \text{s}^{-1}$	0.0001	biology
blg	"beta" photoinhibition	$\text{mgC mgchl}^{-1} \text{h}^{-1}$	0.00155	biology
bsm	"beta" photoinhibition	$\text{mgC mgchl}^{-1} \text{h}^{-1}$	0.00175	biology
carbchl	carbon:chl	$\text{mgC mg chl}^{-1}$	50	biology
deepn	deep water nitrate concentration	$\text{umoles l}^{-1}$	5.0	boundary
gzoo_1	zooplankton grazing rate 1	$\text{d}^{-1}$	0.2	biology
gzoo_2	zooplankton grazing rate 2	$\text{d}^{-1}$	0.1	biology
klg	half-saturation constant for nitrate	$\text{umoles l}^{-1} \text{h}^{-1}$	1.2	biology
kount	1-1st temporal, 2-not 1st temporal	dimensionless	0	control
ksm	half-saturation constant for nitrate	$\text{umoles l}^{-1} \text{h}^{-1}$	0.5	biology
lgalph	large alphaB	$\text{mg C (mg chl)}^{-1} (\text{uE m}^{-2} \text{s}^{-1})^{-1}$	0.05	biology
lgchcell	large chlorophyll per cell	$\text{ug chl cell}^{-1}$	$2.1\text{e-}6$	biology
lgdiam	large cell diameter	microns	20.0	biology
lgmort	mortality of large cells	$\text{d}^{-1}$	0.01	biology

lgpmx	large pmaxB	mgC mgchl <sup>-1</sup> h <sup>-1</sup>	8.0	biology
mld	mixed layer depth	m	50.0	boundary
pycno	thinkness of pycnocline	m	s	biology
resp	respiration rate	d <sup>-1</sup>	0.1	biology
site_name	site name	ascii name	camppend	control
smalph	small alphaB	mg C (mg chl) <sup>-1</sup> (uE m <sup>-2</sup> s <sup>-1</sup> ) <sup>-1</sup>	0.064	biology
smchcell	small chlorophyll per cell	ug chl cell <sup>-1</sup>	0.2e-6	biology
smdiam	small cell diameter	microns	5.0	biology
smmort	mortality of small cells	d <sup>-1</sup>	0.01	biology
smpmx	small pmaxB	mgC mgchl <sup>-1</sup> h <sup>-1</sup>	11.50	biology
<b>Output Files</b>				
cell.dep	depth of euphotic zone	m	-----	-----
cell_5.1m	cell number concentration at 1 m for 5 micro cell	cells ml <sup>-1</sup>	-----	-----
cell_20.1m	cell number concentration at 1 m for 20micro cell	cells ml <sup>-1</sup>	-----	-----
cell_5.zee	cell number concentration for 5 micro cell at base of euphotic zone	cells ml <sup>-1</sup>	-----	-----
cell_20.zee	cell number concentration for 20 micro cell at base of euphotic zone	cells ml <sup>-1</sup>	-----	-----
nitrate.1m	nitrate concentration at 1m	cells ml <sup>-1</sup>	-----	-----
nitrate.zee	nitrate concentration at zeepar	cells ml <sup>-1</sup>	-----	-----

# DESCRIPTION OF PARAMETERS FOR BIO\_OPTIC

Input File & Parameter				
File Names	Description	Units	Default Value	Parameter Type
bio_input	contains files biofile1 and biofile2 representing the number of 5 and 20 micro cells	N/A	-----	-----
Parameter Names				
lgchcell	large chlorophyll per cell	ug chl cell <sup>-1</sup>	2.1e-6	biology
refim1	Imaginary part of refractive index for core	dimensionless	0.015000	optics
refre1	Real part of refractive index for core	dimensionless	1.200000	optics
smchcell	small chlorophyll per cell	ug chl cell <sup>-1</sup>	0.2e-6	biology
wavel	optical wavelength	microns	0.530000	const
Output Files				
bio_op490.abs	absorption coefficient at 490 microns	m <sup>-1</sup>	-----	-----
bio_op490.att	diffuse attenuation coefficient at 490 microns	m <sup>-1</sup>	-----	-----
bio_op490.bck	backscattering coefficient at 490 microns	m <sup>-1</sup>	-----	-----
bio_op490.ext	total attenuation coefficient at 490 microns	m <sup>-1</sup>	-----	-----
bio_op490.prf	profile at 490 microns		-----	-----
bio_op490.sca	scattering coefficient at 490 microns	m <sup>-1</sup>	-----	-----
bio_opbot.abs	absorption coefficient 1 meter above ocean bottom	m <sup>-1</sup>	-----	-----
bio_opbot.att	diffuse attenuation coefficient 1 meter above ocean bottom	m <sup>-1</sup>	-----	-----

bio_opbot.bck	backscattering coefficient 1 meter above ocean bottom	$m^{-1}$	-----	-----
bio_opbot.ext	total attenuation coefficient 1 meter above ocean bottom	$m^{-1}$	-----	-----
bio_opbot.sca	scattering coefficient 1 meter above below sea surface	$m^{-1}$	-----	-----
bio_optic.abs	absorption coefficient 1 meter abovebelow sea surface	$m^{-1}$	-----	-----
bio_optic.att	diffuse attenuation coefficient 1 meter below sea surface	$m^{-1}$	-----	-----
bio_optic.bck	backscattering coefficient 1 meter below sea surface	$m^{-1}$	-----	-----
bio_optic.ext	total attenuation coefficient 1 meter below sea surface	$m^{-1}$	-----	-----
bio_optic.prf	profile 1 meter below sea surface	$m^{-1}$	-----	-----
bio_optic.sca	scattering coefficient 1 meter below sea surface	$m^{-1}$	-----	-----

### DESCRIPTION OF PARAMETERS FOR BIOXPORT

Input File Parameter				
File Name	Description	Units	Default Value	Parameter Type
bioxport.inp	contains intialzation parametrs	N/A	-----	-----
cell.dep	depth of euphotic zone	m	-----	-----
cell_5.1m	cell number concentration at 1 m for 5 micro cell	cells $ml^{-1}$	-----	-----
cell_5.zee	cell number concentration at 1 m for 20micro cell	cells $ml^{-1}$	-----	-----

cell_20.1m	cell number concentration for 5 micro cell at base of euphotic zone	cells ml <sup>-1</sup>	-----	-----
cell_20.zee	cell number concentration for 20 micro cell at base of euphotic zone	cells ml <sup>-1</sup>	-----	-----
<b>Parameter Names</b>				
ak2_bio	upper layer mixing length coefficient	dimensionless	0.00001	hydrodynamics
deltat	size of temporal step	hours	2	control
fb	survival rate	dimensionless	0.95	biology
fm	boundary layer power law parameter	dimensionless	50.0	hydrodynamics
ibins_bio	number of particle bins	dimensionless	2	control
igrdx	x column number of selected grid point, 1-200 W-E	grid number	84	control
igrdy	y index number of selected grid point, 1-200 S-N	dimensionless	100	control
nx	number of points in grid	dimensionless	200	control
ny	number of points in grid	dimensionless	200	control
persw	swell period, in seconds	seconds	12.000000	temporal
rhos1	mean bulk density of small particles	gm/cc	1.15	biology
rhos2	mean bulk density of big particles	gm/cc	1.069	biology
ro	mean density of small particles	gm/cc	1.021	hydrodynamics
site_name	site name	ascii name	camppend	control
sx	horizontal grid spacing = to 3 sec lon	meters	77.5	GIS
sy	vertical grid spacing = to 3 sec lon	meters	92.6	GIS
w01	settling rate for small particles	cm/sec	.0001736	hydrodynamics
w02	settling rate for big particles	cm/sec	.0009259	hydrodynamics

Output Files				
xcell_5.1m	cell number concentration at 1 m below the surface for 5 micro cell	dimensionless	-----	-----
xcell_5.bot	cell number concentration at 1 m above the bottom for 5 micro cell	dimensionless	-----	-----
xcell_5.pic	cell number concentration for 5 micro cell at pycnoline	dimensionless	-----	-----
xcell_5.zee	cell number concentration for 5 micro cell at base of euphotic zone	dimensionless	-----	-----
xcell_20.1m	cell number concentration at 1 m below the surface for 20 micro cell	dimensionless	-----	-----
xcell_20.bot	cell number concentration at 1 m above the bottom for 5 micro cell	dimensionless	-----	-----
xcell_20.pic	cell number concentration for 20 micro cell at pycnoline	dimensionless	-----	-----
xcell_20.zee	cell number concentration for 20 micro cell at base of euphotic zone	dimensionless	-----	-----



# DESCRIPTION OF PARAMETERS FOR BOTTMBOUND

Input Files & Parameter				
File Name	Description	Units	Default Value	Parameter Type
bottmbound.inp	gridded bathymetry	meters	-----	-----
Parameters Names				
ak	boundary layer mixing length coefficient	dimensionless	0.00000000 0492	hydrodynamics
hsw1	nowcast swell wave height,	meters	0.495000	temporal
hsw2	forecast swell wave height	meters	0.495000	temporal
hwin1	nowcast windwave wave height	meters	0.390000	temporal
hwin2	forecast windwave wave height	meters	0.390000	temporal
igrdx	x column number of selected grid point, 1-200 W-E	grid number	84	control
igrdy	y index number of selected grid point, 1-200 S-N	dimensionless	100	control
nx	number of points in grid	dimensionless	200	control
ny	number of points in grid	dimensionless	200	control
persw	swell period, in seconds	seconds	12.000000	temporal
perwin1	nowcast windwave period	seconds	8.000000	temporal
perwin2	forecast windwave period	seconds	8.000000	temporal
rci	total bottom sediment concentration	gm/cc	0.300000	hydrodynamics
site_name	site name	ascii name	camppend	control
sx	horizontal grid spacing = to 3 sec lon	meters	77.5	GIS
sy	vertical grid spacing = to 3 sec lon	meters	92.6	GIS
u0	coastal mean tidal current	m/s	0.5948	temporal

Output Files				
bin1.bot - bin9.bot	bulk density for each size bin	gm/cc	-----	-----

## DESCRIPTION OF PARAMETERS FOR OCEANRDS

Input Files & Parameter				
File Name	Description	Units	Default Value	Parameter Type
oceanrds.inp	contains input parameters for oceanrds.f	multiple	-----	-----
Parameters Names				
asw	swell direction, degrees from tn	degrees True	238.167007	temporal
hsw1	nowcast swell wave height,	meters	0.495000	temporal
hsw2	forecast swell wave height	meters	0.495000	temporal
icoast	wave exposure 1=west, 2=east, 3=north, 4=south	dimensionless	1	control
nx	number of points in grid	dimensionless	200	control
ny	number of points in grid	dimensionless	200	control
persw	swell period, in seconds	seconds	12.000000	temporal
site_name	site name	ascii name	camppend	control
sx	horizontal grid spacing = to 3 sec lon	meters	77.5	GIS
sy	vertical grid spacing = to 3 sec lon	meters	92.6	GIS
tide_elev	tide height above MSL	meters	0.826000	hydrology
Output Files				
site_name.an1	ascii wave angle	degrees True	-----	-----
site_name.ba1	binary wave angle	degrees True	-----	-----
site_name.bra	wave height, wave angle, depth	meters, degs, meters	-----	-----
site_name.bw1	binary wave height	meters	-----	-----
site_name.dep	ascii wave bathymetry	meters	-----	-----
site_name.wh1	ascii wave height	meters	-----	-----

site_name.wvn	ascii wave number	meters <sup>-1</sup>	-----	-----
---------------	-------------------	----------------------	-------	-------

## DESCRIPTION OF PARAMETERS FOR SEDXPORT

<b>Input Files &amp; Parameter</b>				
<b>File Name</b>	<b>Description</b>	<b>Units</b>	<b>Default Value</b>	<b>Parameter Type</b>
bulk_density.d at	bulk density data	gm/cc	-----	-----
dmix_wind.dat	wind coefficients	dimensionless	-----	-----
sedxport3.inp	constains input parameters for sedxport.f	multiple	-----	-----
timestep.sed	time step	seconds		
<b>Parameter names</b>				
ak	boundary layer mixing length coefficient	dimensionless	0.00000000 0492	hydrodynamics
ak2	upper layer mixing length coefficient	dimensionless	0.00000001 2400	hydrodynamics
ak2_1	lower layer mixing length coefficient	dimensionless	0.0001	hydrodynamics
ak3	horizontal layer mixing length coefficient	dimensionless	1.000000	hydrodynamics
ak3s	ocean salinity horizontal mixing length coefficient	dimensionless	0.000236	hydrodynamics
ak3s_1	ocean salinity horizontal mixing length coefficient	dimensionless	0.000236	hydrodynamics
ak3_1	lower layer horizontal diffusion coefficient	dimensionless	10.0	hydrodynamics
ak4	surfzone mixing length coefficient	dimensionless	1000	hydrodynamics
ak5	river plume mixing length coefficient	dimensionless	1000	hydrodynamics
ak5s	river plume salinity	dimensionless	62	hydrodynamics
ak5s_1	river plume salinity	dimensionless	62	hydrodynamics
ak5_1	lower layer river plume mixing length coefficient	dimensionless	1000	hydrodynamics
ak7	null point coefficient	dimensionless	0.00001	hydrodynamics
ak8	wind friction coefficient	dimensionless	1	hydrodynamics

akb	beach packing parameter	dimensionless	.000006	hydrodynamics
aks	suspended load efficiency	dimensionless	0.78	hydrodynamics
aksal	reciprocal salinity diffusivity	s m <sup>-1</sup>	100000	hydrodynamics
aksal_1	reciprocal salinity diffusivity	s m <sup>-1</sup>	100000	hydrodynamics
ak_1	lower layer vertical diffusion coefficient	dimensionless	0.01	hydrodynamics
alay1	layer 1 hardwired to surface - 1 meter	meters	0.000000	control
alay2	layer 2 hardwired to local bottom + 1 meter	meters	0.000000	control
alay3	distance relative to datum for layer 3	meters	4.000000	hydrodynamics
alay4	distance relative to datum for layer 4	meters	6.000000	hydrodynamics
bottom	bottom resuspension switch, 1=yes, 0=no	dimensionless	1	switch
delsal_1	ocean salinity difference between surface and bottom layer	ppt	0.1	hydrodynamics
deltat	size of temporal step	hours	2	control
dmix_for	dmix forecast switch, 0=mixed layer depth calculation internally	dimensionless	1	switch
domback	minimum value of cdom absorption	m <sup>-1</sup>	0.07	boundary
dominter	intercept of cdom absorption with salinity	m <sup>-1</sup>	2.266	biology
domslope	slope of cdom absorption with salinity	m <sup>-1</sup> (parts per thousand) <sup>-1</sup>	0.07161	biology
dr	river 1 depth at it's mouth	meters	1.000000	GIS
dr2	river 2 depth at it's mouth	meters	1.000000	GIS
gamma	slope of hyperbolic distribution far offshore	dimensionless	2.500000	boundary
hsw1	nowcast swell wave height,	meters	0.495000	temporal
hsw2	forecast swell wave height	meters	0.495000	temporal
hwin1	nowcast windwave wave height	meters	0.390000	temporal

hwin2	forecast windwave wave height	meters	0.390000	temporal
ibins	number of particle bins	dimensionless	9	control
igrdx	x column number of selected grid point, 1-200 W-E	grid number	84	control
igrdy	y index number of selected grid point, 1-200 S-N	dimensionless	100	control
irx	x grid cell number of river mouth 1	dimensionless	112	GIS
irx2	x grid cell number of river mouth 2	dimensionless	144	GIS
iry	y grid cell number of river mouth 1	dimensionless	98	GIS
iry2	y grid cell number of river mouth 2	dimensionless	64	GIS
n0	background number of particles far offshore	dimensionless	10	boundary
n0_1	background number of particles far offshore, lower layer	dimensionless	10	boundary
numlay	number of layers (1-4 surface=layer1.xxx) for particle# output	dimensionless	2	control
nx	number of points in grid	dimensionless	200	control
ny	number of points in grid	dimensionless	200	control
persw	swell period, in seconds	seconds	12.000000	temporal
perwin1	nowcast windwave period	seconds	8.000000	temporal
perwin2	forecast windwave period	seconds	8.000000	temporal
qbig1	nowcast river 1 discharge rate	meters <sup>3</sup> /sec	89.760002	temporal
qbig2	forecast river 1 discharge rate	meters <sup>3</sup> /sec	89.760002	temporal
qsm1	nowcast river 2 discharge rate	meters <sup>3</sup> /sec	17.950001	temporal
qsm2	forecast river 2 discharge rate	meters <sup>3</sup> /sec	17.950001	temporal
rci	total bottom sediment concentration	gm/cc	0.300000	hydrodynamics

rhos	mean particle density, offshore	gm/cc	2.650000	hydrodynamics
rhosr	mean particle density, river	gm/cc	2.650000	hydrodynamics
rhosr2	mean particle density, river 2	gm/cc	2.650000	hydrodynamics
river	river switch, 1=yes, 0=no	dimensionless	1	switch
river2	river 2 switch, 1=yes, 0=no (1 if 2nd river output considered)	dimensionless	1	switch
rrsi	river 1 suspended load bulk density	gm/cc	0.000500	hydrology
rrsi2	river 2 suspended load bulk density	gm/cc	0.000500	hydrology
rszi	beach bulk density	gm/cc	1.690000	hydrodynamics
rwidth	width of river	meters	100.000000	GIS
rwidth2	width of river 2	meters	100.000000	GIS
salol	ocean salinity	ppt	33	temporal
salol2	ocean salinity	ppt	33	temporal
site_name	site name	ascii name	campend	control
surf	surfzone resuspension switch, 1=yes, 0=no	dimensionless	1	switch
sx	horizontal grid spacing = to 3 sec lon	meters	77.5	GIS
sy	vertical grid spacing = to 3 sec lon	meters	92.6	GIS
tanbeta	beach slope	radians	0.030000	GIS
tconriv	coefficient to modify riversettling temporal step model	dimensionless	631.299988	hydrodynamics
tconriv_l	coefficient to modify riversettling temporal step model, lower layer	dimensionless	631.299988	hydrodynamics
tconsal	coefficient to modify salinity decay for temporalstep model	dimensionless	25.6203	hydrodynamics
tconsal_l	coefficient to modify salinity decay for temporalstep model, lower layer	dimensionless	25.6203	hydrodynamics

tcon_1	coefficient to modify settling for temporal step model, lower layer	dimensionless	1	hydrodynamics
timestep	number of temporal step	dimensionless	5	control
two_layer	two-layer calculation switch 0=single layer, 1=two-layer	dimensionless	1	switch
u0	coastal mean tidal current	m/s	0.5948	temporal
v	surface wind speed	knots	0.0	temporal
verdat	vertical datum; 1 = surface, 0 = local bottom boundary layer	dimensionless	1	switch
w0sal	vertical mixing fresh water	N/A	0.00103	hydrodynamics
w0sal_1	vertical mixing fresh water, lower layer	N/A	0.00103	hydrodynamics

#### Output Files

layer1.dm2	dissolved organic 2	m-1	-----	
layer1.dom	dissolved organic material	m-1	-----	-----
layer1.sal	salinity	o/oo	-----	-----
layer1.sed	sediment concentration	gm/l	-----	-----
layer1.slp	size distribution slope	dimensionless	-----	-----
layer2.dom	dissolved organic material	m-1	-----	-----
layer2.sal	salinity	o/oo	-----	-----
layer2.sed	sediment concentration	gm/l	-----	-----
layer2.slp	size distribution slope	dimensionless	-----	-----
layer3.dom	dissolved organic material	m-1	-----	-----
layer3.sal	salinity	o/oo	-----	-----
layer3.sed	sediment concentration	gm/l	-----	-----
layer4.dom	dissolved organic material	m-1	-----	-----
layer4.sal	salinity	o/oo	-----	-----
layer4.sed	sediment concentration	gm/l	-----	-----

### DESCRIPTION OF PARAMETERS FOR SED\_OPTIC

Input Files & Parameters				
File Name	Description	Units	Default Value	Parameter Type
sed_input	contains input and output file names	N/A	-----	-----
Parameters Names				
refim1	Imaginary part of refractive index for core	dimensionless	0.015000	optics
refre1	Real part of refractive index for core	dimensionless	1.200000	optics
wavel	optical wavelength	microns	0.530000	const
Output Files				
sed_optic.abs	absorption coefficient	m <sup>-1</sup>	-----	-----
sed_optic.att	attenuation coefficient	m <sup>-1</sup>	-----	-----
sed_optic.bck	backscattering coefficient	m <sup>-1</sup>	-----	-----
sed_optic.ext	extinction coefficient	m <sup>-1</sup>	-----	-----
sed_optic.sca	scattering coefficient	m <sup>-1</sup>	-----	-----

### DESCRIPTION OF PARAMETERS FOR TIDCUR1DAY

Input Files & Parameters				
File Name	Description	Units	Default Value	Parameter Type
tidcur1day.inp	contains the amplitude and phase of the local tidal constituents	multiple	-----	-----
Parameters Names				
iday	simulation day	2-digit	23	const
imo	simulation month	2-digit	01	const
iyр	simulation year	4-digit	1993	const
Output Files				



tidcur1day.dat	contains the predicted tidal amplitudes at 6 minute intervals for a 24 period beginning at local time 00:00 of the day month and year selected in the input file	meters	-----	-----
----------------	--	--------	-------	-------

### DESCRIPTION OF PARAMETERS FOR TIDECUR

Input Files & Parameter				
File Name	Description	Units	Default Value	Parameter Type
site_name.grd	binary bathymetry	meters	-----	-----
site_name.bra	breaker height, breaker angle, breaker depth	meters, degs, meters	-----	-----
Parameter Names				
cbl	coastal bounday layer	---	1000	hydrodynamics
coastdir	shoreline orientation clockwise from true North	degrees from true North	142	GIS
nx	number of points in grid	dimensionless	200	control
ny	number of points in grid	dimensionless	200	control
prtide	tide switch, 0=standing tide, 1=progressive tide	dimensionless	1	switch
site_name	site name	ascii name	camppend	control
sx	horizontal grid spacing = to 3 sec lon	meters	77.5	GIS
sy	vertical grid spacing = to 3 sec lon	meters	92.6	GIS
udir	inertial current direction relative to coastline	degrees	0 or 180	temporal
uint1	coastal inertial current	m/s	0	temporal
uint2	coastal inertial current	m/s	0	temporal
uintdir1	coastal inertial current direction	degrees True	142	temporal

uintdir2	coastal inertial current direction	degrees True	142	temporal
<b>Output Files</b>				
ycur.xpt	y-component of current	m s <sup>-1</sup>	-----	-----
xcur.xpt	x-component of current	m s <sup>-1</sup>	-----	-----

### DESCRIPTION OF PARAMETERS FOR TOT\_OPTIC

<b>Input Files &amp; Parameter</b>				
	Description	Units	Default Value	Parameter Type
sed_optic.abs	absorption coefficient	m <sup>-1</sup>	-----	-----
sed_optic.att	attenuation coefficient	m <sup>-1</sup>	-----	-----
sed_optic.bck	backscattering coefficient	m <sup>-1</sup>	-----	-----
sed_optic.ext	extinction coefficient	m <sup>-1</sup>	-----	-----
sed_optic.sca	scattering coefficient	m <sup>-1</sup>	-----	-----
bio_optic.abs	absorption coefficient	m <sup>-1</sup>	-----	-----
bio_optic.att	attenuation coefficient	m <sup>-1</sup>	-----	-----
bio_optic.bck	backscattering coefficient	m <sup>-1</sup>	-----	-----
bio_optic.ext	extinction coefficient	m <sup>-1</sup>	-----	-----
bio_optic.sca	scattering coefficient	m <sup>-1</sup>	-----	-----
<b>Parameter Names</b>				
<b>Output Files</b>				
dom.abs	dissolved organic material absorption	m <sup>-1</sup>	-----	-----

### DESCRIPTION OF PARAMETERS FOR WINDWAVE

<b>Input Files &amp; Parameters</b>				
File Name	Description	Units	Default Value	Parameter Type

windwave.inp	contains input data used in windwave.f	N/A	-----	-----
<b>Parameter Names</b>				
awin1	nowcast windwave direction, degrees from true north	degrees True	255.832993	temporal
awin2	forecast windwave direction, degrees from true north	degrees True	255.832993	temporal
hwin1	nowcast windwave wave height	meters	0.390000	temporal
hwin2	forecast windwave wave height	meters	0.390000	temporal
perwin1	nowcast windwave period	seconds	8.000000	temporal
perwin2	forecast windwave period	seconds	8.000000	temporal
icoast	wave exposure 1=west, 2=east, 3=north, 4=south	dimensionless	1	control
nx	number of points in grid	dimensionless	200	control
ny	number of points in grid	dimensionless	200	control
site_name	site name	ascii name	campend	control
sx	horizontal grid spacing = to 3 sec lon	meters	77.5	GIS
sy	vertical grid spacing = to 3 sec lon	meters	92.6	GIS
tide_elev	tide height above MSL	meters	0.826000	hydrology
<b>Output Files</b>				
site_name.an2	ascii wave angle	degrees True	-----	-----
site_name.br2	wave height, wave angle, depth file	meters,degs, meters	-----	-----
site_name.dep	ascii bathymetry	meters	-----	-----
site_name.grd	binary bathymetry	meters	-----	-----
site_name.wh2	ascii wave height from wind wave period	deg relative	-----	-----
site_name.wht	ascii wave height file sum	meters	-----	-----
site_name.wn2	ascii wave number	m <sup>-1</sup>	-----	-----
site_namewh1	ascii wave height file from oceanrds.f	meters	-----	-----

## **APPENDIX B**

### **Geographic Information Systems (GIS) Input for the Predictive Visibility Model: Basemap Module Summary**

1.0 Introduction.....	1
2.0 GRASS GIS .....	1
3.0 BASEMAP Summaries.....	3
3.1 Bathymetry .....	3
3.2 Elevation.....	4
3.3 Land Cover.....	5
3.4 Land Use.....	8
3.5 Coastline.....	8
3.6 Hydrology.....	9
3.7 Bottom Types.....	10
4.0 Off-line BASEMAP Summaries.....	11
4.1 Sediment Concentration.....	11
4.2 Chlorophyll Concentration.....	12
4.3 Hydraulic Modeling of the Santa Margarita Watershed .....	12
REFERENCES .....	17

## 1.0 Introduction

This is a summary of the work performed in support of the BASEMAP module of the coastal water clarity model contract. The primary purpose of the BASEMAP module is to provide a variety of geocoded data to various other modules in the model processing stream. Accurate geocoded data produced by the BASEMAP module is critical to the success of the model. The sources of initial data are quite diverse and often unrelated. Possible sources include maps and charts, remotely sensed images, and digital data. Coordinate systems for the initial data often vary and the data must be registered in a single georeferenced coordinate system, usually managed by a Geographical Information Systems (GIS) software package, for data analysis. The GIS must be able to import, georeference and perform operations on the various data layers to produce the necessary inputs required by the model, and serve these data layers to the model, through output data disk files. Therefore, the BASEMAP module consists not only of the final product data, but also includes the initial digital and hardcopy maps and remotely sensed images, the GIS and any intermediate data products.

## 2.0 GRASS GIS

The GIS selected for the BASEMAP module is the Geographical Resources Analysis Support System (GRASS) developed primarily by the U.S. Army Construction Engineering Research Laboratory (USACERL) at Champaign, Illinois. We investigated several different GIS packages from various vendors and GRASS satisfied nearly all GIS requirements, including the following:

- It is public domain and free of charge.
- It is supported by USACERL and a growing community of military, government, and commercial users.
- It consists of over 200 individual C programs that are command line driven and can be easily integrated with other C applications.
- It integrates raster and vector data.
- It runs on a variety of platforms: UNIX, PC's, MAC's.
- It can import many types of digital data.
- It has a mixed raster resolution capability. It resamples data at runtime into a user selected region and resolution.

- It has an interactive 3D capability for visualizing digital elevation model (DEM) and other data on Silicon Graphics workstations.
- It has several data export capabilities, including ASCII, PPM, TIFF and HDF formats.
- It has a robust capability for defining and managing the settings of the user's geographic region of interest.

To be used by GRASS programs, data must be digitally imported in a GRASS database. Data can be entered into GRASS in one of the following ways:

- Hardcopy data such as maps may be either digitized as a vector layer or scanned as a raster layer.
- Data may already be in binary GRASS format and may be imported without any changes
- Data already available in another digital format (like ARC/INFO, TIFF, HDF, ASCII) may be converted into GRASS's digital file format.
- GRASS analysis programs can be used to create new GRASS data from data already stored in GRASS digital file format.

There are a few preliminaries that must be taken care of before collecting data and importing it into the GIS. A decision has to be made as to which datum and which earth coordinate system will be used for the georeferenced coordinate system. The North American Datum 1927 (NAD27) was chosen because most of the data we were importing was already NAD27. We also decided to register all data in the Universal Transverse Mercator (UTM) coordinate system rather than latitude/longitude since it is a linear coordinate system and we were able to acquire data from remote sensors georeferenced in UTM coordinates. Tools exist to convert data between datums and coordinate systems, but we wanted to exercise those tools as infrequently as possible. Once the datum and coordinates system were finalized, a new GRASS database file system had to be created. A GRASS database is simply a hierarchical directory structure that GRASS creates and maintains. The database consists of data layers, both raster and vector. Each layer has an associated geographical area called a region that encompasses the data. Other regions may also be established that are not associated with a particular layer but delimit a specified area. For our demonstration, a 10x10 arcminute computational region was established which includes approximately 15 miles of the Camp Pendleton Marine Corps Base, California

coastline. However, a larger region is required to perform certain operations, such as hydrologic runoff modelling. In addition, each region has both a north-south and east-west resolution. For example, the USGS DEM layer has a resolution of 30m in both directions and the LANDSAT-5 images have a 25m resolution in both directions. The computational region has 3 arc second resolution in both directions, 92.3m north-south and 77.7m east-west.

### 3.0 BASEMAP Summaries

Each BASEMAP data layer is discussed individually in a subsequent section. Two products of BASEMAP layers, sediment and chlorophyll concentration computation and hydrology model computation, are computed "off-line" and are discussed after the BASEMAP layer sections. All GRASS programs referenced appear in *italics*. The discussion for each BASEMAP will be in outline format with the following sections:

- Possible Data Sources. This includes some of the potential sources of digital and non-digital data.
- Actual Source of Data. This section specifies the original source of the actual data used.
- Format. Formats include raster, vector, or site (point) data
- Region. This indicates the boundaries and resolution of the data.
- Remarks.. Data import, GIS processing, etc. are discussed.

#### 3.1 Bathymetry

Possible Data Sources: Any accurate map that includes printed soundings or bathymetry contours. NOAA and/or DMA have digital bathymetry available for some areas, however, worldwide resolution is typically not adequate for our purposes.

Actual Data Source: National Oceanic and Atmospheric Administration (NOAA) Nautical chart #18774 Gulf of Santa Catalina.

Format: Digitized vector and subsequently converted to raster.

Region: Complete coverage of the ocean area in the computational region. The demonstration example extends into the Gulf of Santa Catalina. Resolution: 1:100,000 Mercator Projection NAD 83.



Remarks: The NOAA nautical chart was digitally scanned at 150 dpi, yielding a resolution of 16.9 meters (Figure 1). This TIFF file was imported into GRASS using the TIFF import utility, *r.in.tiff*. This chart was rectified by identifying points in common with previously rectified USGS scanned quadrangle maps using *i.group*, *i.points* and *i.rectify2*. An alternative rectification method would have been to manually draw a grid of latitude/longitude crossings and use those points (entered in UTM NAD 27 coordinates) as horizontal control points. Once the chart image was rectified, bathymetry contours were digitized using *v.digit* and stored as a vector layer. The coastline was digitized using *v.digit* following the mean lower low water contour and was stored as a separate vector layer. The bathymetry contour vectors were then converted to a site file using *v.to.sites*. The site file was then converted into a raster file using *s.surf.tps* which interpolated a surface from site data using a spline with tension (Figure 2). In addition, raster masks for both the land and ocean areas were created using the digitized coastline as the boundary. These masks were used to compute layers that are valid in either the ocean or land areas, but not both.

### 3.2 Elevation

Possible Data Sources: digital elevation data is available from various sources.

- The Defense Mapping Agency (DMA) distributes DTED-1 and DTED-2 data.
- DTED-1 data covers  $1^{\circ} \times 1^{\circ}$  areas that correspond to the east or west half of a 1:250,000 DMA map. DTED-1 resolution is 3 seconds of arc and coverage is available for many regions worldwide, although predominantly in North America. The USGS has DTED-1 data available via UNIX file transfer protocol (ftp) on the Internet from [edcftp.cr.usgs.gov](http://edcftp.cr.usgs.gov). These digital elevation models (DEM's) may also be retrieved using the World Wide Web (WWW) browser, MOSAIC. The USGS homepage is <http://info.er.usgs.gov/>. MOSAIC is available free of charge from the National Center for Supercomputer Applications (NCSA) at the University of Illinois at Champaign-Urbana, Illinois and is supported on most platforms.

- DTED-2 data is extremely limited. Parts of Nevada and Germany are available with 30 meter resolution roughly equivalent to a 1:50,000 scale..
- The USGS has digital elevation data available for most 7.5' x 7.5' quadrangles in the United States. The resolution is about 30 meters at a 1:24,000 scale. These must be ordered from the USGS.
- Private companies are also a source of elevation data.

Digital elevation data may also be generated by digitizing elevation contours appearing on a map. It is important to understand what map standards, if any, the map adheres to in order to determine the accuracy and confidence of the digitized elevations.

Actual Data Source: For the demonstration example, we purchased the digital elevation models for four 7.5' USGS quadrangles with 30 meter resolution. These arrived on a single 9 track tape and were imported into GRASS using *m.dem.extract*. These were then combined into a single raster file using *r.patch*. Some cells along quadrangle boundaries needed to be edited using *r.rast.edit*. We also imported a 1° by 1° DEM (santa\_ana\_w) with 3-second by 3-second (roughly 92m by 76m) resolution using MOSAIC from USGS on the Internet. This dem was imported into GRASS using *r.USGSread*, *m.rot90* and *r.ll2u*.

Format: raster

Region: Four 7.5' quadrangles (Las Pulgas Canyon, Morro Hill, Oceanside, San Luis Rey) This 15' by 15' area included 33°7.5'N to 33°22.5'N latitude and 117°15'W to 117°30'W longitude. The 1° by 1° DEM, sanata\_ana\_w, included the area 33°N to 34°N latitude and 117°W to 118°W longitude.

Remarks: The USGS digital elevations are in meters (Figure 2). Once imported into GRASS using *m.dem.extract* and patched together using *r.patch* into a single raster file, problems were noted along one quadrangle boundary. Some of the cells contained a zero value. These were corrected by linearly interpolating using adjacent values in *r.rast.edit*. These zero values could also have been interpolated using *r.resample*.

### 3.3 Land Cover

Possible Data Sources: The USGS has land use/land cover (LULC) maps at 1:250K scale for the US. They are available in two formats: Geographic Information Retrieval and Analysis System (GIRAS) and Composite Theme Grid (CTG) via ftp from edcftp.cr.usgs.gov. GRASS can import the CTG format maps. Multispectral remote sensors can also provide information regarding land cover. Orthophotography may also be used independently, or in conjunction with remote sensed imagery to identify land cover.

Actual Data Source: USGS LULC 1:250K Scale Map and LANDSAT-5 Thematic Mapper Image

Format: raster

Region: 1 degree x 1 degree at 25 meter resolution

Remarks: The goal of this basemap was to assign land cover classifications to the demonstration area utilizing the LANDSAT-5 satellite images. This process involved performing an unsupervised classification of the LANDSAT-5 band 2,3,4,5 spectra, resulting in 15 groups (Figure 3). The land cover classification of each group was then assigned using the information contained in the USGS LULC digital layer, the NDVI layer, and LANDSAT-5 composite images using bands 1,2,3 and 2,3,4. Some of the classification categories contained more than one group. For instance, the shrub and brush class was assigned to three different groups. The assignment of some classes is clear, others are more subjective and, therefore, less accurate. To assist in assigning classes to groups, it is suggested that groups be separated into individual layers, permitting easier identification of the precise area covered by each group. These separate layers may then be overlayed on other base layers to aid in determining the content of the group.

The LANDSAT-5 scene we received was registered in UTM coordinates based on NAD27. Land cover is the result of a multispectral classification operation. There are many methods of multispectral classification, but generally, they fall into three groups: supervised classification, unsupervised classification, and a combination of supervised and unsupervised classification. GRASS supports both supervised and unsupervised classification schemes. Supervised classification is the process of identifying areas called training areas, having a known signatures and classifying other areas

using a maximum likelihood algorithm that utilizes the known signatures. An unsupervised classification produces a specified number of groups of classes by clustering pixels with similar signatures using a minimum distance algorithm. We performed an unsupervised classification using *i.cluster* and *i.maxlik*. *i.cluster* generates the spectral signatures for the land cover types in the image using a clustering algorithm. It results in a signature file that is used as input for the second pass program *i.maxlik*. The clustering algorithm operates by reading through the imagery data and building pixel clusters based on the spectral reflectance of the pixels. *i.maxlik* is a maximum likelihood discriminant analysis classifier. It uses the cluster means and covariance matrices from *i.cluster* to determine which class (or cluster) each pixel in the image has the highest probability of belonging. The resulting file is an image in which each pixel has been assigned to a spectral class or category. LANDSAT-5 bands 2,3,4,5 were used to generate 15 land cover groups. The correspondence of a particular group with a specific type of land cover class must then be made.

The Normalized Digital Vegetation Index (NDVI) was used in assigning land cover types (Figure 5). The NDVI is computed using the electromagnetic reflectance in the visible red (LANDSAT-5 Band3 660 $\mu$ ) and the near-infrared (LANDSAT-5 Band4 830 $\mu$ ) bands. Chlorophyll pigment in green vegetation and the leaf scattering mechanisms cause low spectral reflectance in band3 and high reflectance in band4. The difference between the values of these two bands is a measure of the greenness of the vegetation. the NDVI is defined as:

$$\text{NDVI} = (\text{Band4} - \text{Band3}) / (\text{Band4} + \text{Band3})$$

NDVI is a good measure of the amount of green vegetation. Low values indicate bare soil, rocks and desert areas. High values indicate areas of lush vegetation and agriculture.

The USGS 1:250K LULC map that contained the demonstration area was retrieved via ftp. There are a total of 36 attribute codes in the USGS scheme of which 20 appear in the demonstration area (Figure 4). The USGS processing steps included manual interpretation of aerial photographs acquired from NASA high-altitude missions, earlier land use maps, and field surveys to create LULC maps. These maps were digitized to create a national digital LULC database. The evolution of this process resulted in the creation of GIRAS.

### 3.4 Land Use

Possible Data Sources: Any accurate map that contains land use information. Digital data from U.S. Census Bureau TIGER may contain land use. In addition to the 1:250K LULC digital maps mentioned earlier in the land cover section, USGS has 1:100K Digital Line Graphs (DLG's) available via ftp from edcftp.cr.usgs.edu. DLG vector layers include hydrography, transportation, and hypsography. These DLG's are derived from USGS topographic maps. published as 30- by 60-minute quadrangles.

Actual Data Source: USGS 7.5' quadrangle maps

Format: Vector and raster

Region: Computational area (extended) at 4 meter resolution (scanned)

Remarks: Portions of USGS 7.5' maps were scanned at 150 dpi resulting in raster images with a resolution of 4 meters (Figure 6). These images were rectified using *i.group*, *i.points* and *i.rectify2*. Marks were manually drawn on each map prior to scanning where UTM easting and northing values crossed. These points were evenly distributed over the entire area which resulted in an accurate rectification. *v.digit* was then used to digitize the land use features. This included separate land use vector layers for interstate highways, primary highways, secondary highways, light duty roads, unimproved roads, trails, railroads, airports, buildings, residential areas, marshes and swamps.

### 3.5 Coastline

Possible Data Sources: Any map that contains an accurate coastline or a remotely sensed image with a visible coastline at a known tidal level. Digital coastline data includes the World Vector Shoreline (WVS) from DMA, however, WVS does not have adequate resolution. Some DEM's also contain a coastline.

Actual Data Source: NOAA nautical chart and DEM's.

Format: Vector

Region: Computational area (extended) at 16.9 meter scanned resolution

Remarks: The lower low water contour coastline was digitized from the scanned nautical chart (see BASEMAP 1 above) using *v.digit*. It was stored as a separate vector layer. Raster layers were then produced using the coastline to provide masks for either the land or ocean areas. Another method involves using a DEM. The DEM is reclassified so that land cells (DEM cells having a value greater than zero) have a category value equal to one and the ocean cells have a category value equal to zero. The GRASS tool *r.poly* computes a vector layer that displays boundaries of raster layer containing areas with disparate values, in this case, the DEM coastline. Note that chart (mean lower low water) and map (mean tide) coastlines must be reconciled. While this difference is minimal for the Camp Pendleton demonstration site, it could be much greater for other worldwide locations.

### 3.6 Hydrology

Possible Data Sources: Hydrology raster layers include watershed basins, half watershed basins, slope, slope direction, accumulation, stream network, and infiltration parameters. Most of these layers are the result of processing a DEM. The infiltration parameter layers are created from soil type information. Therefore, the fundamental layers for hydrology are accurate DEM's and soil type maps. Hydrology layers are used as input layers to hydraulic models that produce time dependent hydrographs, runoff and infiltration layers.

Actual Data Source: USGS 30 meter DEM; USGS 1° by 1° DEM; Soil type maps from the Soil Conservation Service, U.S. Department of Agriculture;

Format: raster

Region: Initially four 7.5' quadrangle DEM's (Las Pulgas Canyon, Morro Hill, Oceanside, San Luis Rey) at 30 meter resolution were used. Subsequently, a 1° by 1° DEM at 3 second resolution that included nearly the entire Santa Margarita river watershed was used.

Remarks: Before any DEM is used to create layers for a hydraulic model, it must be checked for suitability, i.e., it must provide an accurate and satisfactory drainage surface, and may require editing. It should route water and not form pits, lakes, or ponds. Editing was primarily performed in the areas where roads crossed over rivers and streams and where river mouths spread out upon reaching the coastline using *d.rast.edit*. The edited digital elevation data was then input to the GRASS watershed utility *r.watershed*. The ocean area was masked (see BASEMAP 5: Coastline above) to prohibit computations in that area. The minimum exterior basin size threshold was set 200 cells. An exterior basin is a drainage basin into which no other basin drains. *r.watershed* output raster layers included accumulation (number of cells that drain through each cell), basins, half-basins, aspect (the direction of slope), and streams. *r.slope.aspect* was used to compute the slope.

For the demonstration area, the soil survey of San Diego county was obtained from the Soil Conservation Service (SCS), along with detailed soil type maps and a general soil map. No digital soil type data was available from the SCS or any local government agencies. Digitizing the actual soil types would prove to be too time consuming for this project, so the general soil map was digitized. The general soil map is 1:253,440 scale and contains soil association information. Infiltration parameters were assigned based on the predominant soil type for each digitized soil association. Soil type infiltration parameters are documented in (Rawls, et. al., 1983) The hydraulic model that was selected is called *r.water.fea*. For a discussion of the actual hydraulic model used, see a later section.

### 3.7 Bottom Types

Possible Data Sources: Any accurate maps that include printed bottom types designations may be used. Digital bottom type information is not available. In the absence of area coded designations, subjective assumptions based on isobath contours must be employed.

Actual Data Source: National Oceanic and Atmospheric Administration (NOAA) Nautical chart.

Format: Digitized vector areas subsequently converted to a raster layer.

Region: Complete coverage of the ocean area in the computational region, extending into the Gulf of Santa Catalina. Resolution: Original chart was 1:100,000 Mercator Projection NAD83.

Remarks: Bottom type information on the NOAA nautical chart was somewhat sparse. The nautical chart was scanned and rectified (see BASEMAP 1: Bathymetry above). The bottom types were then digitized using *v.digit* as areas, visually interpolating category boundaries. The vector layer was then converted to a raster layer using *v.to.rast*.

#### **4.0 Off-line BASEMAP Summaries**

Some BASEMAP layers involve extensive processing of existing data layers and are not suited to direct computation within the CWC model software. These layers include sediment and chlorophyll concentration and hydraulic model infiltration and runoff. These layers were computed using the concentration algorithms of Tassan (Tassan 1987) and a GRASS integrated model contributed by the University of Oklahoma for the off-line hydrologic calculations (Vieux and Gaur 1993).

##### **4.1 Sediment Concentration**

The basic procedure for computing sediment concentration,  $S$ , in  $\text{g/m}^3$  from LANDSAT-5 imagery is described in (Tassan, 1987). Two LANDSAT-5 images were ordered from EOSAT: January 23, 1993 and April 13, 1993. Both images were path 40, row 37 and were map products, projected using the Clark 1866 spheroid into UTM coordinates. The LANDSAT-5 imagery product was rectified into the GRASS database. Stripes were noticeable in the images, especially over the ocean. We made several attempts to destripe the images, however, no suitable algorithm was found and the images were processed including the stripes. The image digital numbers were converted to radiance values, using the procedure described in the EOSAT "Fast Format Document for TM Digital Products" that was shipped with the products. There are several methods to accomplish atmospheric correction. We chose a simple method that assumes the minimum radiance value is due to aerosol scattering in the atmosphere. Histograms for pixels over the ocean area were created and the minimum radiance value was subtracted from the entire scene. The scene was then filtered using a 5X5 spatial average filter. The sediment concentration may then be computed using the following equations:



$$\log(S) = (2.70 \pm 0.08) + (1.06 \pm 0.05) \log(R(660\mu))$$

where the spectral reflectivity at the satellite is given by

$$R(\lambda) = \frac{\pi n^2 L_w(\lambda)}{(1 - \rho) F^0(\lambda) \cos \theta^o}$$

where:

$n$  = refractive index of sea water ( $n=1.341$ )

$\rho$  = Fresnel reflectivity from below the water surface ( $\rho=0.021$ )

$F^o$  = true solar irradiance at the top of the atmosphere

202.7 mw/(cm<sup>2</sup>μ) for Band 1

184.8 mw/(cm<sup>2</sup>μ) for Band 2

157.5 mw/(cm<sup>2</sup>μ) for Band 3

103.5 mw/(cm<sup>2</sup>μ) for Band 4

$L_w$  = water upwelling spectral radiance

$\theta^o$  = solar zenith angle

The following suggestions would improve this computation:

- Implement a more accurate atmospheric correction algorithm.
- Destripe the original scene.

## 4.2 Chlorophyll Concentration

The chlorophyll concentration,  $C$ , in mg/m<sup>3</sup> is calculated in a manner very similar to the sediment calculation described in the preceding paragraph. There are differences which include the following:

Chlorophyll concentration values are valid in areas where the sediment concentration is below 5 g/m<sup>3</sup> and valid in the range  $0.1 < C < 17$  mg/m<sup>3</sup>. A mask was created that only allowed chlorophyll concentration analysis in those areas.

Chlorophyll concentration was computed using in terms of the spectral reflectivity given above the following equation:

$$\log(C) = (0.057 \pm 0.04) + (-2.73 \pm 0.19) \log(R(485\mu) / R(570\mu))$$

## 4.3 Hydraulic Modeling of the Santa Margarita Watershed

The Santa Margarita river is the only unimpeded river (i.e. no dams, spillways, etc.) emptying into the Pacific Ocean in Southern California. This unique feature makes the Santa Margarita river an attractive specimen for hydraulic modeling. The goal of the hydraulic model is to produce simulated hydrographs for event-based storm rainfall runoff. The hydraulic modeling software selected is the GRASS tool *r.water.fea*. The tool uses a finite element numerical technique to model kinematic overland and channel flow and a finite difference technique to compute time dependent hydrographs. Results of *r.watershed* can be used as input in the analysis. *r.water.fea* is a distributed and deterministic hydrologic model. It can analyze a given watershed and produce individual basin hydrographs, stream junction hydrographs, and individual basin flow depth animation maps. *r.water.fea* has the following limitations:

- Interstorm modeling, interflow, or baseflow are not considered.
- Backwater effects are not considered.
- The kinematic wave analogy is appropriate where the land surface slope and channel slope is large. this may not be true in flat, marshy terrain and in slow, meandering river channels.
- The drainage map should route the water and not form pits, lakes, or ponds. This does not imply that the DEM by itself should not have any pits.

The following summarizes the input required by *r.water.fea*:

- Accumulation, basin, stream network, slope and slope direction layers. These may all be computed using a DEM as input to *r.watershed* with the exception of the slope, which may be computed using *r.slope.aspect*.
- An ASCII file containing the time dependent rainfall rates. This file has two columns: the time in minutes relative to an arbitrary reference and the rainfall rate in cm/hr.
- The length of time for which you want to monitor the hydrograph
- Channel characteristics for each segment of the stream network. A channel cross section is approximated as an inverted trapezoid. You must input the length of the trapezoid bottom, the slope of the sidewall, and the

Mannings roughness coefficient for that segment of the stream network.

- Infiltration parameters for each basin. These parameters include the Mannings roughness coefficient, the saturated hydraulic conductivity (m/s), the capillary suction head at the wetting front (m), and the effective porosity. These parameters may be input individually for each basin over which they are constant, or they may be input as layers with varying values over all basins.
- The degree of saturation for each individual basin. This is input for each basin and cannot be input as a data layer.

The user interactively selects the basins to be included in the hydraulic model. The user also has the option to view basin level hydrographs and to view flow depth maps animated as a function of time.

Once the input process is complete, a hydrograph is computed that contains curves for each stream network junction and the final node in the network that reflects the time-dependent discharge for the entire modeled watershed.

The Santa Margarita river watershed was first modeled using four 1:24,000 scale 7.5' quadrangle DEMs with 30m resolution. The 15' x 15' region resolution was modified from 30m to 120m because the maximum number of basins that may be modeled is 15 and the suggested upper limit for the number of cells per basin was 750. The rainfall rate profile for the two squall storm event of January 23, 1993, was obtained from the National Weather Service. A mask was created so computations would only take place over the land area. *r.watershed* was run with an exterior basin threshold of 200 cells (0.0144 sq. km.). A very simple check that may be performed without any infiltration parameters and only requires the DEM and it's related layers and the rainfall rate profile, is to run *r.water.fea* and compute a hydrograph assuming total runoff, i.e.. zero infiltration. *r.water.fea* was run, using 15 basins to model the Santa Margarita watershed and the total runoff hydrograph curve is plotted in Figure 7, along with the measured discharge at a gauge station not far upstream from the river mouth. It is immediately apparent that the total runoff for the area modeled is less than the measured discharge. It is clear that more of the river watershed area must be modeled in order to predict the discharge accurately.

A 1:250,000 scale 1° x 1° DEM with 3" (3 arcsec) resolution covering virtually the entire Santa Margarita river watershed was obtained from the USGS via the Internet. The 3" resolution (roughly 92m x 73m) was modified to 500m x 500m for reasons explained in the preceding paragraph. A new mask was created so computations would take place over the land area only. Once again, a total runoff scenario was modeled. The hydrograph is plotted in Figure 7, and the discharge is now greater than the measured discharge, as it should be. The next step is to model the infiltration parameters. This was done by obtaining the soil survey for San Diego county from the Soil Conservation Service, U.S. Department of Agriculture. The survey consists of a two part report, describing the general soil map, descriptions of the individual soils and interpretations for various purposes. It also includes a general soil map and 76 detailed soil type maps, each corresponding to a USGS 7.5' quadrangle area. No digital soil data was available from any government agency. Digitizing the detailed soil type maps covering the watershed would be too time consuming, so the general soil map was digitized instead. The general soil map illustrates the location of various soil associations, not individual soil types. A soil association usually consists of two to four soil types that are similar in nature. Once the soil map was digitized, the association areas were reclassified using the Green and Ampt infiltration parameters based on soil type (Rawls, et. al., 1983), using the predominant soil type in the association as the soil type. The north-western area of the watershed is in Riverside county and was assumed to be a foothill area. Infiltration parameters were assigned similar to other foothill areas since a soil map of Riverside county was unavailable. A Mannings coefficient of 0.05 was used, reflecting the lack of vegetation and rocky surface predominant in the region. River channels were assumed to be 15m wide with side slopes of 1:20 and Mannings coefficients of 0.05. Published infiltration parameters (Rawls, et. al., 1983) were used with the exception of the saturated hydraulic conductivity which can vary significantly. It was divided by a factor of 6 for the demonstration case, which was a reflection of the nature of the thin hard layer covering lower layers of soil in the region decreasing the conductivity. Previous rainfall in the area had nearly saturated the soil and a saturation of 95% was assumed for all basins.

The model was simulated for 24 hours with 3 minute timesteps. The resulting hydrograph is plotted in Figure 7. It compares favorably with the measured discharge at the gauge station, although it is slightly lower. The measured discharge rate increases earlier than

the simulation because of the size of the simulated basins. Note that the first simulation using smaller basins also displays an earlier rise in discharge rate.

The following are suggestions to improve the model. The use of digital soil type maps rather than general soil maps to assign infiltration parameters would result in a more accurate representation of infiltration. Also, modification of *r.water.fea* to allow the use of more, smaller basins would result in a more accurate model, especially early in the simulation. It is important to note that using a DEM that encompasses the entire watershed is a necessity. Failure to do so can result in underestimation of the discharge rate profile.

## REFERENCES

Rawls, W.J., Brakensiek, D.L., and Miller, N., "Green-Ampt Infiltration Parameters fro Soils Data", American Society of Civil Engineers' Journal of Hydraulic Engineering, Vol. 109 No. 1, 1983, pp. 62 - 70.

Tassan, S., "Evaluation of the Potential of Thematic Mapper for Marine Application", International Journal of Remote Sensing, 1987, Vol. 8 No. 10, pp. 1455-1478.

Vieux, Baxter, and Gaur, Nalnees, "Performing Hydrologic Simulation in GRASS 4.2: r.water.fea Program Tutorial", U.S. Army Corps of Engineers, 1993.



Digital Elevation Model and Bathymetry  
Digital bathymetry is shown over the ocean.  
USGS digital elevation model (DEM) with 50m  
contours is shown over the land. Streams  
computed from the DEM are shown in blue.

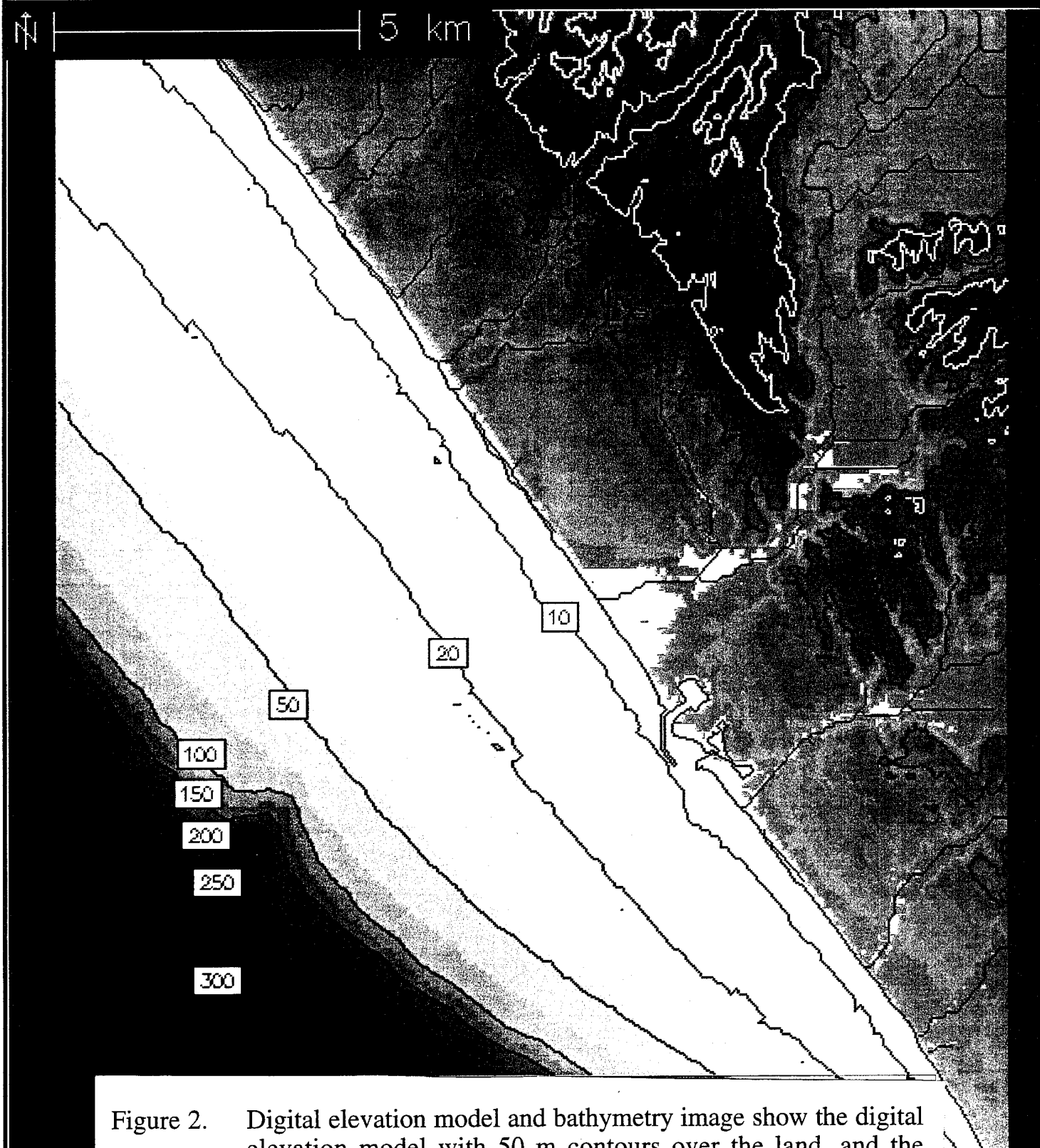


Figure 2. Digital elevation model and bathymetry image show the digital elevation model with 50 m contours over the land, and the bathymetry contours over the ocean



LANDSAT-5 LULC and NOAA Ocean Bottom Types  
 Unsupervised classification of LANDSAT-5 Bands  
 2,3,4,5 resulted in the 15 categories displayed  
 in the legend. Ocean bottom types were digitized  
 from an NOAA nautical chart.

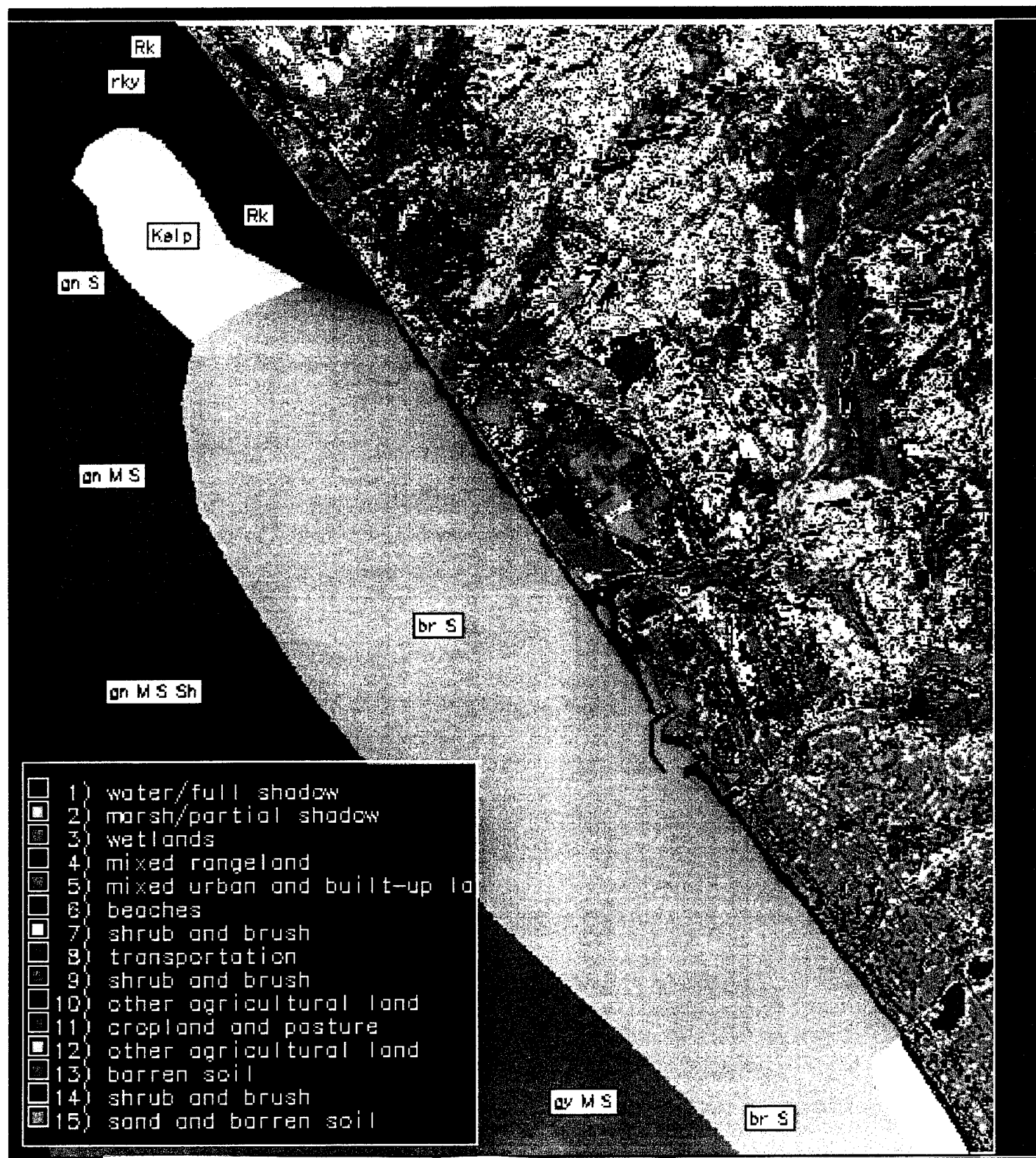


Figure 3. LANDSAT-5 LULC and NOAA ocean bottom types image shows unsupervised classification of LANDSAT-5 Bands 2, 3, 4, and 5

USGS LULC and NOAA Ocean Bottom Types  
 1:250K Scale USGS Land Use and Land Cover Data  
 is shown over the land and category values are  
 displayed in the legend. Ocean bottom types were  
 digitized from an NOAA nautical chart.

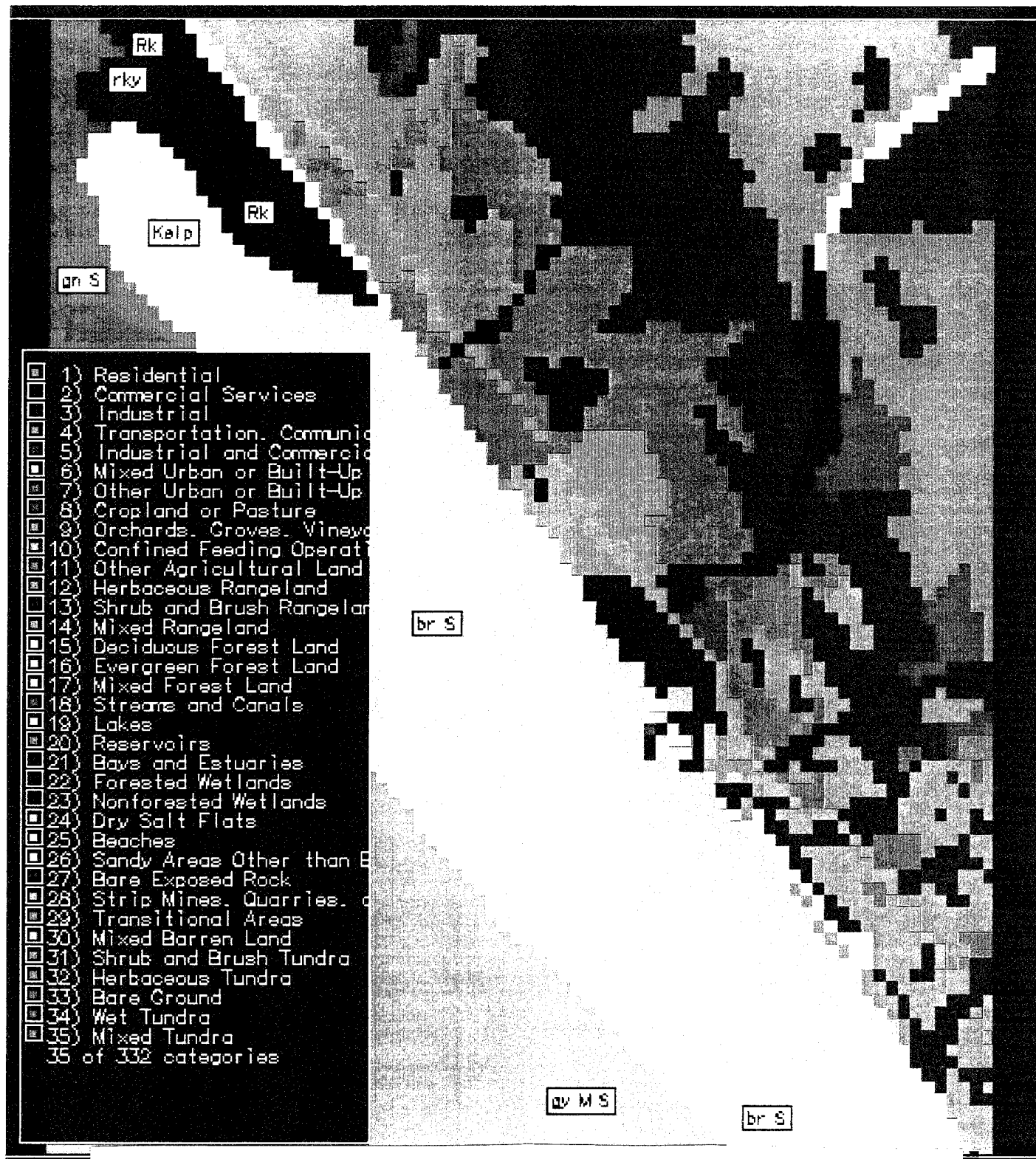


Figure 4. USGS LULC and NOAA ocean bottom types image show scaled USGS land use and land cover data over the land

## NDVI and Bottom Types

The Normalized Digital Vegetation Index (NDVI) was computed from a LANDSAT-5 image. The NDVI has a range 0-100. Bottom types were digitized from an NOAA nautical chart.

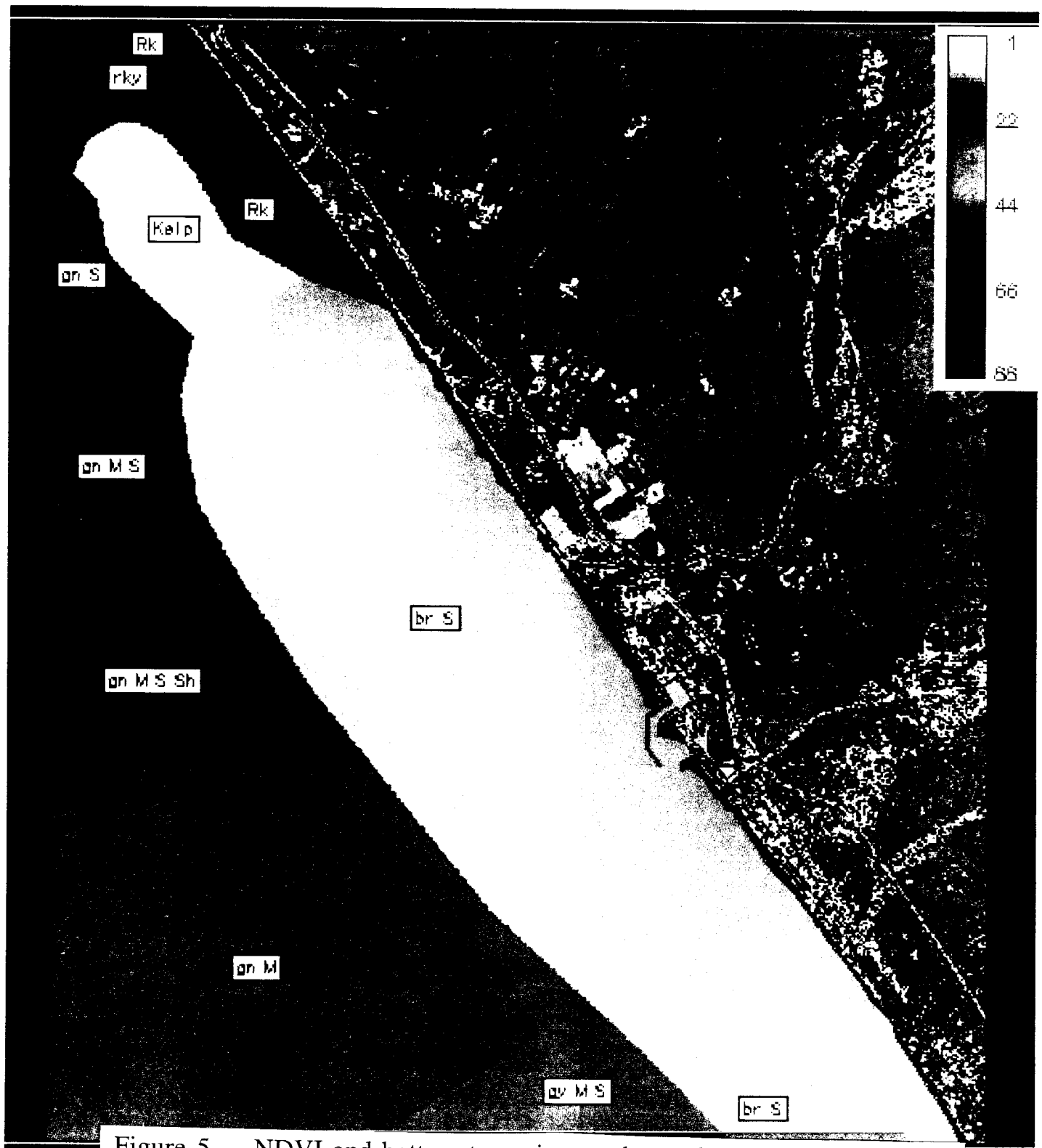


Figure 5. NDVI and bottom types image shows the Normalized Digital Vegetation Index (NDVI) that was computed from a LANDSAT-5 image

## Scanned USGS Quadrangle Detail

This picture illustrates the detail available for digitizing using 150 dpi scanned images. Elevation contours, rivers, roads, etc. may all be easily digitized from this captured digital image.

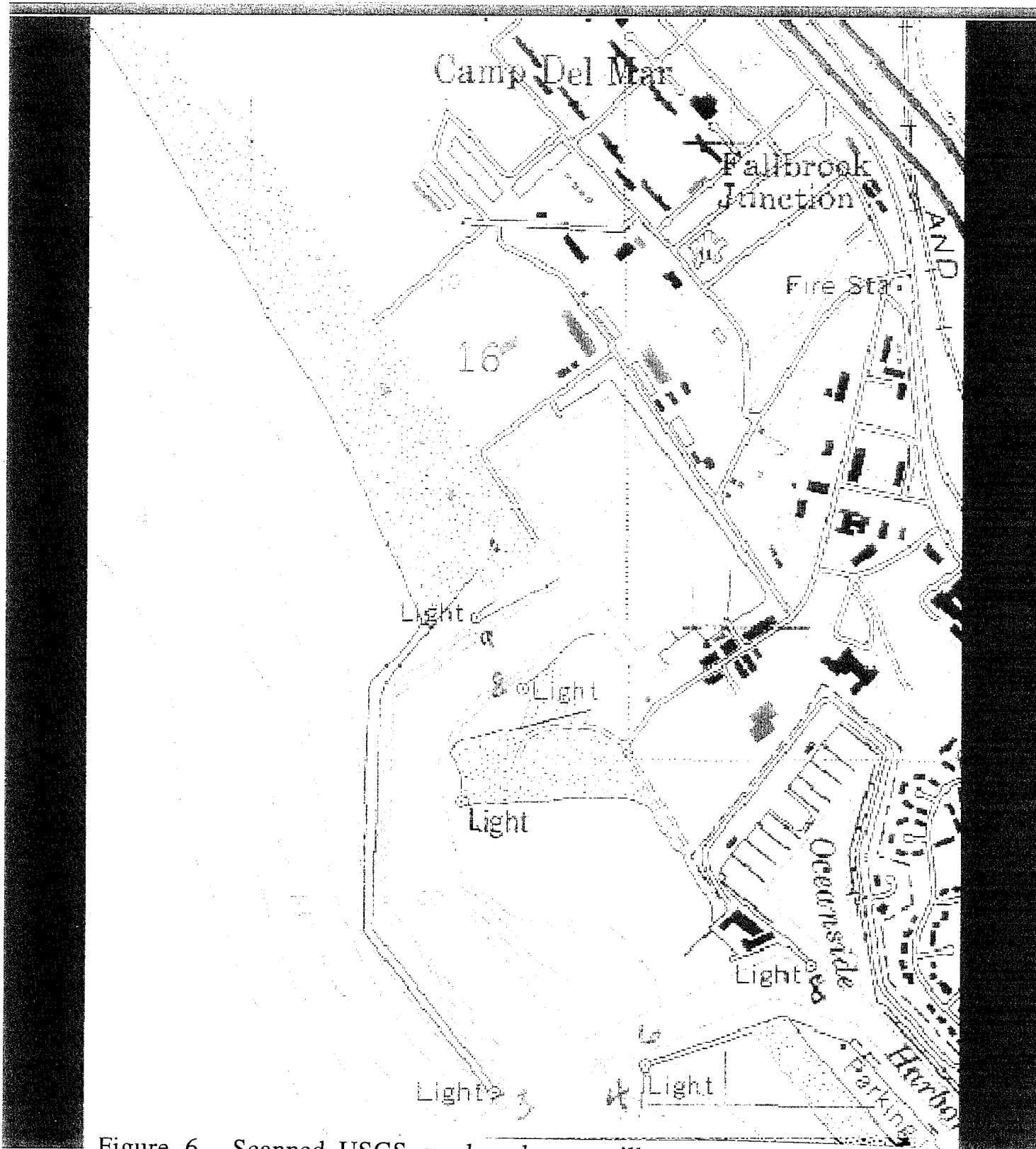


Figure 6. Scanned USGS quadrangle map, illustrates level of detail available for digitizing, using 150 dpi scanned images

# **Discharge Sensitivity of the Santa Margarita River Watershed as a Function of Drainage Area and Terrain Model Parameters**

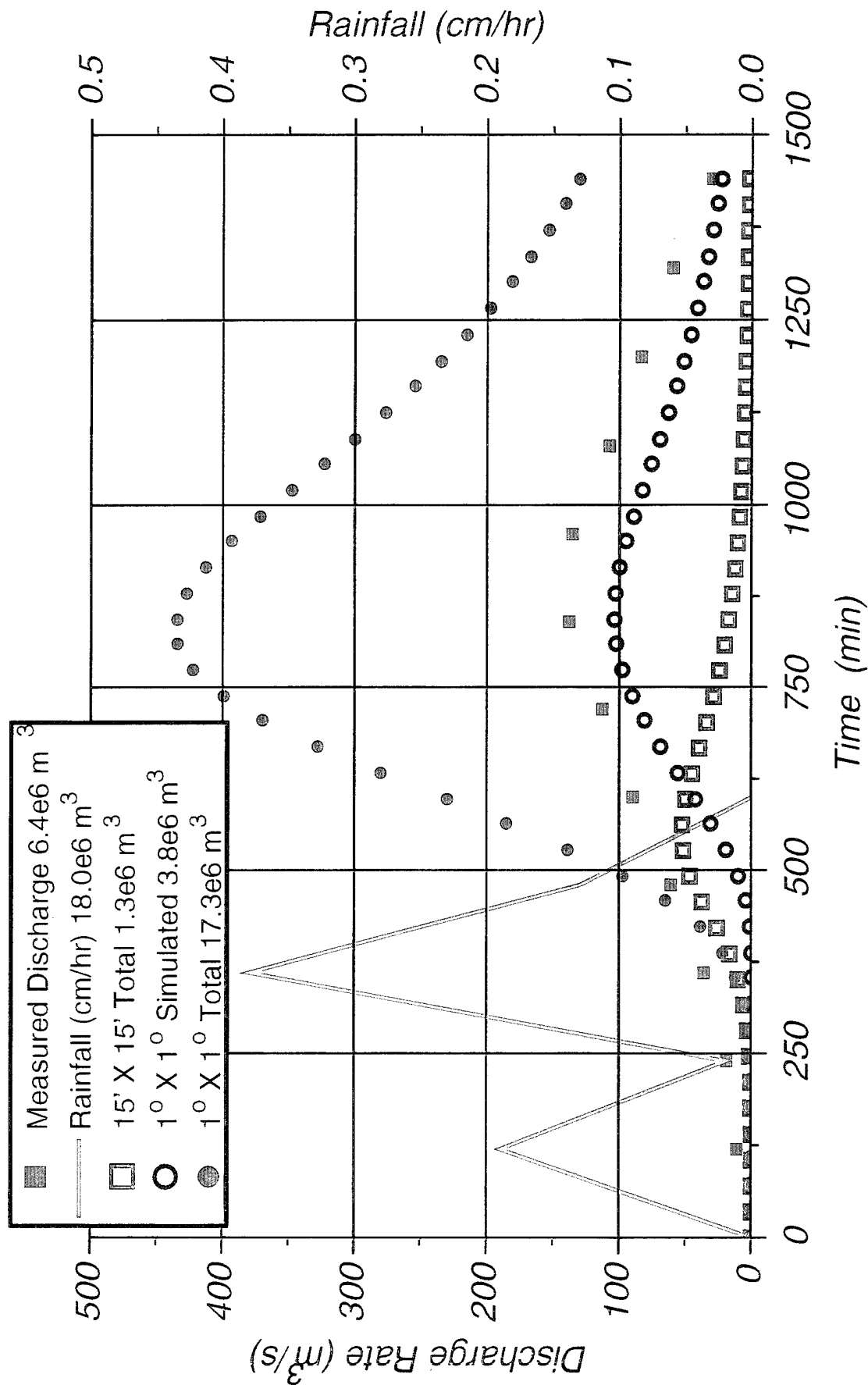


Figure 7. Discharge sensitivity of the Santa Margarita River Watershed as functions of drainage area and terrain model parameters